2010

Investigations of Structure / Property Interrelationships of Organic Thin Films Using Scanning Probe Microscopy and Nanolithography

Zorabel Mallorca LeJeune
Louisiana State University and Agricultural and Mechanical College

Recommended Citation

LeJeune, Zorabel Mallorca, "Investigations of Structure / Property Interrelationships of Organic Thin Films Using Scanning Probe Microscopy and Nanolithography" (2010). *LSU Doctoral Dissertations*. 1151.
https://digitalcommons.lsu.edu/gradschool_dissertations/1151

INVESTIGATIONS OF STRUCTURE / PROPERTY INTERRELATIONSHIPS OF ORGANIC THIN FILMS USING SCANNING PROBE MICROSCOPY AND NANOLITHOGRAPHY

A Dissertation
Submitted to the Graduate Faculty of the
Louisiana State University and
Agricultural and Mechanical College
in partial fulfillment of the
requirements for the degree of
Doctor of Philosophy

in

The Department of Chemistry

by
Zorabel Mallorca LeJeune
B.S., University of the Philippines Los Banos, 1999

December 2010

DEDICATION

I want to dedicate this work to my parents, Jessie and Remedios Mallorca for instilling the value of education in the family; my brother, Franco Lambatin for his assistance and sacrifices for my education; and my husband, Jason Paul LeJeune, for believing in me and for his undying patience and support.

ACKNOWLEDGEMENTS

I would like to thank my research professor, Dr. Jayne Garno for all the mentorship on my graduate career. Her constant support, help and guidance are always and forever be appreciated. I am grateful to Kermit Murray, Phillip Sprunger, Doug Gilman, M. Graca H. Vicente and Jeffrey Hanor for serving on my advisory committee. I would like to extend my gratitude to Eizi Morikawa and Pingheng Zhou of the Center for Advanced Microstructures Devices (CAMD) for all the help in EXAFS and FTIR experiments. I would like to thank all graduate and undergraduate members of the Garno group for the intellectually stimulating discussions inside and outside the laboratories. My sincere gratitude goes to my graduate student mentors, Johnpeter Ngunjiri and Jie-Ren Li for helping me get established with the Garno Research Group. I would also like to acknowledge Stephanie Daniels, Kathie Lusker, Wilson Serem for the all the help, challenges, fun and company during my graduate student years. My special thanks go to Kathie Lusker and Nicholas Gariano for their support and assistance in preparing this manuscript.

TABLE OF CONTENTS

LIST OF TABLES

LIST OF FIGURES

LIST OF SCHEMES

LIST OF ABBREVIATIONS

AFM	Atomic Force Microscopy
CAD	Computer Assisted Design
CMPS	Chloromethylphenyl Trichlorosilane
CPMD	Car-Parrinello Molecular Dynamics
CSAFM	Current-Sensing Atomic Force Microscopy
CP-AFM	Conductive Probe Atomic Force Microscopy
DCM	Dichloromethane
DFT	Density Functional Theory
DNA	Deoxyribonucleic Acid
DPN	Dip Pen Nanolithography
DPP	5,10-diphenyl-15,20-di-pyridin-4-yl-porphyrin
DSU	Dithiobis(Succinimidyl Undecanoate)
EDC	1-Ethyl-3-(3-Dimethylaminopropyl) Carbodiimide Hydrochloride
FACSS	Federation of Analytical Chemistry & Spectroscopy Societies
F-OPE	Monofluoro-Substituted Oligo(Phenylene-Ethynylene)
GIXD	Grazing Incidence X-Ray Diffraction
HCl	Hydrochloric Acid
HOMO	Highest Occupied Molecular Orbital
HOPG	Highly Oriented Pyrolytic Graphite
IR	Infra Red
ITO	Indium-Tin-Oxide
I-V	Current – Voltage
LON	Local Oxidation Nanolithography
LUMO	Lowest Unoccupied Molecular Orbital
MHA	16-Mercaptohexadecanoic Acid
MUA	11-Mercaptoundecanoic Acid
MUD	11-Mercaptoundecanol
NEXAFS	Near-Edge X-Ray Absorption Fine Structure
NMR	Nuclear Magnetic Resonance
NPRW	NanoPen Reader and Writer
NSOM	Near-Field Scanning Optical Microscopy
ODT	Octadecanethiol
OLED	Organic Light Emitting Diodes
OPA	Octadecylphosphonic Acid
OTE	Octadecyltriethoxysilane
OTS	*n*-Octadecyltricholorosilane
PDMS	Poly(Dimethylsiloxane)
SAS	Society for Applied Spectroscopy
SAM	Self-Assembled Monolayer
SNP	Scanning Near-Field Photolithography
SPIE	Society of Photo Optical Instrumentation Engineers
SPM	Scanning Probe Microscopy
SPL	Scanning Probe Lithography
ssDNA	single-stranded DNA
STM	Scanning Tunneling Microscopy

TLC	Thin Layer Chromatography
UHV	Ultra High Vacuum
UV	Ultra Violet
UV-Vis	Ultra Violet-Visible

ABSTRACT

Studies of the surface assembly and molecular organization of organic thin films were studied using scanning probe microscopy (SPM) and scanning probe lithography (SPL). Systems of organic thin films such as *n*-alkanethiols and pyridyl functionalized porphyrins were characterized at the molecular level, and measurements of the conductive properties of polythiophenes containing in-chain cobaltabisdicarbollides were accomplished. Understanding the self-organization and mechanisms of self-assembly of organic molecules provides fundamental insight for structure/property interrelationships. Investigations of the surface assembly of 5,10-diphenyl-15,20-di-pyridin-4-yl-porphyrin (DPP) on Au(111) were done using SPL methods of nanoshaving and nanografting. Automated computer designs were developed for nanofabrication to provide local characterizations of the thickness of DPP films and nanostructures. Nanolithography was accomplished using DPP films as either matrix self-assembled monolayers (SAMs) or as molecules for nanofabrication. Results presented in this dissertation demonstrate that DPP forms compact layers on Au(111), which can be used for inscribing nanopatterns of *n*-alkanethiols. Arrays of DPP nanopatterns with precise geometries and alignment were fabricated within *n*-alkanethiols by nanografting, demonstrating nanoscale lithography with pyridyl porphyrins can be accomplished to produce an upright surface orientation on Au(111) mediated by nitrogen-gold chemisorption. Beyond research investigations, the applicability of atomic force microscopy (AFM) and advancements with automated SPL were applied for teaching undergraduate chemistry laboratories to introduce the fundamentals of surface chemistry and molecular manipulation. New classroom activities were developed for the Chemistry 3493 Physical Chemistry laboratory to give students “hands-on” training with AFM. Undergraduates were trained to prepare nanopatterns of *n*-alkanethiols using software to control the position, force and speed of the AFM tip for nanolithography experiments**.** The sensitivity and nanoscale resolution of current sensing AFM was applied for studies of the conductive properties of electropolymerized thin films of polythiophenes with cobaltabisdicarbollide moieties. Images acquired with AFM furnished views of the morphology of different polymers prepared on gold surfaces. Surface maps of the conductivity of electropolymerized films were acquired with AFM current images. These studies provide new insight of the effects of the bound cobaltabisdicarbollide moiety and coordinated metal centers for the electronic properties of the resulting conducting materials.

CHAPTER 1. INTRODUCTION

The exquisite resolution and precision obtainable with scanning probe microscopy (SPM) enables studies of molecular organization, self-assembly and chemical binding processes on surfaces. The associated physical properties of samples can be investigated at the nanometer scale because of the unprecedented sensitivity of SPM. The main objectives of this dissertation were to develop strategies to investigate the surface assembly of n-alkanethiols and pyridyl-functionalized porphryins; and measure the conductive properties of specific systems, such as organic thins of polythiophenes with cobaltabisdicarbollide moieties and electropolymerized carboranyldithiophenes using SPM. Methods of scanning probe microscopy (SPM) and nanolithography were the tools applied in this dissertation to investigate chemical reactions, surface structures and properties of nanomaterials and organic thin films. Our goals were to achieve new fundamental insight of structure-property relationships for surface reactions. Investigations of surface properties and processes at the molecular level will help advance the field of molecular electronics towards new discoveries for sensing and energy applications.

1.1 AFM Based Nanofabrication with Self-assembled Monolayers

Scanning probe lithography (SPL) is one of the nanofabrication techniques which can be applied for writing nanometer-sized surface patterns of designed chemistry. Combined with computer automation, SPL can be used to create surface patterns ranging from nanometer to micrometer sizes with precise alignment, spacing and arrangement on surfaces. A contemporary review of SPL methods in Chapter 2 highlights the exquisite resolution and precision that can be achieved with SPM-based lithography with self-assembled monolayers(SAMs).[1] Scanning probe instruments used for nanofabrication of SAMs include scanning tunneling microscopy (STM), atomic force microscopy (AFM) and near-field scanning optical microscopy (NSOM). Scanning probe microscopes have progressed beyond basic use as an imaging tool, to become a primary technique for physical measurements of material properties, as well as a tool for manipulation of atoms and molecules at the nanoscale. Approaches for SPL with self-assembled monolayers (SAMs) are reviewed and summarized from research with methods of nanoshaving, nanografting, Dip-Pen Nanolithography (DPN), NanoPen Reader and Writer (NPRW), bias-induced lithography, catalytic probe lithography, and NSOM lithography.

1.2 Automated Scanning Probe Lithography with n-Alkanethiol Self Assembled Monolayers on Au(111): Application for Teaching Undergraduate Laboratories

Controllers for scanning probe instruments can be programmed for automated lithography to generate desired surface arrangements of nanopatterns of organic thin films, such as *n*-alkanethiol self-assembled monolayers (SAMs).[2-4] In Chapter 3, atomic force microscopy (AFM) methods of lithography known as nanoshaving and nanografting were used to write nanopatterns within organic thin films. Commercial instruments provide software to control the length, direction, speed, and applied force of the scanning motion of the tip. For nanoshaving, higher forces are applied to an AFM tip to selectively remove regions of the matrix monolayer, exposing bare areas of the gold substrate. Nanografting is accomplished by force-induced displacement of molecules of a matrix SAM, followed immediately by the surface self-assembly of *n*-alkanethiol molecules from solution.

Advancements in AFM automation enable rapid protocols for nanolithography, which can be accomplished within the tight time restraints of undergraduate laboratories. Example experiments with scanning probe lithography (SPL) are described in Chapter 3 that were accomplished by undergraduate students during laboratory course activities and research internships in the chemistry department of Louisiana State University.[3] Students were introduced to principles of surface analysis and gained “hands-on” experience with nanoscale chemistry. For this report, reproduced by permission from the *Journal of the Association for Laboratory*

Automation, works from three undergraduate researchers were showcased as examples of the capabilities of SPL for student laboratories and research activities. One of the LSU students mentored, Ms. Treva T. Brown received a prestigious 2009 ALA Young Scientist Award from the Analytical Systems Digital Library under my direction. In this chapter, work is consolidated and summarized from several years of effort in directing and mentoring undergraduate research projects based on SPL and high resolution imaging with SPM.

1.3 Surface Assembly of Pyridyl-Substituted Porphyrins on Au(111) Investigated *In Situ* Using Scanning Probe Lithography

A new direction progressing beyond studies with *n*-alkanethiols as a model molecular system was established for this dissertation. Applications of nanografting have been limited to creating patterns with thiol-based chemistries on gold substrates through sulfur-gold chemisorption. Chapter 4 demonstrates that pyridyl-functionalized porphyrins are potentially a new class of self-assembled monolayers which can be grafted directly onto surfaces of Au(111), most likely mediated through nitrogen-gold chemisorption.[5] Our practical goals were to use SPM for studying a more complex and robust system of conjugated molecules such as porphyrins which have valuable technological applications due to inherent photoemissive and photoconductive properties. Our goals were to develop new AFM-based protocols for *in situ* studies in solution, whereas most studies of these systems have been accomplished either in air or UHV environments using STM. Scanning probe characterizations of porphyrin patterns prepared by nanografting in liquid media were accomplished, which provide insight for the molecular orientation and surface assembly of porphyrins bearing pyridyl and phenyl substituents. *In-situ* AFM provides highly local views of the assembly of pyridyl-substituted porphyrins on surfaces of Au(111). Matrix self-assembled monolayers (SAMs) of *n*-alkanethiols were used as a molecular ruler for gauging height measurements. Nanografting was used as an *in situ* tool for local measurements of the thickness of porphyrin films providing side-by-side comparisons against the heights of *n*-alkanethiol nanopatterns. As previously shown for *n*-alkanethiols on Au(111), nanografting alters the assembly pathway through a mechanism of spatial confinement.[6] When nanografted, pyridyl porphyrins were shown to assemble onto gold directly into an upright configuration rather than adopting a coplanar arrangement. The studies presented in Chapter 4 provide further corroborative evidence that steps of surface self-assembly can be altered when nanografting by spatial confinement; thus nanografting provides a tool for controlling molecular orientation.

1.4 Assembly of 5,10,15,20-di-pyridin-4-yl-porphyrin on Au(111) from Mixed Solvents

The mechanism of the surface assembly of porphyrins from solution results from complex intermolecular interactions and the affinity for surface binding. The binding interactions between peripheral groups and the surface as well as the influence of pi-pi stacking between macrocycles dictate the resulting configuration and organization for structures that form. In Chapter 5, high resolution AFM imaging combined with scanning probe lithography was used for investigations of the surface structures that form by natural solution-based assembly and compared to artificial nanostructures prepared by the spatially confined assembly mechanism of nanografting for 5,10-diphenyl-15,20-di-pyridin-4-yl-porphyrin (DPP).[7] Our goals were to understand the mechanisms of solution-based assembly of pyridyl-functionalized porphyrins and to develop new molecular test platforms for measurements of surface properties. By comparing porphyrins with different molecular designs, experiments with SPM and SPL were used to gain insight for structure-property relationships. *In situ* AFM experiments disclosed that for spontaneous self-assembly processes, monolayers of DPP from ethanol/dichloromethane solutions form mixed monolayers with two distinct configurations on Au(111), exhibiting phase segregated domains. Nanoshaving and nanografting provide an *in situ* tool for local measurements of the thickness of DPP films with angstrom precision. High resolution AFM images of DPP reveal that two distinct phase segregated domains of different heights were formed over time. One phase corresponds to the height of a lying-down arrangement of DPP with the macrocycle adapting a coplanar orientation. The thickness of the second phase corresponds precisely to the theoretical height of a 90 degree perpendicular orientation of the molecules (an upright, standing configuration), with two pyridyl groups attached to the surface. The surface coverage of the upright domains increased over time to near saturation. However, for structures of DPP nanografted within a matrix monolayer of alkanethiol SAMs under the conditions of spatial confinement, the heights of nanopatterns correspond to an upright orientation. Complicated designs and geometries of DPP patterns were successfully created by nanografting DPP within matrix SAMs of *n*-alkanethiols of different chain lengths (decanethiol, dodecanethiol, octadecanethiol). In collaborative work with Professor Bin Chen, models with energy minimized structures of pyridyl-substituted porphyrins on Au(111) were computed using Car-Parrinello Molecular Dynamics (CPMD) that corroborate results with AFM.

Results of this research project were disclosed in presentations and garnered the best poster awards at conferences both at Pittcon 2010 in Orlando Florida; and at the Society for Applied Spectroscopy (SAS) symposium during the 34th National Meeting, Federation of Analytical Chemistry & Spectroscopy Societies (FACSS 2007) in Memphis, TN. Also, this research was recognized as one of the finalists for the best poster awards for Material Systems and Processes for Three-Dimensional Micro- and Nanoscale Fabrication and Lithography symposium in 2009 Materials Research Society Spring Meeting in San Francisco, CA.

1.5 Polythiophenes Containing In-Chain Cobaltabisdicarbollide Center

New cobalt(III) bis(dicarbollide) complexes covalently linked to two 2-oligothienyl units were synthesized and electropolymerized to produce the corresponding polythiophene films containing in-chain metallic centers.[8] The incorporation of the metal center in the conjugated chain is expected to improve electronic conductivity and magnetic and optical properties of metallopolymers. The goal of this project was to establish a new unprecedented conducting metallopolymers using metalla-bisdicarbolide complexes. My role was to furnish molecular details of AFM surface studies and conducting probe measurements of charge transport for these novel systems. Detailed characterizations using electrochemistry, UV-Vis spectroscopy and scanning probe microscopy (tapping mode and conducting probe AFM) are presented in Chapter 6, towards understanding how the bound cobaltabisdicarbollide moiety influences the electronic properties of the resulting conducting materials. The polymer films that were electrogenerated from the bithienyl and terthienyl derivatives display redox processes, yielding conducting polymer deposits on the electrode surface. In contrast, the electrochemical oxidation of thienyl units resulted in the gradual passivation of the electrode surface, with no conductive polymers observed. Analysis with UV-Vis spectroscopy demonstrated that the polymer incorporating the sexithienyl segments is more conjugated than that with the quaterthienyl segments. Conducting probe AFM characterizations indicate that polymers with bithienyl and terthienyl behave like heavily doped semiconductors rather than pure semiconductors. The current-voltage (I-V) profile for poly- thienyl exhibits no measurable current over the range of applied voltage which is consistent with the insulating character of the film. Substantial differences for the morphologies of the polymer films were apparent for comparisons with tapping mode AFM. The studies reported in Chapters 6 result from an international collaboration with Professor Bruno Fabre of the Université de Rennes, who is an expert in the area of electrochemistry. Professor M. Graca H. Vicente of the LSU chemistry department contributed expertise in organic synthesis, for accomplishing research overall with a broad interdisciplinary focus.

Conjugated polymers have promising applications in the semiconductor industry for microelectronics, photovoltaics, organic light emitting diodes (OLED), organic field effect transistors, electrochemical switching, and chemical and physical sensing. Structure-property relationships are important in advancing the design and synthesis of conjugated polymers for molecular electronic applications.[9-10]

CHAPTER 2. AFM-BASED NANOFABRICATION WITH SELF-ASSEMBLED MONOLAYERS*

2.1 Introduction

Scanning probe lithography (SPL) is an emerging family of techniques which can be applied for writing nanometer-sized surface patterns of designed chemistry. One of the main advantages in comparison to other nanoscale lithographies is that the versatile approaches of SPL not only enable nanofabrication with designed size and geometry, but also provide precise control of the chemistry on surfaces, as determined by the choice of molecules for writing. The exquisite resolution and precision of scanning probe microscopy (SPM) has brought an evolution of new methods and experimental configurations which can be valuable for multiple disciplines. One can easily predict that SPL will advance new discoveries for future science. This chapter will focus on the scanning probe based lithographies which have been applied to write nanostructures of self-assembled monolayers (SAMs). The chemistry of SAMs has been used previously to tailor the selectivity of surfaces as pattern transfer molds,[11-12] etch resists[13-14] and for microcontact printing.[15-17] To evolve to the next generation of miniaturization at the nanoscale, the immediate benefits of SPL are to enable researchers to probe the fundamental limits of measuring molecular properties and to contribute to the fundamental knowledge of chemical binding, surface organization and self-assembly.

An overview of the various lithography methods according to the type of SPM instrument is presented in Figure 2.1. Scanning probe techniques applied for nanofabrication of SAMs include scanning tunneling microscopy (STM), atomic force microscopy (AFM) and near-field scanning optical microscopy (NSOM). Note that bias-induced lithography can be accomplished using either scanning tunneling microscopy (STM) or conductive-probe AFM. Scanning probe

---

*Reproduced with permission from American Scientific Publishers.

microscopes furnish tools for visualization, physical measurements and precise manipulation of atoms and molecules at the nanometer scale. The additional tools attainable with AFM for nanoscale lithography are accessible to investigators across a broad range of disciplines and do not require expensive instrument modification. In fact, most SPM manufacturers have developed software to give operators complete control of SPL parameters such as the speed, bias, force, direction and residence time of the scanning probe. To progress to the smallest sizes, SPL can be applied to define surface patterns at either nanometer or micrometer scales. With computer automation, the arrangement, alignment and spacing of patterns can be defined precisely at the scale of nanometers.

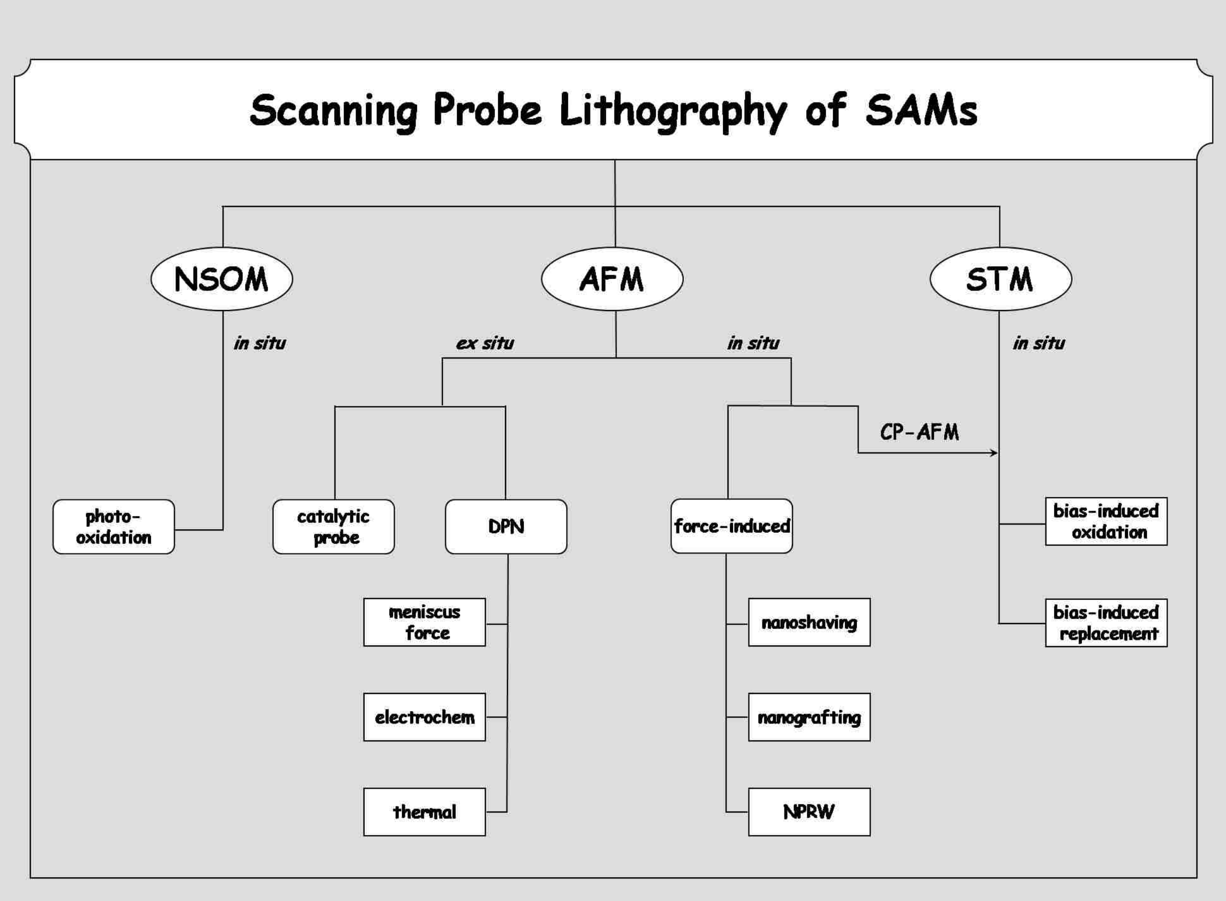

Figure 2.1 Overview of the most commonly used scanning probe lithography methods for nanofabrication of self-assembled monolayers.

There are several key differences when comparing SPL methods beyond the choice of instrument, such as the mechanism of writing, the type of chemical changes that can be achieved, and whether characterization of nanopatterns can be accomplished *in situ*. The writing mechanisms and changes in surface chemistry will be detailed in succeeding sections of this chapter. Lithography methods which enable *in situ* characterization of surface changes use the same SPM probe for writing and subsequent interrogation of the nanostructures that were written. Often, the various steps to modify the surface chemistry of nanopatterns can be accomplished without removing the sample or tip, provided that the tip is not damaged or altered by the fabrication process. There are a few SPL methods such as Dip-Pen Nanolithography (DPN) and catalytic probe lithography which require the use of different probes for the steps of writing and characterizing surface patterns, and these have been categorized as *ex situ* methods. Combined with the capabilities for high-resolution imaging and characterization, SPM enables a molecular-level approach for visualizing changes that occur on surfaces after successive steps of chemical reactions. In essence, SPL furnishes a new variable for experiments by providing a means to manipulate or alter the chemistry of local regions of surfaces. Very small areas of designed chemistry can be inscribed on surfaces with defined reactivity for binding nanoparticles, proteins and other molecules. After the nanopatterned surface is subjected to various chemical treatments, changes in the morphology and thickness of the nanopatterns can assist in the interpretation of surface kinetics and reaction mechanisms.[6,18-19]

Detailed information about the operating principles of SPM instruments can be found in previous publications for AFM,[20-24] STM [25-29] and NSOM.[30-32] The SPM methods for writing patterns are based on an operating platform which uses electronic controllers for piezoelectric positioning of a surface probe. The feedback loop for tip-positioning and mechanisms of surface characterization are quite different for AFM, STM and NSOM; and likewise provide a range of approaches for nanofabrication. The probe for an STM instrument is a conductive metal wire brought within tunneling range of the surface. The imaging and fabrication accomplished with STM are obtained at a proximal distance from the surface, within tunneling range of < 1 nm. Lithography using NSOM is also accomplished in non-contact operation, within the optical near-field regime. For NSOM lithography, a specially constructed aluminum-clad fiber optic probe transmitting light is scanned at a certain distance from the sample. In contrast, AFM-based lithography and imaging usually involve direct contact of the scanning probe with the surface.

The primary consideration for choosing an SPL method is the desired surface chemistry and environment for imaging. A useful analogy is to consider the SPM tip as a '*pen*' which writes molecular '*ink*' on various surfaces or '*paper*.' A comparison of SPL methods using this simple analogy is presented in Table 2.1. The summary focuses on the most widely applied methods for writing nanopatterns of SAMs; there are other specialized SPL methods reported for different surfaces and systems of molecules and nanomaterials which are beyond the scope of this chapter. The table presents a brief synopsis of SPL methods, comparing the mechanism of writing, the environment (ambient air or liquids) as well as the outcome of the chemical or physical changes to the surface. The detailed steps for writing nanopatterns and recent research which apply these methods for the fabrication of SAMs will be presented in later sections. The chapter will begin with a general discussion of the chemistry of SAMs, followed successively by details of force-induced lithography methods of nanoshaving and nanografting. Further sections will describe "Dip-Pen" methods of nanolithography (DPN), NanoPen Reader and Writer (NPRW), and catalytic probe lithography with SAMs. Recent developments in SPL that are evolving with bias-induced lithography methods and NSOM photooxidation of SAMs will also be presented. The chapter concludes with a prospectus of future directions in automated SPL.

Table 2.1 Mechanisms for writing SAM nanopatterns.

SPL method	pen	paper	environment	protocol	writing mechanism	surface chemistry
nanoshaving	bare AFM tip	SAMs including silanes, thiols	air or liquid	*in situ*	force & sweeping tip motion	**uncovered areas of substrate**
nanografting	bare AFM tip in a SAM solution	thiol SAMs/Au	liquid	*in situ*	force & solution replacement	**diverse functional groups of SAMs**
Dip-Pen Nanolithography (DPN)	coated AFM tip	clean, uncoated surfaces	air	*ex situ*	meniscus liquid transfer	**diverse functional groups of SAMs & other materials**
electrochemical DPN	thiol-coated AFM tip	clean, uncoated surfaces	air	*in situ*	Local surface oxidation	**electrochemistry**
thermal DPN	thiol-coated AFM tip	clean, uncoated surfaces	air	*in situ*	heating of tip for deposition of polymer inks	**heating**
NanoPen Reader and Writer (NPRW)	thiol-coated AFM tip	thiol SAMs/Au	air or water	*in situ*	force & molecular replacement	**diverse functional groups of SAMs**
catalytic probe lithography	AFM tip coated with a catalyst	SAM surface groups	air or liquid	*ex situ*	local tip-induced hydrolysis	**patterns written by localized catalysis**
bias-induced oxidation	biased STM or AFM tip in air	conductive or semi-conductive substrates	air	*in situ*	surface oxidation via electrochemistry in the water meniscus between the tip and surface	**oxidized SAMs**
bias-induced replacement	biased STM or AFM tip in a SAM solution	conductive or semi-conductive substrates	liquid	*in situ*	displacement of SAMs under elevated bias & successive replacement	**diverse functional groups of SAMs**
NSOM photooxidation	NSOM probe	SAMs	air	*in situ*	photooxidation of irradiated areas of the SAM	**photooxidized SAMs**
NSOM photoconversion	**NSOM probe**	**SAMs**	**air**	***in situ***	**photoconversion of terminal groups irradiated by the probe**	**photochemistry**

2.2 Surface Chemistry of Self-Assembled Monolayers

Self-assembled monolayers of alkanethiols and alkylsilanes have been applied for surface modification,[15,33-35] corrosion inhibition,[36-38] biosensor design,[39-42] and molecular device fabrication.[43-44] The synthetic flexibility of SAMs provide advantages for designing the chemistry of surfaces with desired spacer lengths and functional groups.[45-46] The surface properties such as wettability, acidity and adhesion can be controlled by choosing the functional headgroups of SAMs. For example, to design the wettability properties of surfaces, SAMs terminated with methyl groups are hydrophobic, whereas SAMs terminated with carboxyl, hydroxyl, or amine groups (moieties that can hydrogen-bond to a polar surface) are hydrophilic.[47-48]

It is well documented that SAMs of *n*-alkanethiols form densely packed, well-ordered monolayers on coinage metal surfaces such as gold or silver.[49-52] The packing density of SAMs is shown to change depending on the alkane chain length or terminal chemistry of the molecule.[46] The basic structure of an *n*-alkanethiol SAM consists of three parts: the tail, the carbon backbone, and the headgroup (Figure 2.2). The tail is composed of thiol molecules for chemisorptive attachment to surfaces. The thiol is bonded directly to a saturated 2 to 18-carbon chain; this carbon backbone forms a spacer for tuning the vertical thickness of SAM nanopatterns. The carbon chain is capped with a headgroup which determines the surface properties. A variety of functional groups (esters, alkyls, hydroxyls, carboxylates, amides, etc.) are commercially available, depending on the desired application. Readers are directed to previous reports for details regarding synthesis, preparation, and characterization of SAMs.[36,46,52-53]

To prepare SAMs of *n*-alkanethiols, Au(111) substrates are submerged in dilute solutions of alkanethiols dissolved in solvents such as ethanol or 2-butanol for various time intervals. As

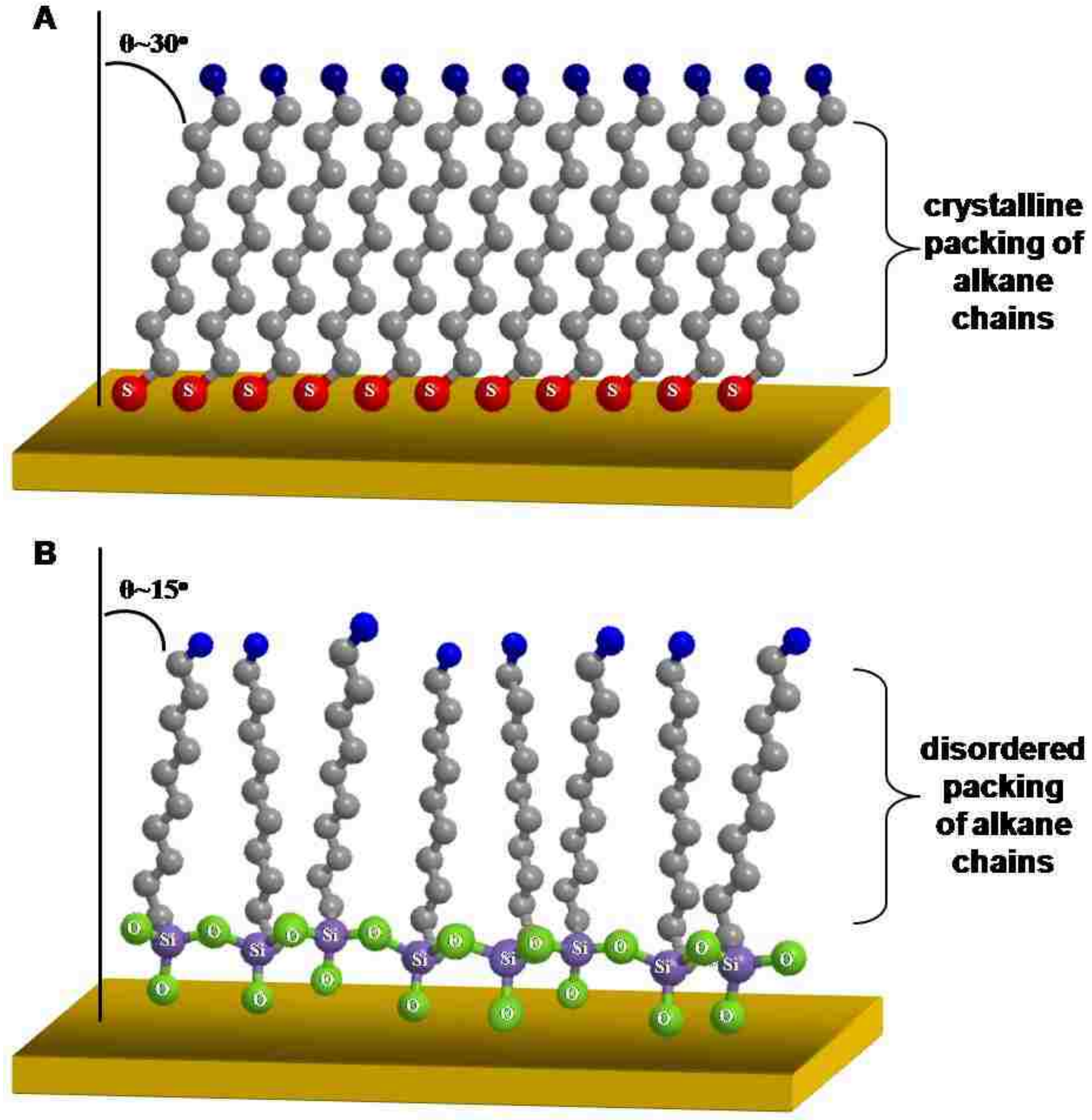

Figure 2.2 Basic structure of self-assembled monolayers. [A] Model of ω-functionalized *n*-alkanethiol SAMs; [B] *n*-alkylsilane SAMs.

examples, the wide range of conditions used to form SAMs of methyl terminated *n*-alkanethiols and alkylsilanes on various surfaces is summarized in Table 2.2. The concentration and the amount of time the substrate remains in solution will vary depending on the solubility of the molecule in the chosen solvent, and the nature of the SAM headgroups. Controlling variables such as the solution concentration and intervals of immersion may prohibit the formation of double layers and ensures sufficient surface coverage to produce mature, densely-packed SAMs.[25] It has also been reported that minimizing exposure to light serves to prevent oxidation of thiols.[54-55] For UHV studies, vapor deposition has also been used to prepare SAMs.[52,56-57]

Table 2.2 Protocols for preparing SAMs.

SAM	Substrate	Concentration (mM)	Time (hr)	Temperature (°C)	Solvent	Ref.
hexanethiol, octanethiol, decanethiol, dodecanethiol, benzenethiol	Au(111)	0.001-1 mM	24 h	RT	ethanol	58
dodecanethiol	Au(111)	1 mM	24-36 h	RT	ethanol	59
hexadecanethiol	Au(111)	0.0002 mM	< 1 h	21	ethanol	60
octadecanethiol	Au(111)	0.0001 mM	< 1 h	21	ethanol	61
octadecyltriethoxysilane	mica	1 mM	< 1 h	RT	mixed solvents, water, tetrahydrofuran, hydrocholoric acid, cyclohexane	62
octadecyltrichlorosilane	silica	5 mM	30 s	RT	bicyclohexyl	63

According to studies conducted using IR, near-edge X-ray absorption fine structure (NEXAFS) spectroscopy, and grazing incidence X-ray diffraction (GIXD), the alkyl chains of *n*-alkanethiol SAMs are tilted approximately 30° with respect to the surface normal.[64-68] Thiol atoms of SAMs bind to triple hollow sites of a Au(111) lattice by chemisorption.[35,46,54,69] The solution self-assembly of *n*-alkanethiol SAMs on bare gold surfaces is reported to occur in two phases. The stripe phase forms when thiol molecules initially make contact with the surface, in which the backbone of the molecules are oriented parallel to the substrate in a lying-down configuration.[70] However, over time the *n*-alkanethiol molecules rearrange into a standing position with the molecular backbone tilted ~30^o from surface normal.[70] The mature crystalline phase forms an enthalpy favorable, close-packed commensurate $(\sqrt{3}\times\sqrt{3})R30^o$ configuration with respect to the plane of the Au(111) lattice.[51,71-73] The exquisite details of the surface structure and long range ordering of *n*-alkanethiol SAMs has been revealed with STM and AFM to enable a direct view of defect sites such as etch pits, steps and dislocations within films.[51-53] Etch pits are small depressions observed in high resolution images that result from the displacement of atoms of the Au(111) substrate, caused by reconstruction when thiols of the SAM endgroups bind to a gold surface.

A representative AFM topographic image of a naturally-formed *n*-alkanethiol SAM/Au(111) acquired in liquid is presented in Figure 2.3. High-resolution images obtained with AFM disclose substrates that are not truly smooth and flat; rather, from the atomic perspective, surfaces contain defects such as pinholes, missing atoms, and scars. When SPM images reveal these natural defects then true molecular or atomic resolution has been achieved. Looking at the AFM images, the surface may appear rather rough and irregular. However, the surface is actually very flat from an atomic perspective. The height of gold steps is only 0.25 nm and thus the overall surface roughness of the underlying gold substrates for these samples is less than 1 nm. The topography images in Figure 2.3 display height changes according to color contrast from dark to light, analogous to a height map of the surface terrain. The dark colors indicate shallow features whereas brighter areas are taller. In the wide view image (500×500 nm^2) of an octadecanethiol (ODT) SAM in Figure 2.3A, the terrace domains of the underlying gold surface are clearly observed. The AFM image captures a detailed view of a concentric spiral arrangement of overlapping gold steps, which are often observed for surfaces of epitaxially grown gold thin films. The step edges of the terraces are not smooth; rather the uneven and angular profiles at edges reflect the true surface morphology. The ODT-covered surface is decorated with tiny holes called etch pits, which are 0.2 nm deep, corresponding to the depth of one atomic layer of gold. Etch pits or gold vacancy islands are defect sites resulting from the reconstruction of Au(111) during the chemisorption of thiol molecules.[74] A close-up view (200 × 200 nm^2) of a terrace area is displayed in Figure 2.3B which begins to reveal the ordered molecular domains between areas of etch pits. The size and density of etch pits varies widely for various samples, according to sample preparation conditions such as age and oxidation. Details of the surface morphology of *n*-alkanethiol SAMs on Au(111) substrates has also been investigated with STM.[58,75-76]

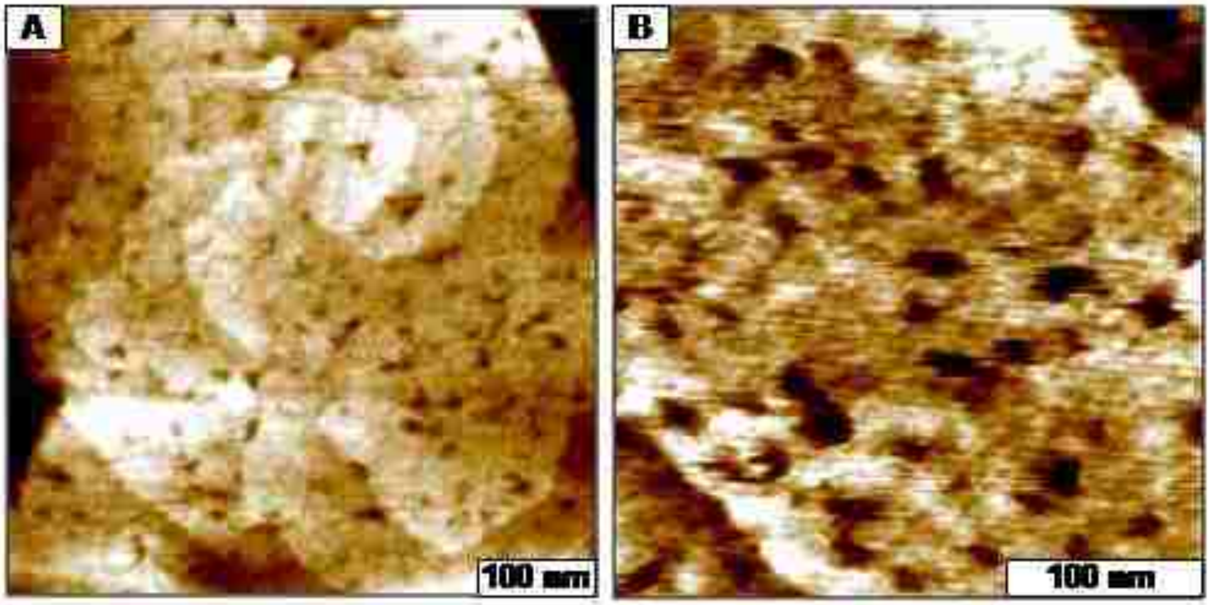

Figure 2.3 Views of a self-assembled monolayer of octadecanethiol on gold. [A] Topograph of a 500 x 500 nm^2 area; [B] zoom-in view of a single terrace.

The properties of alkylsilane SAMs are quite different from alkanethiol SAMs. A key difference is that alkylsilanes can be covalently formed on a wide variety of surfaces, such as oxide surfaces (silicon, aluminum, and germanium), mica, glass, zinc, quartz, and selenide.[45,53,62,77-78] Alkylchlorosilanes, alkylalkoxysilanes and alkylaminosilanes require hydroxyl groups on surfaces to form polysiloxane, which connect to surfaces via a network of Si-O-Si bridges (Figure 2.2B).[78] Alkylsilane monolayers typically consist of domains separated by boundaries of mica. Within these domains, silane molecules form structures without long-range order or periodicity.[79] The anchoring groups of silane SAMs form a cross-linked network on surfaces, and the chains tilt approximately 15° from surface normal.[67,79]

The self-assembly of thiol and silane SAMs supply a convenient and efficient means for designing surface chemistry. Depending on the mechanism of molecular writing, SAMs furnish a practical and effective "ink" for writing nanostructures with molecular dimensions using SPL.

2.3 Fabrication of SAMs Using Nanoshaving

Nanoshaving can be accomplished by applying mechanical force to the probe during scans; essentially small areas of the SAM are "shaved" away by the action of a scanning AFM tip.[34] Nanoshaving is used to uncover selected regions of surfaces which are surrounded by a passivating matrix SAM; these uncovered regions are then available for deposition of new molecules and materials. Information about the thickness of molecular layers on surfaces can be derived by using the nanoshaved areas as a baseline for cursor measurements.[80-81] Nanoshaving was introduced in 1994 for a SAM of octadecyltriethoxysilane (OTE); changes in the observed lattice were used to confirm that molecules were displaced from the surface.[79,82]

The process of nanoshaving is achieved by scanning several times over a small local area of a surface with an AFM tip, while applying a higher force than that used for imaging (Figure 2.4). After molecules are removed, the AFM probe can still be used to image the surface by returning to low force. In nanoshaving, a high local pressure is applied by an AFM tip to the area of contact. This pressure causes high shear forces, and thus displaces SAM adsorbates as the tip is scanned back and forth across the surface. As a result, the bare substrate is exposed. By carefully controlling the amount of force applied, the AFM tip is not damaged during fabrication. The three basic steps of nanoshaving are shown in Figure 2.4. The first step uses an AFM tip under minimal force (less than 1 nN). The surface is characterized at low force to locate an area for writing. A flat plateau area of the surface with few scars and defects is desirable for shaving patterns. Next, a higher force is applied (ranging from 2-20 nN depending on the monolayer adsorption properties) which causes the AFM tip to push through the matrix SAM to make contact with the surface. The molecules directly under the tip are shaved away, to uncover areas of the surface. Sufficient force is applied to the AFM probe to ensure that matrix SAM molecules are removed, without disturbing the underlying gold substrate.[34] In the final step, the newly fabricated areas of the surface are characterized with the same AFM tip using a reduced force (less than 1 nN). Thus, nanoshaving enables *in situ* fabrication of SAMs.

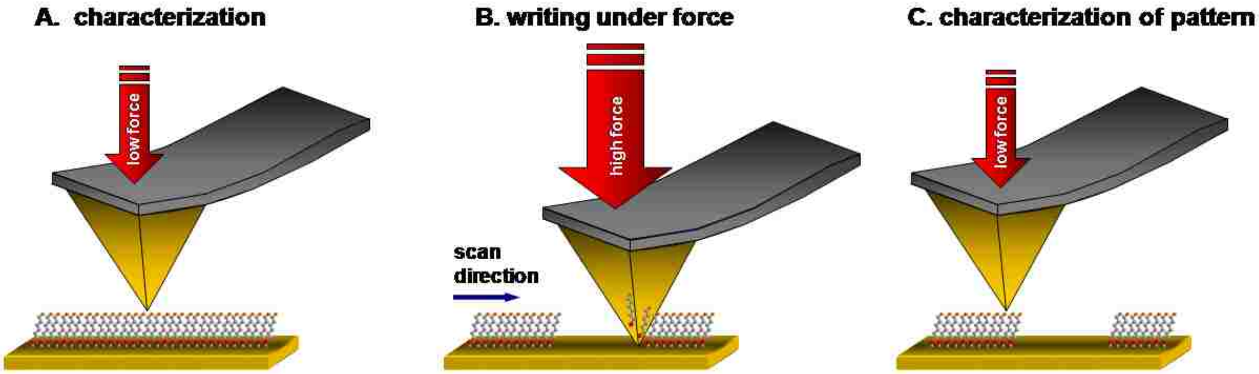

Figure 2.4 Steps of nanoshaving. Areas of a matrix self-assembled monolayer are "shaved" away under high force by a scanning AFM tip.

It is critical to optimize the amount of force applied to the AFM tip for nanoshaving SAMs. Of course, if too much force is applied the sharp apex of the tip can be broken; therefore it is important to find a minimum force to remove molecular layers without damaging the tip. Atomic force microscope controllers provide precise control of the force applied to AFM tips using electronic feedback. The threshold force is determined for each experiment by successively incrementing the amount of force applied during scans. As the force is increased the tip is pushed though the matrix SAM to contact the underlying substrate. The tip is then rastered several times to sweep molecules from the surface, since the actual area of contact is very small between the tip and surface. If too much force is applied, the torsion on the cantilever will cause the tip to twist and produce non-linear movements. At the optimized minimum force threshold, the desired square, linear or circular geometries will be produced.

The imaging media and the nature of the molecule influence the success of nanoshaving. When imaging in air, displaced SAM molecules often pile up at the sides of the trenches or holes that are uncovered; whereas in liquid media the molecules dissolve in the surrounding solvents. Nanoshaving has not been accomplished for *n*-alkanethiols with fewer than ten carbons because holes or trenches refill with short-chain molecules. Immediately after the molecules have been removed by the scanning AFM tip, molecules of short-chain thiol SAMs backfill into the uncovered areas. In contrast, SAMs of any chainlength of *n*-alkylsilanes are irreversibly displaced by nanoshaving in either liquid or ambient environments.[82-83]

An example array of nanoshaved patterns produced within an octadecanethiol (ODT) SAM is presented in Figure 2.5. The topographic image displays twelve dark squares written into an ODT matrix in ethanol. The squares correspond to uncovered areas of Au(111). The areas of brighter contrast indicate taller features whereas the dark areas are shallower. Even when writing with an open-loop AFM scanner, there is very precise alignment of the rows and columns of the array and well-defined square geometries for nanoshaved patterns. The high-resolution image of Figure 2.5A was acquired after nanoshaving and evidences that after writing under force the tip has not become blunt or damaged. The *in situ* topograph clearly exhibits the indicators of a high-resolution image, such as circular gold terraces, concentric circular steps and line scars. The friction image (Figure 2.5B) provides a spatial map of the changes in chemistry for nanoshaved patterns. The matrix areas of ODT show uniform contrast, which is clearly distinguishable from the brighter nanoshaved areas. Within the nanoshaved squares the homogeneous color evidences clean removal of the matrix SAM. A cursor profile along the bottom row of nanoshaved patterns reveals the height difference between the ODT SAM and the underlying surface measures 2.0 ± 0.2 nm. This value agrees closely with the expected thickness (2.1 nm) for an ODT SAM.

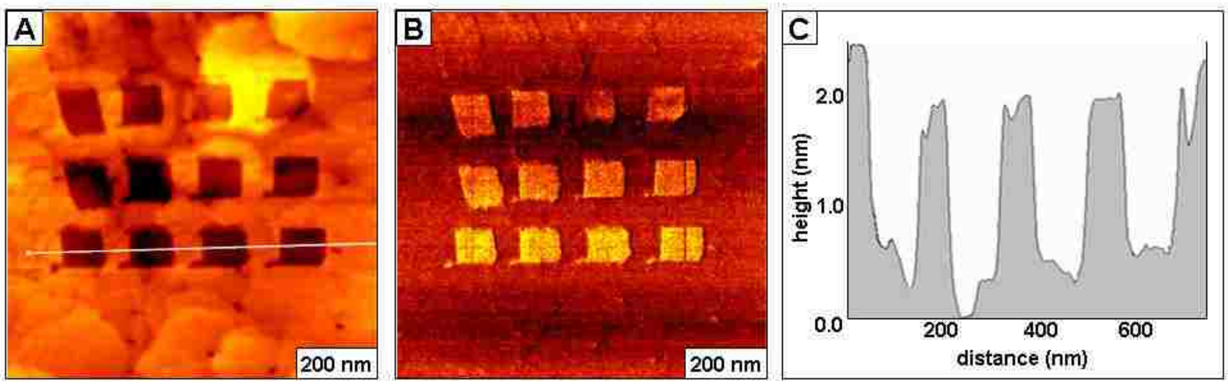

Figure 2.5 Nanoshaved array of 100 x 100 nm^2 squares in an octadecanethiol matrix. [A] topography; [B] frictional force image; [C] corresponding cursor profile along the bottom row of nanopatterns.

The thickness of the films can be measured from cursor profiles across the film and uncovered substrates. Nanoshaving can be applied to determine the thickness of thin films with angstrom precision by referencing the substrate as a baseline for cursor measurements. In addition to alkanethiol SAMs, nanoshaving has been used for characterizations of molecularly thin films of porphyrins,[84] alkylsilanes,[79,85-86] sexithiophene,[87] dimercaptobiphenyl multilayers,[88] and DNA.[89] After local areas of the surface have been uncovered by nanoshaving, new molecules or nanomaterials can then be selectively deposited on the exposed areas to form nanopatterns.[90]

2.4 Nanografting of *n*-Alkanethiol SAMs

Nanografting was introduced in 1997 by Xu and Liu.[80] A useful analogy for describing AFM-based lithography is to consider the AFM tip as a pen, a matrix SAM on gold as the paper, and fresh *n*-alkanethiols in solution as the “ink” for writing patterns. Nanografting basically uses the same procedure as nanoshaving, except that the steps are accomplished while the tip and the sample are immersed in a dilute solution of new thiol molecules chosen for writing (Figure 2.6). The matrix SAM is first characterized in liquid media by applying a low force, less than 1 nN.

Imaging in liquids enables one to achieve high resolution with low, nondestructive forces.[91-92] After choosing an area for writing, a greater force (1-10 nN) is applied to the AFM tip (*pen*) to shave the matrix molecules from the gold substrate. The SAM molecules which are removed from the surface (*paper*) are either deposited at the edges of the nanopatterns, or are dissolved in the surrounding solvent. New thiol molecules from solution immediately self-assemble onto the shaved areas following the scanning track of AFM tip. The written patterns can then be characterized *in situ* without changing tips by returning to low force.

For nanografting, it is critical to control the amount of force to ensure that the tip remains sharp after writing nanopatterns. Unfortunately, the microfabrication processes used to manufacture tips have not yet achieved nanoscale reproducibility for the shape and spring constants for each lever, thus, an *in situ* approach is useful to derive the optimized threshold force for each AFM tip. To optimize the writing force, a simple computer script can be used to write several patterns at incrementally increasing force. The lowest force at which a complete pattern is observed is then chosen as the optimized force for nanografting. When too much force is applied to the AFM probe while scanning, it is possible to scratch away the underlying surface or to break the apex of the probe. If the selected threshold force is too great, the torsion on the cantilever will cause the tip to write irregular shapes and produce stray lines and marks around the patterns. When a minimum force is used for nanografting, hundreds of patterns can be written with the same AFM tip without sacrificing topographic resolution. In fact, often the resolution of AFM imaging is improved by the sharpening process or cleaning of the tip by scratching the surface.

Depending on the choice of molecules, nanografting can generate patterns that are taller or shorter than the SAM matrix. For example, A cross-shaped pattern of 11-mercaptoundecanol (MUD) was written into matrix of ODT in Figure 2.7A. The simultaneously acquired frictional

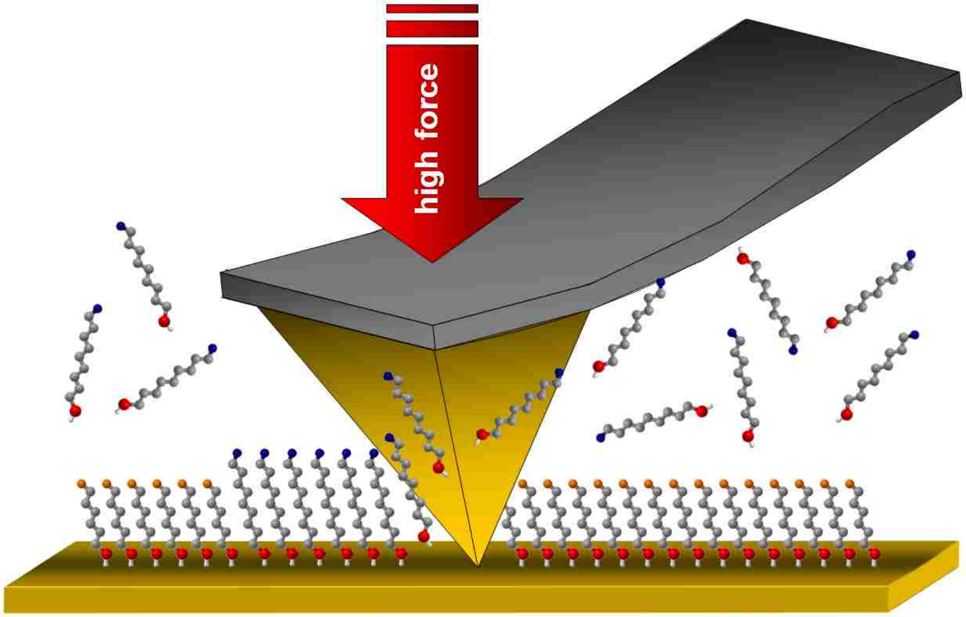

Figure 2.6. Principle of nanografting. Molecules self-assemble from solution following the scanning track of an AFM tip.

force image exhibits dark contrast for the MUD areas of the cross, which are terminated with hydroxyl groups. The surrounding methyl-terminated matrix areas of ODT exhibit lighter frictional contrast, clearly distinguishing the differences in surface chemistry after nanografting. The line profile of Figure 2.7C indicates the nanostructure is 0.7 ± 0.3 nm shorter than the matrix SAM, in close agreement with the theoretical differences in thickness, (ODT measures 2.1 nm, MUD is 1.5 nm). The measurements of film thicknesses with nanografting are highly dependent on the flatness of the surface; in this example the error term for the nanografted domains take into consideration the roughness of gold step edges (± 0.25 nm).

An example is presented for a positive height pattern of 16-mercaptohexadecanoic acid (MHA) in Figure 2.7D. The square nanopattern (200 x 200 nm^2) was written within a dodecanethiol matrix and is well-centered on a terrace step of Au(111). The friction images provide additional information about the chemical changes on the surface which take place after writing new molecules. The corresponding friction image shows bright contrast for the carboxylic acid areas of the square pattern, whereas the surrounding methyl-terminated matrix

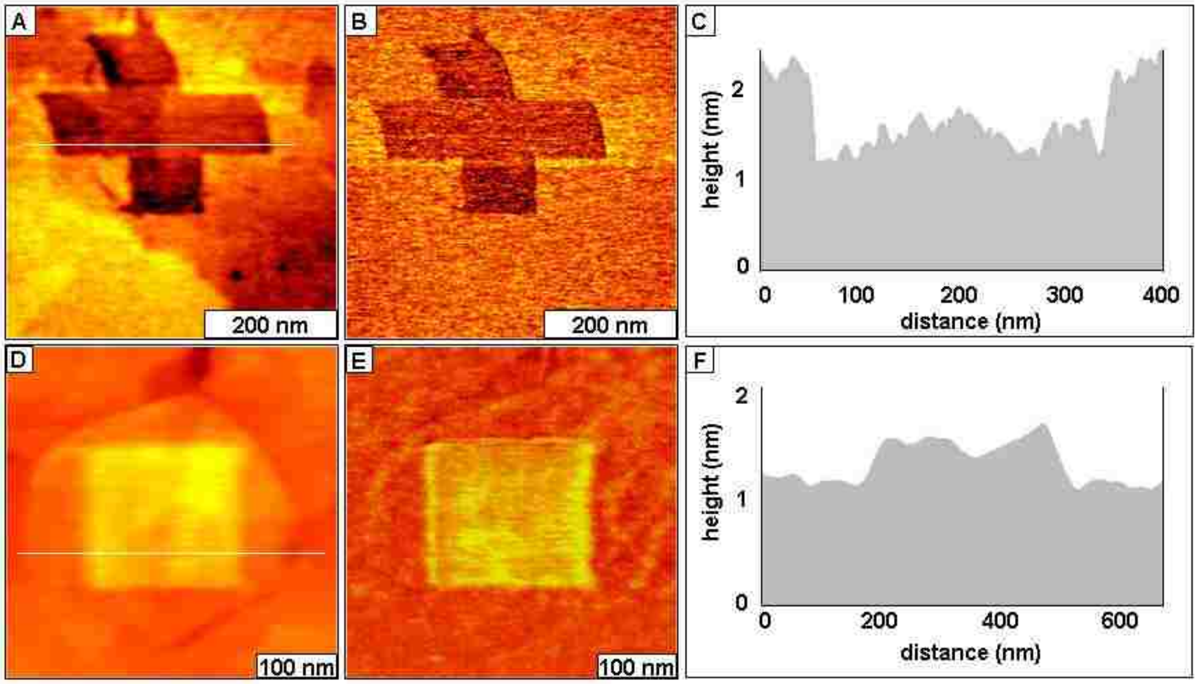

Figure 2.7 Nanografted patterns of self-assembled monolayers. [A] Cross-shaped pattern of 11-mercaptoundecanol fabricated within a matrix of octadecanethiol; [B] corresponding frictional force image; [C] cursor profile for the white line in **A**. [D] Mercaptohexadecanoic acid forms a taller pattern within a dodecanethiol matrix, the square has bright contrast; [E] friction image; [F] cursor profile across the nanopattern in **D**.

has dark contrast. There is adhesion between the tip and surface of the square nanopattern, which caused linespikes only on the patterned area along the horizontal direction of the scanning AFM tip. The line artifacts are clearly visible in the friction image. In contrast, the methyl-terminated areas do not exhibit the stick-slip adhesion because the methyl groups do not interact as strongly with the tip. The expected thickness for MHA is 1.9 nm, and for dodecanethiol is 1.5 nm. A representative cursor profile (Figure 2.7F) indicates that the pattern is 0.4 ± 0.2 nm taller than the molecules of the matrix, in close agreement with the theoretical height difference. An attribute of the nanografting process with thiol SAMs demonstrated with these examples is the remarkable angstrom to nanometer precision for edge resolution, even when using open-loop feedback for electronics. Such well-formed regular geometries at the square edges and corners of patterns are routinely achievable with AFM, because the piezocontrollers enable exquisite control of small forces applied to the tip.

Arrays of patterns can also be produced with automation software when nanografting. An array of squares of 11-mercaptoundecanoic acid (MUA) was fabricated within a matrix of ODT in Figure 2.8. The sides of the square elements measure 100 ± 10 nm, and each pattern is separated vertically and horizontally at intervals of 60 ± 10 nm. Depending on the number of line scans used to write the patterns, it took approximately 30 seconds to write each pattern in Figure 2.8A. The patterns were inscribed using 50 linesweeps per square, advancing 2 nm after each line was scanned while the AFM tip was rastered in continuous contact with the surface. The corresponding friction image clearly displays the changes in surface chemistry after the patterns were written. The nanografted squares of carboxyl-terminated MUA exhibit bright frictional contrast against the darker background of the methyl-terminated ODT SAM. The expected thickness difference is 0.7 nm, in good agreement with the experimental measurement of the cursor profile in Figure 2.8C which averages 0.6 ± 0.3 nm.

Multiple patterns with various shapes and components can be quickly created and modified with nanografting, and all of the steps of nanofabrication and characterization are accomplished *in situ*.[34,93] Nanografting enables precise control of the size, geometry, chemical functionality and location of structures on the surface. A spatial precision of 1 nm and edge-

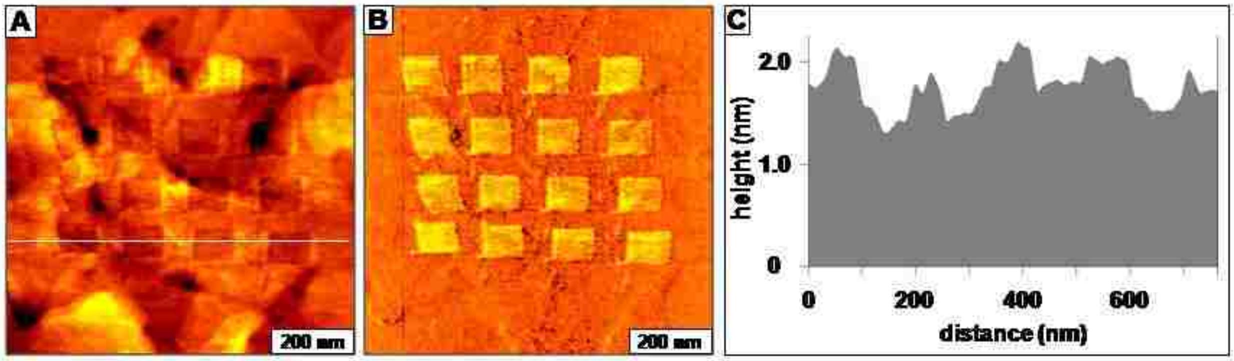

Figure 2.8 Automated nanografting can rapidly produce arrays of nanopatterns. [A] Array of 100 nm squares of mercaptoundecanoic acid written within octadecanethiol; [B] corresponding friction image; [C] line profile across the bottom row of the array.

resolution better than 2 nm have been demonstrated using nanografting.[80] Patterns written by nanografting consist of well-ordered, close-packed thiol molecules with selected functionalities and chain lengths.[80,93-94] Nanopatterns of thiolated molecules with different chain lengths and terminal groups have been written.[93] A positive or negative height of patterns can be achieved (with reference to the matrix SAM) depending on the chain length of the grafted molecules. For *n*-alkanethiol SAMs, chain lengths ranging from 2 to 37 carbons have been grafted successfully on Au(111) and within the nanopatterns the molecules display a periodic arrangement.[70,80] In a multiple ink experiment, nanopatterns of different composition were nanografted; parallel arrangements of nanopatterns of octadecanethiol and docosanethiol were nanografted side-by-side to provide molecularly-resolved views of close-packed SAMs.[34]

A key element of nanografting is that *n*-alkanethiols chemisorb spontaneously to surfaces in an upright arrangement to form a crystalline phase, due to a mechanism of spatial confinement.[6] When *n*-alkanethiols assemble naturally, there is a phase transition from a side-on orientation with the backbone of the molecule oriented along the surface, to a standing orientation in which the molecules adopt a tilted orientation as in Figure 2.2.[52,57,70] When nanografting, it is thought that the molecules bypass the lying-down phase and assemble immediately into a standing configuration because there is not sufficient space for the molecules to assemble on the surface in a horizontal direction.[6] A kinetic Monte Carlo model of natural and nanografted deposition of alkanethiols on gold surfaces was developed by Ryu and Schatz, which reproduces experimental observations for the variation of SAM heterogeneity with AFM tip writing speed.[95] The speed of the AFM tip influences the composition of the monolayers formed along the writing track.

After nanografting a pattern, new molecules or nanomaterials can be attached to the reactive sites of the fabricated area by selective adsorption. For example, mercaptoundecanoic acid was grafted into an octadecanethiol matrix, and then the nanopatterns were further reacted with octadecyltricholorosilane for positive and negative pattern transfer.[19] The hydroxyl terminal groups reacted with trichlorosilane headgroups of molecules in solution to form a new layer of molecules on the surfaces. The nanografted patterns provide spatial selectivity for anchoring molecular assemblies with desired spacer lengths and terminal functionalities.

Metal nanostructures were produced on nanografted SAM patterns using electroless deposition of copper onto carboxylic acid terminal groups.[96] Selectivity for adsorption on acid-terminated nanopatterns was accomplished by writing within a resistive matrix of hydroxyl-terminated SAMs. Combining automated AFM-based nanografting with electroless metal deposition enables high-resolution investigation of metal deposition processes at the nanoscale. First, a series of nanopatterns with a programmed gradient of densities was written within a resistive hydroxyl-terminated SAM matrix. Next, copper deposition was accomplished *in situ* from an alkaline copper plating solution. The lateral dimensions of the metal deposits were defined by the nanografted areas of the nanopatterns. The vertical dimensions of the patterns could be controlled with parameters of the surface density of reactive acid groups, and by the concentration of reactants in the plating solution. This approach offers promise for preparation of metal-molecule-metal junctions for fundamental investigations of electron transport in nanoscale junctions.

Structures of thiolated single-stranded DNA (ssDNA) were written by nanografting.[97] The sulfur headgroup of thiolated oligonucleotides adsorbed to uncovered areas of gold surfaces to adopt a standing orientation. Line patterns as small as 10 nm were written by nanografting. *In situ* AFM investigations revealed surface changes for ssDNA nanopatterns after adding solutions of enzyme to the liquid cell. The nonrestriction endonuclease (DNase I) cleaves ssDNA randomly to cause a decrease in the heights of the ssDNA patterns, and the free fragments were released into the surrounding buffer solution. Label-free hybridization of ssDNA nanostructures was also accomplished for nanografted ssDNA patterns using complementary segments of designed sequences.[98] These investigations provide fundamental information about the specificity and selectivity of surface-bound ssDNA towards the complementary strands, which is important for constructing DNA-based devices and surface assays.

Micropatterning of proteins has already been applied for biosensors and biochips.[99-102] In fact, patterning is essential for the integration of biological molecules into miniature bioelectronic and sensing devices since the sensing element consists of a layer of biomolecules for capture of target molecules and analytes. Protein patterning has been accomplished at the micrometer level using microcontact printing,[103-108] photolithography,[109-111] and microfluidic channels.[112-113] Thus, capabilities for micrometer scale methods offer valuable research capabilities at a size scale of hundreds of nanometers or larger. One may predict that nanoscale studies will advance the development of approaches for immobilization and bioconjugation chemistries, particularly with regard to understanding the parameters which influence protein activity, structural integrity and function. Precisely engineered surfaces can be used for the exploration of biochemical reactions in controlled environments and provide insight on the mechanisms of surface adsorption and molecular recognition.[114-116]

Spatially well-defined regions of surfaces can be constructed with reactive or adhesive terminal groups for the attachment of biomolecules. In biochips and biosensors, SAMs with certain functional groups such as carboxylate and aldehyde have been used as linkers for the immobilization of proteins and other biomolecules on surfaces.[49] Researchers have begun to apply nanografting to study proteins and biomolecular reactions on surfaces, towards resolving reactions with single molecules.

Thiolated proteins can be written directly on gold surfaces using nanografting. *De novo* proteins that were designed to contain a single cysteine thiol at the C-terminus were nanografted within a matrix layer of octadecanethiol.[117-118] Both a 3-helix metalloprotein and 4-helix bundle protein were successfully patterned and imaged using AFM. Measurements of the heights of protein nanopatterns matched the predicted dimensions, thus nanografting was demonstrated to enable coupling of the protein to the gold surface while preserving the tertiary structure of the protein.

Nanografted patterns of SAMs can be applied to immobilize proteins for *in situ* nanoscale surface assays. The dimensions of the apex of AFM tips are on the order of tens of nanometers, however, depending on the applied force and the geometry of asperities on the tip apex, the actual physical area of contact between the tip and surface is much smaller. The smallest feature yet produced by nanografting is a 2×4 nm^2 dot pattern which would accommodate approximately 32 thiol molecules.[119] Patterns written by nanografting provide an ideal size for defining the placement of proteins on surfaces, since the dimensions of proteins are on the order of tens to hundreds of nanometers. The terminal moieties of SAM nanopatterns mediate the mechanism for binding proteins, such as through covalent,[120-121] electrostatic,[114] specific interactions[122] or molecular recognition.[123] Lithography writing parameters can be used to precisely control the arrangement and density of SAM binding sites at the nanometer level.

A key advantage of using nanografting for protein assays is the ability to conduct experiments *in situ*. The successive changes in surface topography after the steps of nanopatterning SAMs, rinsing, and introducing buffers or protein solutions can be viewed with high resolution AFM imaging after each reaction step. Protein patterns are not dried or exposed to air, rather the *in situ* steps enable immersion of proteins in a controlled buffered environment. Nanoscale studies with AFM offer new approaches to refine essential parameters used to link and organize proteins on surfaces of biochips and biosensors. The orientation, reactivity and stability of protein molecules adsorbed on nanostructures of SAMs can be monitored with successive time-lapse images in near-physiological conditions. These investigations provide molecular-level information through the visualization of biomolecular reactions on surfaces for advancing biotechnology towards the nanoscale.

Adsorption of proteins such as lysozyme, rabbit IgG and BSA onto nanografted SAM patterns was first accomplished in 1999 by Wadu-Mesthrige et al.[114] The general steps for *in situ* protein immobilization investigations with nanografting are (1) to write nanopatterns of SAMs which are adhesive for proteins within a resistive matrix monolayer; (2) accomplish selective protein adsorption on nanografted patterns by adding buffered protein solutions to the liquid cell; (3) to achieve further reactions of the proteins with antibodies or small molecules without the use of radiolabels or fluorescent tags. Electrostatic binding of proteins such as IgG and lysozyme was demonstrated for nanografted patterns with carboxylic acid terminal groups, and covalent binding was accomplished by forming imine bonds to lysine residues of IgG and lysozyme.[114] The methyl-terminal groups of alkanethiol SAMs furnished a resistive matrix to ensure that proteins attached selectively to either carboxylate or aldehyde nanopatterns. Each of the reaction steps for IgG nanostructures was captured *in situ* with AFM images when patterns were reacted with anti-IgG.[116] The electrostatic immobilization of proteins (lysozyme, rabbit IgG and carbonic anhydrase) was investigated by Zhou et al. for nanografted patterns at varied pH conditions to reveal changes in surface coverage of proteins with differences in surface charge.[124] A side-by-side comparison of nanografted patterns with three different surface functionalities was accomplished in a single experimental platform, within a resistive matrix of hexa(ethylene glycol) SAM. Proteins can be anchored on reactive SAM patterns using robust covalent binding strategies. The surface moieties of nanografted SAM patterns were reacted with coupling reagents such as 1-ethyl-3-(3-dimethylaminopropyl) carbodiimide hydrochloride (EDC) and dithiobis(succinimidyl undecanoate) (DSU) to mediate covalent linkages with proteins. By reacting 11-mercaptoundecanoic acid with EDC and DSU for chemical activation, Kenseth et al. demonstrated covalent immobilization of IgG onto nanografted patterns within a glycol-terminated monolayer.[125] Nanografting and AFM characterizations provide valuable new tools for exploring binding strategies for proteins with unprecedented nanoscale views of surface changes after biochemical reactions.

2.5 Fabrication of SAMs Using Dip Pen Nanolithography

Dip Pen Nanolithography (DPN) is an AFM-based method for writing molecules on surfaces developed by Professor Chad Mirkin and coworkers in 1999.[126] The AFM tip (*pen*) is coated with the molecules or nanomaterials to be written (*ink*), and a clean substrate serves as the paper. The molecular ink must have an affinity for both the AFM tip and for the substrate. For example, *n*-alkanethiols attach to silicon nitride AFM tips through physisorption (physical adsorption) however, molecules bind through chemisorption to surfaces of coinage metals. For DPN writing, molecules are transported to the surface via capillary diffusion through the nanoscopic water meniscus formed between the tip and sample in an ambient environment (Figure 9A). The transfer of the ink has been found to depend on the relative humidity, which affects the size of the water meniscus formed between the tip and the surface. Writing with DPN does not require applying additional force to the AFM tip, instead the tip is held in contact with the surface for certain time intervals. For DPN, the naturally formed water meniscus in ambient environments enables capillary transport of inks to the surface. The duration of contact and the nature of the ink molecules affect the size of written nanostructures, as shown for the examples in Figure 2.9.Individual dots, lines, and grid patterns of alkanethiols can be written by DPN. Examples of octadecanethiol and mercaptohexadecanoic acid nanopatterns written with DPN are shown with lateral force AFM images (Figure 2.9). The duration of contact between the tip and surface, the humidity and the nature of the ink influence the size of the dot patterns as evident in Figures 2.9B and 2.9C. To reproducibly generate an array of dot patterns the tip motion and contact intervals were programmed, (Figure 2.9D) to precisely translate the tip and maintain contact with the surface for 20 seconds. By scanning the tip along a defined design (Figure 2.9E), line patterns can be generated as shown for a grid pattern of 100 nm width lines. Each line of the grid was written in 90 seconds using octadecanethiol ink.

The resolution of DPN depends on several parameters, such as the geometry of the AFM tip, the humidity of the ambient environment, as well as by the duration in which the inked tip is placed in contact with the surface – typically for 1 to 10 seconds. With typical cantilevers, DPN routinely generates feature sizes down to 15 nm. The resolution for writing nanostructures using DPN also depends on factors such as the grain size of the substrate, the scan rate and relative humidity.[126-127, 128] Coating an AFM tip is accomplished by dipping the probe into a drop of ink molecules, or immersion of tips in a liquid containing molecules to be written. The surfaces of AFM tips are highly suitable for writing thiol molecules, because the sulfur groups have a strong affinity for silicon and silicon nitride surfaces. Since molecules coat the AFM tips through physisorption, a liquid meniscus enables the flow of molecular ink to chemisorb to clean surfaces.

The transfer of ink during DPN has been found to depend on the relative humidity, which affects the size of the water meniscus formed between the tip and surface. Several researchers have investigated the transport mechanism for writing nanopatterns with DPN.[128-136] The smallest size of patterns written with DPN is on the order of 10-20 nm, with an ultrasharp probe.[137] Dip-pen nanolithography has begun to emerge as an important and versatile method for producing multicomponent arrays of SAM nanopatterns, as well as other molecules and nanomaterials. Readers are directed to previous reviews of experimental work applying DPN for further examples and applications.[138-140]

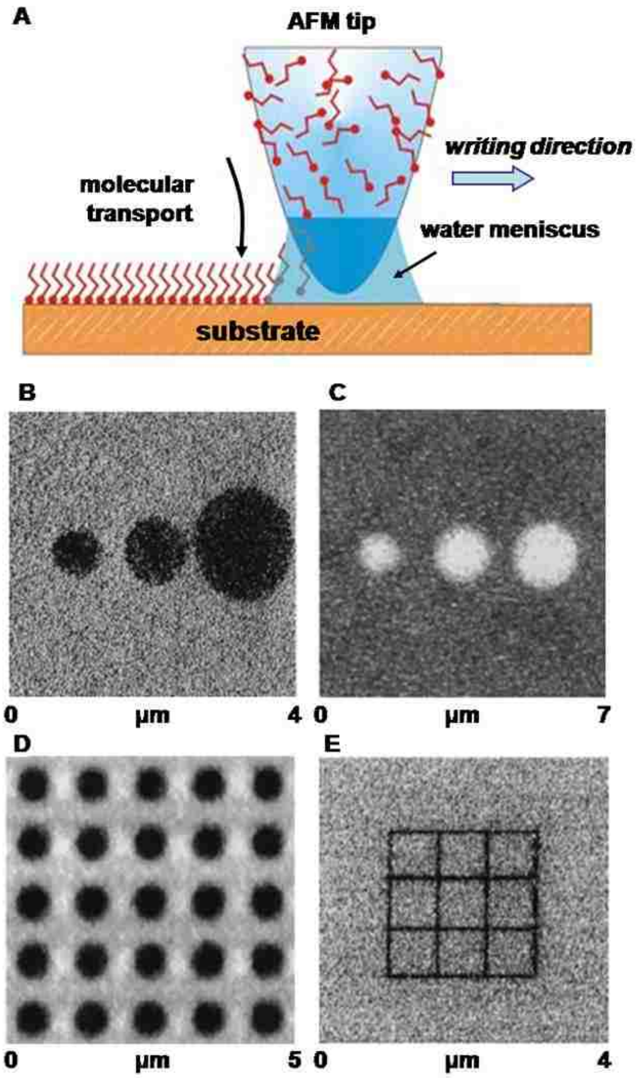

Figure 2.9 Principle of Dip Pen Nanolithography (DPN) and example nanopatterns. [A] Schematic representation of DPN writing. [B] Lateral force microscopy images of dots of octadecanethiol after 2, 4, 16 seconds contact with the substrate. [C] Lateral force microscopy images of mercaptohexadecanoic acid after 10, 20, 40 seconds contact with the surface. [D] Array of octadecanethiol dots generated with 20 second contact intervals. [E] A grid written with octadecanethiol. (Reprinted with permission from Ref.[126], R. D. Piner et.al *Science* **283**, 661 (1999) Copyright@ American Association for the Advancement of Science.

Dip Pen nanolithography is not limited to thiols as ink and has been applied successfully for other molecules. A wide range of molecules and nanomaterials have been nanopatterned on various surfaces using DPN. For ambient DPN, the choice of ink must be compatible with water for transfer of molecules through a water meniscus to deposit on surfaces, and the molecules should not be susceptible to hydrolysis reactions. The most commonly used inks reported for DPN are octadecanethiol and mercaptohexadecanoic acid (MHA).[126-131,136,141-147] Higher molecular weight compounds such as octadecylphosphonic acid (OPA), 2-mercaptobenzothiazole, 4-amino-5-hydrazino-1,2,4-triazo-3-thiol, 4-mercaptopyridine, and 2-mercaptoimidazole were used successfully as inks for writing nanopatterns with DPN, by increasing the humidity as high as 85%.[148] Other molecules and nanomaterials used for inks include silanes on semiconductive substrates;[137,149-150] peptides on GaAs substrates;[151] dendrimers,[152] dyes,[153-155] proteins,[156-157] and DNA[158-159] on gold or silicon surfaces; metal salts on silicon substrates;[160-165] and certain polymers on silicon.[166-169] In addition to direct writing of proteins, protocols have been developed for attaching proteins[123,170-175] or viruses[176-177] to nanopatterns written by DPN.

An approach for inking an AFM tip for DPN was developed using a poly(dimethylsiloxane) (PDMS) coating for ink transfer.[178] This approach is a hybrid of microcontact printing and DPN, and was successfully demonstrated for ink molecules of 16-mercaptohexadecanoic acid, 1-octadecanethiol, PAMAM dendrimers and cystamine. The polymer coating provides a reservoir which adsorbs various inks, and the tip can be used for imaging nanostructures after writing patterns due to differences in diffusion rates of inks from PDMS coatings.

Ink solutions for DPN are not limited to molecules at ambient temperatures. A method of thermal DPN was developed using a heated AFM cantilever and tip, to deposit solid inks.[179-182] An advantage of this approach is that the ink-coated cantilever can be used for fabrication as well as for *in situ* imaging of the nanostructures that were written, by changing the temperature of the tip. At cold or ambient temperatures, the ink molecules remain attached to the tip, and the tip can thus be used for imaging without unintended deposition of ink molecules during AFM characterizations. When the cantilever is heated near the melting temperature of the solid ink, the molecules are transferred to the substrate following the scanning path of the AFM tip. The melted liquid flows from the heated tip to the surface. Ink molecules that have been used successfully with thermal DPN include octadecylphosphonic acid at 122°C,[179] a conductive polymer of poly(3-dodecylthiophene) at 134°C,[181] a mixed polymer film of diazide-diyne at 170°C,[182] and nanosoldering of indium at 500°C.[180] Thus, thermal DPN enables writing with molecular inks that have poor solubility in water.

2.6 Writing Patterns of *n*-Alkanethiol SAMs Using NanoPen Reader and Writer, NPRW

An SPL method of “NanoPen Reader and Writer” (NPRW) was invented in 1999 by Amro et al.[183] For NPRW, the paper is a resistive methyl-terminated surface of a SAM. As with DPN, an AFM tip is inked with thiol molecules and writing is accomplished in air. At low force, molecules stay on the tip and provide high-resolution images of surface topography. Tip coatings provide a lubricant to minimize the stick-slip adhesion that is often present with ambient AFM imaging. When the force is increased, the thiol-coated tip pushes through the matrix SAM to deposit molecules from the tip onto the underlying gold substrate. The thiols within the nanopatterns were demonstrated to be well-ordered and close-packed with the evidence of molecularly resolved images acquired with a coated AFM tip.[184] Patterns can be written in air or in certain solvent media that are immiscible with the ink molecules. The NPRW approach combines the advantages of nanografting and Dip-Pen Nanolithography so that the same ink-coated AFM tip can be used for both writing and characterizing (reading) inscribed nanopatterns. The resolution of NPRW depends on the sharpness of the tips used for writing and the capabilities of the AFM scanner.

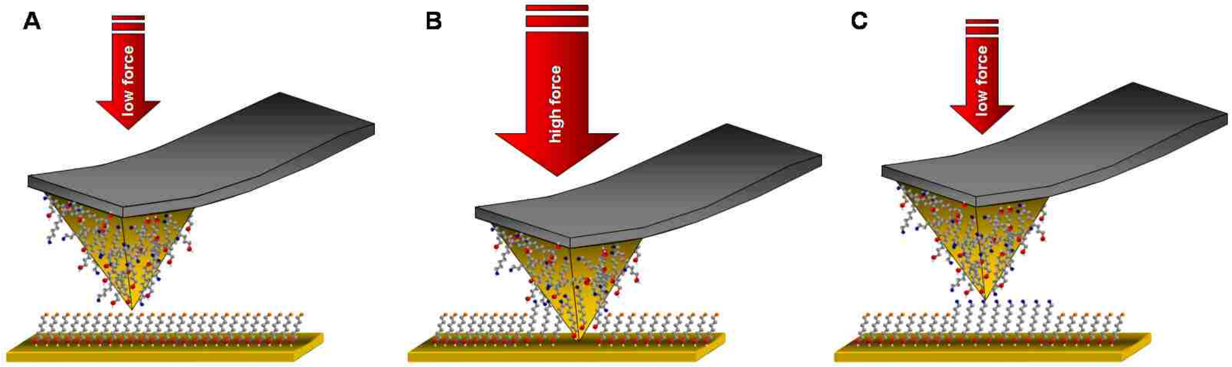

Figure 2.10 Principle of "NanoPen Reader and Writer."

The *in situ* steps for NPRW are illustrated in Figure 2.10. Under low imaging force, the ink molecules remain attached to the AFM tip and do not deposit on the surface of a methyl-terminated *n*-alkanethiol SAM matrix or '*paper'* (Figure 2.10A). Thiolated molecules readily physisorb to the surfaces of silicon or silicon nitride AFM tips, but are not chemically bonded. Thus, when the force is increased to a certain threshold, the tip is pushed through the resist layer of the matrix SAM to make contact with the underlying gold substrate for writing nanopatterns (Figure 2.10B). Simultaneous with the shaving action of the AFM tip operating under high force, surface molecules are displaced and scraped away and fresh ink molecules from the tip chemisorb to the uncovered gold surface. By returning to low force, the same tip can be operated to "read" or characterize the patterns that were written (Figure 2.10C). An advantage of NPRW in comparison to DPN is that ink can be deposited only when higher forces are applied to the AFM tip, to enable selectivity for writing. At low forces the ink molecules do not transfer to methyl-terminated SAMs of the '*paper*.' An intrinsic capability of AFM scanners is to provide exquisite control of the vertical forces applied to the tips, even in the range of piconewtons. For NPRW, the SAM-coated gold '*paper*' resists nonspecific deposition of thiol inks throughout areas of the surface, because the coating remains on the tip while scanning at low force. The ink also serves as a lubricant to facilitate high-resolution imaging in air. It has previously been established that coating AFM tips with organic molecules can substantially improve resolution by minimizing stick-slip adhesion.[185-187]

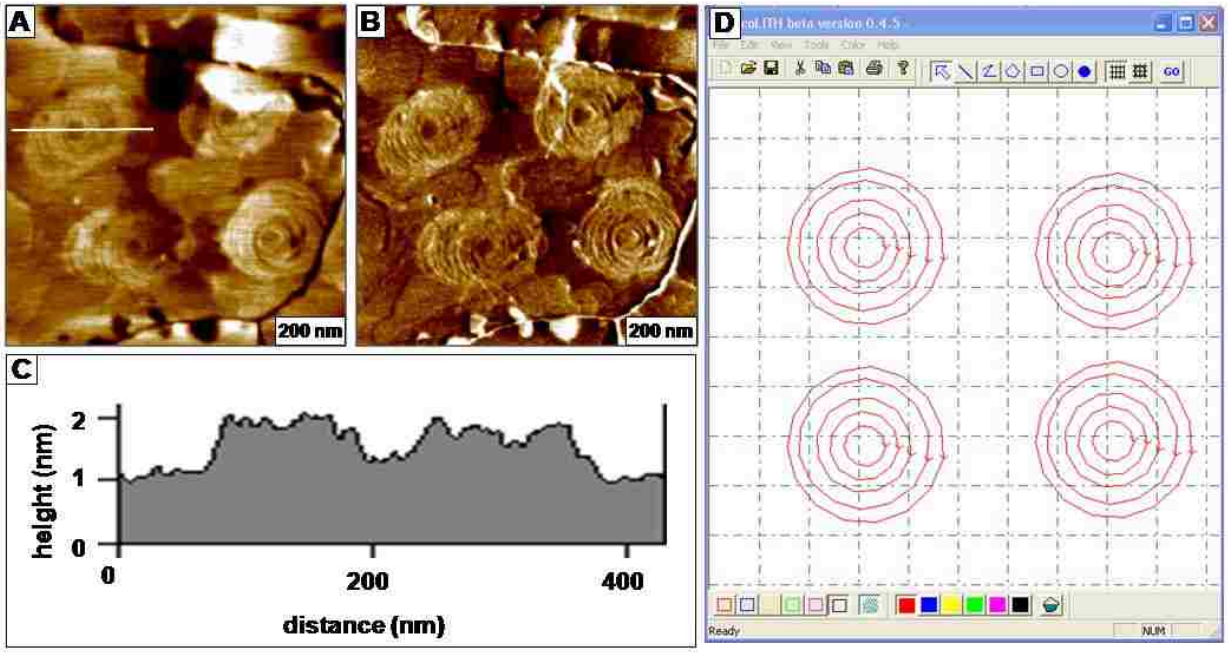

Figure 2.11 Circle patterns of mercaptohexadecanoic acid written in a dodecanethiol matrix using NanoPen Reader and Writer (NPRW). [A] Topograph of four sets of concentric circle patterns; [B] Corresponding frictional force image; [C] Cursor profile for the line in **A**. [D] Map of the lithography design.

The key difference between DPN and NPRW is the mechanism of writing. For DPN, ink is transferred through a narrow water meniscus, and the size of the written patterns largely depends on the length of time the tip is held in contact with the surface, according to the diffusion rate of the ink molecules used for writing. For NPRW, an increased force on the AFM tip is required for writing nanopatterns; the writing mechanism provides removal of a matrix SAM followed by rapid replacement with new molecules from the tip via sulfur-gold chemisorption.

An example set of nanopatterns written in air using NPRW is displayed in Figure 2.11 using hexadecanethiol ink and a matrix SAM of hexanethiol. An Agilent 5500 AFM/SPM system with Picoscan v5.3.3 and Picolith beta version 0.4.5 software was used to write and characterize the nanopatterns. An oxide-sharpened silicon nitride probe with an average force constant of 0.5 N/m (Veeco ProbeStore, Santa Barbara, CA) was used for writing nanopatterns of SAMs. The tip was immersed in a neat solution of hexadecanethiol for 15 minutes and dried in air under ambient conditions. By applying an increased load on the AFM tip, the shorter molecules of the hexanethiol matrix were replaced by ink molecules of hexadecanethiol following the scanning track of the probe. The speed used for writing via NPRW was 0.05 μm/s.

Circular nanopatterns of hexadecanethiol SAM were written within a hexanethiol matrix using NPRW (Figure 2.11). Four sets of patterns were written within a 1 x 1 μm^2 area, as viewed in the AFM topograph of Figure 2.11A. The gold contains a dark line scar which traverses the top, side and bottom of the image. The depth of this natural defect limits the attenuation of the color scale for clearly resolving the contours of the nanopatterns for topography, however, the corresponding friction image in Figure 2.11B clearly distinguishes the outlines of the circular patterns. The patterns were written by outlining concentric rings, and thus the composition of the patterns contains a mixture of the matrix and ink molecules. Writing for all four patterns was completed in 2 minutes using NPRW. The sets of patterns consist of five concentric rings which were outlined once. The cursor profile across one of the patterns exhibits a thickness difference of 1.0 ± 0.3 nm in close agreement with the 0.9 nm theoretical difference in thickness between hexadecanethiol (1.9 nm) and hexanethiol (0.8 nm).

User-friendly software with a graphical user interface for designing nanopatterns has been developed by Agilent Technologies, as displayed in Figure 2.11D. The shapes of the patterns can be sketched using different colored outlines, and the attributes of the patterns (bias, speed, force) can be assigned by choosing the pattern colors that are drawn on the computer. In this example, four sets of concentric circles were designed; the execution of the drawing parameters is viewed in Figures 2.11A and 2.11B. By changing colors and assigning a range of variables the nanopatterning protocols can be systematically tested. Thus, automation of AFM-based lithography with improvements in controller software enables the experimentalist to rapidly optimize the writing parameters such as speed and force for different surfaces and ink molecules.

Nanopatterns of thiol-modified gold nanoparticles were written within a decanethiol SAM/Au(111) using NPRW (Figure 2.12).[188] The probe was inked with gold nanoparticles by inverting the AFM tip and placing a droplet of nanoparticle solution onto the tip. An example rectangular nanopattern of thiol-encapsulated gold nanoparticles written by NPRW within a $C_{10}S$ SAM matrix is presented in Figure 2.12. The shapes of individual nanoparticles can be resolved within the nanostructure, and only a single layer of nanoparticles formed on the gold surface. For NPRW with nanoparticle ink, the decanethiol matrix was replaced with gold nanoparticles following the shaving track of the tip for particle sizes between 1.2 - 8.2 nm. The methyl-terminated matrix SAM was an effective resist layer and prevented the non-specific adsorption of nanoparticles when imaging at low force. When higher force was applied, the nanoparticle "ink' could be precisely written on surfaces as defined by positioning the AFM tip. After writing, the nanoparticle patterns could be characterized *in situ* using the same AFM tip under low force.

Nanoscale characterization of the thickness of monofluoro-substituted oligo(phenylene-ethynylene) (F-OPE) thiolated SAMs on gold was accomplished by combining AFM characterizations and nanofabrication. Topographic images provide high resolution views of the surface morphology, and lithography enables measurements of the thickness of organic films at the level of angstroms. Nanopatterns of dodecanethiol and octadecanethiol were written within a matrix of F-OPE using NPRW, to measure the thickness of the films.[189] Since the heights of *n*-alkanethiols are well established, the nanopatterned SAM molecules provide an internal height reference or molecular ruler for nanoscale measurements. Frictional force images were also acquired using a coated AFM tip, to pinpoint the locations of inscribed nanopatterns.

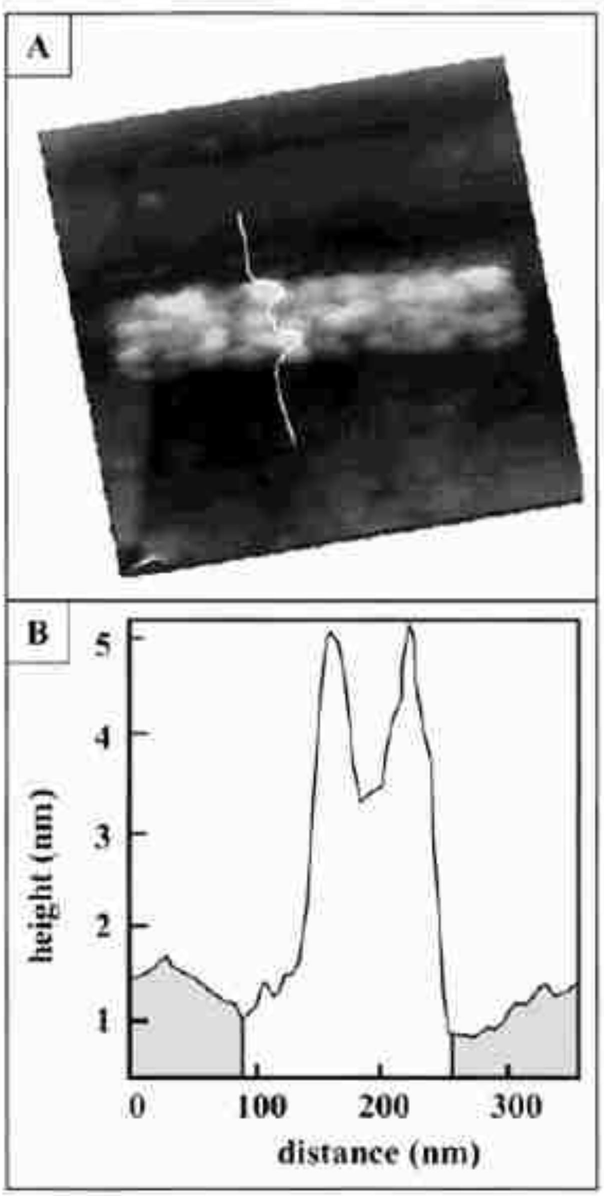

Figure 2.12 Nanopattern of gold nanoparticles written with NPRW. The surface of the nanoparticles were modified with a mixture of alkanethiols and written within a decanethiol monolayer. (Reprinted with permission from Ref. [90], J. C. Garno *et al.*, *Nano Lett.* **3**, 389 (2003). Copyright@American Chemical Society.

2.7 Catalytic Probe Lithography

Catalytic probe lithography is a recently developed and promising strategy for chemical modification of surfaces with nanoscale resolution. For catalytic probe lithography, an AFM tip is coated with molecules or metals that will catalyze a chemical reaction on the sample surface. The catalysis reaction occurs in areas where the coated tip makes contact with the surface (Figure 2.13). For example, the terminal chemistry of SAMs can be changed to a different functional group. As the catalytic probe is scanned in contact with the surface, nanopatterns are generated following the scanning track of the AFM tip to produce designed nanopattern geometries. The linewidth resolution of patterns written by catalytic SPL corresponds to the size of the contact area between the tip and sample. Depending on the nature of the catalysis reaction, the same tip can be used to image the nanopattern by changing certain experimental parameters, or optical microscopy has also been applied to view nanopatterns after site selective surface reactions.

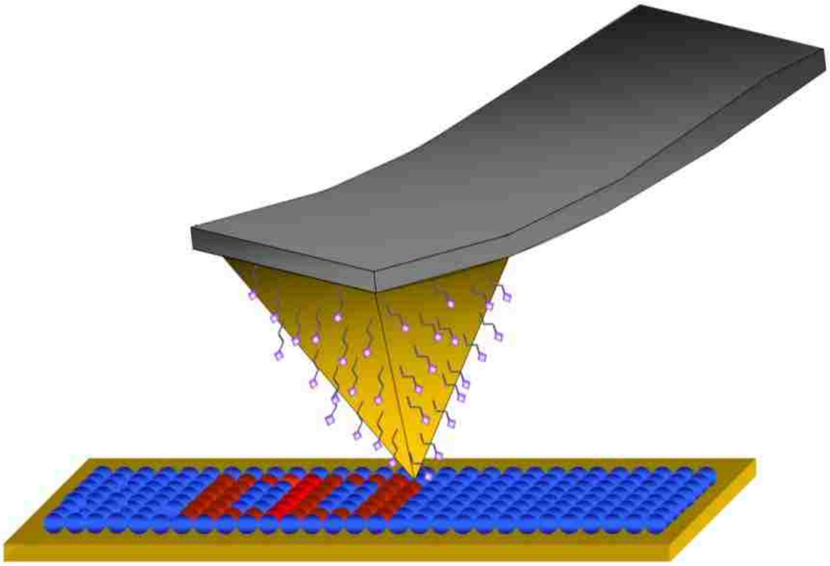

Figure 2.13 Principle of catalytic probe lithography.

Unlike DPN or NPRW lithographies, the transfer of ‘ink’ from the tip to the surface is not part of the process for writing patterns with catalytic probe lithography. The catalytic coating on the AFM probe is not the product or reactant, the role of the catalyst is to either initiate or accelerate the rate of a chemical reaction. The catalyst is not consumed by the reaction and is not deposited on the surface to create patterns. The length of contact time and the amount of force applied to the tip affect the resolution of writing and these parameters are reaction specific. Tip coatings used for catalytic probe lithography include platinum,[190] palladium[191-192] and gold films with molecular coatings.[193-194]

The earliest report of localized catalysis with an AFM probe was reported in 1995 by Müller et al.[190] Chemical modification of the terminal azide group of SAMs was achieved with a platinum-coated AFM tip as the catalyst to produce amine-terminated patterns. After writing patterns, the samples were reacted with aldehyde-modified latex or fluorescent tags which attached selectively to the SAM patterns. The fluorescent patterns were then imaged using optical microscopy.

A palladium-coated AFM tip was used to catalyze the chemical conversion of azide, carbamate, and alkene terminal groups of organosiloxane SAMs on glass substrates.[192] Three reaction schemes were demonstrated for palladium-catalyzed addition and transfer reactions to produce amine-terminated patterns. To demonstrate that the reactions occurred, the patterns were labeled with fluorescent probes and also with biotin, which selectively binds streptavidin-functionalized gold nanoparticles. The labeled nanopatterns were imaged by tapping-mode AFM with an uncoated probe and also by confocal microscopy.

A Suzuki coupling reaction was accomplished by catalytic probe lithography using a palladium-coated AFM tip.[195] A gold surface was coated with an aryl bromide monolayer, and the palladium-coated probe and surface were immersed in a boronic acid reagent solution. Nanopatterned areas could be resolved by frictional force images in the absence of the reagent media. Further reactions were demonstrated for the nanopatterns with amine-specific fluorophores and aldehyde-functionalized nanospheres, which were viewed using optical microscopy.

Catalytic probe lithography was accomplished with a gold AFM tip that was further coated with an acidic SAM.[193] When brought into contact with the surface, the acid groups on the tip induced hydrolysis of the silyl ether groups of a reactive SAM, bis-(ω-tert-butyldimethyl-siloxyundecyl)disulfide (Figure 2.14). The tip was scanned across the SAM layer to produce well-defined patterns of different sizes and the shapes. Patterns were imaged by frictional force AFM using the functionalized AFM tip. A written resolution of 25 nm linewidths was achieved for these experiments, comparable to the area of contact between the coated AFM probe and the surface.

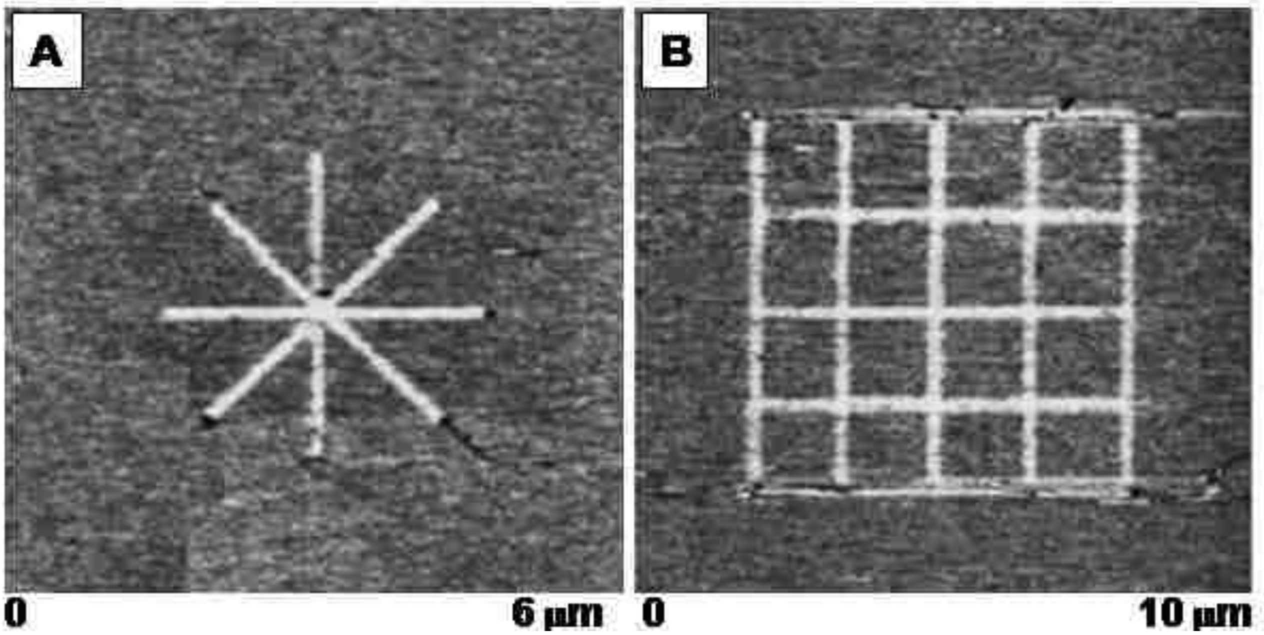

Figure 2.14 Patterns with well defined sizes and geometry can be produced using catalytic probelithography. [A] Friction image of line structures written on bis(*ω-tert*-butyldimethyl-siloxyundecyl)disulfide (TPDMS) monolayer using a tip functionalized with 2-mercapto-5-benzoimidazole sulfonic acid. [B] Example of a grid pattern written by selective hydrolysis of TBDMS. (Reprinted with permission from Ref. [193], 184, M. Peter *et al.*, *J. Am. Chem. Soc.* **126**, 11684 (2004). Copyright@American Chemical Society.

2.8 Biased-induced Lithography of SAMs

When an electric field is applied between a conductive SPM tip and sample, at certain bias voltages the area beneath the tip undergoes chemical or physical changes. Such surface changes provide a mechanism for local fabrication of surfaces at elevated bias. Both STM and AFM have been used for bias-induced lithography, in which voltages between a conductive tip and sample are controlled to selectively alter the surface chemistry of local areas scanned by the probe. Scanning probe based oxidation using STM was discovered in 1990 by Dagata et al.[196-197] A hydrogen-terminated silicon surface was locally oxidized when an elevated bias voltage was applied between an STM tip and the surface. It was later demonstrated in 1993 that local oxidation of surfaces could also be achieved using AFM, oxide lines were written on silicon surfaces using a metal-coated AFM tip.[198]

The general concept for surface fabrication using AFM for bias-induced lithography is depicted in Figure 2.15. For nanofabrication of SAMs, bias-induced lithography is accomplished by generating an electric field between the tip and the sample, either to oxidize or to replace surface molecules. As the AFM or STM tip is rastered over the surface at elevated bias, a pattern is generated for the areas scanned by the conductive probe. Typically, short (microsecond to millisecond) pulses of tunneling current or bias voltage are applied between a conductive tip and sample, in the range of 10-30 volts. The current generated during nanofabrication is very small, in the range of picoamperes or less. To accomplish bias-induced lithography, the tip must be conductive and the substrate must also be conductive or semi-conductive. Conductive AFM tips are prepared by sputtering a thin film of metal onto a tip. Conductive probes for bias-induced lithography are available commercially with coatings of cobalt, diamond-like carbon, doped diamond, platinum, platinum/iridium, tungsten carbide, titanium nitride, and nickel. The substrates that have been used are flat metal films (titanium tantalum aluminum, molybdenum, nickel, niobium) and compound III-V semiconductors.[197,199]

There are several mechanisms that have been proposed for nanofabrication using bias-induced lithography, depending on the nature of the environment and surfaces. The factors that

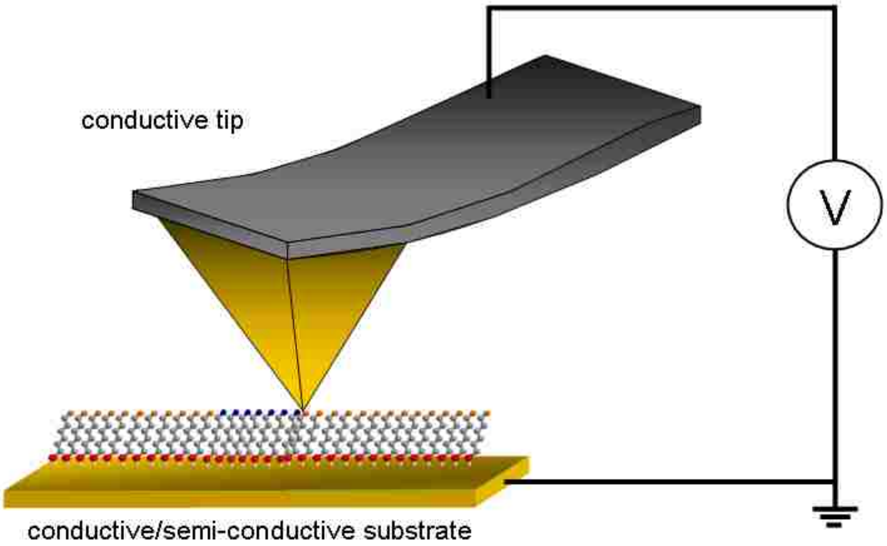

Figure 2.15 Principle of bias-induced nanolithography.

determine the size of features are the duration of the applied bias, the magnitude of the applied electric field, humidity and also the dimensions of the SPM tip. With bias-induced oxidation, the changes produced by an electric field often do not induce changes in molecular heights, and thus cannot be detected by topographic images. However, other AFM or STM imaging modes, such as lateral force imaging, force modulation and current imaging can be used to clearly resolve differences for oxidized areas. Tip proximity is a key difference for using AFM versus STM. For STM, the tip is brought very close, within tunneling distance (< 1 nm), but remains out-of-contact with the surface. For AFM, the tip is brought into direct contact with the sample during bias-induced lithography. Thus, the mechanisms for surface modification are quite different for STM versus AFM. In a UHV environment with STM where water is essentially removed, the surface changes are a consequence of Ohmic heating, which induces evaporation or desorption of surface layers.[200-201] In ambient conditions, when the tip is in contact with the surface, changes result from electrochemistry reactions at either the tip or sample which are caused by electric field effects.[160] There are advantages for using AFM rather than STM for bias-induced nanofabrication, because of differences in the positional feedback for STM. With STM, the tunneling current depends on the physical distance or gap between the tihp and sample, which varies exponentially with distance. Thus nanofabrication with STM is accomplished without physical contact between the tip and surface. In contrast, for AFM the tip touches the surface directly with well-controlled force, and voltage can be applied directly to the tip-surface contact. Direct contact with the surface intrinsically enables better control of the voltages applied for surface modification.

For the mechanism of local surface oxidation of surfaces using bias-induced lithography in ambient environments, the tip functions as a cathode, the substrate acts as the anode, and the water meniscus formed between tip and surface serves as the electrolyte. The applied bias induces an electric field between the tip and surface, ionizing the water molecules of the meniscus to effect electrochemical reactions on the surface.[202-203] The narrow capillary meniscus formed in ambient environments is essentially an ultra miniaturized electrochemical cell. This process is generally known as bias-induced nanolithography; however other terms used to describe this method of writing are local oxidation nanolithography (LON), scanning probe oxidation, nano-oxidation or local anodic oxidation.[197,204]

Considerable work has been published for bias-induced lithography of metals,[197,203,205-207] and semiconductor surfaces such as gallium arsenide,[208] silicon nitride[209] or silicon.[198,210-219] Examples which follow will present results applying bias-induced lithography for writing nanopatterns with SAM surfaces, such as silane SAMs on silicon or alkanethiol SAMs on gold surfaces. A summary of the SAM surfaces and fabrication conditions is presented in Table 2.3. Parameters such as the amount of bias voltage applied and speed of writing vary according to the nature of the surface to be patterned. Voltages reported for bias-induced lithography with surfaces of SAMs range from -7 V to +17 V. When writing SAMs on silicon, patterns with a positive height with respect to the surface are formed at negative bias, whereas at positive

Table 2.3 Examples of bias-induced lithography.

SAM/Surface	Lateral resolution of nanopatterns	Volts applied	Reference
octadecyltrichlorosilane/silicon surface methyl groups oxidized to carboxylate	10-40 nm	+ 8.5-8.7 V	220-222
thiol-functionalized silane monolayer/silicon defined sites for electrodeposition of silver	30 nm	+ 5-8 V	223
octadecyltrichlorosilane/silicon surface methyl groups oxidized to carboxylate	60-300 nm dots	+7-10 V	224
trimethylsilyl SAM prepared on silicon patterns were chemically etched	80 nm grooves	+5 V	202,225
18-nonadecenyltrichlorosilane/silicon surface vinyl groups oxidized	9 nm lines	- 8.0-9.5 V	226
oligo-(ethylene glycol)-terminated SAM/silicon bias-induced desorption	90 nm holes	+ 17 V	122
octadecyltrichlorosilane/silicon patterns were used for grafting of polymers, or for adsorption of gold nanoparticles	40 nm	- 8-10 V	227
octadecylphosphonic acid monolayer on silicon molecules desorbed at positive bias; oxides formed at negative bias	50-80 nm	± 6-7 V	228
octadecanethiol SAM on Au(111) bias-induced replacement with decanethiol ink	50 nm	+ 4-5 V	229
dodecanethiol SAM on Au(111) bias-induced replacement	10-15 nm lines	+2.7-3.8 V	230-231
octanethiol, decanethiol, dodecanethiol and tetradecanethiol SAMs on Au(111) bias-induced replacement	12 nm lines	+1.9-3.3 V	200
palmitic acid monolayer on silicon positive height patterns formed at negative bias; desorption observed at positive bias	60-80 nm	± 10 V	213
***n*-octadecyl mercaptan SAM/Au(111)**	10-50 nm	+3 V, -3 V	232-233

voltage the molecules desorb to form trenches or holes in the surface layer. Also, depending on the nature of the surface headgroups, at certain positive bias thresholds, the endgroups can be oxidized without evidencing a change in height.[223]

Bias-induced lithography can convert the endgroups of SAMs via oxidation reactions. Local oxidation of methyl terminal groups of an *n*-octadecyltricholorosilane (OTS) monolayer on silicon was accomplished by Liu et al. to produce carboxylate nanopatterns.[220] Topography and simultaneously acquired frictional images of the nanopatterns produced within an OTS monolayer are shown in Figure 2.16. The ultrasmall dot patterns (40 ± 4 nm) are vaguely distinguishable in the topographic view; however the changes in surface chemistry are clearly evident in the friction image. The 9 x 9 array of dot patterns was written using contact mode AFM by applying 8.8 volt pulses for 3.0 ms/point in ambient humidity of 60%. Patterns written in OTS monolayers with bias-induced oxidation were found to be stable for months under ambient conditions in air. Various methods of constructive nanolithography have been developed by Sagiv et al. to build complex assemblies with additional steps of chemical derivatization and adsorption of nanoparticles.[220-223] The bottom-up approaches combining bias-induced lithography with chemical processing have potential for preparing components of nanodevices.

Desorption of silane molecules to form nanosized holes was accomplished for oligo-(ethylene glycol) terminated monolayers on silicon substrates at +17 V bias.[122] Biomolecular arrays were formed by attachment of proteins in further steps using avidin and biotinylated BSA. The glycol-terminated SAM provided an effective resist layer to prevent non-specific adsorption of proteins on the non-patterned areas. This approach offers promise for producing high-density arrays of protein patterns for biosensing platforms.

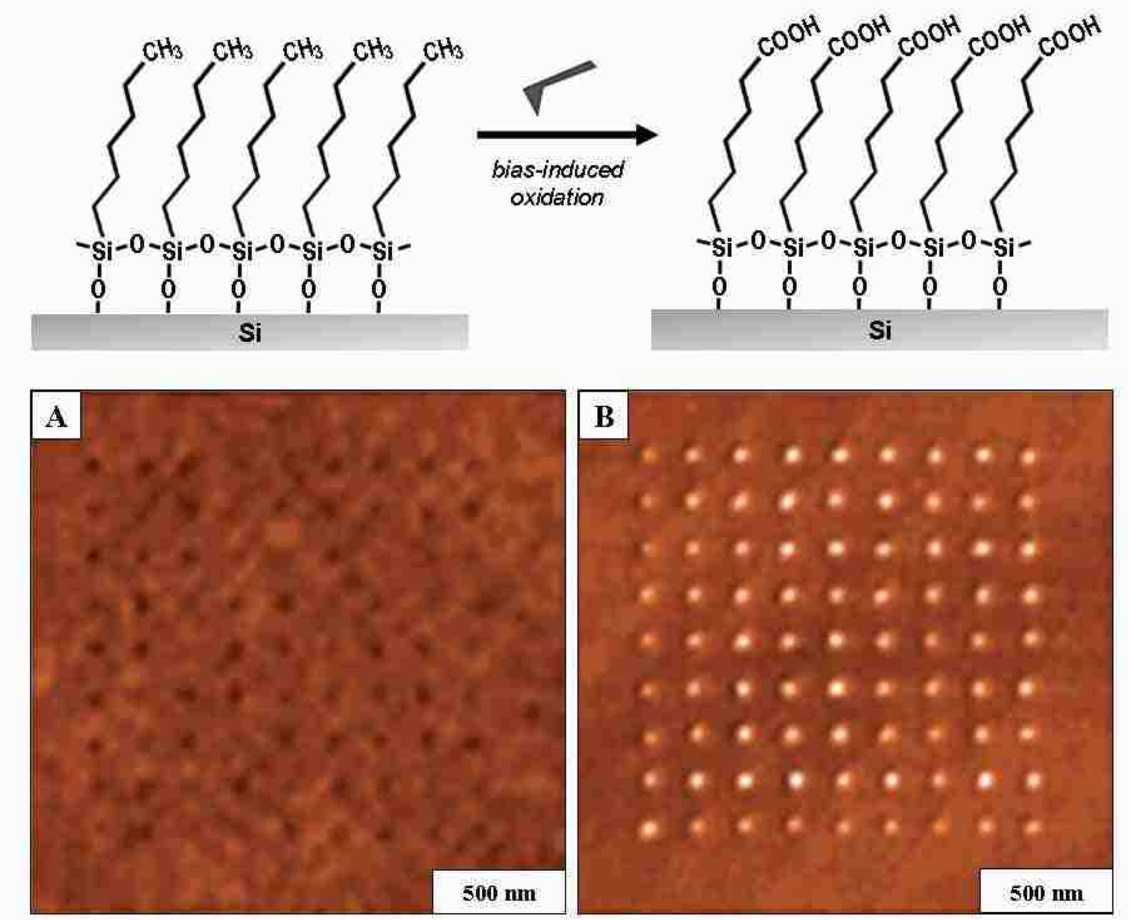

Figure 2.16 Nanopatterns within *n*-octadecyltrichlorosilane were generated by bias-induced lithography (+8.8 V) to oxidize methyl headgroups. Patterned dots in the simultaneously acquired [A] topography and [B] friction image have carboxylic acid terminal groups. (Reprinted with permission from Ref. [220], S. T. Liu *et al.*, *Nano Lett.* **4**, 845 (2004). Copyright@American Chemical Society.

Oxidative desorption of *n*-alkanethiol SAMs on gold surfaces can be applied for an STM-based replacement lithography as developed by Gorman et al.[231] Writing nanopatterns of thiol SAMs was accomplished *in situ* by increasing the STM bias in a nonpolar solvent containing new molecules to be written. At elevated bias, the molecules under the STM tip desorb and are replaced by thiol molecules in solution. Returning to nondestructive imaging conditions, the nanopatterns can be characterized. The newly written patterns display height differences corresponding to the thickness of the *ink* molecules from solution. Bias replacement lithography was used to selectively desorb areas of a dodecanethiol SAM on gold and replaced with ferrocenyl-undecanethioacetate molecules (Figure 2.17).[230] Thiol desorption was accomplished at +3.0 V bias voltage. Gradient patterns were fabricated by adjusting the replacement bias, tip scan rate and the relative humidity. The resolution of the line patterns measured 10 to 15 nm. The structure and electrochemical desorption properties of the surface monolayer determines the bias conditions for lithography; for example, SAMs composed of longer-chain molecules require higher bias.[200]

Approaches have been developed which combine bias-induced lithography with various coatings on AFM tips. A method of electrochemical Dip-Pen Nanolithography was demonstrated using a silicon cantilever coated with platinum salts (H_2PtCl_6).[160] When the tip was scanned in a humid environment across a P-type Si(100) surface at positive DC bias (+1 to +4 V), platinum metal was generated at the cathodic surface.

In another example, SPM-induced cathodic electrografting was accomplished with different alkyne molecules.[234] Molecular inks of 1-octadecyne, 1-dodecyne or 1,4-diethynylbenzene were loaded onto silicon cantilevers for writing with bias-induced lithography. A negative bias (-1.0 to -2.2 V) was applied to the tip for writing. The alkyne molecules were shown to bind covalently to the surface forming patterns with heights corresponding to the thickness of a monolayer.

Electro Pen Nanolithography uses a tip coated with ‘ink’ molecules for writing, and requires that a bias pulses (+9 V) be applied to a conductive AFM tip. Trialkoxysilanes were used as inks (mercaptopropyltrimethoxylsilane, 3-aminopropyltrimethoxysilane, octadecyl-trimethoxysilane) to write patterns on an OTS-coated silicon wafer. The width of the lines increased with humidity, achieving linewidth resolution of 50 nm. The ink does not transfer to the surface unless a bias is applied, therefore the coated AFM tip can be used interchangeably for imaging and writing patterns by changing the voltage.

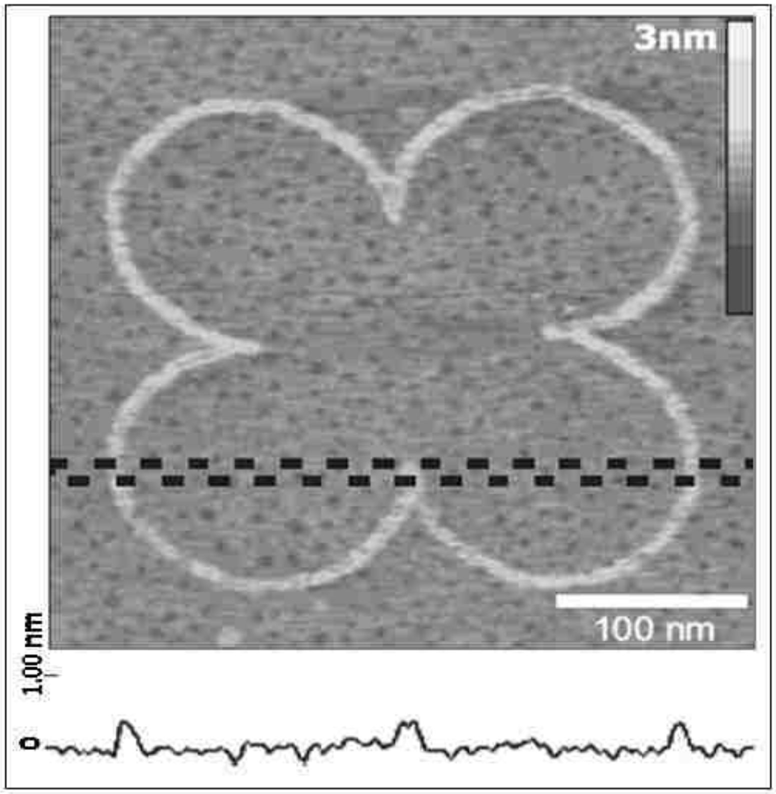

Figure 2.17 Bias-induced replacement lithography was used to write a nanopattern of ferrocenyl undecanethioacetate within a dodecanethiol SAM. (Reprinted with permission from Ref. [230], R. Fuierer *et al.*, *Adv. Mater.* **14**,154 (2002). Copyright@ John Wiley & Sons, Inc.

2.9 NSOM Lithography with SAMs

Photolithography with SAMs has become a practical tool for constructing biosensor arrays,[235] fabricating microfluidic channels[236-237] and for development of microelectronic devices/components.[238-239] Chemical reactions of photolithography are accomplished by irradiating selected small areas of a surface, while masking other areas to prevent photodegradation. By irradiating SAMs with certain wavelengths of light the molecules become oxidized and detach from the surface. The exposed areas of the surface can then be etched to produce 3D structures. Depending on the choice of molecules, photolithography can be used to change the surface chemistry of photoreactive monolayers,[240-242] or can be applied for oxidation/degradation of SAMs.[243-246] Photolithography is the primary tool used for preparing computer memory chips and the manufacture of photoresists has become a multimillion dollar industry.[247] The resolution for conventional photolithography is limited by optical diffraction; structures that are smaller than the wavelength of incident light cannot be produced. Near-Field Scanning Optical Microscopy (NSOM or SNOM) combines the technology of scanning probe instruments with optical spectroscopy in the near field regime.[32] The resolution of NSOM surpasses the diffraction limit, and is determined by the size of aperture and the gap distance between the probe and sample.[32] Lithography with NSOM does not require a photomask, since only selected areas are irradiated by the NSOM probe. The point light source of the probe is scanned above the sample surface to enable selective irradiation of well-defined nanosize regions to accomplish photochemical conversion or oxidation reactions.

In NSOM lithography, nanopatterns are created by exposing an area of the surface to a light source from a fiber optic probe. Instruments for NSOM are operated in noncontact mode and use an illuminated aperture as a light source. A tapered optical fiber coated with metal provides a conduit for light, with a nanoscopic aperture at the end of the sharp probe. The Typical distance of the probe to the sample is in the range of 10 nm and the size of aperture is smaller (<200 nm) than the wavelength of light used for imaging.[31]

Scanning near-field photolithography (SNP) uses an intense collimated light source, such as a laser coupled to an NSOM.[248] Patterns as small as tens of nanometers have been fabricated with SNP.[249] Scanning near field lithography has been applied to create patterns on sol-gel films,[250] silicon,[251-254] azobenzene polyester,[252] triglycine sulfate ferroelectric surfaces,[255] polymers,[256] chloromethylphenylsiloxanes,[257] oligo(ethylene glycol) SAMs[258] and alkanethiol SAMs.[249,259]For SNP with SAMs, a metal-clad fiber optic probe (aperture size ~50nm) that is coupled to a laser is scanned at a distance of 5-10 nm from the surface. Either photooxidation[249,260] or photochemical conversion[257] occur selectively on the areas of the surface that are irradiated when the NSOM probe is scanned above the SAM. An example of SNP by

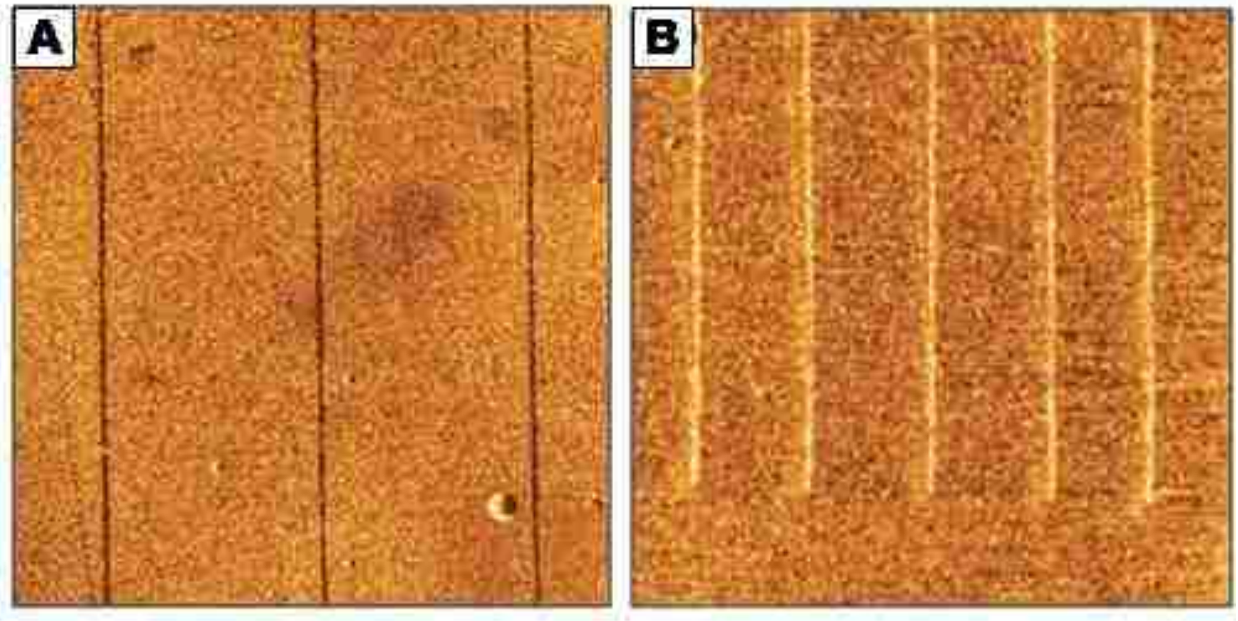

Figure 2.18 Scanning near-field optical photolithography of SAMs. [A] Lines written by SNP photooxidation of dodecanethiol followed by immersion in 11-mercaptundecanoic acid (6x6 μm^2). [B] Reverse protocol with an acid-terminated matrix after immersion in dodecanethiol. Images are frictional force AFM views (6x6 μm^2). Reprinted with permission from Ref. 260, S. Sun *et al., J. Am. Chem. Soc. (communication)* 124, 2414 (2002). Copyright@American Chemical

photooxidation of decanethiol SAMs is presented in Figure 2.18. The line patterns were formed by irradiation of selected regions of the surface with an argon laser (254 nm), to form alkane-sulfonates by photooxidation (Figure 2.18). The oxidized SAMs of exposed areas are readily displaced from the surface.[259] Nanopatterns of different molecules can be created by immersing the sample into a second thiol solution. Alternatively, the sample can be placed in an etchant solution for selective etching of the photooxidized areas of the surface.[259,261] The size of patterns generated by SNP is not limited by the size of the probe aperture, patterns as small as 20 nm have been written for hexadecanethiol SAMs.[249] Examples of nanoscale patterns of SAMs fabricated using SNP are shown with friction images in Figure 2.18.[260]

Line patterns of dodecanethiol were successfully written within mercaptoundecanoic acid (11-MUA) as evident by the color contrast of the images. In the patterned regions, 11-MUA was oxidized. Molecules within the oxidized areas were displaced when the sample was immersed in a dodecanethiol solution. The reverse protocol using a SAM of dodecanethiol as the matrix was accomplished in Figure 2.18B. The changes in frictional contrast are caused by differences in tip-surface adhesion between methyl and carboxyl headgroups. [260]

Nanopatterns produced with SNP are not limited to photooxidation reactions of thiolate molecules. Scanning near-field photolithography can also be accomplished for monolayers with photoactive terminal groups. As regions are scanned by the NSOM probe, exposure to light causes the photoconversion of headgroups to different functionalities.[257] Spatially defined chemical reactions can be achieved by photoconversion of certain terminal groups using SNP. For example, the terminal groups of monolayers of chloromethylphenyl trichlorosilane (CMPS) monolayers on silicon oxide surfaces were converted to carboxylic acid moieties by irradiation with a 244 nm laser source.[257] The patterns were reacted with further chemical steps to anchor nanoparticles and DNA molecules.

2.10 Automated Scanning Probe Lithography

Computer automation can precisely and accurately control the tip position, speed, bias voltage, and fabrication force. All of the SPL strategies presented in Table 2.1 can be coupled with computer automation to enable fabrication of complex patterns. Automated nanografting of SAMs was accomplished with computer assisted design (CAD) software using an open-loop AFM scanner.[4] However, nanoscale imperfections in writing were introduced by creep and drift of the piezoscanner electronics. Also, artifacts may be introduced by the twisting motion of the cantilever under force. Closed-loop AFM controllers which incorporate a secondary sensor to correct for scanner non-linearities provide better alignment and precision for patterning larger sized areas (micron) of surfaces. Writing individual patterns is not practical as a strategy for manufacturing devices, in which millions of structures may be needed for a single memory chip or circuit design. The serial nature of SPL is problematic for future applications, which will require high throughput and speed. This problem has been addressed by creating arrays of multiple probes for parallel writing and by increasing the speed of writing processes.[262]

Parallel writing using DPN has been accomplished with 2-D arrays of cantilevers. Probe arrays with 2,[263] 8,[264] 10,[265-268] 26,[141] 32[264] and 55,000[269] AFM tips have been successfully applied for DPN. The individual probes of the arrays are spaced at intervals ranging from 30 to 310 microns. For the 2-D arrays, all of the tips can be moved in unison to draw identical patterns, while only one of the probes is used for positional feedback by the AFM controller. Alternatively, 2-D arrays have been designed to activate each of the individual probes through various strategies for positional feedback. Probe arrays which use electrostatic actuation,[268] conductivity-based sensing of surface contact[265] and thermal bimorph actuation[266-267] have been developed for parallel writing with DPN. An optical micrograph of a probe array of cantilevers is presented in Figure 2.19. For this example, the tips touch the surface through gravity-driven alignment under the weight of the whole array.

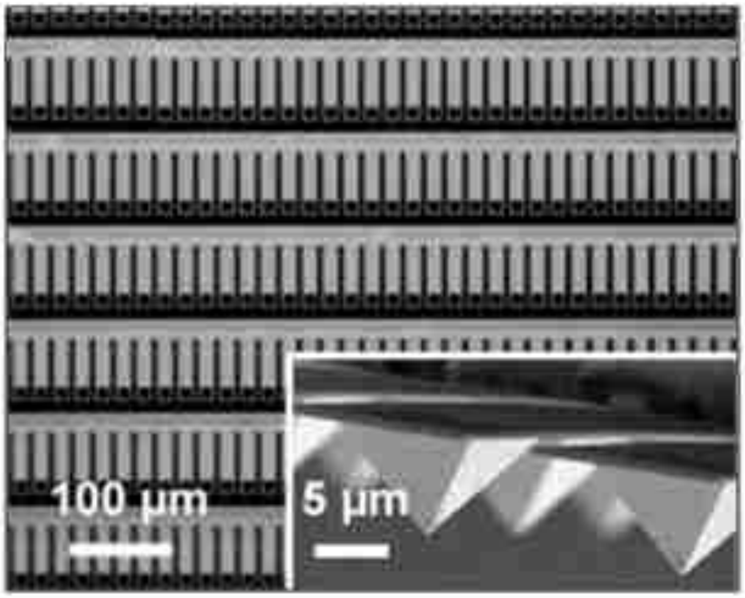

Figure 2.19 Section of a 55,000 probe array used for parallel DPN. (Reprinted with permission from Ref. [269], K. Salaita *et al.*, *Angew. Chem. Int. Ed.* **45**, 7220 (2007). Copyright@ John Wiley & Sons, Inc.

Several design strategies have been tested for AFM imaging which provide activation of individual probes within the 2-D arrays. Parallel imaging was demonstrated with a microfabricated 4 × 4 array of cantilevers with integrated piezoresistive sensors.[270] High speed (4 mm/s) imaging was achieved with an array of 50 cantilevers spaced at 200 µm pitch.[262] The design integrated a piezoresistive sensor and zinc oxide actuator for each cantilever to enable individual control of the set point, gain and feedback for imaging.[271] Thermal actuation of individual cantilevers was demonstrated with an array of 128 probes for parallel AFM imaging.[272] The cantilevers were driven to vibrate by thermal actuation at the probe resonance frequency, and the magnitude of the current established the cantilever deflection.

A 32 × 32 "Millipede" array with 1024 AFM tips was constructed by IBM corporation, and is envisioned for applications for data storage media.[273] The platform design uses thermal sensing for read/write operations of the array. The 2-D array of probes has an approximate size of 3 x 3 mm and was fabricated entirely of silicon. The Millipede concept does not enable individual control of each cantilever, rather feedback is provided by three sensors for the entire chip.

2.11 Summary and Future Prospectus

The examples of SPL described in this chapter are based on writing mechanisms using force, elevated bias, electrochemistry, diffusion and surface adsorption, catalytic reactions and photochemistry with SAMs. Depending on the nature of the molecules chosen for nanolithography, we predict that further innovations for writing strategies will be advanced in future research. Besides the commercial goals of nanotechnology, SPL methods are becoming an indispensable approach for fundamental investigations of the interrelations between chemical structure and properties. Surface structures of SAMs furnish test platforms for size-dependent studies of physical properties. Writing with SAMs provides a way to tune the properties of surfaces for specific applications, e.g. hydrophobicity, surface pKa, reactivity, etc. Surfaces can be designed to anchor materials such as DNA, proteins, polymers, metals, organic molecules and polymers for bottom-up assembly of nanomaterials.

Scanning probe lithography provides an efficient and versatile tool for fabrication or local modification of SAMs on surfaces and enables precise spatial control over chemical functionality, shape, dimension and spacing at the level of nanometers. Combining molecular self-assembly and scanning probe lithography is a viable route towards nanotechnology. Although perhaps SPL is not yet practical for high-throughput manufacturing, substantial progress has been advanced. One can anticipate that there will be future significant contributions for biotechnology, molecular electronics, engineered materials, and chemical/biochemical sensors.

CHAPTER 3. AUTOMATED SCANNING PROBE LITHOGRAPHY WITH n-ALKANETHIOL SELF ASSEMBLED MONOLAYERS ON Au(111): APPLICATION FOR TEACHING UNDERGRADUATE LABORATORIES*

3.1 Introduction

Since the invention of atomic force microscopy (AFM) in 1986,[274-275] scanning probe methods for imaging and nanolithography have become increasingly valuable as tools for basic and applied research. Advances in computer software and hardware, as well as continued improvements of instrument designs have progressively improved the ease-of-use for scanning probe microscopes (SPM). Scanning probe instruments can be operated in a range of environments (UHV, air, liquids) and can measure current, magnetic forces, surface charge, friction, electrostatic forces, etc. with nanoscale sensitivity. The imaging and measurement capabilities of scanning probe microscope have been introduced for undergraduate laboratories in several disciplines including chemistry laboratories. However, the capabilities of SPM for nanolithography have not been as widely applied for undergraduate teaching. New trends in software and improvements in the automation of SPM instruments hold promise for bringing nanoscale experiments into the undergraduate curriculum, and eventually may even be integrated into high school science labs. Optical microscopes have become common in educational labs for a wide range of science disciplines, and the next generation of young scientists will benefit from gaining skills with SPM instruments. To advance beyond the resolution limits of optical microscopes, SPM enables direct views, measurements and manipulation of nanoscale phenomena.

A diverse range of experiments can be planned for educational lab exercises using SPM instruments, which have dozens of different measurement modes and instrument configurations integrated within a single instrument platform. The instruments are inherently a multidisciplinary

---

*Reproduced with permission from Elsevier.

toolkit because nanoscience measurements extend across all of the science disciplines of physics, chemistry, materials science, biology, medicine, and engineering.[276]For example, college laboratory exercises have been developed to illustrate principles of nanoscale measurements for magnetic, electronic, adhesive or frictional forces.[277-278]A basic example would be to illustrate force-displacement profiles and calculations to demonstrate molecular bond rupture events by developing experiments using AFM probes with molecular coatings.[279-280] Other lab exercises could illustrate the imaging capabilities of AFM or scanning tunneling microscopy (STM),[281] particularly for resolving atomic or molecular lattices.[282-286,287] Educational lab exercises with SPM have been reported for imaging surface changes caused by chemical reactions,[288-291] nanopatterning,[277,292] and studies with biomolecules.[284,293] Student experiments with SPM provide 2D and 3D surface maps for illustrating the analysis of data such as height histograms, roughness measurements and digital image processing.[294] Students obtain hands-on experience with molecules and nanoscience, and there are also intangible benefits of the "wow" factor for stimulating intellectual curiosity and enthusiasm for scientific discovery. Examples of SPM systems designed for college laboratories include instruments from NanoInk such as the NanoProfessor,[295] and the model 5400 system from Agilent.[296-297] These systems were designed with intuitive software and ease-of-use for installing probes and samples. Most of the laboratory time is occupied with the use of software interfaces, which minimizes possible damage to the scanners. Meanwhile, SPM probes are relatively inexpensive to replace, as a consumable item. Students can learn to tune in "slow TV" as the images are gradually generated on the computer monitor to reveal exquisite details of molecularly-resolved surface landscapes.

Along with the unprecedented advantages for imaging and measurements of surfaces, a further compelling attribute of SPM instruments for educational activities are the capabilities for nanoscale manipulation of molecules and nanomaterials using scanning probe lithography (SPL), as described in this report. Significant advances in instrument automation to provide intuitive, user-friendly software offers exciting new possibilities for integrating cutting-edge technologies into the undergraduate laboratory curriculum.

3.2 Basic Operating Principle of AFM

The most common set-up for positional feedback with AFM is the deflection-type configuration illustrated in Figure 3.1**.** An AFM tip is attached directly to a piezoceramic scanner for directing tip movement in the x, y or z direction. The piezoceramic material of the scanner tube expands and contracts upon the application of small voltages causing movement at the level of angstroms. An electronic feedback circuit is used to control the amount of force applied between the tip and sample by adjusting the voltages sent to the scanner tube, to maintain a constant deflection of the cantilever.[21] The light of a diode laser is reflected off the back of the cantilever and detected by a position sensitive quadrant photodetector, as shown with the red lines of Figure 3.1. The amount of light impinging on the four photodetector elements changes as the tip is scanned across the surface, and the signals are used for positional feedback. As the AFM tip is scanned in a raster pattern, the up-down and left-right motion of the tip is profiled by the photodetector changes, and this signal is amplified and converted into digital images of topography and lateral force. Topographic images are maps of the surface morphology and are represented by an arbitrary color scale. Lateral force images

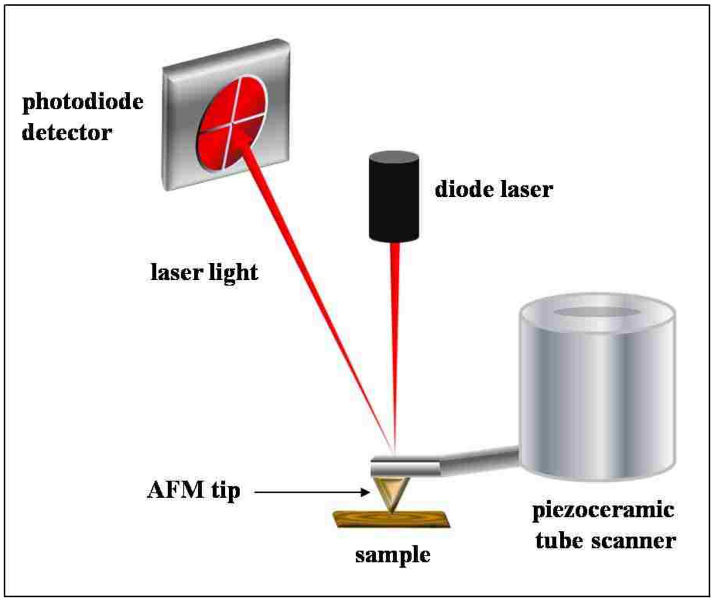

Figure 3.1 Basic instrument configuration for AFM imaging and nanolithography.

indicate variations in the chemical nature of the molecules on the surface, which result from changes in the attractive and repulsive forces experienced by the tip. Topographic and lateral force images are acquired simultaneously. Most importantly, the force applied to an AFM tip can be precisely controlled at the level of nano- to pico- Newtons.[298] Low forces are used when characterizing surfaces to prevent unintentional damage to the sample, whereas higher forces are used for steps of nanofabrication for nanoshaving and nanografting of organic thin films.

A typical set-up for "contact-mode" AFM is presented in Figure 3.1, in which the tip is scanned in continuous contact with the surface. Other protocols can be accomplished by lifting the tip from the surface at a controlled distance for modes of "non-contact" imaging. A further imaging mode known as "intermittent-contact" mode is accomplished with a vibrating tip which intermittently taps the surface, also known as "tapping" mode. Readers are directed to previous publications for further details of SPM imaging modes.[24,299] Images presented in this article were acquired using continuous contact mode AFM imaging.

3.3 Approaches for AFM-based Nanolithography

Mechanisms for SPM-based nanolithography

As methods for imaging and measurements with SPM were developed, researchers observed that under certain experimental conditions small areas of the surface could be accidentally altered or damaged. For example, when too much force was applied to the probe, the surface could be scratched or rearranged. Contaminants on the surface could be picked up by the tip and redeposited in other locations. Nanoscale lithography methods came to be developed by carefully controlling the changes that were made to surfaces, to selectively and intentionally change the chemistry of small areas under the tip. Bias-induced nanolithography, dip-pen nanolithography (DPN), catalytic-probe lithography, nanoshaving, nanografting and NanoPen Reader and Writer (NPRW) are examples of SPL which have different mechanisms for writing nanopatterns.[300-302] The nature of the desired changes in surface chemistry will help determine which nanolithography methods are most suitable and convenient for experiments.

A summary of different techniques for writing nanopatterns using SPM-based lithography is presented in Table 3.1. Very little modification of AFM instruments are needed to accomplish nanolithography. Methods of nanoshaving,[34,303] nanografting[80,93] and NPRW[184] require controlling the force applied to an AFM probe to inscribe patterns within self-assembled monolayers (SAMs). For DPN, the tip is coated with molecules or nanomaterials to be written. The writing of molecules on surfaces is accomplished by transfer from the tip through a liquid meniscus to a clean substrate.[126] For catalytic probe lithography, an AFM tip is coated with catalyst molecules or metals. The coating is not transferred to the surface, instead the catalyst coating of the probe is used to catalyze a chemical reaction and selectively alter the chemistry of areas where the tip is placed in contact with the surface.[190] The catalytic reaction only occurs at areas touched by the tip. Bias-induced lithography is achieved using a conductive tip with a conductive or semi-conductive substrate, in which an electric field is generated between the tip and the sample. As the AFM tip is scanned in contact with the surface at elevated

Table 3.1 Approaches for scanning probe lithography

Method	Mechanism for Patterning	Reference
Nanoshaving	Displacement of a surface layer by mechanical force	34, 304
Nanografting	Simultaneous nanoshaving and replacement of surface molecules by applying force to an AFM tip.	80,93
NPRW	Force is applied to a coated AFM tip to replace surface molecules of SAMs	184
DPN	Transfer of ink molecules from a coated tip through a water meniscus	126
Catalytic probe	A tip coated with a catalyst is used to locally catalyze a surface reaction	190
Bias-induced nanolithography	Local oxidation, desorption or replacement of surface molecules is accomplished under elevated bias voltage	122, 198,200, 305

bias, molecules are either oxidized,[304] desorbed or replaced to create nanopatterns.[122,198,200]Details of strategies and mechanisms for patterning with SPL have previously been reviewed. [34,138,197,203,300,302,305-307]

3.4 Experimental Approach

3.4.1 Materials and Chemicals

Reagent grade dodecanethiol, octadecanethiol, 11-mercaptoundecanol (MUD), and 16-mercaptohexadecanoic acid (MHA) were obtained from Sigma Aldrich (St. Louis, MO, USA) and used without further purification. Ethanol (200 proof) was purchased from AAper Alcohol and Chemical Co. (Shelbyville, KY, USA). Flame-annealed ultra flat films of Au(111) prepared on mica substrates were obtained from Agilent Technologies, Inc. (Tempe, Arizona, USA).

3.4.2 Preparation of Self-assembled Monolayers (SAMs)

Because of the ease of preparation, stability and reproducibility for preparing well-ordered surface structures, SAMs of *n*-alkanethiols are good models for nanolithography experiments. Monolayer films of defined thickness and designed properties can be generated by changing the functional (head) groups of the alkyl chain; these functional groups can also be used for further chemical reactions in later chemical steps. The preparation, characterization, and properties of SAMs have been described and reviewed previously.[36,46,52-53] Samples of matrix monolayer films were prepared by immersing gold substrates in 0.01 mM ethanolic solutions of the chosen *n*-alkanethiols for at least 12 hours. The samples were then removed from the thiol solution, rinsed copiously with fresh ethanol and placed into a liquid cell holder for AFM imaging and lithography. Ethanol solutions of MHA (10^{-9} M) and MUD (10^{-6} M) were freshly prepared for nanografting protocols.

3.4.3 Scanning Probe Microscopy (SPM)

Experiments were accomplished in solution using either an Agilent 5500 SPM system or an RHK system interfaced with a PicoSPM scan head. The Agilent system was equipped with PicoScan version 5.3.3 software and PicoLITH beta v.0.6.0 for nanolithography. Images were acquired at a scan rate of 3.0 nm/s using 512 lines/frame. The RHK system was operated with XPMPro v1.1.0.9 software using SPM100 controllers. Oxide sharpened V-shaped silicon nitride probes from Veeco Probes (MSCT-AUHW, Santa Barbara, CA) were used for imaging and nanofabrication. The probes have an average force constant of 0.5 N/m. Image processing was accomplished using either Gwyddion software, version 2.5, which is freely available for download and is supported by Czech Metrology Institute[308] or with PicoScan version 5.3.3 from Agilent.

3.5 Results and Discussions

3.5.1 Creating Patterns Within a SAM Matrix Using Nanoshaving

Nanoshaving describes AFM-based methods of nanofabrication in which the tip is operated under force to uncover or scratch away selected regions of substrates that are covered with a matrix layer of an organic thin film. Nanoshaving can be accomplished in air or in liquid media. In air, the molecules that are displaced tend to accumulate at the edges of nanopatterns, whereas in liquid the displaced molecules can be dissolved in the surrounding solvent. Imaging in liquids has the advantage of improving resolution, since strong shear forces and tip-surface attraction caused by capillary forces in air are greatly decreased when imaging in liquids.[91-92] Nanoshaving is accomplished by applying a high mechanical force to an AFM tip as it is raster scanned across the surface to sweep away molecules of the surface layer as shown in Figure 3.2.

The process of nanoshaving is completed in three basic steps. First, a flat area of the surface is identified and imaged under low force (Figure 3.2A). For the characterization step, typically forces less than 1 nN are applied to the probe to enable high resolution characterization of the topography without damaging the sample surface. An area with few defects is chosen for

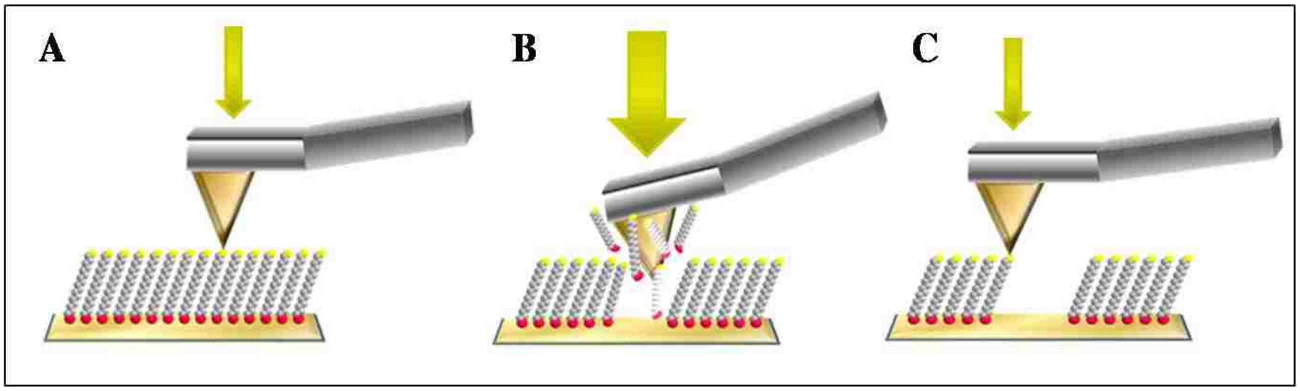

Figure 3.2 Basic steps for nanoshaving with an AFM tip operated under different forces. [A] Characterization under low force. [B] Nanoshaving is accomplished when the force is increased. [C] Returning to low force, the nanoshaved patterns can be imaged.

inscribing patterns, preferentially a flat gold plateau which is wide enough to write the desired pattern sizes. Next, a greater force ranging from 1–10 nN is applied to the AFM tip to shave away the matrix molecules from the substrate as it is scanned with a pattern design (Figure 3.2B). A sufficient amount of force is needed to ensure complete removal of the matrix SAMs without damaging the underlying gold substrate. After molecules are shaved away, the same AFM probe is used for imaging the newly fabricated patterns by returning to a low force (Figure 3.2C). With careful control of the forces applied to the tip, hundreds of patterns can be fabricated within a few hours of an experiment. The uncovered regions created from nanoshaving are then available for deposition of new molecules and materials.[19,90,114] Nanoshaving has also been used to provide information about the thickness of molecular layers on surfaces.[88,309] The uncovered areas of the substrate provide a baseline for thickness measurements of SAMs with angstrom precision.

3.5.2 Automated Nanolithography Using Designs Created with Picolith Software

Computer automation of scanning probe instruments enables the rapid fabrication of complex patterns with intricate designs and arrangements at the nanoscale to be a relatively routine accomplishment. Patterns with nanometer dimensions can be readily achieved with precision and accuracy using software that controls the position, force, bias and speed of the probe. Example designs used for creating nanopatterns are shown in Figure 3.3 using PicoLITH software from Agilent. Automated nanoshaving is more complicated than producing images for a computer printer, since the user must consider where the tip is picked up or placed down on the surface. When the tip is picked up and placed down this can lead to gaps or stray marks for designs. Better fidelity is achieved when the tip is moved continuously across the surface without removing the tip. The analyst will need to experiment with different designs to determine how many times to outline the features to observe which scanning paths work best for sweeping material from the surface. Sketches of the desired patterns are outlined with PicoLITH scripts using a computer mouse or pen stylus to draw the patterns. For the examples in Figure 3.3, arrows indicate the writing direction for translating the AFM tip. The overall size of the patterns is defined by the size of the view window selected within the data acquisition window of the PicoSPM operating software, e.g. $1\times1\ \mu m^2$. Patterns can be outlined once or traced several times. The colored squares at the bottom of the PicoLITH design (Figure 3.3) are the scientific pallets that can be used to assign specific parameters for operating the probe. For example, experimental parameters for the speed, amount of force or bias voltage applied to an AFM tip are assigned by choosing a color and assigning values. Automated lithography with an RHK SPM is accomplished with a computer controlled vector scan module as previously described by Cruchon-Dupeyrat, et al.[4] Computer statements to control the motion of the probe are written and compiled into lithography scripts to designate the writing speed, length, direction and force applied for inscribing nanopatterns.

3.5.3 Writing Patterns of Self-assembled Monolayers with Nanoshaving

Patterns for the designs of Figure 3.3 with different shapes and geometries written are shown in Figure 3.4, for nanoshaving within a matrix SAM of *n*-octadecanethiol.

Octadecanethiol has 18 carbons aligned in a chain as the backbone of the molecule, and is anchored to the surface by a single gold-sulfur bond. The headgroups at the surface of the molecular layer are methyl groups (CH_3), and the overall thickness of the SAM film is approximately 2.1 nanometers. Topography images acquired with AFM are displayed by a selected color scale; in this report the shorter features are dark and taller structures are brighter in color. Nanoshaving was accomplished in ethanol by applying a high force to the AFM tip as it was scanned, to sweep away and remove selected areas of the matrix monolayer from the gold surface following the outline of the designs shown in Figure 3.3. After writing patterns, the same AFM probe was used to immediately characterize the patterns *in situ*. The images in Figure 3.4 reveal intricate details of the surface morphology of octadecanethiol as directly viewed by nanosize defects such as scratches, scars, pinholes and etch pits. Overlapping terrace steps and the outlines of the gold substrates underlying the SAM are also visible in the images. Although the surface may appear somewhat rough, the terrace steps are only 0.25 nm in height and are characteristic landmarks of a high-resolution image of a SAM. At the nanoscale, even very small features such as etch pits, which are only 0.2 nm deep can be resolved using AFM. The small

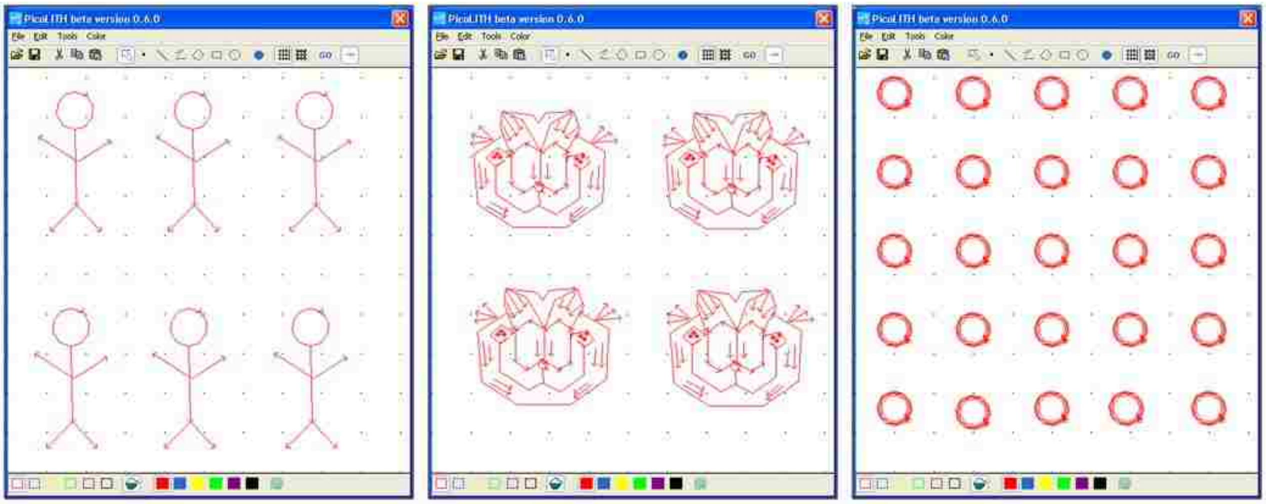

Figure 3.3 Example designs created using PicoLITH software by undergraduate students, during a Physical Chemistry laboratory at Louisiana State University. From left to right, sketches for patterns of stick people, cartoons of the face of a cat, and a 5 × 5 array of rings.

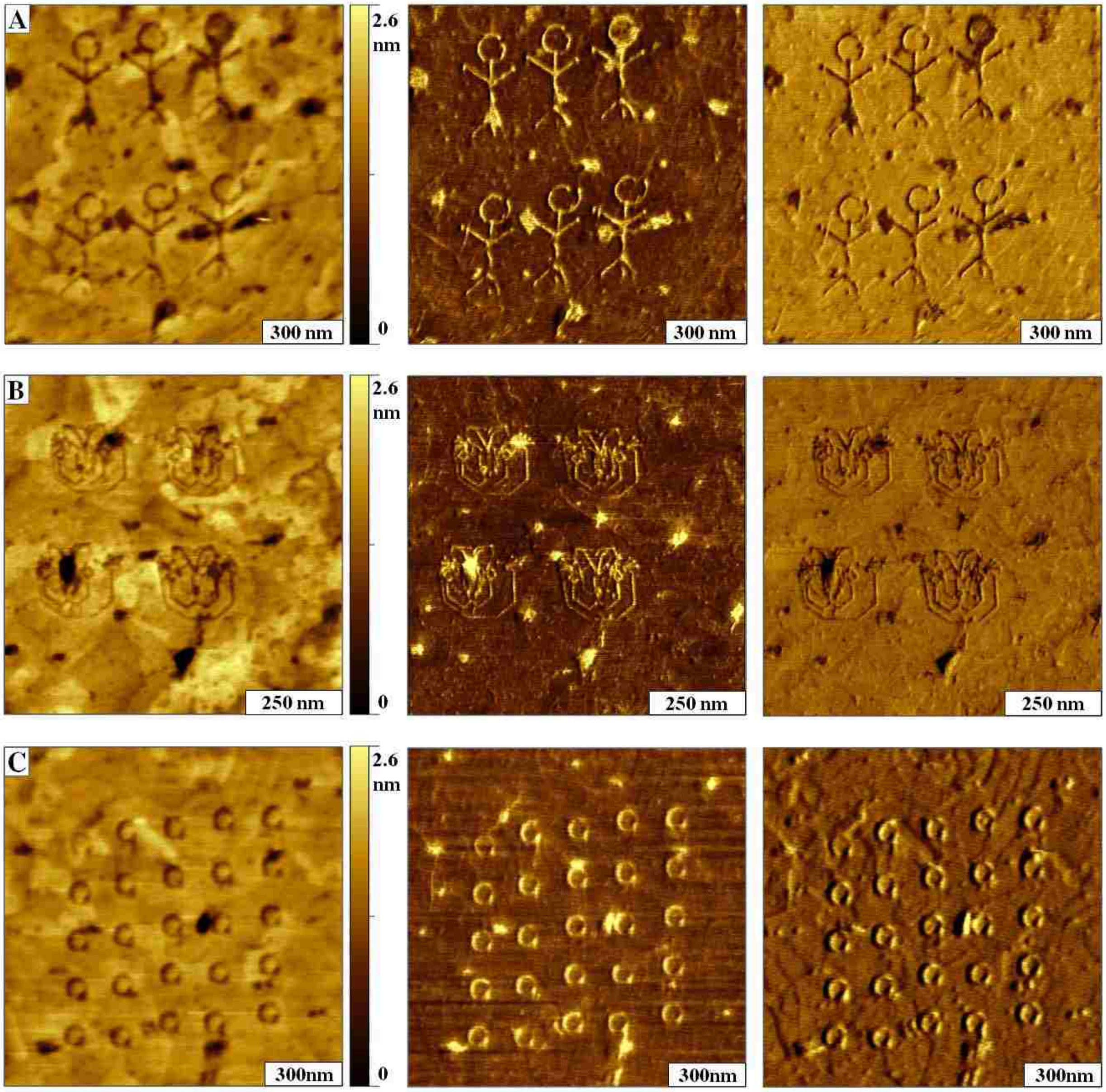

Figure 3.4 Nanoshaved patterns created with the designs of Figure 3 within a matrix monolayer of octadecanethiol on a gold substrate. [A] AFM topography view of six stick figures and the corresponding trace and retrace lateral force images (from left-to-right). [B] Topography and lateral force images of the cat cartoon patterns produced with nanoshaving. [C] Topography and lateral force images of an array of ring nanopatterns.

holes scattered over the surface are commonly called etch pits, (also known as molecular vacancy islands) which are produced by surface reconstruction.[74] The fine details of the irregular contours of the edges of the gold terraces can only be observed with a sharp tip. Such high-resolution images can be routinely acquired by using AFM in liquid environments.

Figure 3.4A displays images of six stick people inscribed within octadecanethiol using nanoshaving. The images and nanopatterns were produced by undergraduate students during a 3 hour laboratory session of Physical Chemistry (Chem 3493). The trace and retrace lateral force images do not show height information; rather the changes in tip-surface friction are mapped to disclose variations in surface chemistry for the areas of the nanopatterns. Lateral force images are acquired simultaneously with contact mode topography images and provide additional chemical information of the sample nature. For these examples, the tip-surface adhesion between the AFM tip is markedly different for the uncovered gold substrate of the nanopatterns compared side-by-side with the methyl-terminated molecules of the SAM matrix areas. The patterns of stick people were written using a single pass of the AFM probe to outline the design and were completed in one minute. The linewidth measures approximately 10 nm, and varies according to the sharpness of the AFM probe.

A more sophisticated pattern was nanoshaved (Figure 3.4B) to outline a cartoon of a cat design. This example was accomplished within 3 minutes using a writing speed of 0.1 μm/s and an applied force of 2 nN. The speeds used for nanoshaving are comparable to the optimized speeds for acquiring images; of course if the tip is rastered too quickly it can break contact with the surface to produce discontinuous patterns. One might be concerned that operating an AFM tip under force might cause it to become dull or break the apex of the probe, however this example exhibits superb resolution for resolving etch pits, pin hole defects and the lacey contours of step edges, despite having used the tip under force for nanoshaving. We have found that silicon nitride probes are quite robust within the typical operating range of 2–10 nN of force used for SPL. Often the tip becomes sharper and resolution improves over time when nanoshaving. The patterns of Figure 3.4B were traced once and measure 7 nm in linewidth.

Using nanoshaving, 25 ring patterns were inscribed within an octadecanethiol SAM (Figure 3.4C), however for this example the designs were outlined four times. A force of 2 nN was applied for nanoshaving to produce rings measuring 80 nm in diameter with widths of 18 nm. Scanner hysteresis and drift can produce small changes in the nanoscale registry of the pattern arrangements, as viewed for the misalignment along the *x* direction. This is likely caused by using too much force to write the patterns, leading to a slight drift in probe motion across the array of ring designs. However, the precision for writing rows of patterns in the y direction is near perfect, with uniform 100 nm spacing between each ring in the x and y directions.

3.5.4 Automated SPL Using Computer Scripts

Examples of sixteen nanoshaved patterns of interconnected circles created within octadecanethiol are presented in Figure 3.5, generated with an in-house designed computer script with an RHK controller. The exquisite reproducibility for controlling nanoscale lithography is evidenced by the precise, regular shapes and interpattern spacing and alignment at the nanoscale. The topography frame of Figure 3.5A shows a $1.2 \times 1.2\ \mu m^2$ view of the nanopatterns and the corresponding design is sketched in Figure 3.5B. The design of each pattern was produced by outlining four circles with a common focal point. The rings are shallower than the surrounding monolayer of octadecanethiol. Each individual ring measures 60 nm in diameter, with the smallest line width measuring approximately 10 nm. A few stray marks are apparent above the patterns, which results from up-down translation of the tip when it is picked up or placed at locations for writing. For this example, the scars of the underlying gold film influence the brightness of the image color scale, since the nanoshaved patterns are shallower in depth (2.1nm) than the defects of the substrate (10 nm). However, the fidelity of nanoshaving for writing precise nanoscale designs can still be sufficiently well resolved at this size scale.

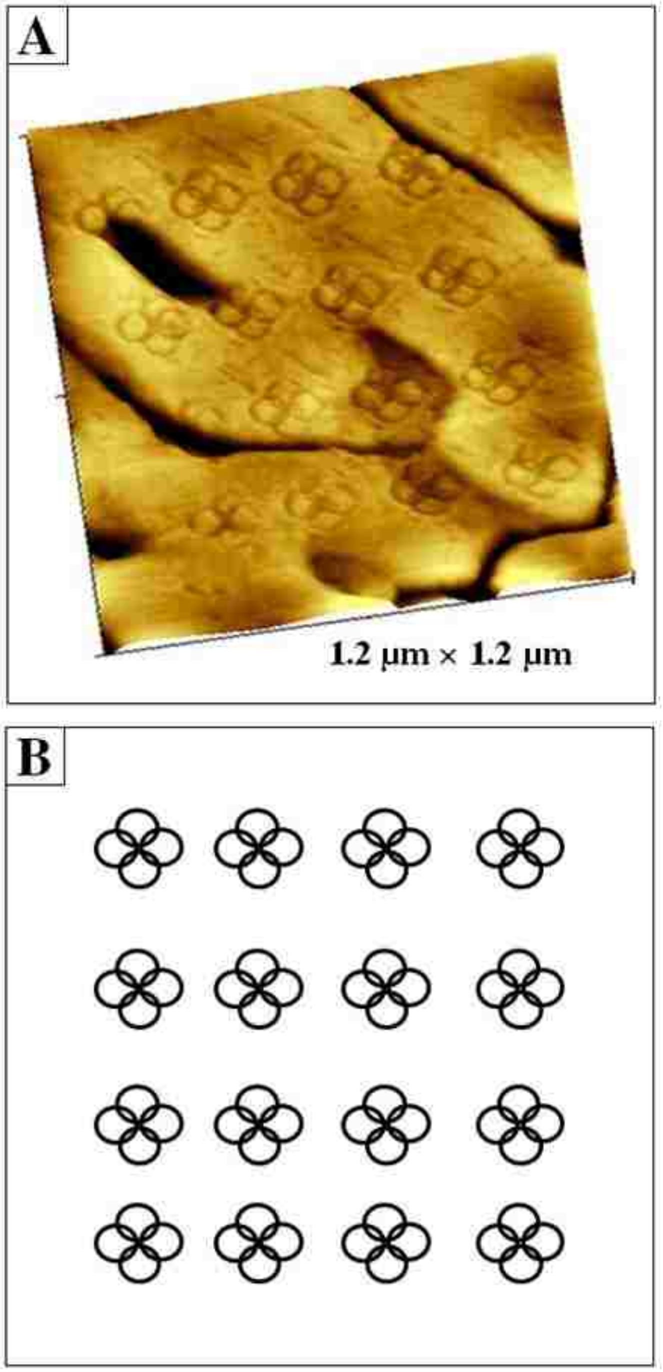

Figure 3.5 Example nanopatterns produced by nanoshaving selected regions of octadecanethiol using an SPM instrument from RHK Technologies. [A] Contact mode topograph; [B] sketch for the corresponding patterns in ***A***.

3.5.5 Using Nanografting to Write Designed Patterns of *n*-Alkanethiols

Nanografting is likewise accomplished by increasing the force applied to an AFM probe;

however, instead of operating the tip in clean solvent, the imaging media was replaced with a freshly prepared, dilute solution of *n*-alkanethiols to be patterned. Nanografting was developed in 1999 by Xu, et al. and since then has been used for writing a range of molecules with thiol groups.[93,302] Similar to nanoshaving, there are three basic steps for nanografting as outlined in Figure 3.6. In the first characterization step, a flat area that has few defects is selected for inscribing patterns by imaging under low force, typically less than 1 nN (Figure 3.6A). Next, the force is increased to push through the surface monolayer to make contact with the gold surface underneath. As the tip is scanned under force, the matrix molecules underneath the tip are shaved away and immediately replaced with new molecules from the surrounding solution (Figure 3.6B). Following the scanning path of the AFM tip, molecules assemble and bind to the areas of gold that were uncovered by the probe to produce designed patterns. Returning to low force (Figure 3.6C) the same probe is used to characterize the nanopatterns that were fabricated. When the tip is operated under low force the surface is not disturbed and no patterns are formed. Patterns are produced only when the force has been increased.

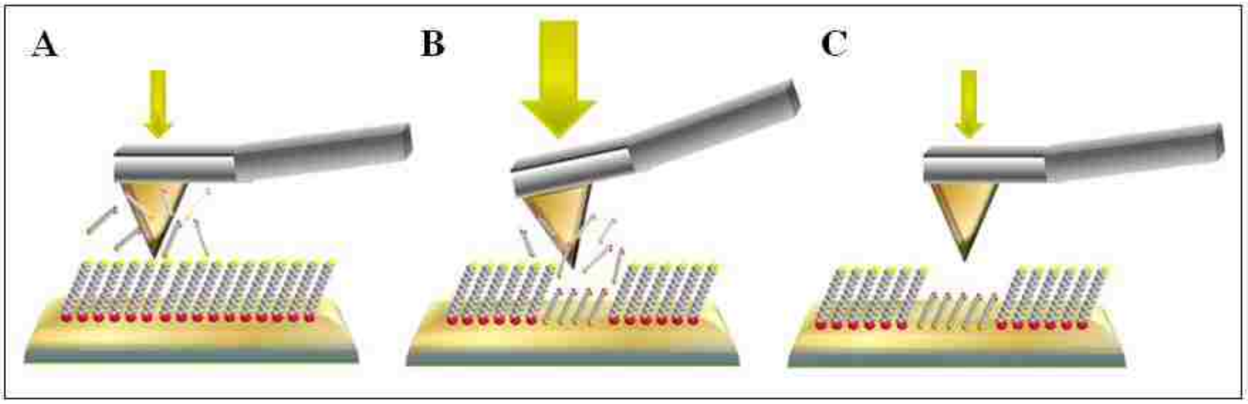

Figure 3.6 Steps for nanografting are accomplished by scanning with a tip under high force, while the tip is immersed in a solution containing molecules to be written. [A] Surface characterization is accomplished under low force while imaging in a solution containing thiol molecules. [B] Nanografting is accomplished by increasing the force applied to the AFM tip; fresh molecules from solution assemble following the path of the scanning probe. [C] Returning to low force, the nanografted patterns can be imaged.

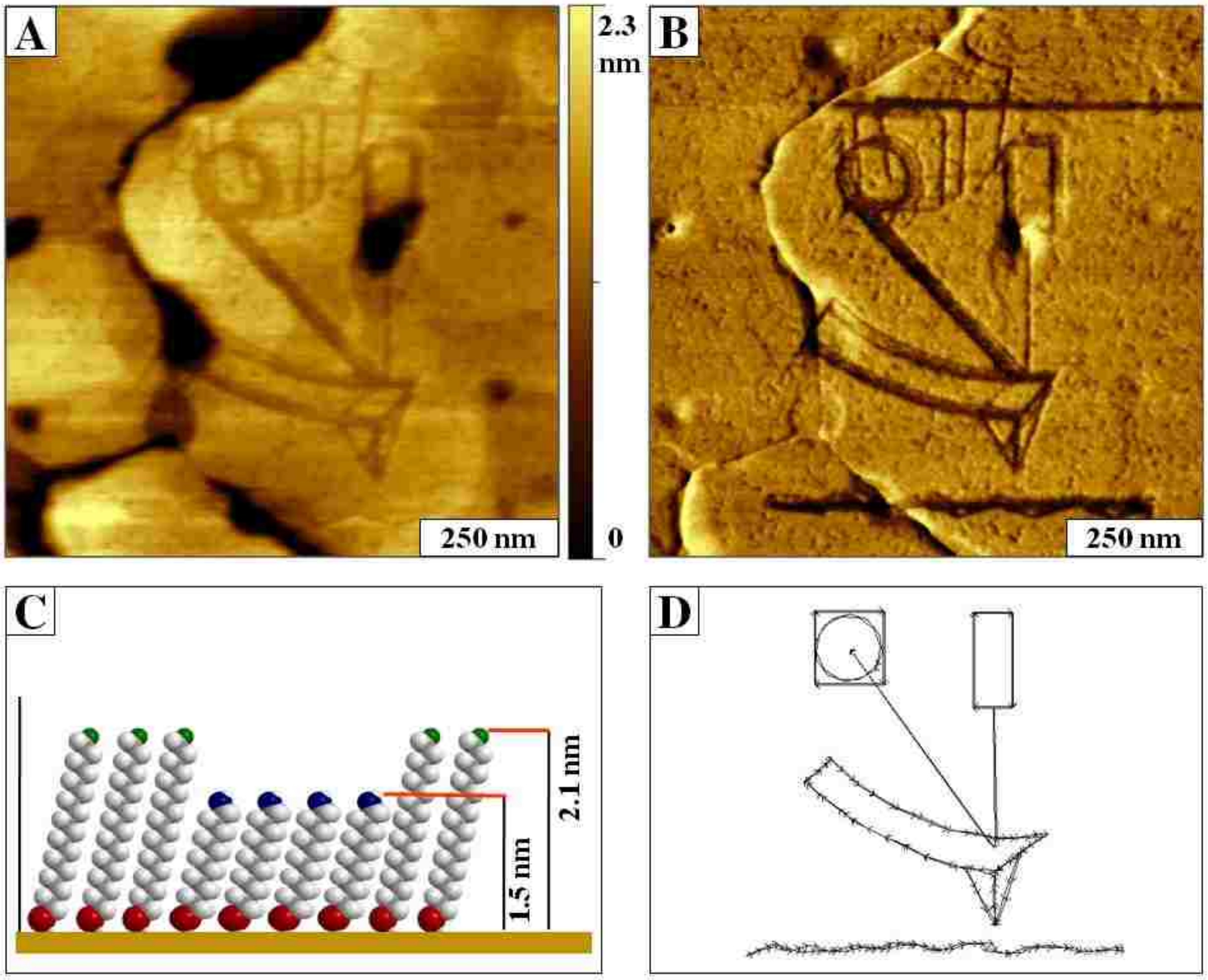

Figure 3.7 A nanoscale AFM instrument diagram written with 11-mercaptoundecanol within an octadecanethiol SAM. [A] Contact mode AFM topograph for a 1×1 μm^2 scan area; [B] corresponding lateral force image; [C] molecular model showing height differences between the pattern and matrix monolayer; [D] design used for nanografting.

When designing nanografting protocols, the analyst can choose from a range of commercially available thiol molecules with different lengths and head group chemistries. Examples are shown in Figure 3.7 of nanografted patterns with heights that are shorter than the matrix monolayer. The topography and corresponding lateral force images of the design for an AFM instrument schematic are presented in Figures 3.7A and 3.7B, respectively. The instrument components were described previously in Figure 3.1. Characteristics of the general morphology of an *n*-alkanethiol SAM are apparent in the topography frame, such as etch pits and terrace steps. The lateral force image more prominently reveals the pattern design, because the

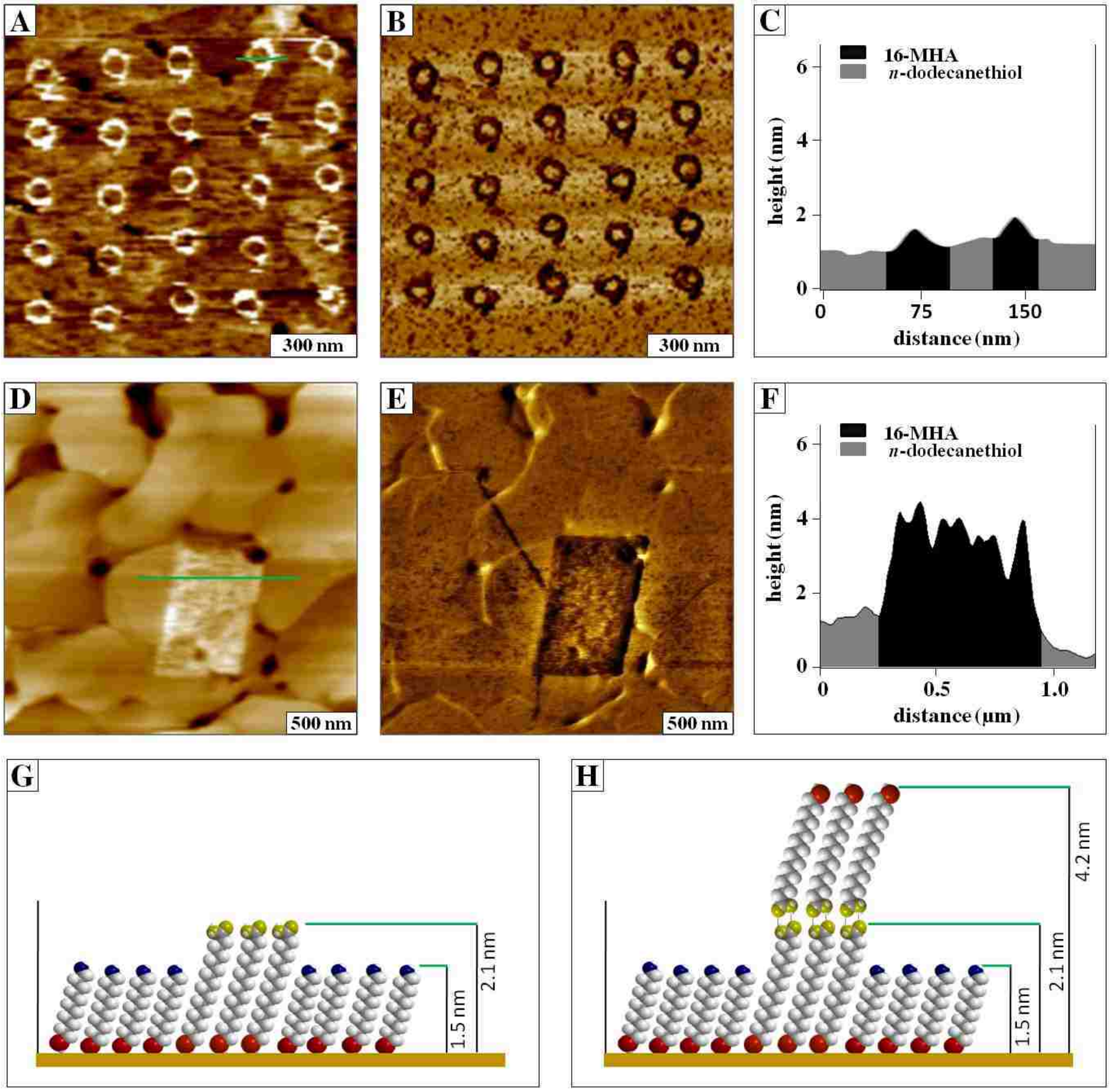

Figure 3.8 Nanografted patterns of 16-mercaptohexadecanoic acid written within a SAM of dodecanethiol. [A] Topography image (1.2×1.2 μm^2) of an array of ring patterns; [B] corresponding lateral force image; [C] height profile for the line in ***A***; [D] topograph of a rectangular pattern (2.5×2.5 μm^2); [E] lateral force image for ***D***; [F] line profile across the pattern in ***D***; [G] height model for the nanografted pattern of ***A***; [H] model of the double-layer pattern of ***D***.

headgroups of the pattern areas are chemically different than the matrix SAM which provides frictional contrast. The areas surrounding the pattern are methyl-terminated octadecanethiol and the patterns were written with hydroxyl-terminated 11-mercaptoundecanol, which is 0.6 nm shorter than the matrix SAM. A model of the molecular heights is shown in Figure 3.7C. The script used to outline the nanopatterns is shown in Figure 3.7D, with excellent correspondence between the design and resulting nanografted patterns for such small size scales. The smallest linewidth achieved for this pattern was accomplished with a single sweep for the vertical line between the backside of the cantilever and the diode laser, measuring 13 nm in width. With an ultra sharp AFM probe, the smallest feature produced with nanografting is an island of a 2×4 nm^2 dot pattern, which is an area that would accommodate approximately 32 thiol molecules.[119] Examples of nanografted patterns with heights that are taller than the matrix monolayer are shown in Figure 3.8. Interestingly, the same molecules were used for Figures 3.8A and 3.8D, however the concentration of the imaging media was increased for Figure 3.8D. The topography and corresponding lateral force images of an array of ring patterns shown for the design of Figure 3.3 are presented in Figures 3.8A and 3.8B, respectively. At low concentration, (10^{-9} M) 16-mercaptohexadecanoic acid (MHA) forms patterns with heights corresponding to a monolayer.

For these examples, the matrix monolayer is dodecanethiol, which has 12 carbons in the hydrocarbon backbone chain. Dodecanethiol is ~0.5 nm shorter than MHA, which is consistent with the height measured for a line profile across one of the nanopatterns (Figure 3.8C). When the concentration of the imaging media of MHA was increased to 10^{-6} M, molecules with carboxylic acid-terminated headgroups form dimers and assemble to generate double layers (Figure 3.8D).[310-311] Dimers of MHA are produced in solution by coupling of the acid headgroups. Height models of the MHA nanopatterns are shown in Figures 3.8G and 3.8H for the single and double layer patterns, respectively. The acid headgroups of the nanopatterns exhibit strong tip-surface adhesion, producing line spike artifacts in the topography frames. The differences in surface chemistry between the nanografted patterns (carboxylic acid headgroups) and the dodecanethiol matrix SAM (methyl headgroups) provide excellent contrast for the lateral force image of Figure 3.8B. However, for the lateral force image of Figure 3.8E, the headgroups of the rectangular pattern are most likely terminated with a thiol endgroup.

These examples of nanografted patterns illustrate the inherent capabilities of SPL for 3-dimensional control of nanostructures by selecting the molecular length, headgroups, and pattern geometries. Nanoscale characterizations and lithography are valuable tools for directly studying surface chemical reactions at the nanoscale within a well-controlled, liquid environment. After producing nanopatterns with nanoshaving or nanografting, further chemical reaction steps can be accomplished by exchanging the imaging media, for example by introducing solutions of new molecules,[19]copper salts[96] or proteins[116,312] to build complicated architectures from the bottom-up.

3.6 Applications of Scanning Probe Nanolithography

Scanning probe lithography approaches such as nanoshaving and nanografting with organic thin films extend beyond simple fabrication of nanopatterns to enable control of surface composition and reactivity at the nanoscale. Methods to precisely arrange molecules on surfaces already contribute to discoveries that are advancing future technologies in molecular electronics, nanomedicine and surface chemistry. Automation of SPL will likely have a significant role for implementing nanotechnology in commercial products.

3.6.1 Impact of SPL for Advancements in Molecular Electronics

Writing individual patterns of organic films one at a time will not be a practical strategy for manufacturing devices in which billions of structures are needed, such as for designs of computer memory chips and circuits. Future nanotechnology applications will require much higher throughput and speed for generating patterns. This problem is being addressed by the development of arrays of multiple probes for parallel writing.[269,273] For semiconductor-based technologies, organosilane thin films are widely used as resist layers for microfabrication of circuits, wires, transistors and memory chips. As the size of components achieves ever smaller dimensions, the inherent advantages for miniaturizing to the nanometer level will be the benefits of higher information density and faster processing time. Nanotechnology holds promise for advantages of smaller, cheaper and more energy efficient electronic devices. To achieve smaller elements will require molecular-level precision such as the capabilities provided by automated SPL.

3.6.2 Application of SPL for Nanomedicine

Nanoscale assays provide intriguing possibilities for the direct detection and *in situ* visualization of the binding of small molecules, DNA, antibodies or proteins to nanopatterns, while enabling surface changes to be monitored with time-lapse AFM images.[301-302] Nanostructures of SAMs written by SPL provide highly controllable test environments for exquisite images of surface changes during biochemical reactions.[313]Although electron microscopies can be used for high-resolution 2D imaging of biomolecules that have been freeze-dried and sputter-coated with conductive films, reactions conducted in aqueous (physiological) media or buffers cannot be accomplished in the UHV environments of electron microscope chambers. Approaches with SPM provide 3D images of fragile biomolecule systems and cells with minimal sample preparation. Tools of SPL extend the capabilities of high-resolution scanning probe imaging to enable experimentalists to control surface arrangements of biomolecules at the molecular level. Examples of fundamental studies incorporating tools of SPL for investigations of biomolecules include the regulation and control of multiplexing, reactivity, and polyvalent interactions; nanoscale assays with oligonucleotides[98]or receptors for sensing or bioassays;[314-315] as well as construction of DNA[97,316-318] and protein[116,312] nanostructures.

3.6.3 Role of SPL for Fundamental Investigations of Surface Chemistry

Intuitively, binding between molecules is a nanometer-sized phenomenon, thus a close-up view of molecules on surfaces can provide a fresh perspective for mechanisms of how reactions occur. Nanografted patterns can be incubated with desired nanomaterials or molecules, and time-lapse AFM provides direct views to monitor the successive changes in height and surface morphology as reactions proceed over time. The reaction sites are spatially constrained to nanosized areas defined by the headgroups of nanografted/nanoshaved patterns, providing exquisite control of reaction parameters at the nanoscale. Such studies provide insight about surface reaction mechanisms and kinetics. For example, *in situ* investigations with nanografting have been reported for adsorption of proteins[114,118,124-125] electroless deposition of copper on nanografted SAMs,[96]templated growth of ionic self-assembled multilayers,[319]and pattern transfer reactions with polymers.[19]

3.7 Underlying Themes for Undergraduate Instruction

The take-home message from a scanning probe lab exercise would perhaps be that we “looked at molecules” and learned how to write nanopatterns on surfaces. The existence of atoms or molecules in materials is a critical concept for understanding chemistry and physics, along with calculations of the size and number of molecules/atoms that are present. Many students have difficulties in understanding concepts of atomic and molecular scale phenomena, and the challenge of visualizing the shapes and arrangements of atoms and molecules has been implicated as a core issue.[287] Scanning probe experiments offer premiere opportunities for students to learn interactively to visualize surfaces, measure properties and to manipulate surface chemistry at resolutions down to molecular and atomic length scales. Advancements in software and automation have made scanning probe instruments relatively easy to operate, and the new capabilities are ideally suited for undergraduate laboratories. As the field of nanoscience research has evolved, SPM methods have mostly been limited to professional researchers and graduate students; however, there is increasing interest for advancing nanoscience education at the undergraduate level.[320] Our practical strategy at LSU has been to accomplish undergraduate teaching activities using our research instruments, with the slight expense of a few broken probes.

The background information to be presented for SPM laboratories will depend on the timeframe and type of experiments that are designed. A complete grasp of nanoscale concepts most likely exceeds the scope of an undergraduate course. However, a basic introduction and illustration of selected topics of nanoscience can certainly be accomplished to provide a spark for future student interest. During the past four years at LSU, we have successfully integrated SPM modules into the third-year undergraduate physical chemistry lab course. During each semester, 12–16 students are given an opportunity for hands-on experiments with AFM/STM instruments. One session is devoted to an introduction of the basic principles of nanoscale imaging and instrument operation, and a second session is used for nanolithography experiments. As an indicator of the level of student enthusiasm, the afternoon class is scheduled for 3 hours duration, but usually several students persist late into the evening to capture additional frames and to experiment with designs for writing nanopatterns (Figure 3.9). From these classroom groups, 30 undergraduates have further elected to take additional hours of supervised research credit, choosing to work with projects using SPM. The undergraduates have all made contributions as

Figure 3.9 Undergraduate students from an LSU physical chemistry laboratory engaged in learning new skills with an AFM instrument.

co-authors of research posters and/or journal articles, and have participated in fundamental studies with systems of nanoparticles, proteins or self-assembled monolayers.

3.8 Future Prospectus

Impressive accomplishments have been attained by manufacturers of scanning probe instruments for the automation of SPL and for providing user-friendly software for routinely imaging at the nanoscale, as evidenced by the nanofabrication examples of this report. One can easily predict that such capabilities will become ever more widely applied in education, research and technology in the near future. There is an emerging need for workers with scanning probe skills, since methods of SPM and SPL are becoming indispensable for fundamental investigations related to nanotechnology. Data published on the National Nanotechnology website (www.nni.gov) estimates that 20,000 researchers are currently working in nanotechnology worldwide, and the National Science Foundation has estimated that 2 million workers will be needed to support nanotechnology industries globally within 15 years.[321]

A skilled scientific workforce will be an essential requirement for implementing nanoscience discoveries in future manufacturing or technology applications. Knowledge and experience in modern methods of surface measurements and analysis will be pivotal to the rapid transfer of nanotechnology into commercial products. At present, scanning probe microscopes and scanning probe-based lithography aru primarily used for laboratory research investigations rather than as tools for manufacturing. The transfer of new technologies developed in academic research labs to the public sector will require dissemination of skills and information from cutting-edge nanoscience research to the undergraduate curriculum across scientific disciplines. The latest advances in automation of SPM instruments enable new possibilities for educational modules using SPL, providing opportunities for designing diverse and compelling student activities to teach the concepts of chemistry and nanoscience, showcased at the molecular level.

CHAPTER 4. SURFACE ASSEMBLY OF PYRIDYL-SUBSTITUTED PORPHYRINS ON Au(111) INVESTIGATED *IN SITU* USING SCANNING PROBE LITHOGRAPHY*

4.1 Introduction

Porphyrin and metalloporphyrin systems are excellent materials for molecular electronics due to their diverse structural motifs, associated electrical, optical and chemical properties, and thermal stability.[322] Structures of porphyrins have been proposed as components for molecule-based information-storage devices,[323-324] photovoltaic cells,[325-326] organic light-emitting diodes,[327-328] and molecular wires.[329] The function and efficiency of porphyrins in devices is largely attributable to how the molecules are organized on surfaces.[43,330-331] The surface assembly of porphyrins is influenced by complex intermolecular interactions between the macrocycles as well as by the binding interactions between the surface and peripheral groups. There is a problem with processability for producing monolayer films of porphyrins on surfaces, because at high concentrations the pi-pi interactions between macrocycles tend to produce aggregate structures in solution such as nanocrystals or stacked arrangements. In previous reports, porphyrins have been shown to form a coplanar arrangement on surfaces, usually exhibiting low-density, incomplete surface coverage.[332-338] The conditions which produce liquid crystals of porphyrins are not well-suited for producing monolayer films on surfaces. A problem of solubility in certain solvents is posed for nanofabrication protocols, which can be addressed by using mixed solvent systems.

In this report, nanografting was applied for patterning pyridyl-functionalized porphyrins. A model porphyrin functionalized with two pyridyl and two phenyl groups was chosen for nanofabrication studies. Patterns of 5,10-diphenyl-15,20-di-pyridin-4-yl-porphyrin (DPP) were nanografted within *n*-alkanethiol self-assembled monolayers (SAMs) on gold substrates. Our

---

*Reproduced with permission from Society of Photo Optical Instrumentation Engineers (SPIE).

goal was to direct the surface orientation of DPP to generate single layer nanostructures with an upright configuration. We hypothesized that the mechanism of spatial confinement[339] that occurs when nanografting in ethanolic solutions would generate an upright configuration of DPP, rather than produce stacks of multilayered structures with coplanar arrangements. Pyridyl groups provide a means to attach porphryins to the substrate mediated by nitrogen-gold chemisorption. Nanostructures of DPP fabricated using nanografting can be compared side-by-side with the well-known dimensions of *n*-alkanethiol SAMs to gain molecular-level views of the surface orientation of DPP. The well known heights of *n*-alkanethiol SAMs as a surface matrix layer provide a molecular ruler for local measurements of the thickness of DPP nanopatterns.

Nanografting was introduced in 1997 by Xu and Liu for fabricating patterns of thiolated molecules on gold surfaces.[80] With nanografting, a mechanical force is applied to the tip of an atomic force microscope (AFM) to write thiolated molecules directly in an upright orientation, and surface attachment occurs through sulfur-gold chemisorption. Nanografting is accomplished in dilute solutions of molecules selected for patterning and has been used with a broad range of thiolated molecules such as alkanethiols and alkanedithiols. Nanostructures of SAMs produced using nanografting can then be used as a foundation for bottom-up assembly of complex nanostructures of polymers,[19] metals,[96] and proteins.[118,301] Nanografting was also used to study the assembly mechanism of *n*-alkanethiol SAMs in a spatially confined environment.[6] Significant advantages for *in situ* investigations have been achieved with nanografting since the steps of characterization and writing are accomplished in liquid media without exchanging AFM tips. Since experiments are conducted in liquid media, tremendous resolution can be achieved for AFM images because the strong capillary interactions between the AFM probe and sample that are present in ambient air are reduced or eliminated when imaging in a liquid environment.[2,185-186] Details of the successive changes in morphology of the surface can be viewed with high resolution AFM after successive steps of characterization and nanopatterning. With *in situ* writing, the nanopatterns remain in a carefully controlled environment and solutions within the liquid cell can be exchanged to introduce new reagents for further chemical reactions.

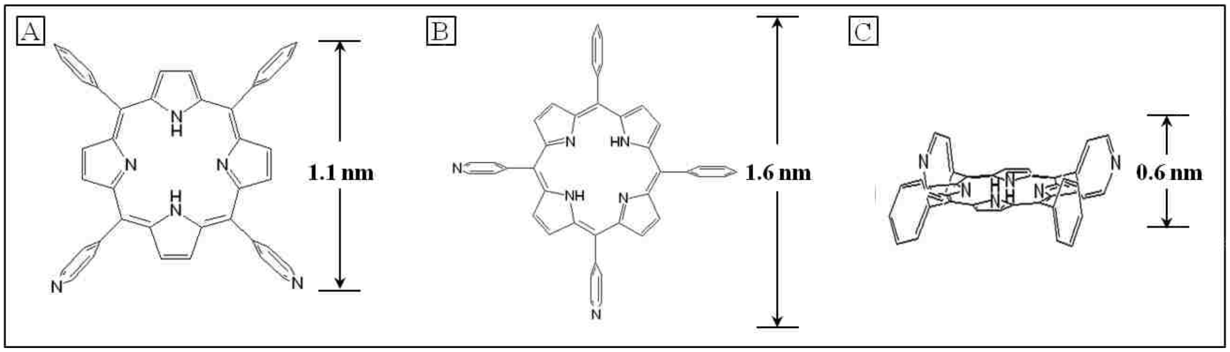

Figure 4.1. Structure and possible configurations of 5,10-diphenyl-15,20-di-pyridin-4-yl-porphyrin (DPP) on Au(111).

Diphenyl dipyridyl porphyrins could form either upright or co-planar orientations, with one or more surface linkages to the surface. Possible configurations of 5,10,15,20-di-pyridin-4-yl-porphyrin(DPP) on Au(111) are presented in Figure 4.1. An upright configuration with linkages through two pyridyl rings anchored on the surface is shown in Figure 4.1A, measuring 1.1 nm in height if the molecule is oriented perpendicular to the substrate. If the linkage is through a single pyridyl group, the fully extended molecular height would measure 1.6 nm for a perpendicular orientation (Figure 4.1B). A coplanar orientation would have a height measuring 0.6 nm with the plane of the macrocycle aligned parallel to the surface (Figure 4.1C). The peripheral substituents of phenyl or pyridyl rings are oriented 90 degrees relative to the plane of the porphyrin macrocycle for all three structures.

4.2 Experimental Approach

4.2.1 Materials and Reagents

Matrix thiols such as octadecanethiol (ODT) and decanethiol were obtained from Sigma Aldrich (St. Louis, MO) and used without further purification. Ethanol (200 proof) was obtained from AAper Alcohol and Chemical Co. (Shelbyville, KY) and dichloromethane was purchased from EMD Chemicals (Gibbstown, NJ). The substrates used for nanolithography were flame-annealed Au(111) film of 150 nm thickness, supported on mica (Agilent Technologies, Phoenix, AZ). Self-assembled monolayers (SAMs) of *n*-alkanethiols were prepared by immersing gold substrates in a 0.01 mM ethanolic solution of *n*-alkanethiols for at least 12 h. The SAMs on Au(111) were then copiously rinsed with fresh ethanol and placed in the AFM liquid cell. Stock solutions of porphyrins were prepared by dissolving 5,10-diphenyl-15,20-di-pyridin-4-yl-porphyrin (DPP) in dichloromethane. To prepare a nanografting solution of DPP, the dichloromethane solution was further diluted with absolute ethanol to 10^{-6} M.

4.2.2 Atomic Force Microscopy

An Agilent 5500 AFM/SPM system operated in contact-mode was used for AFM characterizations and lithography (Agilent Technologies, Chandler, AZ). Images were acquired at a scan rate of 3.0 nm/s with 512 lines/frame using Picoscan v5.3.3 software. Oxide-sharpened silicon nitride probes (MSCTAUHW) from Veeco (Santa Barbara, CA) were used for AFM experiments. The probes have V-shaped cantilevers and force constant, *kavg* = 0.5 N/m. The same probes were used for both imaging and nanofabrication. Picolith v2.2 was used to design and write patterns for nanografting.

4.2.3 Procedure for Nanografting

Nanografting of DPP was accomplished by applying a local mechanical force to an AFM tip to replace matrix alkanethiols on the gold surface with DPP molecules from solution, following the scanning track of the AFM tip. Nanografting is accomplished *in situ* while the tip and the sample are immersed in a dilute solution of new molecules chosen for writing, with three basic steps as shown in Figure 4.2. In the first step, the surface of a SAM was characterized with minimal force to select a relatively flat area with few defects. A small nondestructive force, typically less than 1 nN was used for the characterization step with contact mode AFM imaging.

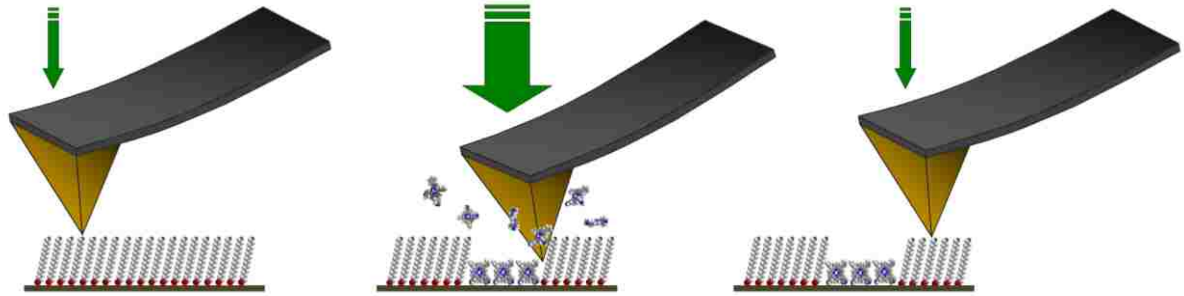

Figure 4.2 Steps for nanografting DPP within an *n*-alkanethiol self-assembled monolayer.

Next, the force was increased to 2-5 nN to push the tip through the matrix layer to touch the underlying gold surface. As the tip was raster scanned across the surface under high force, molecules from the substrate were shaved away to leave areas of the gold surface uncovered. Immediately following the path of the tip, DPP molecules from solution attach to the uncovered areas. The area of contact between the AFM tip and substrate is quite small, producing a spatially confined area for surface assembly. In the final step, the force was reduced for AFM imaging to characterize the nanopatterns of DPP *in situ*. For nanografting, the amount of force applied to the tip must be carefully controlled to preserve the sharpness of the AFM probe. The optimized minimal force to successfully write a complete pattern was chosen by writing a series of patterns at different force settings and choosing the minimal force setting which successfully produced a pattern.

4.3 Results and Discussions

The liquid media used for imaging and nanofabrication was a solution of mixed solvents, 1% dichloromethane in ethanol with 10^{-6} M DPP. Solvents which evaporate quickly such as dichloromethane or toluene are not suitable for AFM experiments; however solutions of ethanol, sec-butanol and water work well for AFM imaging in liquids. Unfortunately, porphyrins are mostly insoluble in alcohols or aqueous solvents so a two-step protocol was developed with mixed-solvents in which the porphyrin was first dissolved in a chlorinated solvent, then the stock solutions was subsequently diluted further in ethanol to prepare the liquid media for nanografting.

4.3.1 Nanografting of DPP Within a Decanethiol SAM

Example nanopatterns of DPP produced by nanografting in a decanethiol matrix SAM are shown in Figure 4.3 before and after nanografting. For the AFM topographs, (Figures 4.3A and 4.3D) the heights are displayed with a relative color scale, where taller structures have brighter contrast and shallow features appear darker. As revealed in high resolution images, surfaces are not truly flat and uniform at the nanoscale; rather there are defects such as scratches, scars and pinholes. A selected area of the surface shown in Figures 4.3A and 4.3B shows a staircase arrangement of overlapping terrace steps of a decanethiol covered gold substrate.

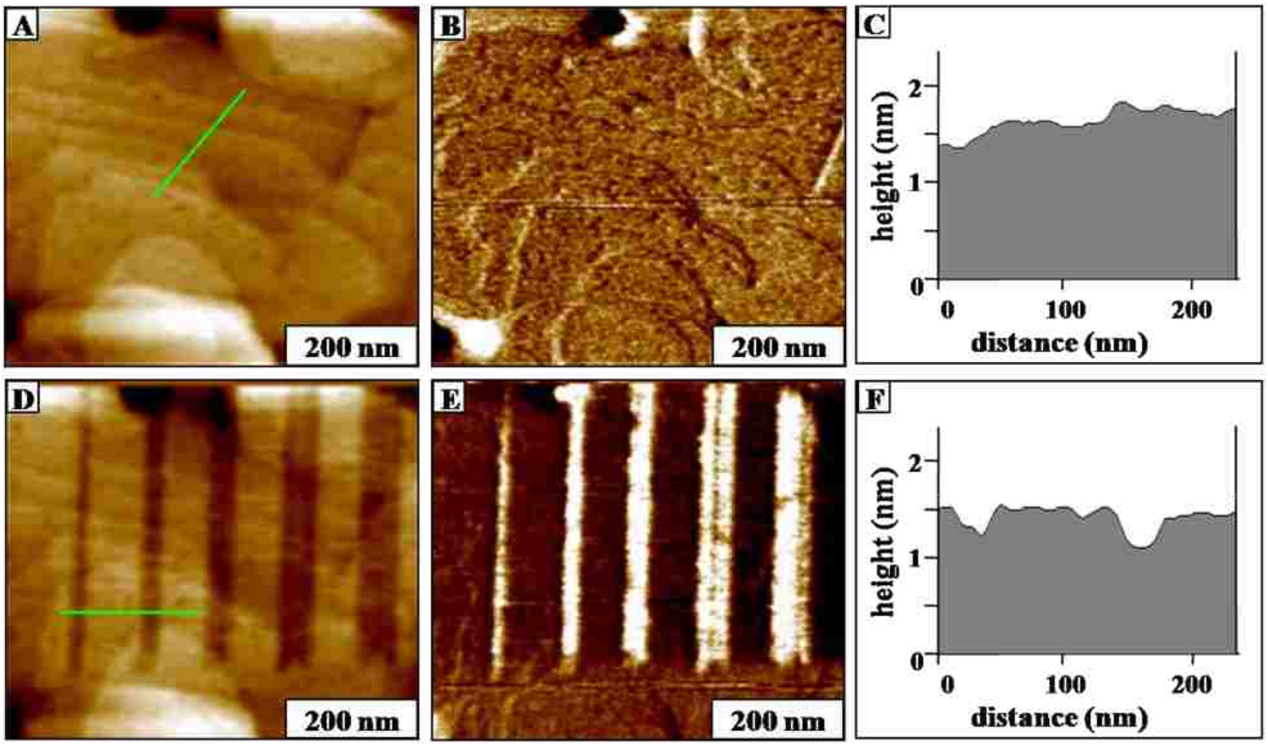

Figure 4.3 Nanografted patterns of DPP produced within a SAM of decanethiol/Au. [A] Contact mode AFM topograph of the SAM before nanografting; [B] corresponding lateral force image for ***A***; [C] cursor profile for the line in ***A***. [D] Nanografted line patterns of DPP written in the same area; [E] lateral force image for ***D***; [F] cursor profile for ***D***.

The surface morphology of the SAM exhibits the characteristic features of molecular vacancy islands or etch pits, measuring approximately 0.2 nm in depth. Etch pits result from the displacement of gold atoms during surface reconstruction upon chemisorption of *n*-alkanethiols to gold.[46] Eight overlapping terraces of the gold surface are visible in the selected area. The heights of the terrace steps provide an internal reference for Z calibration with AFM measurements. The simultaneously acquired lateral force image (Figure 4.3B) also defines the edges of overlapping gold steps. A line spike in the middle of the image results from the tip sticking to the surface during the scan. A representative cursor line profile is shown in Figure 4.3C across several gold steps. After nanografting with DPP, topography and lateral force images of the surface are presented in Figures 4.3D and 4.3E, respectively for the same area that was shown in Figure 4.3A. Five vertical line patterns were written within the decanethiol matrix, by programming the direction, force and motion of the AFM tip. The dark lines in Figure 4.3D correspond to areas where DPP molecules were nanografted, revealing a shorter height than the surrounding matrix areas of decanethiol. A force of 2.3 nN was used for nanografting; however the sharpness of AFM probe was retained after writing under force, as evidenced by views of high resolution features characteristic of gold steps and etch pits. The lateral force image (Figure 4.3E) shows brighter contrast for the patterned areas compared to the surrounding matrix indicating that the surface chemistry of the fabricated areas has changed. The expected height of the decanethiol matrix is 1.4 nm. The thickness of DPP patterns are 0.4 ± 0.2 nm shorter than the surrounding decanethiol SAM which indicates that DPP adopts a standing up configuration with two pyridyl linkages to the surface, corresponding to the model of Figure 4.1A.

A map of the path programmed for the AFM tip is shown in Figure 4.4. The patterns were written with automated software using a single pass of the AFM tip across the surface following the direction of the arrows. The array of lines was completed within 1 minute. The line resolution and pattern fidelity are remarkable, considering that an open loop AFM scanner was used for writing nanopatterns. The line patterns have progressively wider lateral dimensions of 20, 33, 50, 60, and 66 nm (from left to right), with a uniform vertical length of 400 nm.

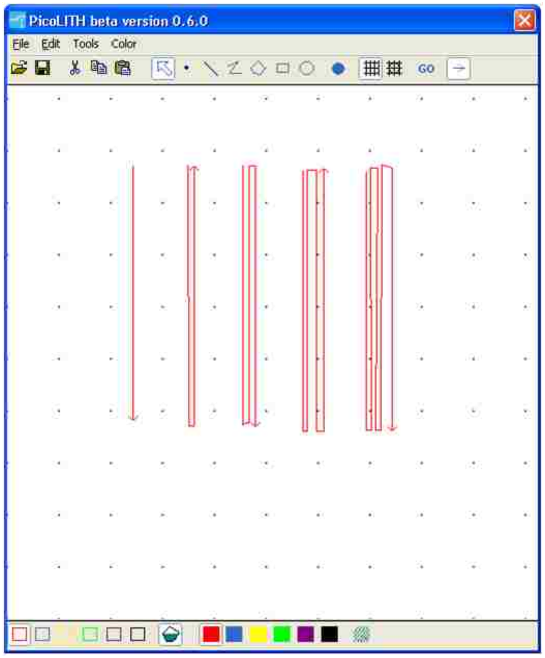

Figure 4.4 Computer design used for nanografting line patterns of DPP within a decanethiol matrix

4.3.2 Nanografting of DPP Within an Octadecanethiol SAM

Further experiments were accomplished for nanografting DPP in mixed solvent media with a taller matrix SAM of n-octadecanethiol (ODT). A circular pattern filled with DPP was successfully nanografted within an ODT matrix as shown in Figure 4.5. The pattern was written in 2 min using a force of 3.4 nN. The diameter of the filled circle measured 300 nm and the design of the pattern was achieved by outlining 50 concentric rings of successively increasing sizes. The filled circle is mostly sited on a single terrace area of Au(111) except for a small area at the top left corner where it is situated on the next gold step. The trace and retrace lateral force images disclose the pattern edges and changes in surface chemistry for the area patterned with DPP. Bands at the sides of the pattern were introduced artificially during image processing and are not true changes in heights or frictional force. The expected thickness of an ODT SAM is 2.1 nm, and the DPP nanopattern is approximately 1.0 ± 0.3 nm shorter than the ODT matrix (Figure 4.5D). The height closely corresponds to a standing configuration for the nanografted patterns with two pyridyl linkages, as shown in Figure 4.5E.

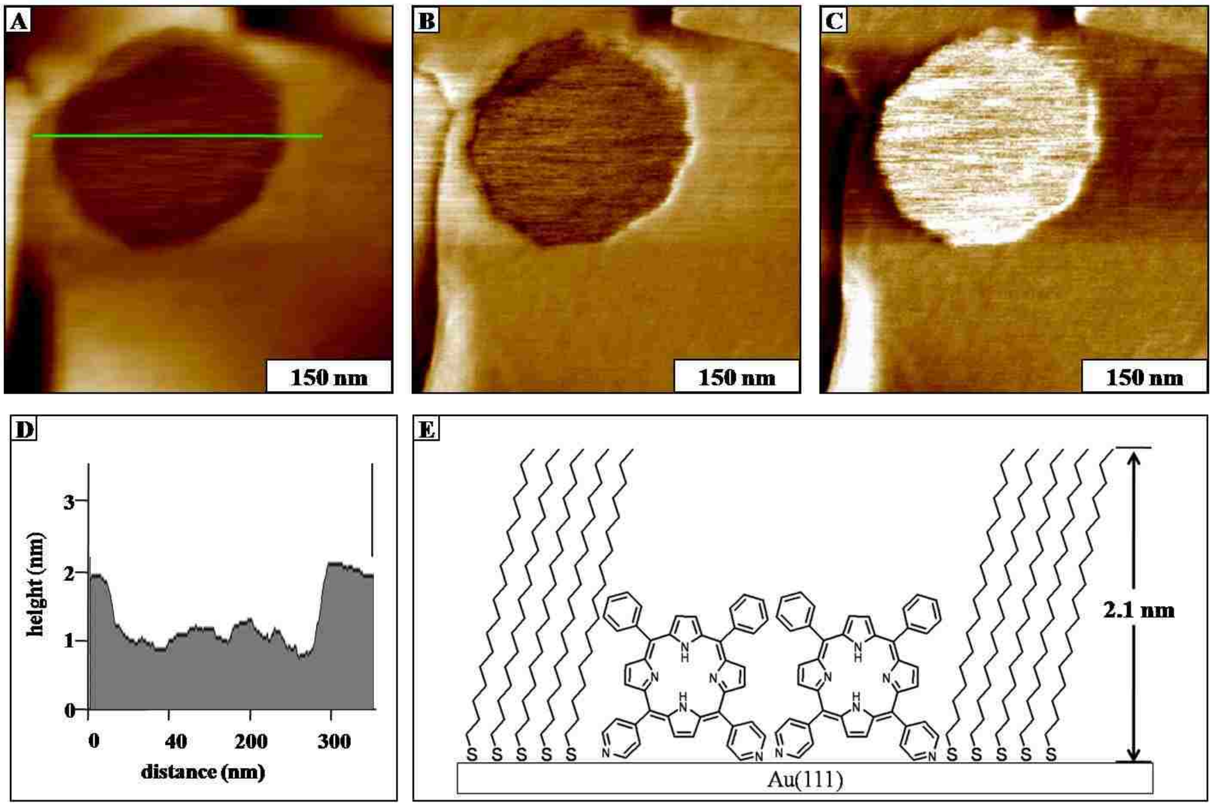

Figure 4.5 Circular nanopattern of DPP written within an ODT SAM. [A] contact mode topograph; corresponding [B] trace and [C] retrace lateral force images of the nanopattern; [D] corresponding line profile for *A*. [E] Height model for patterns of DPP nanografted within an ODT matrix.

During nanografting, the surface assembly of DPP porphyrins most likely follows a similar reaction pathway previously described for alkanethiol SAMs due to spatial confinement.[339] Unlike the zig-zag backbone of alkanethiol molecules, porphyrins have wider overall dimensions which are bulkier for surface assembly within a confined space. It is interesting to note that the heights of nanografted patterns of DPP match closely with the height expected for a perpendicular configuration with respect to the surface. It is likely that the rotated orientation of the phenyl and pyridyl groups relative to the macrocycle provides a block-like geometry which stabilizes the upright orientation and serves to prevent a tilted arrangement. Under conditions of nanografting the transient reaction environment confined between the scanning AFM tip and surrounding matrix SAM is sufficiently small to prevent DPP molecules from assembling in a coplanar, lying-down orientation. When nanografting, a small local area of freshly exposed gold substrate is produced by scanning the AFM tip under high force. The transient bare area of the surface is confined between the AFM probe and thiol matrix molecules with dimensions less than the molecular length of the DPP molecules, therefore nanografted molecules assembling on the surface do not have sufficient space to assemble in a lying-down configuration. According to the height measurements, DPP molecules assemble directly onto gold with a standing configuration when nanografted.

4.4 Conclusions

Nanopatterns of pyridyl porphyrins (DPP) were successfully produced by nanografting within different *n*-alkanethiol matrices, revealing that pyridyl porphyrins can directly assemble on Au(111) into an upright configuration. Nanografting in liquid media was accomplished by using a mixed solvent system, to solve the problem of solubility with porphyrins. Matrix monolayers of decanethiol and octadecanethiol were used as a molecular ruler to evaluate the thickness and surface orientation of nanografted patterns of DPP. These investigations suggest that a mechanism of spatially-confined self-assembly occurs when writing patterns of dipyridyl porphyrins during nanografting, and it is likely that surface linkages of DPP are formed through nitrogen-gold chemisorption. Nanografting enables surface assembly in a dilute regime with mixed solvent systems, e.g. dichloromethane/ethanol. With nanografting, DPP molecules assemble directly onto gold with a standing-up configuration due to spatially constrained self-assembly.

CHAPTER 5. ASSEMBLY OF 5,10,15,20-DI-PYRIDIN-4-YL-PORPHYRIN ON Au(111) FROM MIXED SOLVENTS

5.1 Introduction

Porphyrins and metalloporphyrins are useful materials for devices because of photoelectric, catalytic and electronic properties. For surface and structural characterizations, porphyrins have been deposited on surfaces of Ag,[340] Au,[341-343] HOPG,[344-345] Si,[346-347] and sapphire.[344] The properties and surface morphology are largely determined by the length, composition, nature and position of the peripheral groups attached to the macrocycle.[84,348-349] For example, the electrical conductance of linear dithiolated porphyrin arrays was found to be influenced by molecular length.[350] Porphyrins have applications for molecular electronics,[351-353] switching devices,[354] sensors,[355-357] photonic devices,[358] photovoltaic cells[348] and photoelectrochemical cells for light-harvesting applications.[359-361] The organization of molecules on surfaces determines the function and efficiency of devices.[330-331,362] Understanding the self-organization and assembly of porphyrins is important for optimizing the function of these molecules for potential device applications.

The assembly of porphyrins on surfaces is a complex process resulting from the interplay of interactions between porphyrin macrocycles, attached substituents and the nature of the surface chemistry. Unlike thiol[363-365] and organosilane[366] molecules that have been extensively investigated, the solution phase assembly of porphyrins has not been widely studied. The ability of linear molecules with thiol and silane moieties to form ordered monolayers on surfaces results from interactions between the alkane chains of the individual molecules as well as endgroup chemistry.[367] In contrast, the planar macrocycles of porphyrins have a fully conjugated π electron system which enables intermolecular interactions between planar rings, which tends to result in self-aggregation to form crystals. Complex intermolecular interactions, such as pi-pi stacking between macrocycles or binding interactions between peripheral groups and surfaces dictate the overall assembly processes of porphyrins from solution.[368-369]

Porphyrins have been reported to adopt a coplanar arrangement with surfaces, forming stacks and clusters on surfaces because of strong pi-pi interactions.[332-338] Deposition methods and the nature of organic solvents have also been found to influence the formation of porphyrin clusters on surfaces.[370-371] Different structures can be observed on the surface depending on methods of sample deposition, the nature of the solvent that was used and the overall molecular architecture. At high concentration, samples of porphyrins often spontaneously form crystals.[372-373] Porphyrins have limited solubility in certain solvents, and are often immiscible in water or alcohol which limits the processing ability for producing organic thin films for surface studies.

In this report, high resolution imaging combined with scanning probe lithography were used to investigate the surface assembly of 5,10,15,20-di-pyridin-4-yl-porphyrin (DPP) on Au(111) from mixed solvent solutions. Details of changes in the surface morphology of pyridyl-functionalized porphyrins were captured over time using atomic force microscopy (AFM) imaging. Scanning probe lithography (SPL) approaches of nanografting and nanoshaving were used make local measurements of the thickness of porphyrin nanostructures. Nanoshaving has previously been used to characterize films of *n*-alkanethiol SAMs,[3,88] organosilane SAMs,[85,374] polymers, [375-376] DNA[377-378] and molecular micelles.[379] Selective patterning of molecules has been accomplished with nanografting to write patterns of different thiolated molecules such as *n*-alkanethiols,[2,34] alpha,omega alkanedithiols,[380] thiolated proteins,[118,381] nanoparticles,[90] and thiolated DNA.[382] Nanografting is known to alter the assembly of *n*-alkanethiols through a mechanism of surface confinement.[6] By designing the arrangement of pyridyl and phenyl substituents linked to the macrocycle our goal was to gain molecular level insight for controlling the orientation of porphyrins on Au(111) surfaces, to prepare a densely packed monolayer of defined thickness. We hypothesized that the assembly of porphyrins which typically assemble in a coplanar orientation on surfaces could likewise be disrupted by spatially confined self-assembly with nanografting to form an upright orientation on Au(111), mediated by nitrogen-gold surface linkages of pyridyl groups.

5.2 Materials and Methods

5.2.1 Materials and Reagents

Silica gel from Sorbent Technologies 32-63 μm was used for flash column chromatography. ^{1}H- and ^{13}C-NMR were obtained on a ARX-300 Bruker spectrometer. Electronic absorption spectra were measured on a Perkin Elmer Lambda 35 UV-Vis spectrophotometer and fluorescence spectra were measured on a Perkin Elmer LS55 spectrometer. Mass spectra were obtained with an Applied Biosystems QSTAR XL. All solvents used for synthesis were purchased from Fisher Scientific (HPLC grade) and used without further purification.

Reagents such as ethanol (Aaper, Shelbyville, KY), dichloromethane (EMD Chemicals, Gibbstown, NJ), sulfuric acid (EMD Chemicals, Gibbstown, NJ), hydrogen peroxide (Fisher Chemical, Fairlawn, NJ) were used without further purification. Flame annealed gold-coated mica substrates (150 nm thickness) were acquired from Agilent Technologies, Inc. (Chandler, AZ). Highly ordered pyrolytic graphite (MikroMasch, Wilsonville, OR) and polished silicon wafers (Virginia Semiconductor, Inc. Fredericksburg, VA) were also used as substrates for AFM samples. Alkanethiols such as octadecanethiol, dodecanethiol and decanethiol were purchased from Sigma Aldrich (St. Louis, MO, USA) and used without further purification.

5.2.2 Synthesis of Bis(pyridyl)bis(phenyl)porphyrin

The bis(pyridyl)bis(phenyl)porphyrin was prepared via a mixed porphyrin condensation in refluxing propionic acid, as previously reported.[383-385] This procedure is known as the Adler and Longo methodology[386] and afforded all six porphyrins in yields varying from 0.5 to 5%. To a refluxing solution of benzaldehyde (7.0 mL, 138 mmol) and pyridine-4-carboxaldehyde (3.0 mL, 63.0 mmol) in propionic acid (250 mL) was added pyrrole (6.25 mL, 180 mmol), dropwise. This caused the solution to rapidly change from yellow to black in color. The solution was stirred and refluxed for 1.5 h. To the cooled reaction solution diethylene glycol (175 mL) was added and the solution was refrigerated overnight. The precipitate formed was isolated by vacuum filtration and washed with methanol. The crude product was loaded on a silica gel column and eluted with CH_2Cl_2 to remove any tetraphenylporphyrin in the mixture. A second silica gel column was loaded with the remaining compound and eluted with 1-5% methanol/CH_2Cl_2 mixture, slowly increasing the polarity of the eluent to obtain separation of the five pyridylporphyrins. The compounds eluted in the following order: 5,10,15,20-tetraphenylporphyrin, 5-(4'-pyridyl)-10,15,20-tri(phenyl)porphyrin, *cis*-5,10-bis(4'-pyridyl)-15,20-bis(phenyl)porphyrin, *trans*-5,15-bis(4'-pyridyl)-10,20 bis(phenyl) porphyrin, 5,10,15-tri(4'-pyridyl)-20-(phenyl)porphyrin and 5,10,15,20-tetra(4'-pyridyl) porphyrin. The *cis*-5,10-bis(4'-pyridyl)-15,20-bis(phenyl)porphyrin was obtained in 1 % yield (0.0620 g), and its spectroscopic characterization agreed with the reported values.[383-385]

5.2.3 Preparation of Substrates

Prior to sample deposition, pieces of HOPG were freshly cleaved with a piece of adhesive scotch tape to expose a clean surface. Silicon wafers were first immersed in solution of concentrated sulfuric acid and hydrogen peroxide (3:1) for 1 h, then copiously rinsed with deionized water, followed with ethanol and sonicated for 30 min in 99% ethanol. The acid cleaned silica pieces were then exposed to UV light (Spectroline, Westbury, NY), 254 nm for 15 min prior to use. Gold substrates were used without further treatment.

5.2.4 Preparation of Dried Samples

Stock solutions of porphyrins were prepared by dissolving 5,10-diphenyl-15,20-di-pyridin-4-yl-porphyrin (DPP) in dichloromethane(DCM). The solution was further diluted with absolute ethanol to the desired concentration (10^{-3} – 10^{-6} M). A single 10 µL drop of porphyrin solution was placed onto the substrates and dried at room temperature for at least 24 h.

5.2.5 In Situ Investigations of the Assembly of Porphyrin Films

The self-assembly of 5,10-diphenyl-15,20-di-pyridin-4-yl-porphyrin (DPP) in real time was investigated by first imaging Au(111) in ethanol using contact mode AFM to select a flat area with few defects. A solution of 0.01 mM DPP in ethanol/DCM was then injected into the AFM liquid cell. Surface morphology changes were monitored for three hours, with images taken at 5 min intervals. The surface layer of DPP that formed was then further characterized by nanoshaving and nanografting.

5.2.6 Preparation of *n*-Alkanethiol Self-Assembled Monolayers (SAMs)

Freshly prepared octadecanethiols (10^{-9} M) dissolved in absolute ethanol were used as nanografting solutions for *in situ* characterizations of the pyridyl porphyrin film. Matrix alkanethiols such as octadecanethiol, dodecanethiol and decanethiol for writing pyridyl porphyrins were prepared by immersing flame-annealed ultra flat films of Au(111) prepared on mica substrates in a (10^{-3}M) solution of chosen alkanethiol in ethanol for at least 12 h. The SAMs on Au(111) were then removed from the thiol solution, copiously rinsed with fresh ethanol and immediately placed into a liquid cell holder for AFM imaging and lithography to minimize surface oxidation.

5.2.7 Atomic Force Microscopy (AFM)

Samples prepared by the drying method were imaged using tapping mode in air with a model 5500 SPM (Agilent Technologies, Inc. Chandler, AZ). Probes with resonant frequencies ranging from 265-400 kHz were used for tapping-mode imaging (MikroMasch Wilsonville, OR).

Scan rates of 3.0 um/s and 256 line frame per second were used for acquiring images. For in situ investigations, AFM images were acquired in contact mode using a hybrid system, a PicoSPM scanner from Agilent (Chandler, AZ) was interfaced with electronic controllers and software (XPM Pro v.1.2.1.0) from RHK Technology (Troy, MI). Silicon nitride cantilevers with force constants ranging from 0.1 to 0.5 Nm^{-1} were used for imaging in liquids (Veeco Probes, Santa Barbara, CA). Digital images were processed with Gwyddion (version 2.5) open source software which is freely available on the Internet and supported by the Czech Metrology Institute.[387]

5.3 Results and Discussions

The DPP molecule chosen for these studies is a free-base porphyrin with two adjacent phenyl and two adjacent pyridine rings as peripheral groups (Figure 5A). Possible configurations of 5,10,15,20-di-pyridin-4-yl-porphyrin(DPP) on Au(111) are shown in Figures 5.1B-5.1C with energy minimized structural models. Different configurations of DPP are possible on Au(111), depending on whether there is one, two or four linkages to the surface. In these models, DPP will

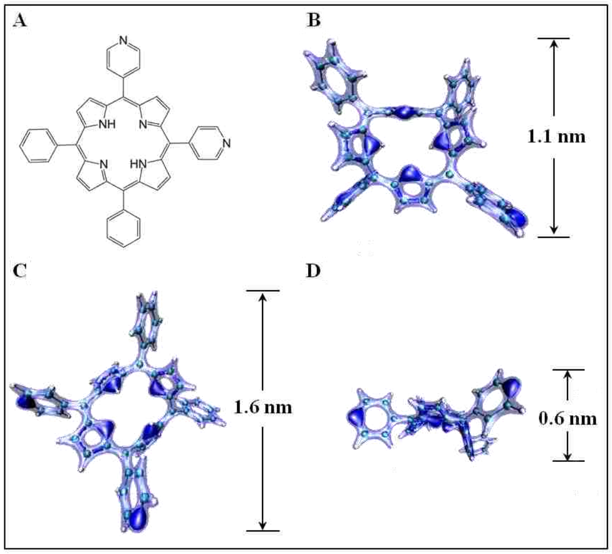

Figure 5.1. Structural formula and possible configurations of 5,10-diphenyl-15,20-di-pyridin-4-yl-porphyrin (DPP) with the corresponding heights on Au(111). [A] Molecular structure of DPP; [B]upright configuration of DPP with two pyridyl rings anchored to surface; [C]perpendicular orientation of DPP with one pyridyl anchoring group; [D] coplanar configuration of DPP on Au(111).

adapt an upright orientation if one (Figure 5.1B) or two (Figure 1C) pyridyl rings attach to the surface. For a coplanar orientation, the ring bends towards the surface with the macrocycle ring oriented as shown in Figure 5.1D.

5.3.1 Assembly of Pyridyl Porphyrins to Form “Stacks” on Surfaces

Surface assemblies of “stacks” of porphyrins often are formed that are oriented in a coplanar arrangement with respect to the surface plane when liquid samples of porphryins are dried on flat surfaces.[388] Depending on the drying conditions, the nature of the solvent and the concentration of the porphyrin in the parent solution, different heights and surface coverage of stacks are produced. Initial investigations of the assembly of 5,10-diphenyl-15,20-di-pyridin-4-yl-porphyrin (DPP) prepared either by methods of drying or immersion of various substrates in porphyrin solutions were found to spontaneously produce stacks when prepared in ambient environments, as shown in Figure 5.2. Dried samples of DPP that were prepared on surfaces of Au(111), HOPG and Si(111) were characterized using tapping mode AFM in air.

Representative AFM topographs of each surface (3×3 um^2 scan) are displayed, which reveal structures of small white islands or stacks distributed throughout the sample areas. (Figure 2). The stacks of DPP formed on Au(111) tend to be located at edges or corners of the irregularly shaped terraces(Figure 5.2A), and range in height from 1 to 10 nm. Analysis of the heights from several images ($n = 100$) show that 70% of the measurements range from 2 – 4 nm, corresponding to 4-8 porphyrin layers per stack, oriented in a planar configuration. The surface of HOPG shows preferential deposition at the step edges of graphite (Figure 5.2B). Size analysis reveals that stacks range in height from 0.3 - 5.0 nm, 52% of which measure ~1.0 nm, indicating two layers of DPP. On polished silicon wafers (Figure 5.2C), the distribution of porphyrin stacks throughout the surface areas was more random, with taller overall dimensions, compared to gold and graphite surfaces. Most of the stacks measured 4 – 8 nm in height, which corresponds to thicknesses of 7 to 13 layers of DPP.

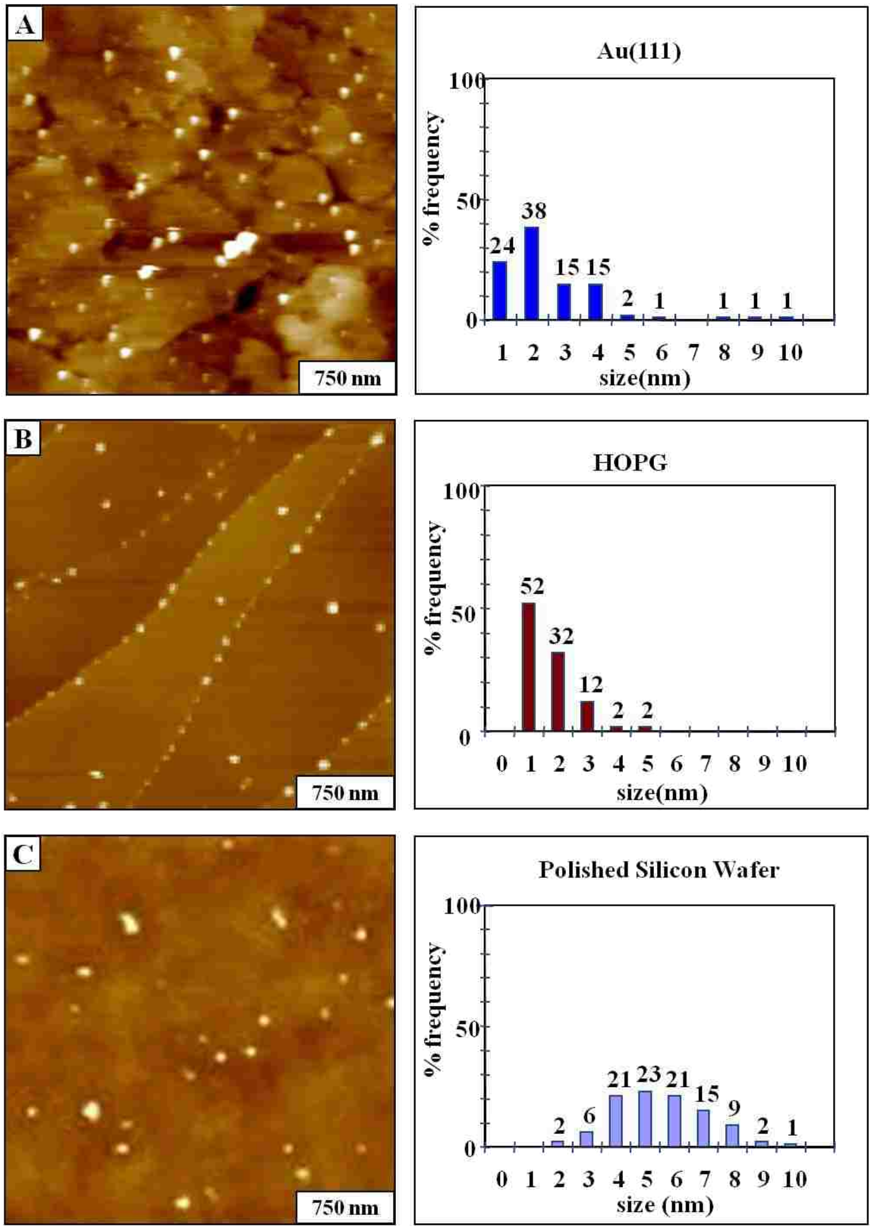

Figure 5.2. Stack strucutures of DPP formed on surfaces of [A] Au(111); [B] HOPG; [C] Si(111); with corresponding height distributions for stack sizes.

Droplet samples of porphyrins dried in ambient conditions produce stacks regardless of the surface, as viewed in Figure 5.2 for samples which were prepared side-by-side using similar conditions of concentration and solvent. The strong pi-pi interactions between the macrocycles predominate to form columnar discotic phases (stacks) when solutions of porphyrins are dried. As the solvent evaporates during the drying step, the capillary forces of the evaporating liquid pulls DPP molecules closer together. The heights of the stacks are influenced by the wettability and resulting surface energy of the substrates. The preferential formation of stacks on step boundaries of gold and HOPG can be attributed to the active sites in terrace edges, as previously reported.[389-391] Density functional theory (DFT) has shown that step edges of gold substrates have a greater concentration of electron density thereby allowing a maximum overlap between molecular orbitals.[389] The same conformational feature has been observed with 5-(4-methylthiophenyl)-10,15,20-tris(3,5-di-t-butylphenyl)porphyrin (MSTBPP) deposited on Au(111).[392] Aggregates of 1-10 nm were formed on polished silicon substrates indicating that the intermolecular attraction between porphyrin molecules was greater than the molecule-substrate interaction. After evaluating a range of different substrates, solvent media, immersion and drying conditions, the predominant outcome of surface morphologies observed for DPP were stack structures. Further experiments were designed for viewing surface assembly processes in situ, without a drying step, as described in the next sections.

5.3.2 Assembly of Pyridyl Porphyrins on Au(111) from Solutions of Mixed Solvents

A requirement for liquid AFM imaging is to use a solvent that does not evaporate rapidly in ambient conditions; common imaging solvents that are suitable for liquid cell imaging are 2-butanol, ethanol or water. However, DPP is nearly insoluble in these solvents so an approach with mixed media was developed, similar to experiments that were previously described for studies of *n*-alkanethiols in water-based media.[393] The media used for studies with DPP was a mixture of ethanol and dichloromethane (DCM). The porphyrin was first dissolved in DCM to prepare a parent solution, and this solution was further diluted in ethanol to approximately 1 vol% DCM.

After imaging a clean surface of Au(111) in ethanol, a solution of 0.01 mM DPP was injected into the AFM liquid cell and the surface morphology was monitored for several hours. Molecular views of the spontaneous self-assembly of pyridyl-porphyrins from mixed solvent solutions were captured *in situ* using contact mode AFM as shown in Figure 5.3. A few minutes after injection of DPP, small islands of porphyrins of various heights begin to appear. The initial changes of the surface morphology are shown in Figure 5.3A after 3 h of immersion, with the appearance of adsorbates, covering 15% of the surface area and a few bright island features. The bright white globular structures observed were about 80 spots/μm^2 area. The simultaneously acquired lateral force image (Figure 5.3B) shows no distinct features.

In the next step of the liquid AFM experiment, a rectangular area (200×300 nm^2) was shaved as shown in the topography and lateral force frames of Figure 5.3D and 5.3E. Nanoshaving is an SPL method in which local areas of a surface are scraped or shaved away by the action of a sweeping AFM tip to remove adsorbates.[34] The uncovered substrate provides a baseline for measuring the thickness of the film. The outline of the edges of the nanoshaved area is distinct both in topography and lateral force image frames. The angular boundaries of step edges of the underlying gold substrate are resolved in the lower corners of the topography image (Figure 5.3D). The clean removal of DPP is also apparent in the lateral force image (Figure 5.3E), showing a uniformly dark contrast for the nanoshaved hole. A cursor line profile was chosen across a central area of the hole without step features, as shown in Figure 5.3F. The height of the DPP film measured ~ 0.6 nm, which matches the expected thickness for a coplanar orientation. The assembly process was continued for 48 h, and then the sample was removed from the DPP solution, rinsed with ethanol and immediately imaged in ethanol. Further changes in surface morphology for the self-assembly process were captured by imaging in ethanol using very low forces to prevent damage to the sample, as shown in Figure 5.4.

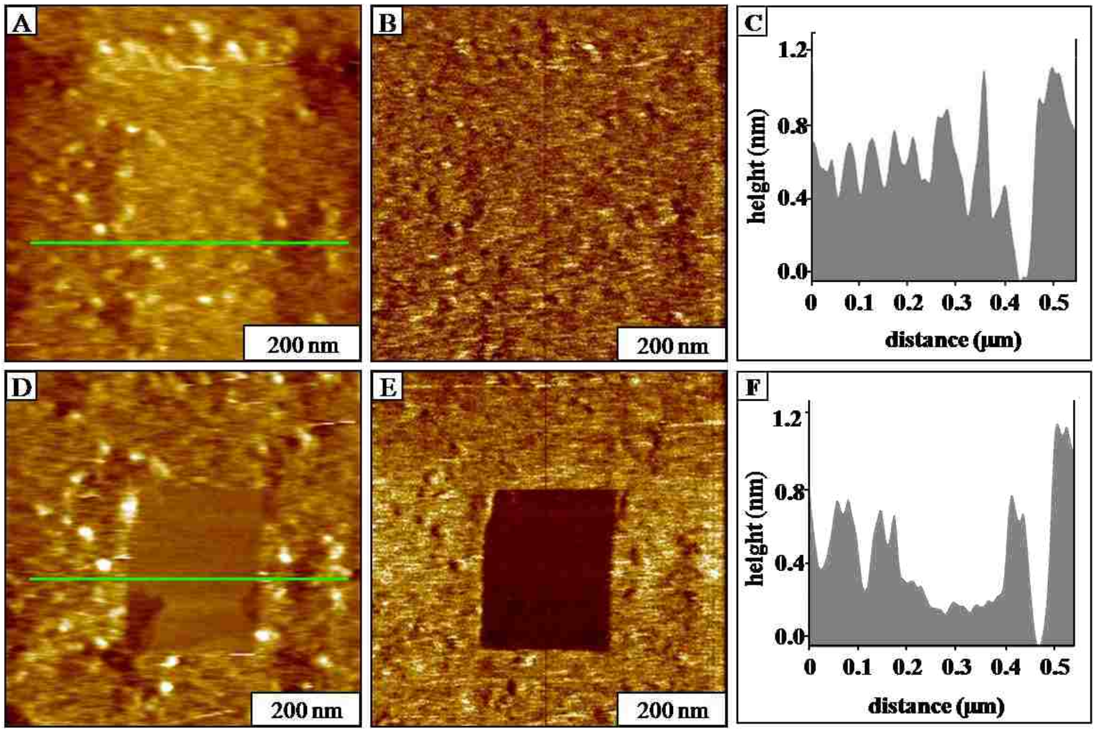

Figure 5.3. Films of DPP on Au(111) after 3 h immersion in mixed solvent media. [A] Topograph of DPP film before nanoshaving; [B] lateral force image of **A**; [C] corresponding cursor profile for the line in **A.** [D] topograph showing the nanoshaved pattern of the DPP film; [E] lateral force image of **D**; [F] corresponding cursor profile for the line in **D.**

Segregated domains of different thicknesses of DPP were observed to form on Au(111) after longer immersion. Distinct areas of brighter islands surrounded by a film with shorter heights are evident in Figure 5.4A. The left side of the image shows a predominance of taller islands of DPP, whereas the left area exhibits very few bright islands, with saturation coverage of the shorter phase. Approximately 65 % of the surface for the area framed has shorter heights, corresponding to the coplanar arrangement. The irregular fractal shapes of the bright islands of DPP in Figure 5.4B cover approximately 53% of surface in Figure 5.4A. A magnified view in Figure 5.4C reveals the detailed domain structures of the mixed phases of coplanar and upright DPP, exhibiting 69% surface coverage for the taller structures. The width between upright domains measures 5-15 nm. The height difference between the taller and shorter phases of Figure 5.4D measures between 0.2 nm-0.4 nm.

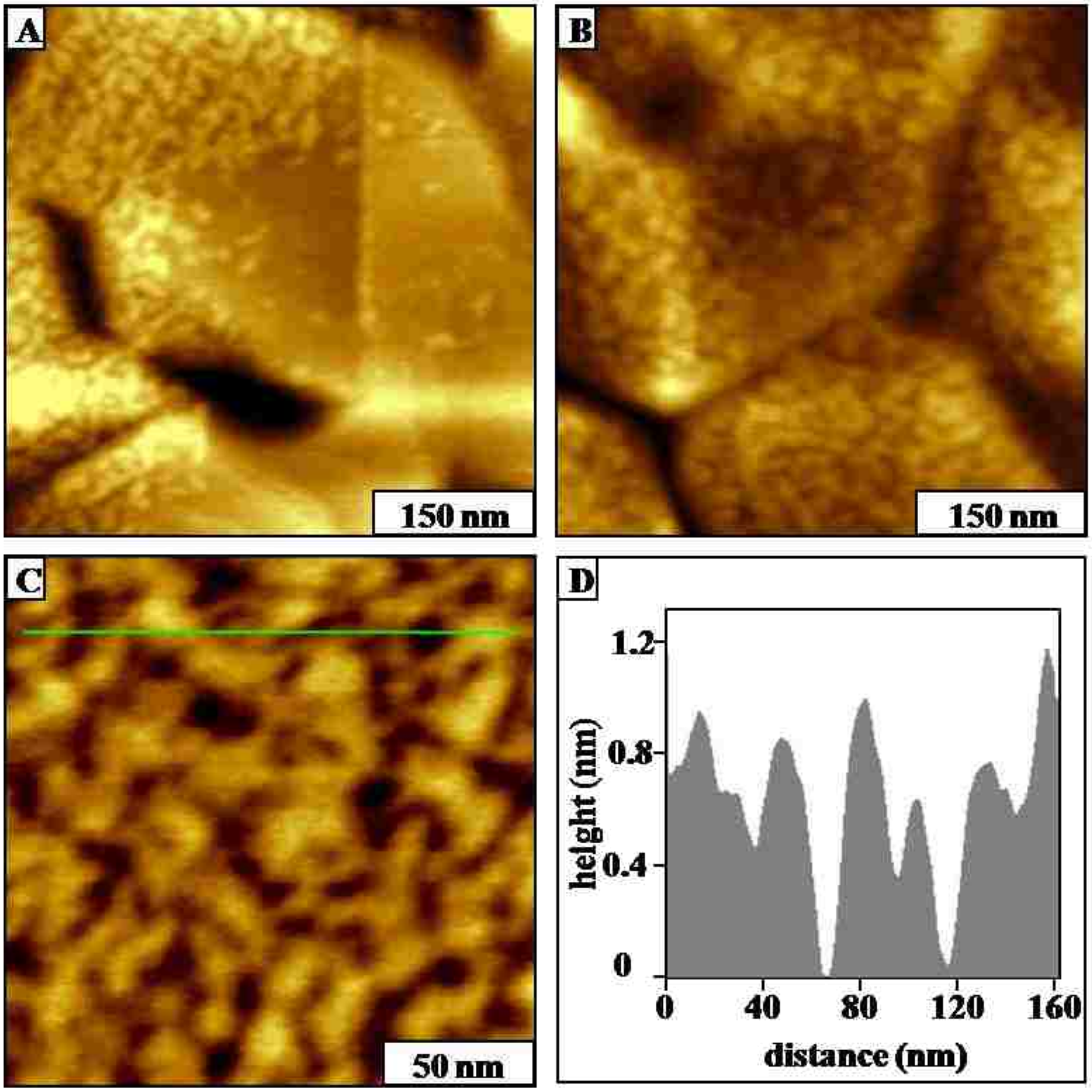

Figure 5.4. Domains of mixed heights of DPP on Au(111) observed under conditions of natural self-assembly. [A] Contact-mode topograph showing taller and shorter DPP molecules on the surface; [B] topograph image of an area with greater coverage of the taller phase of DPP [C] zoom in topographic view of the mixed phases of DPP; [D] cursor profile for the line in C.

The thickness of the DPP film of Figure 5.4 was measured by nanoshaving (Figure 5.5) in ethanol. A 100 × 100 nm^2 hole was neatly shaved within the DPP film, as shown in Figure 5.5A. The thickness of the layer measured 1.1 ± 0.3 nm corresponding to an upright orientation of DPP with two pyridyl groups attached to gold. Nitrogen-gold chemisorption has been previously reported for SAMs terminated with cyano and nitrile end groups.[394] Thus, for the natural self-assembly process of dipyridyl diphenyl porphyrins, mixed domains of both co-planar (lying-down) and upright orientations are observed, with a predominance of the brighter domains of upright DPP increasing as time progressed. Height measurements from Figure 5.4B indicate that coplanar domains of DPP persist in the boundary areas between the bright islands.

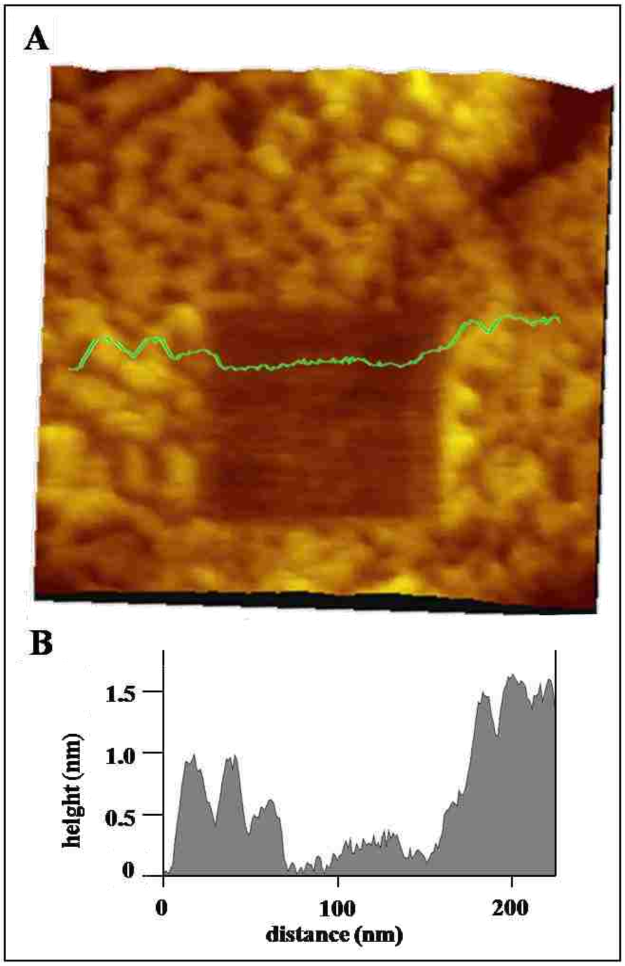

Figure 5.5. Nanoshaved hole within a DPP film formed after 48 hours of immersion. [A] Contact mode AFM topograph of a 100 x 100 nm^2 shaved area within the film; [B] cursor profile for the line in **A**. Scan size is 260 nm.

From liquid AFM experiments captured at 3 h and 48 h time points, the surface assembly of DPP begins with a coplanar orientation on Au(111) and transitions over time to produce an upright configuration as the surface coverage increases. For studies of the assembly of porphyrins in liquid media without a drying step, round domains of stack structuress were not observed. Instead, liquid cell experiments reveal that a continuous monolayer is formed throughout the surface (Figures 5.3 and 5.4). Further studies were conducted with nanografted structures of *n*-alkanethiols/Au as a molecular ruler, to verify the thicknesses obtained with nanoshaving experiments, as described in the next section.

5.3.3 Molecular Rulers: Nanografting of *n*-Octadecanethiol Within a Porphyrin Film

Films of DPP porphyrins formed on Au(111) are sufficiently densely packed that patterns of *n*-alkanethiols can be inscribed within porphyrin films via nanografting. Nanografting can be described as mechanical removal of SAMs under a high force followed with *in situ* replacement of another molecule following the scanning track of the tip.[34,80] A cross-shaped pattern of 0.001 mM octadecanethiol (ODT), was written into the porphyrin film as evidenced by the topograph and lateral force images (Figure 5.6). A cross pattern of taller molecules of ODT surrounded by DPP film are clearly visible in the topograph (Figure 5.6A). The lateral force image in Figure 5.6B shows darker contrast for the methyl-terminated areas of the nanografted pattern of ODT, which is further evidence that a new molecule was successfully inscribed within the monolayer. The thickness of the porphyrin film on Au(111) was evaluated by comparison with the well-known height of ODT. Since the height of ODT is known to be 2.1 nm, ODT serve as a molecular ruler to determine the exact thickness of the porphyrin monolayer with angstrom precision. Both nanografting as well as nanoshaving results reveal that the thickness of the shorter phase of DPP porphyrin films formed *in situ* on Au(111) measures ~0.6 nm, in agreement with a co-planar orientation of a single layer, whereas the taller domains correspond to an upright orientation that is nearly perpendicular to the surface, measuring ~1.2 nm in thickness.

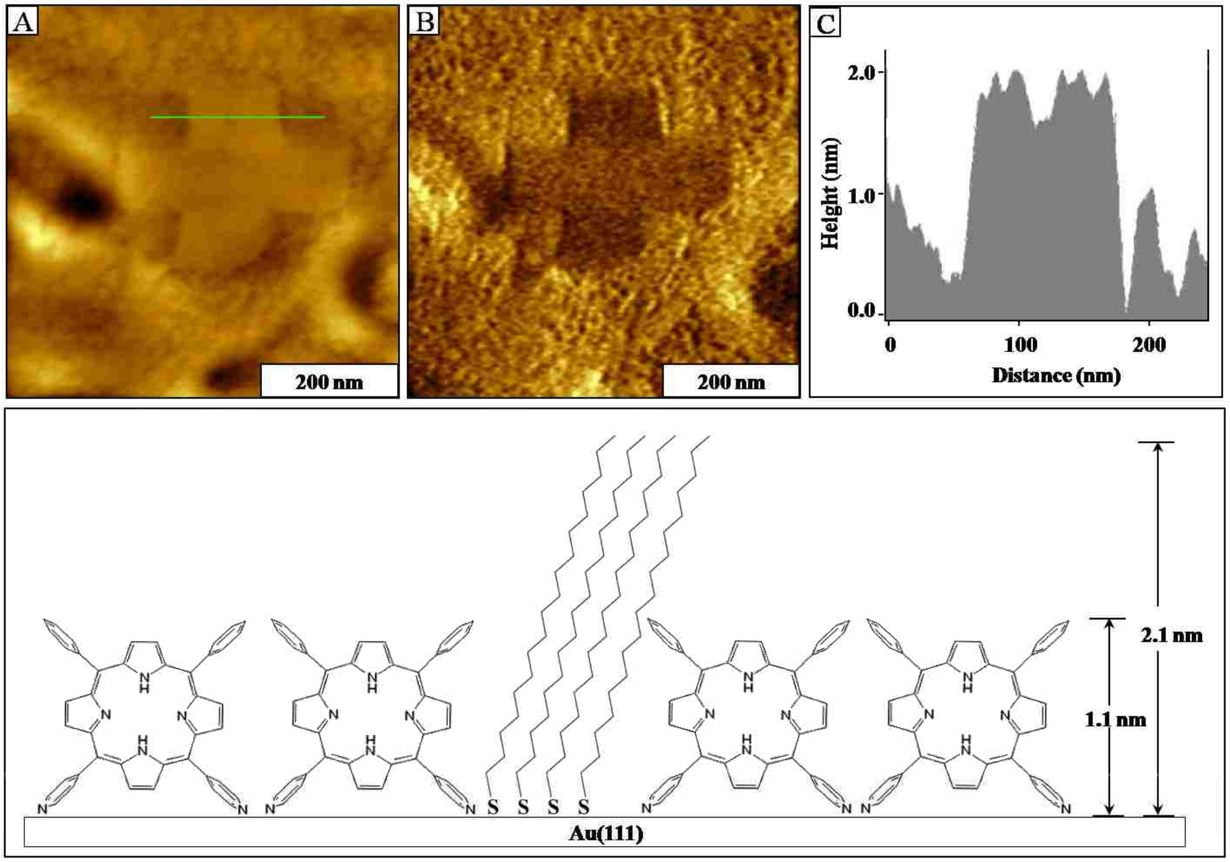

Figure 5.6. Nanografted cross pattern of octadecanethiol placed within a matrix of DPP. [A]Contact mode AFM topograph; [B] corresponding lateral force image; [C]cursor profile for the line in **A**; [D] molecular model showing heights of DPP and octadecanethiol.

The thickness of the upright phase also corresponds to the dimensions a multilayer structure of two macrocycles in a coplanar arrangement; however we would expect to observe a distribution of multiple heights for the nanostructures if stacking assembly takes place rather than a consistent bilayer dimension. It is unlikely that only bilayer structures would form if a coplanar assembly mechanism were followed. Also, the strong interaction between nitrogen and gold chemisorption is more favorable and would tend to produce a rearrangement into an upright orientation.

5.3.4 Nanografted Structures of DPP Formed Under Conditions of Spatial Confinement

During nanografting, assembly of pyridyl porphyrins follows a different reaction pathway due to a spatial confinement, which has been reported previously for *n*-alkanethiol SAMs.[395-396]

Under conditions of local confinement produced during nanografting, the transient reaction environment is sufficiently small to prevent the molecules from assembling in a lying-down position. When nanografting, very small areas of freshly exposed gold are produced by scanning with a high force applied to the AFM tip. The bare area on the surface is confined between the AFM probe and thiol matrix molecules. The confined area uncovered by the AFM tip has dimensions less than the molecular length of the molecules, therefore *n*-alkanethiol molecules from solution do not have sufficient room on the surface to assemble in a lying-down configuration. Thus, the initial physisorbed phase is bypassed and molecules assemble directly onto gold with the favored standing-up configuration.

Nanopatterns of pyridyl porphyrins were successfully prepared by nanografting in mixed solvent media, using different *n*-alkanethiol matrices. Example arrays of nanopatterns of pyridyl porphyrins produced by nanografting while scanning in a solution containing a mixture of solvents (1% dichloromethane in ethanol) and pyridyl porphyrins are presented in Figure 5.7. Automated nanografting enables direct control of parameters such as the size, arrangement, geometry and spacing of pyridyl porphyrins at the nanoscale. The heights of the DPP nanopatterns shown in first column of Figure 5.7 are shorter than the selected alkanethiol SAMs as evidenced by the darker contrast for the patterns in the topography images. The lateral force images shown on the second column of Figure 5.7 exhibit contrast differences with chemistry present on the surface. Since the thickness of *n*-alkanethiol SAMs has been well-established, the matrix SAMs can be used as a molecular ruler to evaluate the orientation of new molecules. Side-by-side comparisons of the dimensions of nanostructures formed on gold surfaces enable precise measurements of the thickness of pyridyl porphyrin patterns.

Rings patterns of pyridyl porphyrins with decreasing diameter ranging from 20-60 nm were nanografted within decanethiol matrix (Figure 5.7A). The theoretical height of the matrix decanethiol is 1.4 nm. The cursor indicates a height difference of 0.3 ± 0.2 nm, which likely corresponds to an upright conformation (1.1 nm) in which both of the pyridyl groups are attached to the surface. To test the reproducibility of nanografting pyridyl porphyrins, ring patterns of the same size (75 nm diameter) were fabricated within dodecanethiol (DDT) matrix as shown in Figure 5.7B. High resolution topograph was captured after nanografting as evidenced by the etch pits and the lacey contours of the step edges on areas covered with dodecanethiol SAMs. The height difference between the DDT and pyridyl porphyrins as indicated in the cursor profile is 0.5 nm ± 0.2 corresponding to the expected thickness between DDT and pyridyl porphyrins if pyridyl porphyrins have an upright orientation on Au(111).

An array of nine filled circles of pyridyl porphyrins (Figure 5.7C) inscribed within the octadecanethiol matrix displayed differences in height and surface chemistry of the pyridyl porphyrin patterns positioned on gold terraces. The diameter of the circular pattern is about 200 nm. The height difference between the matrix ODT and porphyrin patterns measures 1.0 ± 0.3 nm as indicated in the representative line profile in Figure 5.7C corresponding to the expected difference of 1.1 nm. The sizes of the desired patterns can be produced depending on number of line sweeps executed by the AFM probe. With nanografting, the width of the pattern is limited by the size of the AFM probe and the density of the pattern.

5.3.5 Computer Simulation of DPP Structure on Au(111)

The configurations and electronic structures of DPP on Au(111) were tested using Car-Parrinello molecular dynamics ver. 3.11.[397] First, DPP was optimized in the gas phase to remove any potential bad contacts and to create a good starting configuration for the surface studies. Vanderbilt Ultra-Soft pseudopotentials[398] were employed with a kinetic energy cutoff of 35 Ry with a electron density cutoff threshold of 10^{-6}. The gold slab had three layers, containing 150

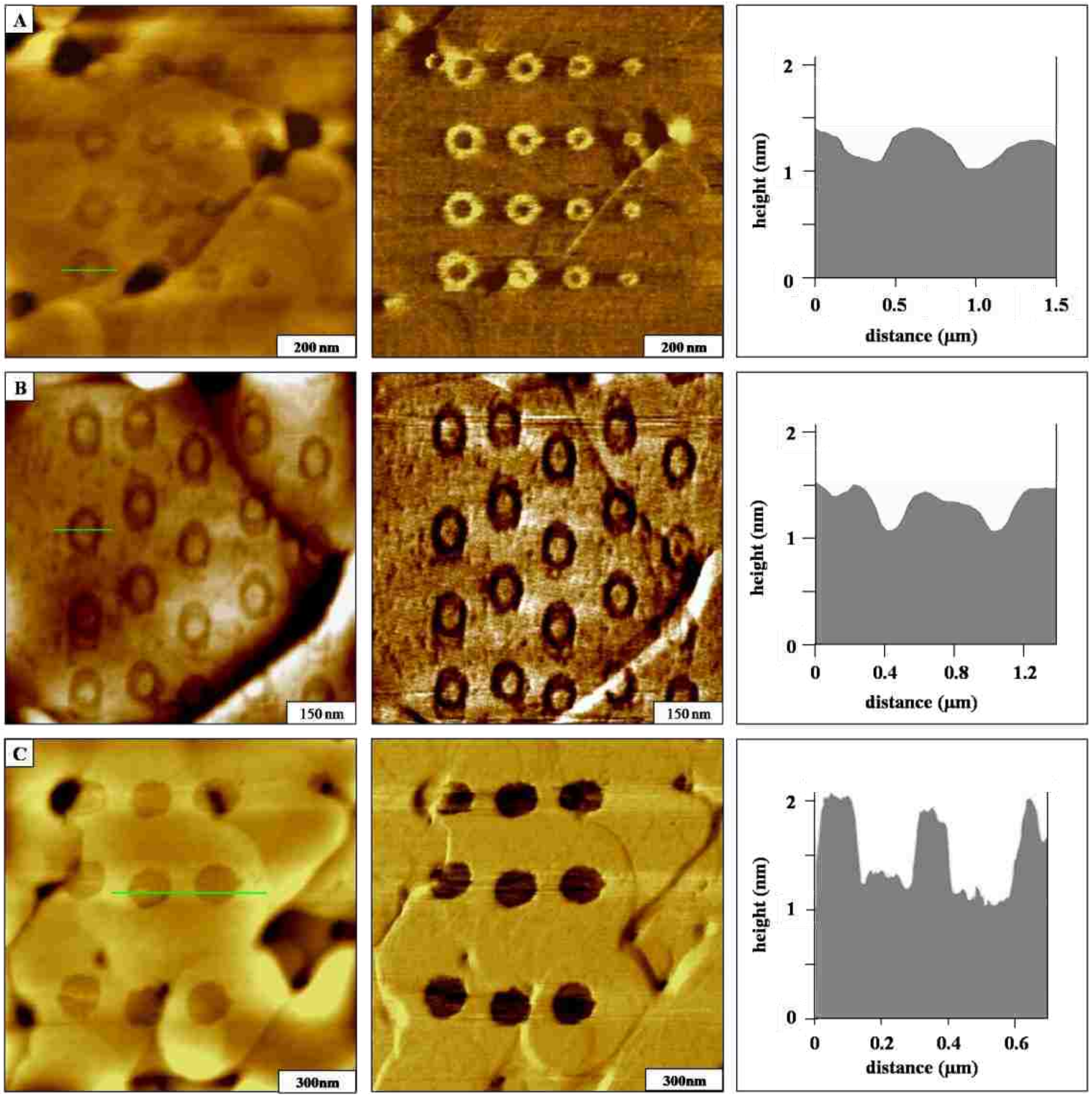

Figure 5.7. Nanopatterns of DPP nanografted within various SAM matrices. AFM topograph; corresponding lateral force image and line profile (from left-to-right) of DPP patterns written within [A] decanethiol; [B] dodecanethiol; [C] octadecanethiol matrices.

atoms fixed to their crystal lattice position to save computational expense. Periodic boundary conditions in the x and y directions were used. The starting configurations of the porphyrin was placed 3.5 angstroms away from the gold surface. A combined geometry and electronic structure optimization was used to initially relax this new configuration. Then a short 200 step CPMD simulation was conducted to refine the structure. The time step used here was 0.14 fs. The co-planar orientation of DPP has two possible flat orientations on Au(111). Both configurations had a slight twist in the porphyrin.

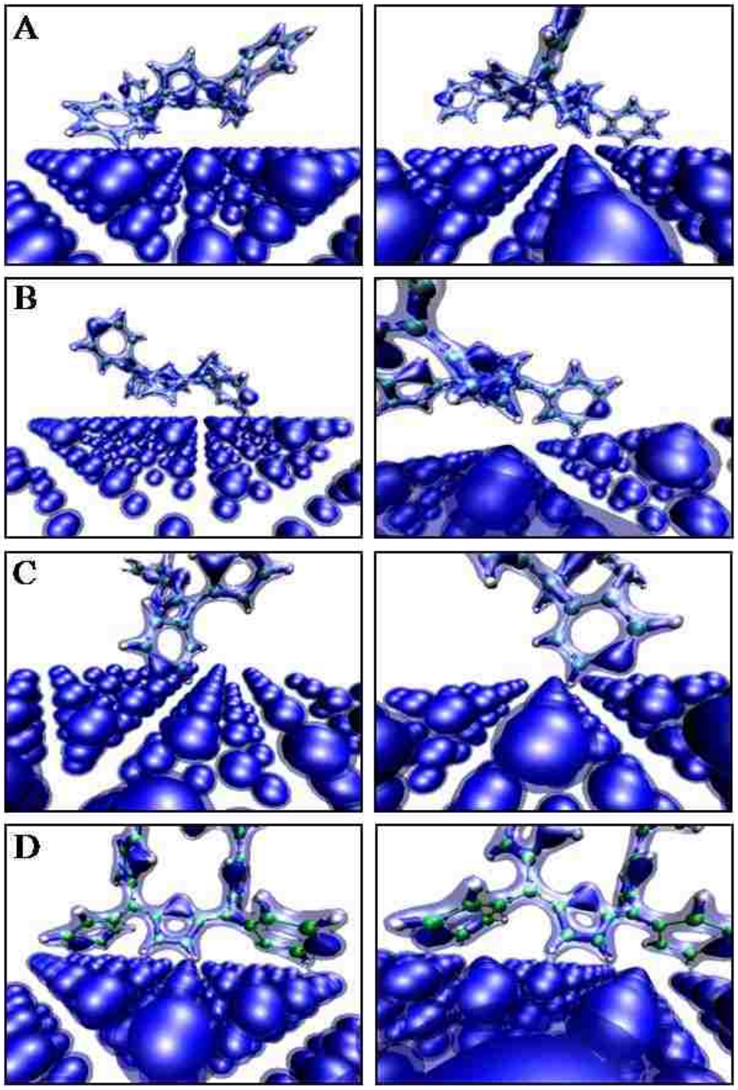

Figure 5.8. Different configurations and electronic structures of DPP on Au(111). [A] Flat-Carbon ring; [B] Flat N- ring; [C] 1-Nitrogen; [D] 2-Nitrogen

The outer 6-membered was brought closer to the surface with and without the nitrogen. For flat C-ring (Figure 5.8A), the ring bends towards the surface with the macrocycle five membered ring. The hydrogen atom provides a density overlap bridge to the gold surface. The flat N-ring conformation exhibited similar overall configuration to Flat-C (Figure 5.8B) as the macrocycle 5-membered ring is also drawn towards the surface. The nitrogen's density is more localized and competes with the pi bonds in the ring which brings a hydrogen closer to the surface ~2.4Å. For porphyrin anchored on the surface with one pyridyl ring as a leg (Figure

5.8C), the 6-membered ring was adjusted by various angles with respect to the surface to find the lowest energy structure. Results show that the nitrogen density is drawn towards the surface. Interestingly, the hydrogen orientates towards an interstitial site on the surface. The overall density of DPP has increased when 2 pyridine rings are anchored to the surface (Figure 5.8D). Both pyridine rings twist so that the pi system and nitrogens can both become closer to the surface. The 5-membered macrocycle is forced to the surface and the electron density overlaps with the hydrogens.

5.4 Conclusions

Scanning probe-based fabrication of nanostructures of porphyrins has been problematic, due to the insolubility of porphyrins in solvents that are typically used as liquid imaging media. In this report, studies of the surface self-assembly of pyridyl-functionalized porphyrins was accomplished using a mixture of solvents. Unconstrained assembly of pyridyl-functionalized porphyrins from solution produced compact monolayers with two distinct configurations on the surface, exhibited by a mixture of upright and co-planar islands. Nanografted patterns of n-alkanethiols were used as a molecular ruler to evaluate the orientations of the porphyrins on Au(111) through side-by-side comparisons of the dimensions of the molecules. Computer simulation correlates with AFM results disclosing that solution phase assembly of pyridyl-functionalized porphyrins adapts different configurations on the surface. However with nanografting, DPP molecules assemble directly onto gold with a standing-up configuration due to a mechanism of spatially constrained self-assembly. Nanografting results demonstrated for the first time that pyridyl porphyrins in a dilute mixed solvent solution can assemble directly on Au(111) in an upright orientation. Understanding the self-organization and assembly of designed porphyrins will contribute to rational designs for applications in electronic and photonic devices.

CHAPTER 6. POLYTHIOPHENES CONTAINING IN-CHAIN COBALTABISDICARBOLLIDE CENTER*

6.1 Introduction

Carboranes, in both neutral and anionic forms, are boron clusters with delocalized electrons and unique properties, including high hydrophobic character, low nucleophilicity, electron-withdrawing nature, and exceptional chemical, thermal, and optical stabilities as a result of their three-dimensional aromatic character. [399-400]Furthermore, complexation of the anionic open cage carborane derivatives with a variety of metal ions (e.g., Fe, Ni, and Co) leads to highly stable sandwich-type metalla-bis(dicarbollide) compounds. [401-402]Depending upon the valence of the metal these compounds can be neutral or charged, usually with one or two negative charges. These metal complexes have received much interest because of their prominent role in the extraction of radionuclides from nuclear wastes,[403] in molecular recognition,[404-405] in biomedicine, [406-407]and in the construction of redox-switched molecular rotors. [408-409]For example, Hawthorne and co-workers have reported that nickel bisdicarbollide has a rotation barrier of 6 kcal/mol and that it rotates depending on the valence of the metal, when actuated by electrical or light energy.[409] Several carborane-containing organic molecules have been synthesized in the last decades and some of these are currently finding applications in medicine [410-412] and in materials science.[413-414] Furthermore, their incorporation within organic materials has been demonstrated to be valuable to confer novel properties upon the host matrix, such as high thermal and chemical stability, unique optoelectronic characteristics and an ordered structure. Several polymers containing carborane groups, usually linked to the host molecule by aromatic spacers, have been synthesized and characterized. [415-420] These macromolecular systems showed extreme resistance to combustion and a two-dimensional grid-shaped structure using the

---

*Reproduced with permission from the American Chemical Society.

boron cage as a molecular connector. However, such materials were usually synthesized in several steps and did not show peculiar electronic conducting properties, which preclude them from certain applications, such as electrochromic and charge storage devices, and electroresponsive sensors. Some years ago, Teixidor's group [421-424] and ourselves [425-429] prepared novel electroconducting polypyrroles and polythiophenes functionalized with various neutral and anionic carboranes, either via side-chain modification or direct incorporation into the polymer backbone. These materials, which were electrochemically generated in one step, exhibited a strong enhancement of their electrochemical stability and overoxidation resistance compared with unsubstituted parent conducting polymers. Recently, carborane-substituted polyfluorenes were prepared which showed advantageous luminescent properties for light-emitting diodes.[430-431]

Within the attractive class of boron clusters, the metalla-bisdicarbollide complexes offer novel opportunities to prepare unprecedented conducting metallopolymers. Toward this goal, we report herein the synthesis and characterization of cobalt(III) bisdicarbollide derivatives covalently linked to electropolymerizable 2-oligothienyl units (Scheme 6.1). It was expected that oxidative coupling of the aromatic rings would lead to polythiophene films with the metal complexes incorporated in the main polymer chain. Metal-containing polymers have been the focus of intense investigations because of their potential applications in catalyses and in ion or small molecule binding. [432]A central issue in the development of conducting metallopolymers is the control of the interactions between metal centers and the conducting organic polymer backbone. Compared with other conducting polymers bearing a metal center, either through a spacer arm or by electrostatic entrapment, the presence of the metal center in the conjugated chain of the polymer is expected to significantly impact on the electronic conductivity and the magnetic and optical properties of such materials. Moreover, in addition to these interesting effects, the presence of in-chain metalla-bisdicarbollide complex may also confer improved thermal and electrochemical stabilities to the host conducting material, as previously demonstrated for other carborane-functionalized polypyrroles [421,423,425,427,429]and polythiophenes.[428-429]The new conducting polymers resulting from electropolymerization of the substituted cobaltabisdicarbollides have been characterized by electrochemistry, UV−vis spectroscopy and conducting probe atomic force microscopy in order to provide significant insights on the effects of the bound cobaltabisdicarbollide moiety on the electronic properties of the resulting conducting materials. Such metallopolymers were used for the electrocatalytic reduction of H^+ and the efficiency of the electrocatalytic process was found to be highly dependent on the thickness of the metallopolymer film.

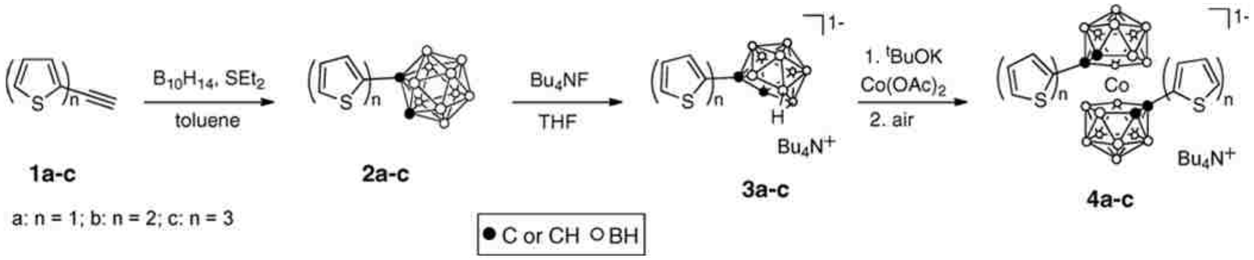

Scheme 6.1 Synthesis of Oligothiophene-Disubstituted Cobaltabisdicarbollide Compounds

6.2 Experimental Section

Synthesis of Oligothiophene-Disubstituted Cobaltabisdi-carbollide Compounds. General All reactions were monitored by thin layer chromatography (TLC) using 0.25 mm silica gel plates with or without UV indicator (60F-254). The carborane clusters were detected by emerging into a solution of $PdCl_2$ in aqueous HCl (1 g $PdCl_2$ in 80 mL water and 20 mL concentrated HCl) and heated until black spot(s) was/were seen on TLC. Silica gel from Sorbent Technologies 32−63 μm was used for flash column chromatography. ^1H and ^{13}C NMR were obtained on either a DPX-250 or a ARX-300 Bruker spectrometer. Chemical shifts (δ) are given in ppm relative to $CDCl_3$ (7.26 ppm, ^1H; 77.2 ppm, ^{13}C), CD_2Cl_2 (5.32 ppm,^1H; 77.2 ppm, ^{13}C) or acetone-d_6 (2.05 ppm,^1H; 54.0 ppm, ^{13}C). MALDI-TOF mass spectra were obtained on a

Bruker ProFLEX III MALDI-TOF mass spectrometer using positive mode and dithranol as the matrix. High-resolution mass spectra were obtained by using ESI-TOF with the negative mode on an Applied Biosystems QSTAR XL quadrupole time-of-flight mass spectrometer. The isotope peaks were matched with the calculated patterns; only the most abundant peaks for each compound are listed. All solvents were obtained from Fisher Scientific (HPLC grade) and used without further purification. Toluene was dried over sodium metal and distilled. Decaborane was obtained from Katchem, Inc. (Czech Republic) and all other reagents were obtained from Sigma-Aldrich and used without further purification.

Compound 2a, Thiophene-2-*o*-carborane. Diethylsulfide (4 g, 44 mmol) was added under N_2 to decaborane (2.44 g, 20 mmol) in 30 mL of dry toluene. The mixture was stirred at 40 °C for 3 h and then at 60 °C for another 2 h. A solution of commercially available 2-ethynylthiophene **1a** (2.16 g, 20 mmol) in 30 mL of dry toluene was added and the final reaction mixture was refluxed for 2 days. The reaction was cooled to room temperature and the solvent was evaporated. Methanol (50 mL) was added and the reaction mixture was stirred for 30 min. After evaporation under reduced pressure, the resulting residue was purified by silica gel chromatography, using 20% dichloromethane in hexane as the eluent. The first major fraction was collected and dried under a vacuum, giving white crystals of **2a** (2.31 g) in 53 % yield. ^{1}H NMR ($CDCl_3$, 250 MHz) δ 7.25−7.27 (1H, m, ArH), 7.20−7.21 (1H, m, ArH), 6.90−6.92 (1H, m, ArH), 3.86 (1H, s, CH), 1.50−3.50 (br, 10H, BH). ^{13}C NMR ($CDCl_3$, 63 MHz) 137.2, 130.4, 128.3, 127.7, 72.4, 63.7. ^{11}B NMR ($CDCl_3$, 128 MHz, $BF_3.OEt_2$)δ −3.3 (d, ^1J(B,H) = 146 Hz, 1B) −6.6 (d, ^1J(B,H) = 147 Hz, 1B), −10.0 to −16.0 (br m, 8B). MALDI-TOF $[M + H]^+$ 226.3. HRMS(ESI) *m/z* calcd for $C_6H_{13}B_{10}S$, 225.1739; found, 225.1746.

Compound 2b, 2,2′-Bithiophene-5-*o*-carborane. To a 100 mL reaction flask was added decaborane (0.61 g, 5 mmol), 2-ethynyldithiophene **1b** (0.57 g, 3 mmol), dry CH_3CN (4 mL), and dry toluene (16 mL). The reaction mixture was stirred under N_2 at 80 °C for 24 h. After it was cooled to room temperature, methanol (10 mL) was added to the reaction mixture and stirred for 30 min. After removal of the solvents under vacuum, the residue was purified by silica gel chromatography, using 10% dichloromethane in hexane as the eluent. The first major fraction was collected and dried under vacuum, giving a light brown solid (0.70 g) in 76 % yield. ^{1}H NMR ($CDCl_3$, 250 MHz) δ 7.27 (1H, d, J = 5.10 Hz, ArH), 7.18 (1H, d, J = 3.00 Hz, ArH), 7.09 (1H, d, J = 3.73 Hz, ArH), 7.03 (1H, t, J = 4.48 Hz, ArH), 6.94 (1H, d, J = 3.71 Hz, ArH), 3.86 (1H, s, CH), 1.50−3.50 (br, 10H, BH).^{13}C NMR ($CDCl_3$, 63 MHz) 140.4, 136.0, 135.2, 131.1, 128.5, 126.2, 125.3, 123.8, 72.4, 63.8. ^{11}B NMR ($CDCl_3$, 128 MHz, $BF_3.OEt_2$)δ −3.4 (d, ^1J(B,H) = 145 Hz, 1B), −6.5 (d, ^1J(B,H) = 141 Hz, 1B), −10.0 to −16.0 (br m, 8B). MALDI-TOF [M + H]$^+$ 309.5. HRMS (ESI) *m/z* calcd for $C_{10}H_{15}B_{10}S_2$, 307.1630; found, 307.1623.

Compound 2c, 2,2′,5′,2″-Terthiophene-5-*o*-carborane. This compound was prepared and isolated as described above for the synthesis of **2b**, starting from **1c** (0.25 g, 0.92 mmol) and decaborane (0.20 g, 1.62 mmol). The result was a light yellow solid (0.19 g) in 53% yield. ^{1}H NMR (CD_2Cl_2, 300 MHz) δ 7.28 (1H, br s, ArH), 7.20 (1H, br s, ArH), 7.05−7.10 (4H, m, ArH), 6.95 (1H, br s, ArH), 3.88 (1H, s, CH), 1.50−3.50 (br, 10H, BH).^{13}C NMR (CD_2Cl_2, 63 MHz) 139.9, 138.0, 136.9, 134.9, 134.5, 131.2, 128.4, 125.9, 125.5, 124.8, 124.6, 123.6, 72.5, 64.0. ^{11}B NMR ($CDCl_3$, 128 MHz, $BF_3.OEt_2$) δ −3.2 (d, ^1J(B,H) = 143 Hz, 1B), −6.4 (d, ^1J(B,H) = 148 Hz, 1B), −10.0 to −16.0 (br m, 8B). MALDI-TOF [M + H]$^+$ 391.3. HRMS(ESI) *m/z* calcd for $C_{14}H_{17}B_{10}S_3$, 390.1468; found, 390.1475.

Compound 3a, tetrabutylammonium Thiophene-2-*o*-nido-carborane. To a solution of compound **2a** (1.13 g, 5.0 mmol) in 50 mL THF was added 10 mL of *n*-Bu_4NF solution (1.0 M in THF). The reaction mixture was stirred at 60 °C for 2 h, until no starting material was visible by TLC, and then poured into 50 mL of water and extracted with ethylacetate (3 × 50 mL). The organic layers were dried over anhydrous Na_2SO_4 and concentrated under vacuum. The resulting residue was purified by passing through a pad of silica gel, using ethylacetate for elution. The title compound was obtained as a white power (2.14 g) in 94% yield. ^{1}H NMR (acetone-d_6, 250 MHz) δ 6.95−6.96 (1H, m, ArH), 6.74−6.76 (1H, m, ArH), 6.65−6.67 (1H, m, ArH), 3.37−3.39 (8H, m, CH_2), 3.35 (1H, br, CH), 1.75−1.77 (8H, m, CH_2), 1.50−3.50 (br, 9H, BH), 1.37−1.45 (8H, m, CH_2), 0.91−1.01 (12H, m, CH_3), −2.03−2.50 (1H, br, BH). ^{13}C NMR ($CDCl_3$, 100 MHz) 150.9, 126.3, 121.9, 121.5, 60.3, 59.0, 24.0, 21.0, 19.7, 13.6. ^{11}B NMR ($CDCl_3$, 128 MHz, BF_3.OEt_2) δ −10.0 to −16.0 (br m, 3B), −18.0 to −20.0 (br m, 3B), −24.6 (d, ^1J (B,H) = 149 Hz, 1B), −34.7(dd, ^1J (B,H) = 43.8 Hz, ^1J (B,H) = 43.7 Hz, 1B), −37.6 (d, ^1J(B,H) = 138 Hz, 1B). HRMS (ESI) $[M\text{-}NBu_4]^-$ *m/z* calcd for $C_6H_{14}B_9S$, 214.1657; found, 214.1664.

Compound 3b, Tetrabutylammonium 2,2′-Bithiophene-5-*o*-nido-carborane. This compound was prepared as described above for the preparation of **3a**, from **2b** (0.62 g, 2.0 mmol) and 4.0 mL of *n*Bu_4NF 1.0 M solution in 20 mL of THF, in 95% yield (1.02 g). ^{1}H NMR (acetone-d_6, 250 MHz) δ 7.27 (1H, dd, *J* = 1.11 Hz, *J* = 4.02 Hz, ArH), 7.08 (1H, dd, *J* = 1.07 Hz, *J* = 2.50 Hz, ArH), 6.98 (1H, dd, *J* =5.04 Hz, *J* =1.43 Hz, ArH), 6.88 (1H, d, *J* = 3.69 Hz, ArH), 6.58 (1H, d, *J* = 3.73 Hz, ArH), 3.36−3.43 (8H, m, CH_2), 2.87 (1H, br s, CH), 1.73−1.83 (8H, m, CH_2), 1.50−3.50 (br, 9H, BH), 1.35−1.46 (8H, m, CH_2), 0.91−1.00 (12H, m, CH_3), −2.51 (br, 1H, BH).^{13}C NMR (acetone-d_6, 63 MHz) 152.1, 138.8, 133.5, 128.6, 124.3, 123.7, 123.2, 122.9, 80.5, 77.1, 59.2, 24.3, 20.3, 13.8. ^{11}B NMR ($CDCl_3$, 128 MHz, BF_3.OEt_2) δ −10.0 to −16.0 (br m, 3B), −18.0 to −20.0 (br m, 3B), −24.6 (d, ^1J (B,H) = 149 Hz, 1B), −34.7 (dd, ^1J (B,H) = 43.8 Hz, ^1J (B,H) = 43.7 Hz, 1B), −37.6 (d, ^1J(B,H) = 138 Hz, 1B). HRMS (ESI) $[M\text{-}NBu_4]^-$ *m/z* calcd for $C_{10}H_{16}B_9S_2$, 298.1582; found, 298.1586.

Compound 3c, Tetrabutylammonium 2,2′,5′,2″-Terthio-phene-5-*o*-nido-carborane. This compound was prepared as described above for the preparation of **3a**, from **2c** (0.18 g, 0.46

mmol) and 1.0 mL of *n*Bu$_4$NF 1.0 M solution in 5 mL of THF, in 85% yield (0.25 g).^{1}H NMR (acetone-d$_6$, 250 MHz) δ 7.43 (1H, d, *J* = 4.91 Hz, ArH), 7.25 (1H, d, *J* = 3.41 Hz, ArH), 7.16 (1H, d, *J* = 3.71 Hz, ArH), 7.05−7.08 (2H, m, ArH), 6.95 (1H, d, *J* = 3.61 Hz, ArH), 6.59 (1H, d, *J* = 3.64 Hz, ArH), 3.40−3.47 (8H, m, CH$_2$), 3.02 (1H, br s, CH), 1.75−1.8 (8H, m, CH$_2$), 1.50−3.50 (br, 9H, BH), 1.36−1.44 (8H, m, CH$_2$), 0.93−0.99 (12H, m, CH$_3$), −2.40 (br, 1H, BH).^{13}C NMR (acetone-d$_6$, 63 MHz) 152.1, 137.2, 137.1, 135.2, 132.6, 128.6, 125.3, 124.9, 124.1, 123.7, 123.6, 122.8, 80.8, 67.7, 59.0, 24.2, 20.0, 13.6. ^{11}B NMR (CDCl$_3$,128 MHz, BF$_3$.OEt$_2$) δ −10.0 to −16.0 (br m, 3B), −18.0 to −20.0 (br m, 3B), −24.6 (d, ^1J (B,H) = 149 Hz, 1B), −34.7 (dd, ^1J (B,H) = 43.8 Hz, ^1J (B,H) = 43.7 Hz, 1B), −37.6 (d, ^1J(B,H) = 138 Hz, 1B). HRMS (ESI) [M-NBu$_4$]$^-$ *m*/*z* calcd for $C_{14}H_{18}B_9S_3$, 380.1462; found, 380.1466.

Compound 4a, Tetrabutylammonium Cobalt(III) Bis-(thiophene-2-*o*-nido-carborane). Compound **3a** (458 mg, 1 mmol), *t*BuOK (1.12 g, 10 mmol), and anhydrous CoCl$_2$ (1.35 g, 10 mmol) were mixed in a 50 mL Schlenk reaction tube and 10 mL of anhydrous dimethoxyethane (DME) was added via syringe. The reaction was refluxed for 30 h under nitrogen, and then cooled to room temperature and filtered to remove the inorganic salt. The filtrate was partitioned between dichloromethane and *n*-Bu$_4$NHSO$_4$ aqueous solution, dried under a vacuum, and purified by silica gel chromatography using dichloromethane as the eluent. The first major fraction was collected and dried under a vacuum, giving a yellow powder (251 mg) in 70 % yield. ^{1}H NMR (acetone-d$_6$, 250 MHz) δ 7.22−7.24 (1H, m, ArH), 7.13−7.15 (1H, m, ArH), 6.89−6.91 (2H, m, ArH), 6.75−6.78 (1H, m, ArH), 6.63−6.64 (1H, m, ArH), 4.27 (1H, s, CH), 3.41−3.47 (8H, m, CH$_2$), 3.22 (1H, s, CH), 1.76−1.78 (8H, m, CH$_2$), 1.50−3.50 (18H, br, BH), 1.37−1.51 (8H, m, CH$_2$), 0.95−1.01 (12H, m, CH$_3$). ^{13}C NMR (CDCl$_3$, 100 MHz) 125.7, 125.8, 123.2, 59.1, 30.9, 24.1, 19.7, 13.7. ^{11}B NMR (CDCl$_3$, 128 MHz, BF$_3$.OEt$_2$) δ 9.0−30.0 (br m, max at 5.9, −0.5, −8.8 and −30.8, 18B) ppm. HRMS (ESI) $[\text{M-NBu}_4]^-$ *m*/*z* calcd for $C_{12}H_{26}B_{18}S_2Co$, 488.26; found, 488.2628.

Compound 4b, Tetrabutylammonium Cobalt(III) Bis(2,2′-bithiophene-5-*o*-nido-carborane). This compound was prepared as described above for the synthesis of **4a**, from **3b** (541 mg, 1 mmol), *t*BuOK (1.12 g, 10 mmol), and anhydrous $CoCl_2$ (1.35 g, 10 mmol), and was obtained (0.28 g) in 63% yield as a dark yellow solid. ^{1}H NMR (acetone-d_6, 250 MHz) δ 7.19−7.28 (3H, m, ArH), 7.06−7.09 (2H, m, ArH), 6.98−7.04 (2H, m, ArH), 6.79 (2H, br s, ArH), 6.41 (1H, br s, ArH), 4.17 (1H, br s, CH), 3.32 (1H, br s, CH), 3.07−3.11 (8H, m, CH_2), 1.60−1.62 (8H, m, CH_2), 1.50−3.50 (18H, br, BH), 1.37−1.46 (8H, m, CH_2), 1.00−1.06 (12H, m, CH_3). ^{13}C NMR ($CDCl_3$, 100 MHz) 127.6, 127.4, 124.7, 123.5, 123.2, 122.8, 59.2, 43.0, 24.0, 19.8, 13.7. ^{11}B NMR ($CDCl_3$, 128 MHz, $BF_3.OEt_2$) δ 9.0−30.0 (br m, max at 5.9, −0.5, −8.8 and −30.8, 18B) ppm. HRMS (ESI) $[\text{M-NBu}_4]^-$ *m*/*z* calcd for $C_{20}H_{30}B_{18}S_4Co$, 652.2346; found, 652.2362.

Compound 4c, Tetrabutylammonium Cobalt(III) Bis-(2,2′,5′,2″-terthiophene-5-*o*-nido-carborane). This compound was prepared as described above for the synthesis of **4a**, from **3c** (0.22 mg, 0.35 mmol), *t*BuOK (0.23 g, 2 mmol), and anhydrous $CoCl_2$ (0.27 g, 2 mmol), and was obtained (0.108 g) in 61% yield as a dark yellow solid. ^{1}H NMR (acetone-d_6, 250 MHz) δ 7.40−7.43 (2H, m. ArH), 7.25−7.27 (2H, m, ArH), 7.16−7.18 (2H, m, ArH), 7.05−7.08 (4H, m, ArH), 6.81−6.97 (2H, m, ArH), 6.50−6.61 (2H, m, ArH), 3.60 (1H, br s, CH), 3.40−3.47 (8H, m, CH_2), 3.10 (1H, br s, CH), 1.73−1.81 (8H, m, CH_2), 1.50−3.50 (18H, br, BH), 1.37−1.45 (8H, m, CH_2), 0.95−1.00 (12H, m, CH_3). ^{13}C-NMR ($CDCl_3$, 100 MHz) 138.1, 137.9, 135.1, 132.5, 127.5, 126.2, 124.8, 123.9, 123.5, 122.7, 68.7, 58.9, 42.6, 24.2, 20.0, 13.6. ^{11}B NMR ($CDCl_3$, 128 MHz, $BF_3.OEt_2$) δ 9.0−30.0 (br m, max at 5.9, −0.5, −8.8 and −30.8, 18B) ppm. HRMS (ESI) $[\text{M-NBu}_4]^-$ *m*/*z* calcd for $C_{28}H_{34}B_{18}S_6Co$, 816.2129; found, 816.2115.

6.2.1 Electrochemical Characterizations

Linear potential sweep cyclic voltammetry experiments were performed with an Autolab PGSTAT 20 potentiostat from Eco Chemie B.V., equipped with General Purpose Electrochemical System GPES software (version 4.5 for Windows). The working electrode was a 1 mm diameter platinum or glassy carbon disk (area: 8×10^{-3} cm^2) and the counter electrode was a glassy carbon rod. Potentials were relative to the system 1×10^{-2} M Ag^+ | Ag in acetonitrile used as the reference electrode (+0.29 V vs aqueous SCE). All reported potentials are referred to SCE (± 0.01 V). Tetra-*n*-butylammonium hexafluorophosphate Bu_4NPF_6 was purchased from Fluka (puriss, electrochemical grade) and was used at 0.1 mol L^{-1} as supporting electrolyte in acetonitrile (anhydrous, analytical grade from SDS). The (CH_3CN + 0.1 M Bu_4NPF_6) electrolytic medium was dried over activated, neutral alumina (Merck) for 30 min, under stirring, and under argon. Alumina was previously activated at 450 °C under a vacuum for several hours. About 7 mL of this solution was transferred with a syringe into the electrochemical cell prior to experiments. All electrochemical measurements were carried out inside a homemade Faraday cage at room temperature (20 ± 2°C) and under a constant flow of argon.

6.2.2 UV−Visible Spectroelectrochemistry

UV−visible absorption spectra were recorded on a Shimadzu Multispec-1501 spectrophotometer (190−1100 nm scan range) interfaced with a microcomputer for data acquisition and using quartz SUPRASIL cells from Hellma (1 cm pathlength). The polymer films were grown on an indium tin oxide (ITO)-coated glass slide electrode.

6.2.3 Computational Details

Geometry optimizations of **4a**−**c** models in a cisoid conformation were carried out with density functional theory (DFT)[433-434] calculations and performed with the hybrid Becke three-parameter exchange functional [435-437] and the Lee−Yang−Parr nonlocal correlation functional [438]

(B3LYP) implemented in the Gaussian 03 (Revision D.02) program suite [439] using the LanL2DZ basis set [440-442] and the default convergence criteria implemented in the program. The figures were generated with MOLEKEL 4.3. [443]

6.2.4 Conducting Probe Atomic Force Microscopy (AFM)

Samples of doped and undoped cobaltabisdicarbollide-functionalized polythiophene films were prepared on gold surfaces on glass (EMF Corporation, Ithaca, NY) using controlled potential electropolymerization. The electropolymerization potentials were previously optimized using cyclic voltammetry experiments with millimetric platinum electrodes. The substrates have a gold coating (1000 Å) on a 50 Å layer of Cr formed on glass. Surface characterizations were accomplished in ambient conditions using a model 5500 scanning probe microscope (SPM) equipped with Picoscan v5.3.3 software (Agilent Technologies, Inc., Chandler, AZ). Characterizations of the surface morphology were accomplished using intermittent or tapping mode atomic force microscopy (AFM). Tapping mode AFM images were acquired at a scan rate of 3.0 nm s^{-1} rastered for 512 lines per frame. Monolithic silicon probes (PPP-NCL) from Nanosensors (Neuchtel, Switzerland**)** were used for tapping mode experiments, with an average force constant of 48 N m^{-1} and resonant frequency of 172 kHz. A multipurpose SPM scanner with a scanning area of 11 × 11 μm^2 was used for imaging, with interchangeable nose cones for either tapping mode or conductive probe AFM experiments. For tapping-mode, the nose cone contains a small piezoceramic chip for tip actuation. For current imaging and $I-V$ measurements, a preamp is integrated within the nose cone. Conductive probe AFM experiments were accomplished using a V-shaped conductive AFM tip (CSC11/Ti-Pt, Micromasch, San Jose, CA) coated with 10 nm Pt layer on a sublayer of 20 nm Ti. All AFM images were processed with free and open source software for data visualization and analysis, Gwyddion (version 2.5) supported by the Czech Metrology Institute (http://gwyddion.net/). Gwyddion is a modular program for

SPM data visualization and analysis. Estimates of surface coverage were obtained with UTHSCA Image Tool.[444] The AFM current images were converted to grayscale bitmaps and a threshold value was selected visually for conversion to black and white pixels. The percentage of colored pixels provided a relative estimate of surface coverage.

6.3 Results and Discussions

6.3.1 Synthesis of Oligothiophene-Disubstituted Cobaltabisdicarbollide Compounds

As shown in Scheme 6.1, compounds **2a−c** were synthesized in 53−76% yield from decaborane, ethyl sulfide and the terminal thienylacetylenes **1a−c.** [445-446] Deboronation of the ortho-carborane cages of **2a−c** using *n*Bu_4NF [447] gave the corresponding nido-carborane derivatives **3a−c** as the *n*Bu_4N^+ salts, in almost quantitative yields. The cobalt(III) complexes **4a−c** were synthesized in a two-step/one-pot procedure, by mixing *t*BuOK and $Co(OAc)_2$ in dimethoxyethane, [448] followed by air oxidation in 61−70% overall yields. The target complexes **4a−c** were characterized by NMR and HRMS, which gave the expected isotope pattern distributions.

6.3.2 Electrochemical Characterization of Oligothiophene-Disubstituted Cobaltabisdicarbollides and Corresponding Conducting Polymer Films

Within the investigated potential range −2.0/2.3 V vs SCE, all compounds show redox activity in CH_3CN medium both due to the reversible reduction of Co(III) to Co(II) and to the oxidation of the thiophene rings (Figure 6.1 and Table 6.1). This assignment is consistent with the results of DFT calculations (Figure 6.2) that show a significant metal character in the LUMOs and a major oligothiophene character in the HOMOs of **4a−c**. First, the reversible one-electron reduction of Co(III) to Co(II) occurs between −1.2 and −1.0 V vs SCE for the three complexes and unexpectedly gives rise to two closely spaced systems for **4a** and **4b** and a single broad system for **4c**. The values of the formal potential $E^{\circ\prime}$ corresponding to each system are listed in Table 6.1 and the cyclic voltammogram of **4a** is shown in Figure 6.1 as a representative example. The separation between the two formal potentials $\Delta E^{\circ\prime}$ is found to decrease with increasing the number of thiophene rings linked to the cobaltabisdicarbollide moiety. It is obvious that the second system cannot be assigned to the reduction of Co(II) to Co(I), as this process is observed at much more negative potentials, below −2.0 V vs SCE. Moreover, the Co(III)/Co(II) process of the unsubstituted cobaltabisdicarbollide is characterized by a single reversible wave at $E^{\circ\prime} = -1.34$ V vs SCE. [407,449] In the case of our study, the presence of two closely spaced systems is directly connected to the presence of the 2-oligothienyl substituents. Based on our electrochemical data, it can be proposed that the reduction of oligothienylcobaltabisdicarbollide complexes involves two redox conformers, both the relative stability and the proportion of which are strongly dependent on the number of bound thiophene rings (Scheme 6.2). Indeed, from Scheme 6.2, the parameter $\Delta E^{\circ\prime}$ can be written as a function of the equilibrium constants (eq 1).

$$\text{eq. 1} \qquad \Delta E^{\circ\prime} = \frac{2.3RT}{F} log\left(\frac{K_{Co(\,II\,)}}{K_{Co(\,III\,)}}\right)$$

Although rotational conformers of nickel- [408-409,450] and cobalt-bis(dicarbollide)complexes [451] have been demonstrated by Hawthorne and Teixidor et al. respectively, electrochemical evidence of such systems has not been reported so far, to the best of our knowledge. Further investigations are required in order to define the structure of the redox conformers involved in the reduction of these oligothienylcobaltabisdicarbollide complexes. The LUMOs of **4a−c** have an antibonding character between the d_{xz} or d_{yz}-type metal atomic orbital and the pπ-type orbitals of the carbon atoms in the two dicarbollide cages. Populating this orbital may then trigger the relative rotation of the cages around the metal towards a more stable redox conformer. In addition, as the length of the oligothiophene substituents increases in **4a−c**, the calculated nature of the LUMO becomes less centered on the metallabisdicarbollide and more delocalized on the oligothiophene substituents. We note that this correlates well with the observed decrease in $\Delta E^{\circ\prime}$ values in **4a**–**c**, Table 6.1.

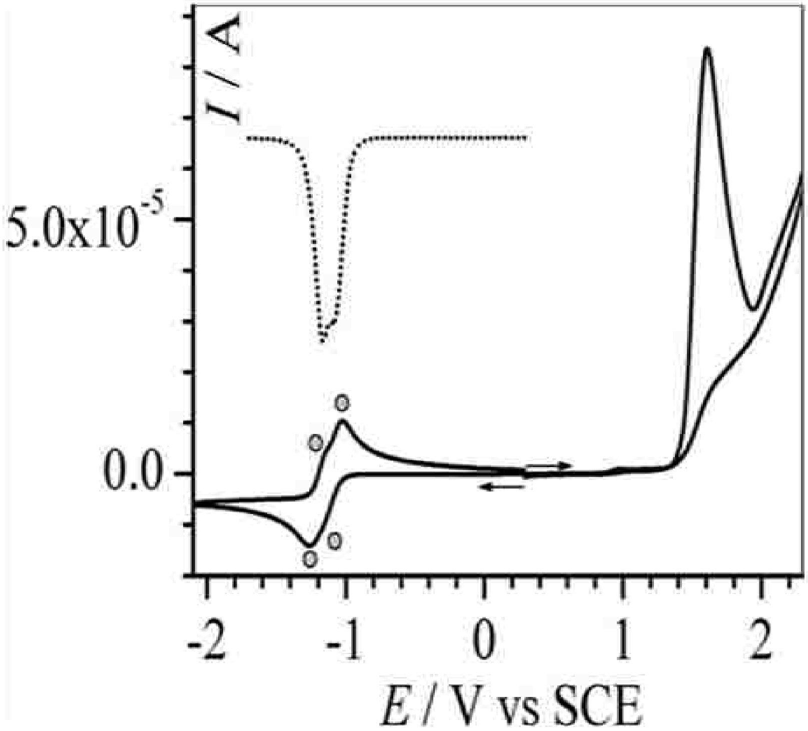

Figure 6.1 Cyclic (solid line) and differential pulse (dotted line) voltammograms of **4a** at 1 × 10^{-2} M in CH_3CN + 10^{-1} M Bu_4NPF_6 (0.1 V s^{-1}).

Table 6.1 Cyclic Voltammetry Data of Oligothienylcobaltabisdicarbollide Complexes at 1 × 10^{-2} M (except for **4c**, 5 × 10^{-3} M) in CH_3CN + 10^{-1} M Bu_4NPF_6; Potential Scan Rate = 0.1 V s^{-1}

Compound	Reduction	Oxidation
	$E^{\circ\prime}$ / V vs SCE ^{a}	E_{pa} / V vs SCE ^{b}
4a	-1.06 (78); -1.19 (83)	1.60_5
4b	-1.03 (60); -1.12 (60)	1.21 (sh); 1.37; 1.58 (sh); 1.85 (sh); 2.18
c	-1.07 (114)	0.88; 0.98; 1.24; 1.49; 1.75 (sh)

[a] Average of anodic and cathodic peak potentials; the peak-to-peak separation in mV is indicated between brackets.

[b] Irreversible processes; sh = shoulder.

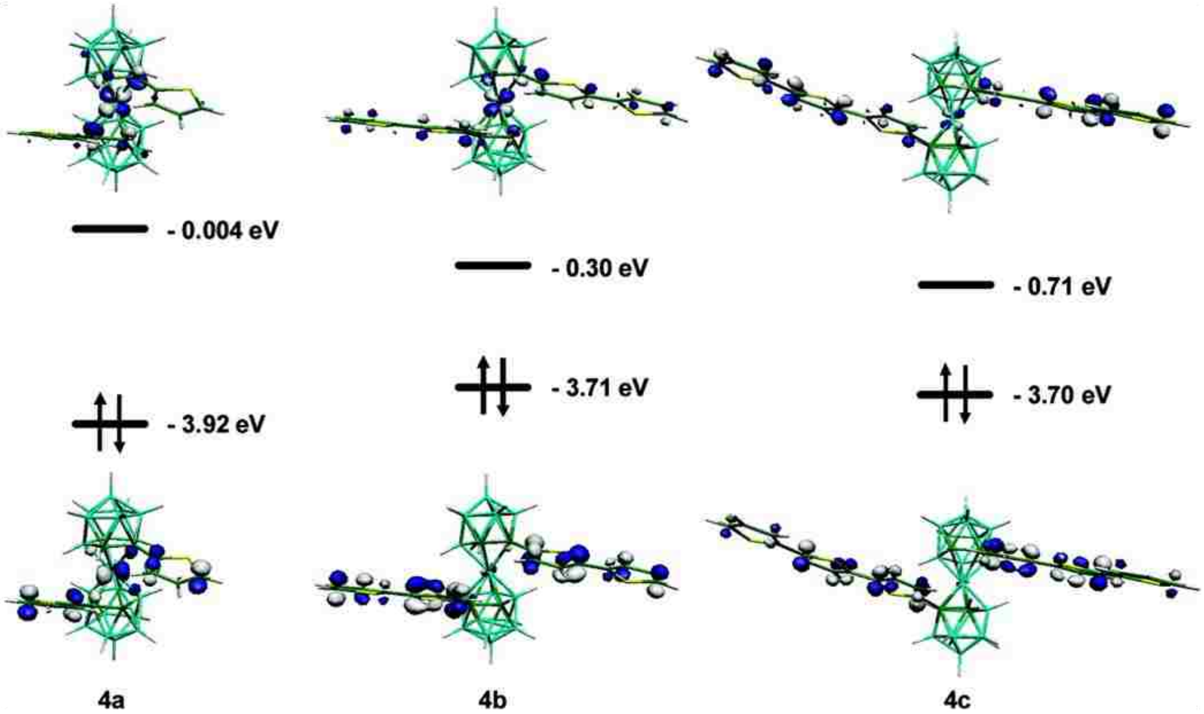

Figure 6.2 HOMOs and LUMOs of **4a**–**c** from DFT calculations.

$$\begin{tikzcd}
{[\mathrm{Co(III)}]_{a} + e^{-}} \arrow[r, shift left, "E^{\circ\prime}_{a}"] \arrow[d, shift left] & {[\mathrm{Co(II)}]_{a}} \arrow[l, shift left] \arrow[d, shift left] \\
{[\mathrm{Co(III)}]_{b} + e^{-}} \arrow[r, shift left] \arrow[u, shift left, "K_{\mathrm{Co(III)}}"] & {[\mathrm{Co(II)}]_{b}} \arrow[l, shift left, "E^{\circ\prime}_{b}"] \arrow[u, shift left, "K_{\mathrm{Co(II)}}"']
\end{tikzcd}$$

Scheme 6.2 Square Scheme Depicting the Different Species Involved in the Reduction of Oligothienylcobaltabisdicarbollide Complexes.[a] [a]$E^{\circ\prime}_{a}$ and $E^{\circ\prime}_{b}$ are the formal potentials corresponding to the Co(III)/Co(II) couple of the two conformers denoted “a” and “b”, respectively. $K_{\mathrm{Co(III)}}$ and $K_{\mathrm{Co(II)}}$ are the related equilibrium constants between the two conformers for the Co(III) and Co(II) forms.

Now, oxidation of these compounds is characterized by a single irreversible peak at ca. 1.6 V vs SCE for **4a** (Figure 6.1) and multiple irreversible peaks in the range 1.2−2.2 V and 0.9−1.75 V for **4b** and **4c** respectively (Figure 6.3A,B). The irreversible nature of anodic electron transfer steps at all investigated potential scan rates (0.02−1 V s^{-1}) is consistent with the multielectronic oxidation of the 2-oligothienyl rings into reactive radical cation species. Furthermore, the oxidation potentials of these systems are found to decrease in the order **4a** > **4b** > **4c**, in agreement with the lengthening of the linked π-conjugated segment and with the result of DFT calculations (Table 6.1 and Figure 6.2). The electrochemical oxidation of **4b** and **4c** leads to the formation of conducting polymer deposits on the electrode surface. Such films could be electrogenerated either potentiodynamically or potentiostatically with no significant effect of the electropolymerization method on their respective electrochemical responses.

Representative cyclic voltammograms corresponding to the potentiodynamical electropolymerization of **4b** and **4c** are shown in Figure 6.3C, D. These are characterized by the regular growth of a new system at less positive potentials. In contrast to the facile electropolymerization of **4b** and **4c**, **4a** does not yield a conducting polymer deposit regardless of the tested experimental conditions (by changing the monomer concentration, the oxidation potential or the solvent). Instead, a poorly electroactive film is electrogenerated, yielding the gradual passivation of the electrode surface. Such a situation has already been encountered in the case of the anodic electrochemistry of other redox-active metallic systems incorporating 2-thienyl units [452-453] and can be explained by the high reactivity of the thiophene radical cation in close proximity of the cobaltabisdicarbollide unit which undergoes a rapid decomposition. DFT calculations indicate that the HOMO of **4a** has a mixed and balanced character between a typical organic thiophene contribution, consistent with a possible electropolymerisation, and a bonding contribution between a d_{xz} or d_{yz}-type metal atomic orbital and the pπ-type orbitals of the carbon atoms in the two dicarbollide cages (Figure 6.2)

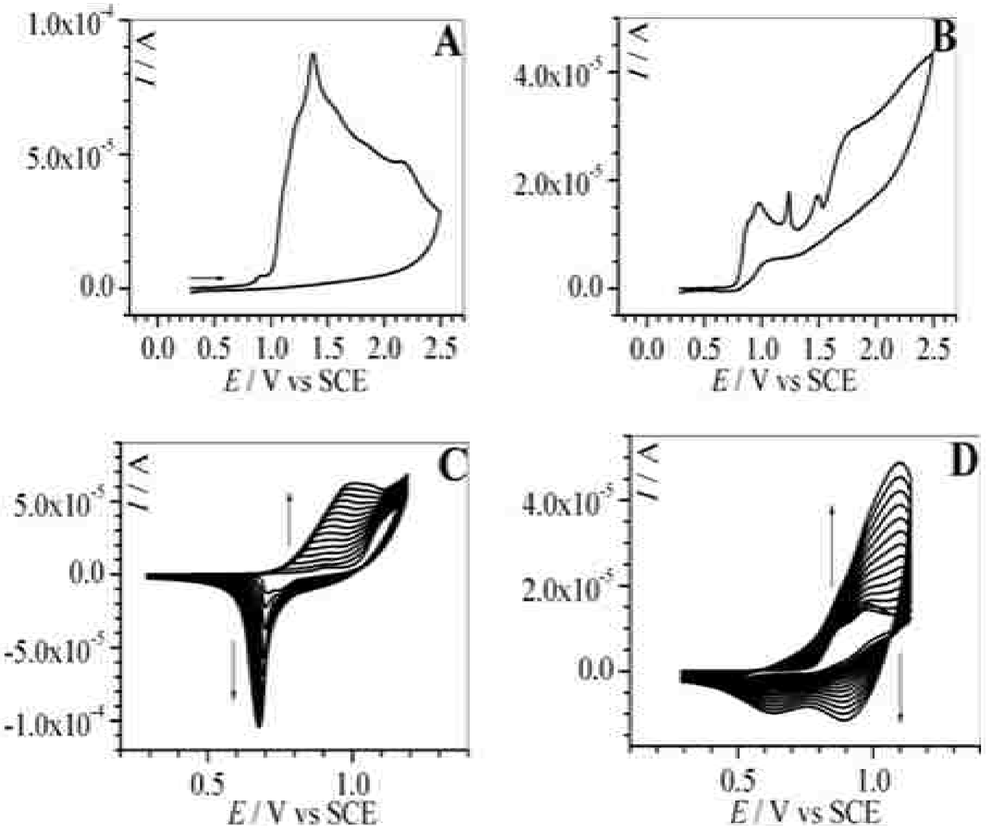

Figure 6.3 Oxidative cyclic voltammograms of (A) **4b** at 1×10^{-2} M and (B) **4c** at 5×10^{-3} M in CH_3CN + 0.1 M Bu_4NPF_6. Potentiodynamical growth of (C) poly(**4b**) and (D) poly(**4c**). Potential scan rate: 0.1 V s^{-1}.

Removing an electron from such an orbital may explain the decomposition of the cobaltabisdicarbollide bridges in the resulting polymer deposit. Hence, the theoretical data are consistent with the experimental passivation of the electrode with an insulating material after anodic oxidation of **4a**. As the length of the oligothiophene substituents increases, in **4b** and **4c**, the metallic and dicarbollide cage carbon atoms contributions in the HOMO decrease dramatically so that the highest occupied frontier orbitals of **4b** and **4c** can be considered as almost purely oligothiophene-based. This corroborates the observed electropolymerisation of these oligothiophenes and the stability (through the robustness of the cobaltabisdicarbollide bridges) and conductivity of the resulting polymers based on **4b** and **4c**.

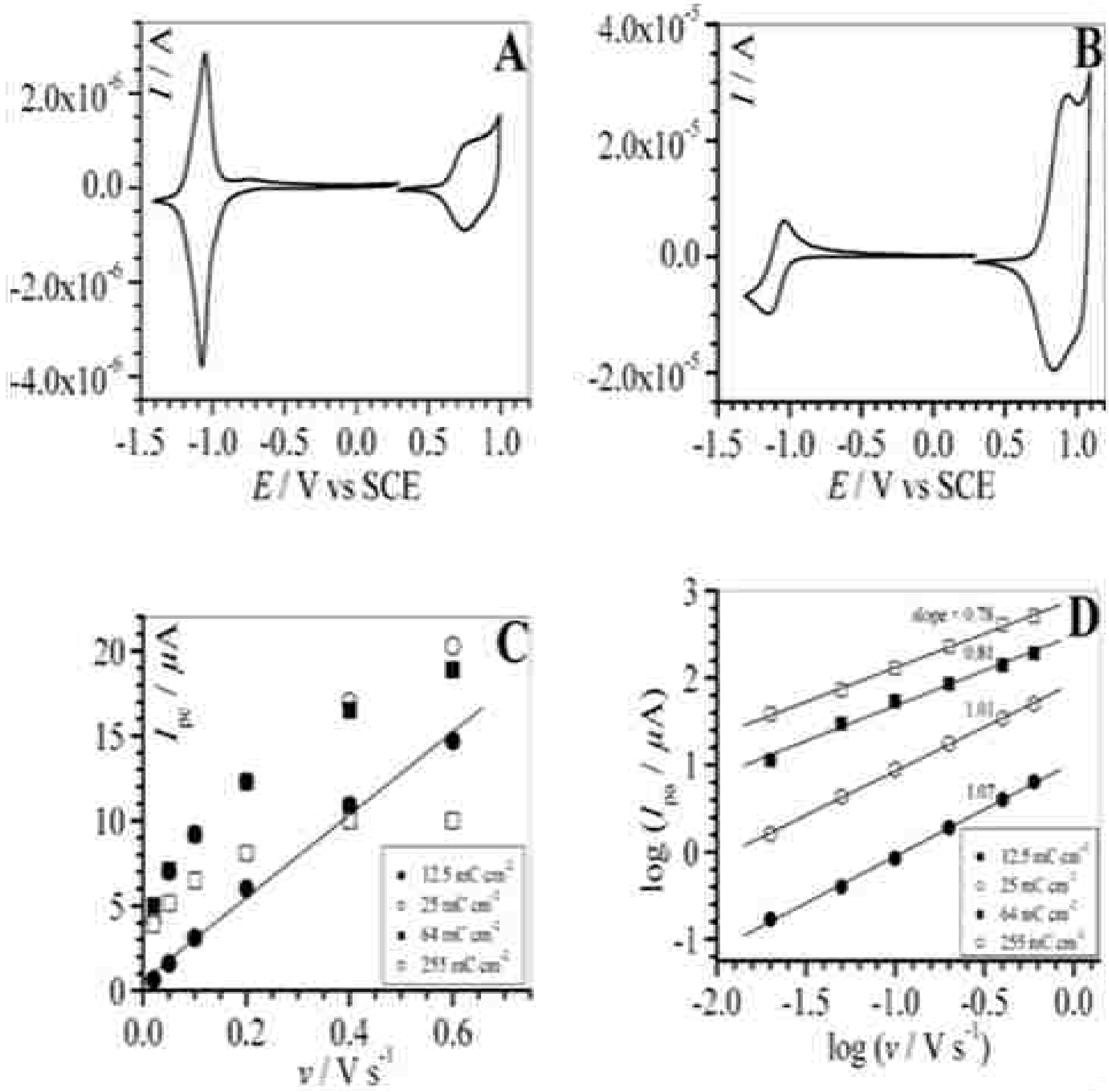

Figure 6.4 Electrochemical response of the electrogenerated poly(**4b**) in CH_3CN + 0.1 M Bu_4NPF_6 at 0.1 V s^{-1}. The consumed electropolymerization charge is 12.5 (A) and 64 mC cm^{-2} (B). (C) Corresponding I_{pc} vs v plots for the Co(III)/Co(II) process as a function of the film electropolymerization charge. (D) Corresponding $\log I_{pa}$ vs $\log v$ for the p-doping/undoping process of poly(**4b**) as a function of the film electropolymerization charge.

Following their electrosynthesis, the electroactive poly(**4b**) and poly(**4c**) films are examined in a monomer-free electrolytic medium. First, the electrochemical response of poly(**4b**) in oxidation is characterized by a broad reversible system at $E°' = 0.80{-}0.85$ V vs SCE corresponding to the p-doping/undoping of the expected quaterthienyl segments (Figure 6.4). The oxidation of sexithienyl segments in poly(**4c**) is characterized by two quasi-reversible redox processes at 0.72 and 1.00 V vs SCE (Figure 6.5). To evaluate the mechanism that controls the charge transport in poly(**4b**) and poly(**4c**), the anodic peak current intensities I_{pa} corresponding to the p-doping process were plotted as a function of the potential scan rate, v, in a logarithmic form. Representative plots are shown in Figure 6.4D for poly(**4b**) but quite similar plots are also obtained for poly(**4c**). The values of the slope for thin films are ca. 1.0, as expected for surface-immobilized electroactive species. [454] A decrease in the slope from 1.0 to ca. 0.8 is observed upon increasing the film thickness. Ideally, a slope of 0.5 is obtained for semiinfinite diffusion-controlled process. These results indicate that for thick films the charge transport mechanism in poly(**4b**) and poly(**4c**) becomes controlled by the diffusion of electrolyte counterions across the polymer film to ensure the electroneutrality of the material. The doping level δ[282]of poly(**4b**) and poly(**4c**) is estimated respectively at 0.30−0.35 and 0.20−0.25 positive charge per monomer (i.e., quaterthienyl and sexithienyl respectively) unit and is somewhat independent on the film thickness. Compared with unsubstituted polythiophene, the oxidation level of both polymers is much lower, which demonstrates the prominent role of the incorporated cobaltabisdicarbollide center on the ion transport in these films. On the basis of these values of δ, the oxidation/reduction of such polymers is expected to involve the transport of electrolyte cations (in our case, Bu_4N^+) to neutralize the negative charge of the metallic center, as opposed to the transport of counteranions as commonly observed for the doping of polythiophenes.

Now, we shall turn towards the electrochemical behavior of these polymers when the potential is scanned towards negative potentials. As shown in Figure 6.4A for poly(**4b**), a perfectly reversible system is observed in reduction at −1.08 V corresponding to the Co(III)/Co(II) couple. For thin films, the peak-to-peak separation and the full width at half- maximum (fwhm) measured at low scan rates (typically 0.05 V s^{-1}) are less than 20 mV and ca. 130 mV, respectively.

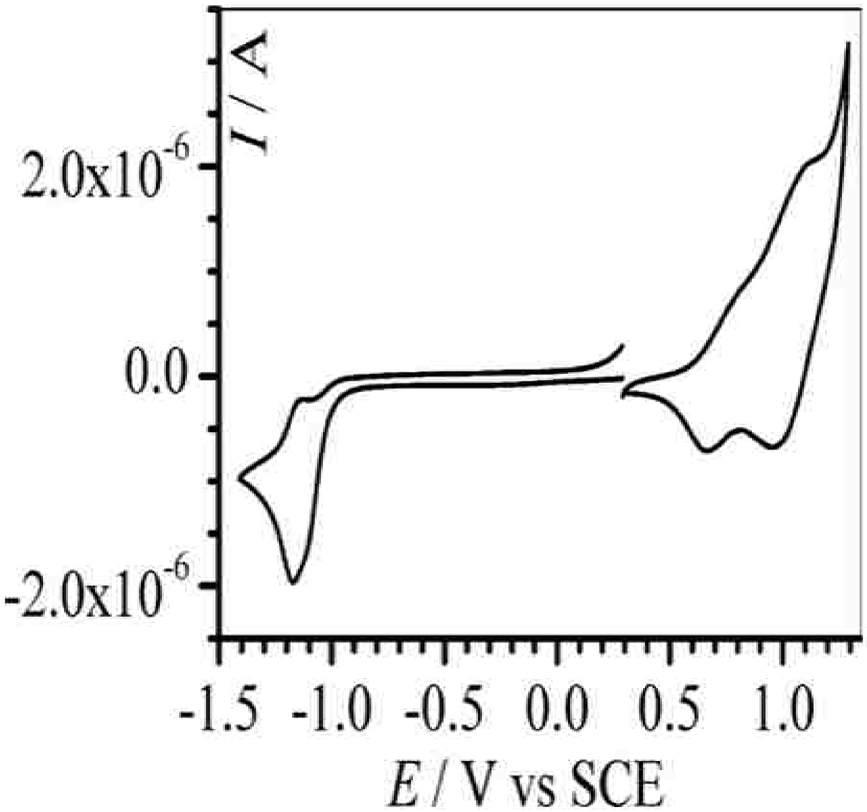

Figure 6.5 Electrochemical response of the electrogenerated poly(**4c**) in CH_3CN + 0.1 M Bu_4NPF_6 at 0.1 V s^{-1}. The consumed electropolymerization charge is 25 mC cm^{-2}.

These values are very close to the theoretically predicted values as a zero peak-to-peak separation and a fwhm of 90 mV are expected for a surface-confined monoelectronic redox center. [454] Consistent with that, the peak currents are found to vary linearly with the potential scan rate *v* (Figure 6.4C). Interestingly, upon increasing the film thickness, the system assigned to Co(III)/Co(II) becomes less and less visible and the variation of the electrochemical parameters are all consistent with a decrease in the electron-transfer rate. Indeed, the peak-to-peak separation and the fwhm increase to 130 and >270 mV respectively, and a deviation from linearity is observed in the peak currents vs *v* plots. Similar effects of the film thickness on the Co(III)/Co(II) response are obtained for poly(**4c**). Nevertheless, even in thin films, the Co(III)/Co(II) system is much less reversible than that observed for poly(**4b**). Indeed, the cathodic step ascribed to the Co(III) reduction is more intense than its related anodic component

(Figure 5). Such intriguing effects of the film thickness on the electroactivity of the surface-confined Co(III)/Co(II) couple have already been reported by others with cobalt salen-based polymers. [455-456]

It must be kept in mind that the cobalt-centered redox process occurs within a potential range where the oligothienyl units are in their neutral reduced state, i.e., in their electronically insulating state. Consequently, the reduction of Co(III) to Co(II) is expected to occur by electron hopping between cobalt centers down to the electrode surface and involves cation migration through the film in order to ensure the electroneutrality of the material. For thick films, a large amount of cobalt centers within the film are not electrochemically addressable because electrolyte cations cannot migrate up to them. Such mass transport constraints can be explained by the more compact and less rough structure of the reduced polymer compared with the polymer in its oxidized state, as evidenced by their AFM analysis (vide infra).

6.3.3 UV−Visible Spectroscopy Analysis of Polymers

To gain further insight into the electronic properties of cobaltabisdicarbollide-substituted polythiophenes, a UV-vis spectroscopic analysis was performed focusing on the electroactive polymers electrogenerated from **4b** and **4c**. First, the UV-vis spectrum of compounds **4a−c** in CH_2Cl_2 consists of four absorption bands within 230−500 nm. The two bands at 260−280 nm and 460−500 nm can be ascribed to the cobaltabisdicarbollide center,[401,405,457]the second less intense one being due to the d−d transition in the Co metal. The bands observed at 250, 325, and 373 nm in the spectra of **4a**, **4b**, and **4c** respectively are assigned to the π−π* transition in the aromatic substituents. However, compared with the unsubstituted parent oligothiophenes,[458] these bands are red-shifted by ca. 15−25 nm in the metallic complexes. Such features indicate a weak electronic delocalization through through the cobaltabisdicarbollide center. The electroactive polymers in their neutral form show an absorption maximum for the interband π−π* transition at 410 and 448 nm for poly(**4b**) and poly(**4c**), respectively (Figure 6.6).

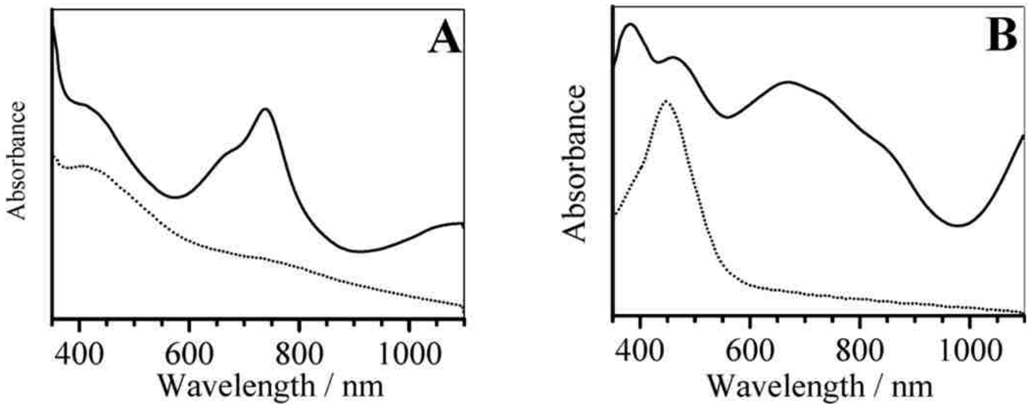

Figure 6.6 Solid-state UV−vis spectra of (A) poly(**4b**) and (B) poly(**4c**) in their doped (solid line) and reduced (dotted line) states.

Expectedly, the polymer incorporating the sexithiophene segments is more conjugated than that with the quaterthiophene segments. Furthermore, poly(**4b**) and poly(**4c**) display a more extended degree of conjugation than the parent oligothiophenes as quaterthiophene and sexithiophene show an absorption maximum at 388 [459] and 432 nm [460-461]respectively. The magnitude of the red-shift is similar to that observed with the monomers (ca. 20 nm), which accounts for the same electronic influence of the cobaltabisdicarbollide on the conjugated aromatic chain of the polymer. It must be stressed that the presence of the cobaltabisdicarbollide center in the polymer films cannot be evidenced from their optical spectra essentially because of the strong absorbance below 350 nm of the used optically transparent electrode and the very weak intensity of the band at 460−500 nm attributed to the cobalt complex. The as-grown oxidatively doped poly(**4b**) and poly(**4c**) films display several new doping-induced bands with maxima at 425, 664, and 738 nm for poly(**4b**) and 465, 669, 739, and 852 nm for poly(**4c**) (Figure 6.6). A further broad band attributed to the formation of the so-called “free carrier tail” [462] is also visible in the near IR region above 1100 nm. Similarly to the neutral forms, the bands of p-doped poly(**4b**) and poly(**4c**) are red-shifted to approximately the same extent with respect to those of oxidized quaterthienyl and sexithienyl moieties. [459] The position of these doping-induced bands and the lowly doped character of the as-grown polymers indicate the formation of polaronic charge states along the polymer chain.

6.3.4 Conducting Probe AFM Characterization of the Cobaltabisdicarbollide-Functionalized Polymers

Nanoscale Comparison of Surface Morphologies

Samples of electropolymerized poly(**4a**−**c**) films in their doped and undoped forms were characterized using tapping-mode AFM in an ambient environment. Substantial differences are apparent for views of the surface morphology of the polymer films, as presented in Figures 6.7 and 6.8. The surface structures of electropolymerized films and subsequently undoped by electrochemical reduction are shown in Figure 6.7. Undoped poly(**4a**) exhibits irregular island domains with angular features having lateral dimensions ranging from 0.45 to 2.8 μm. The height of the domains ranges from 100 to 390 nm. The angular domains cover 66% of the surface and the root-mean-square (rms) surface roughness is estimated at 81 nm. A closer view ($5 \times 5\ \mu m^2$) reveals that the larger domains are made of segments that are tightly packed to form larger assemblies (Figure 6.7A). Interesting features are observed in the corresponding phase image (Figure 6.7B), in which the groove areas are displayed with a bright yellow color due to saturation. Although results for distinguishing differences in surface chemistry are not conclusive, the phase image is still useful for identifying edges of surface features. The surface of the undoped poly(**4b**) exhibits isolated globular structures of different sizes (Figure 6.7C). The smooth round domains range from 0.5 to 2.0 μm in lateral dimension and the heights range from 23 to 180 nm. The smooth globular domains cover 23% of the surface and the local surface roughness measures 19 nm. The simultaneously acquired phase image (Figure 6.7D) displays a relatively homogeneous color for the globular domains and flatter areas of the film, which

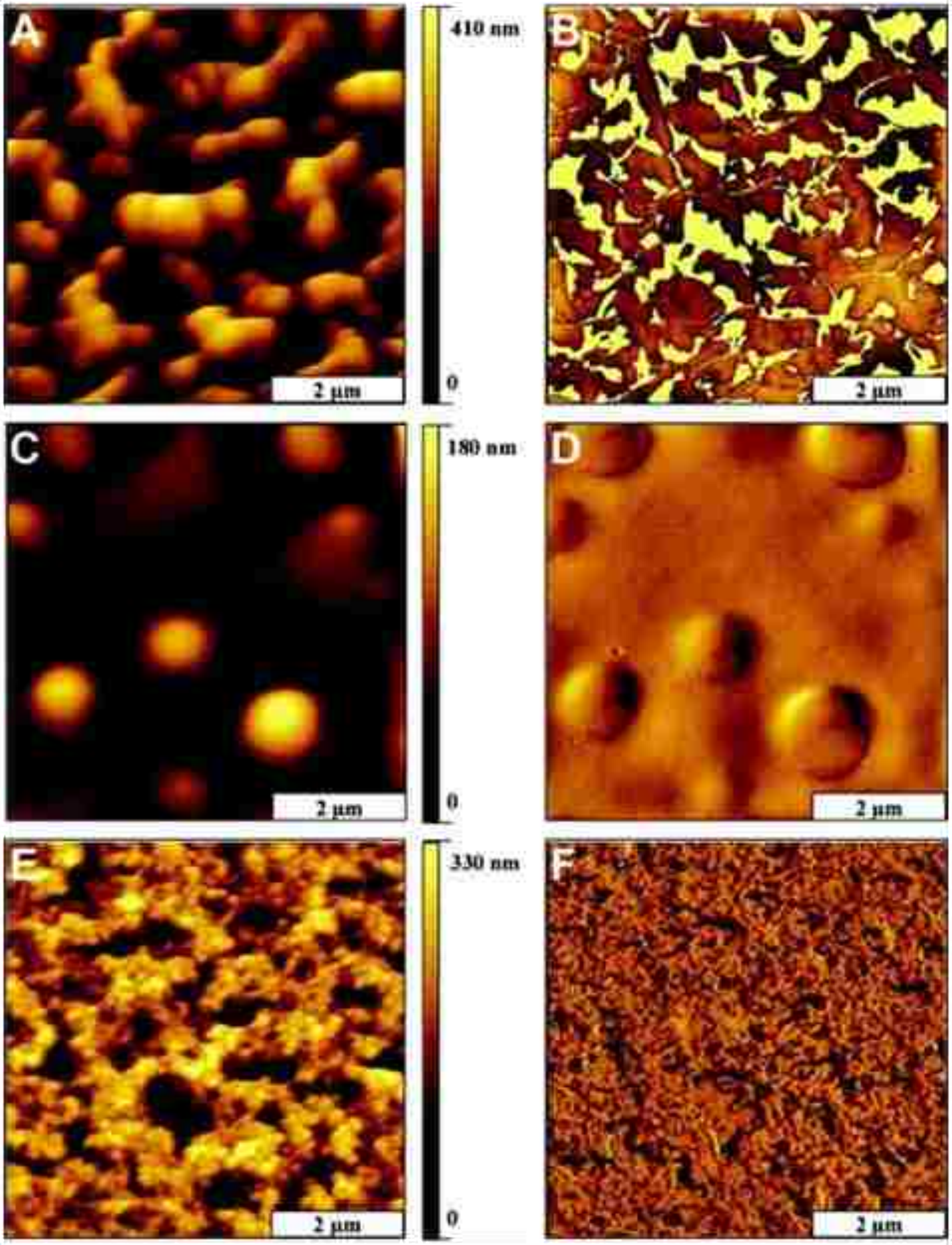

Figure 6.7 (A, C, E) Tapping-mode AFM topographs and (B, D, F) corresponding phase topographs of (A, B) neutral undoped poly(**4a**), (C, D) poly(**4b**), and (E, F) poly(**4c**). The scan size for all topographs is 5 × 5 μm^2.

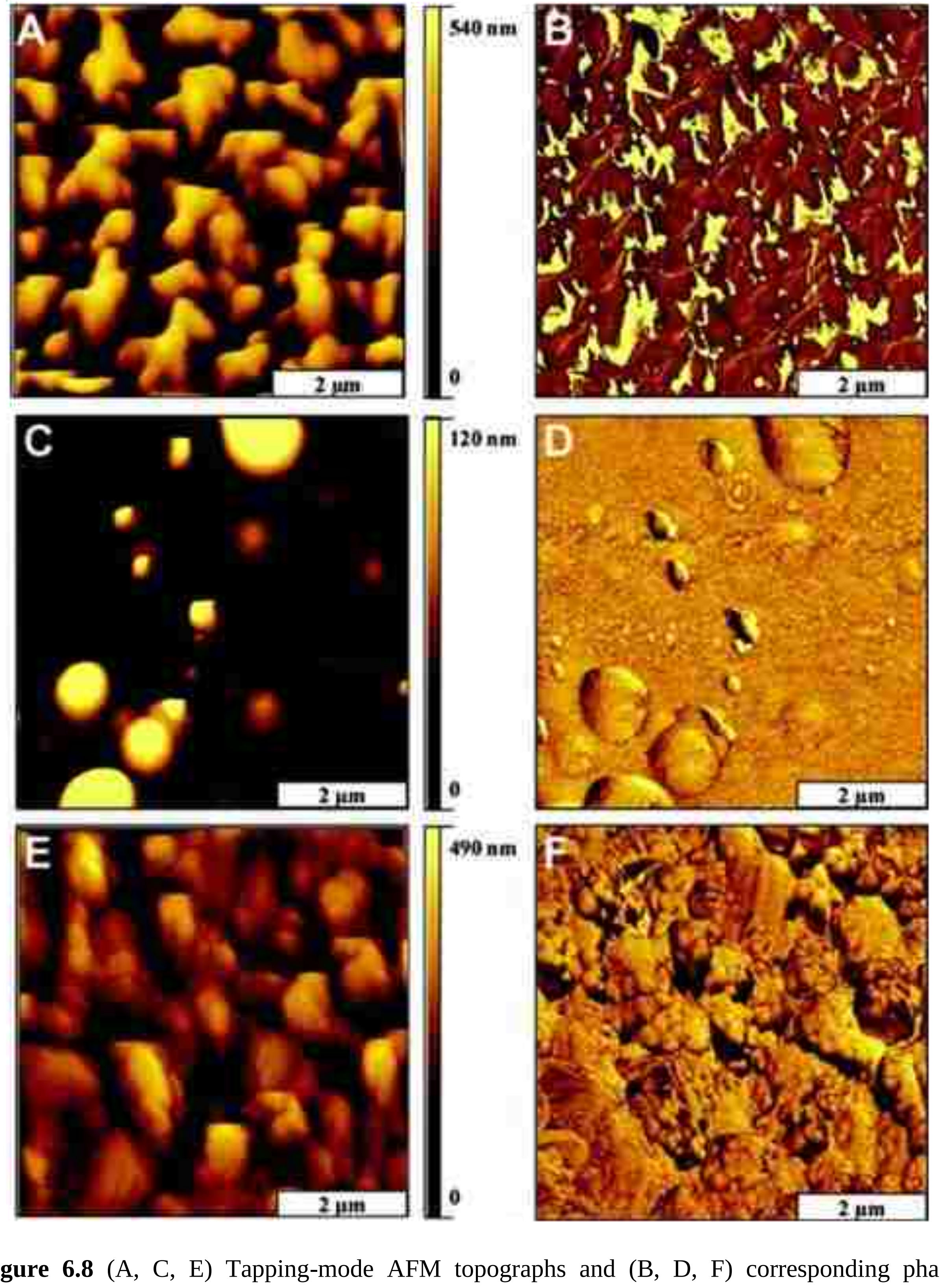

Figure 6.8 (A, C, E) Tapping-mode AFM topographs and (B, D, F) corresponding phase topographs of as-grown *p*-doped (A, B) poly(**4a**), (C, D) poly(**4b**), and (E, F) poly(**4c**). The scan size for all topographs is 5 × 5 μm^2.

indicates a uniform surface composition for the film. The faint dark shadows which outline the round features can be attributed to edge effects as the tapping tip is scanned across the sample. Distinct changes in surface features are evident for the undoped poly(**4c**) (Figures 6.7E) as compared to the previous samples. The surface is composed of small clusters packed tightly into irregular domains. There are valleys or channels between taller clusters, which range from 120 to 260 nm in depth, with a rms roughness of 71 nm. The diameter of the grains comprising the clusters measures 164 ± 66 nm. The phase image exhibits relatively consistent color throughout areas of the surface, except at a few boundary areas of the deeper grooves (Figure 6.7F). Changes in surface composition are not apparent for this phase frame.

A comparison of the surfaces of as-grown p-doped films is shown in Figure 6.8. Irregular islands are evident for poly(**4a**) (Figure 6.8A) ranging from 0.4 to 2.8 μm in lateral dimensions. The heights of the angular domains range from 100 to 540 nm, with an rms roughness of 91 nm which is not significantly different from that of the undoped sample. For the most part, the surface features of the undoped versus doped poly(**4a**) samples are indistinguishable. This is not really surprising because of the nonelectroactive character of this polymer in both reduced and oxidized forms, as demonstrated by cyclic voltammetry experiments. Even the phase frames exhibit markedly similar color contrast. The surface features of the doped and undoped films of poly(**4b**) are found to be slightly different at the nanoscale. Smooth round structures are apparent for doped poly(**4b**), which range from 0.1 to 1.8 μm in lateral dimensions (Figure 6.8C). The globular domains range from 29 to 320 nm in height, and the rms roughness is more than two times higher than that estimated for the undoped sample, namely 50 nm against 19 nm. At a local level, the round globular areas cover approximately 18% of the surface. More significant morphology changes are evident when comparing the doped and undoped poly(**4c**) films. The sizes of the nanoclusters and assembled domains have larger dimensions for the doped sample

(Figure 6.8E). The depth of the channels between taller aggregate domains measures from 68 to 430 nm. The nanoclusters that pack tightly into surface aggregates are slightly larger and have an oval shape which is more elongated for the doped sample. As for poly(**4b**), the rms surface roughness of doped poly(**4c**) is also two times higher than that estimated for the undoped sample, namely 170 nm against ca. 70 nm. The phase image (Figure 6.8F) reveals more clearly the arrangement and packing of the round nanoclusters, which are more irregularly shaped and polydisperse in size. The undoped samples exhibit very small, regular shaped features, whereas the domains of the doped sample contain more random sizes and shapes for the nanoclusters. Globally, the AFM analysis of poly(**4b**) and poly(**4c**) films shows a more compact and less rough structure of insulating undoped samples compared with conducting doped samples, which is in agreement with electrochemical data of these polymers (vide supra).

Conducting Probe AFM Characterizations

For our study, the local conductive properties of the doped cobaltabisdicarbollide-functionalized films were evaluated using conductive probe AFM by measuring the current *I* flowing through the polymer/gold surface junction in ambient conditions, as a function of the applied voltage *V*. The *I*−*V* profiles were generated by measuring the current as the voltage was incrementally swept from −3 to +3 V. A comparison of *I*−*V* profiles plotted for the as-grown doped films is shown in Figure 6.9. Each curve is an average of 12 data sets acquired at different locations of the surface. The differences in the current measured for each polymer can be confidently related to the differences in their conductivity properties because the thickness of the studied polymer films was almost similar (close to 4.0 ± 0.5 μm) and the same contact force was applied to each sample. The *I*−*V* profile for poly(**4a**) exhibits no measurable current over the range of applied voltage (±3 V), which is consistent with the insulating character of this film. The profiles for poly(**4b**) and poly(**4c**) demonstrate that poly(**4c**) is more conducting than poly(**4b**), which is consistent with the more conjugated character of poly(**4c**) as determined from optical data. From corresponding semilog plots, it can be evidenced the almost symmetrical character of conduction profiles. Indeed, the rectification factors measured at ±2.0 V are 0.7 and 0.6 for poly(**4b**) and poly(**4c**), respectively. The non asymmetry of these curves suggests that poly(**4b**) and poly(**4c**) behave like heavily doped semiconductors rather than pure semiconductors for which asymmetrical current responses are usually observed. [463-464] The mean conductivity of these films was estimated using eq 2

$$\sigma = d/(A_t R) \qquad \textbf{eq. 2}$$

where σ is the electron conductivity, *d* is the polymer film thickness, and *R* is the resistance of the polymer sample, which is equal to the inverse of the slope of the *I*−*V* curve. Because the *I*−*V* curve is not linear, the slope was estimated from the linear fit of the curve. A_t is the area of the AFM tip in contact with the surface computed as $A_t = \pi r^2$, with $r \approx 35$ nm, as the contact radius between tip and sample. [463] An average conductivity of 1.4×10^{-4} S cm^{-1} and 7.5×10^{-4} S cm^{-1} were calculated for poly(**4b**) and poly(**4c**), respectively. Such conductivity values well-match those usually reported for other conducting metallopolymers. [465-467]

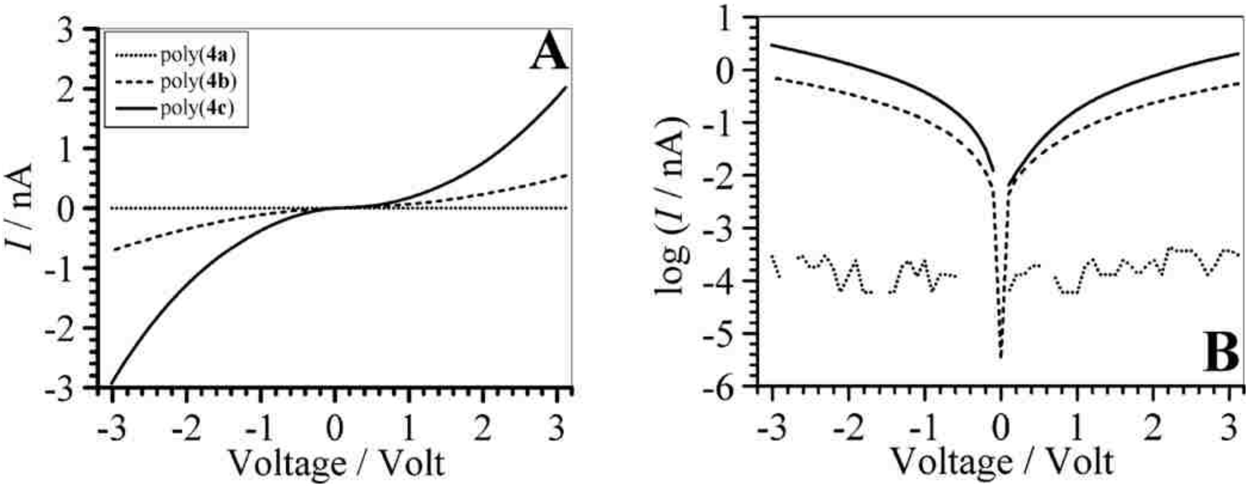

Figure 6.9 (A) Current−voltage curves and (B) corresponding semilog plots for as-grown doped poly(**4a**), poly(**4b**), and poly(**4c**), acquired under ambient conditions.

6.4 Electrocatalytic Reduction of Protons at Cobaltabisdicarbollide-Functionalized Polymers

Redox-active metal centers, such as cobalt(III) bisdicarbollide, can provide efficient sites for electrocatalytic experiments at modified electrodes. As a proof-of-concept, we demonstrate that the reduction of protons to dihydrogen can be efficiently electrocatalyzed by the cobalt(II) form of the metal center incorporated in the host polythiophene matrix. As illustrated for the case of poly(**4b**), the electrochemical response of the bound Co(III)/Co(II) system is dramatically changed upon the addition of H^+ in the electrolytic medium (Figure 6.10A). An increase in the reduction wave of Co(III) to Co(II) is observed, the intensity of which is found to vary linearly with the proton concentration. A simple electrocatalytic mechanism consistent with our data can be written as follows.

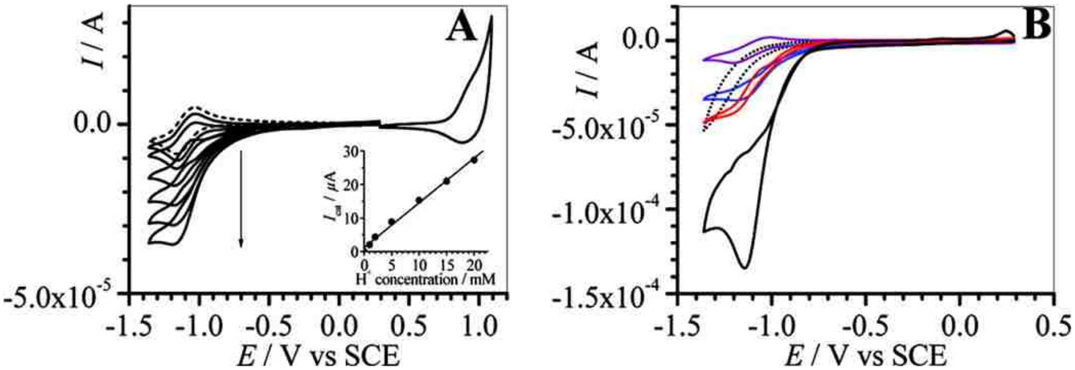

Figure 6.10 (A) Cyclic voltammograms at 0.1 V s^{-1} of a poly(**4b**)-coated glassy carbon (1 mm diameter) electrode in CH_3CN + 0.1 M Bu_4NPF_6 in the absence (dashed line) and in the presence of 1, 2, 5, 10, 15, and 20 mM HBF_4 (solid lines). The consumed electropolymerization charge is 64 mC cm^{-2}. (Inset) Corresponding I_{cat} vs H^+ concentration plot with I_{cat}, the electrocatalytic current (difference between the reduction currents observed in the presence and in the absence of H^+) determined at −1.15 V vs SCE. (B) Effect of the poly(**4b**) thickness on the electrocatalytic reduction of H^+ at 20 mM. The consumed electropolymerization charge is 25 (red), 50 (black), 64 (blue), and 255 mC cm^{-2} (purple). The dotted line corresponds to the cyclic voltammetry curve obtained at the bare glassy carbon electrode.

Compared with the cyclic voltammogram obtained for the direct reduction of H^+ at the bare glassy carbon electrode, the electrocatalytic effect of the immobilized metal center is evident and leads to a significant shift of the cyclic voltammogram towards less negative

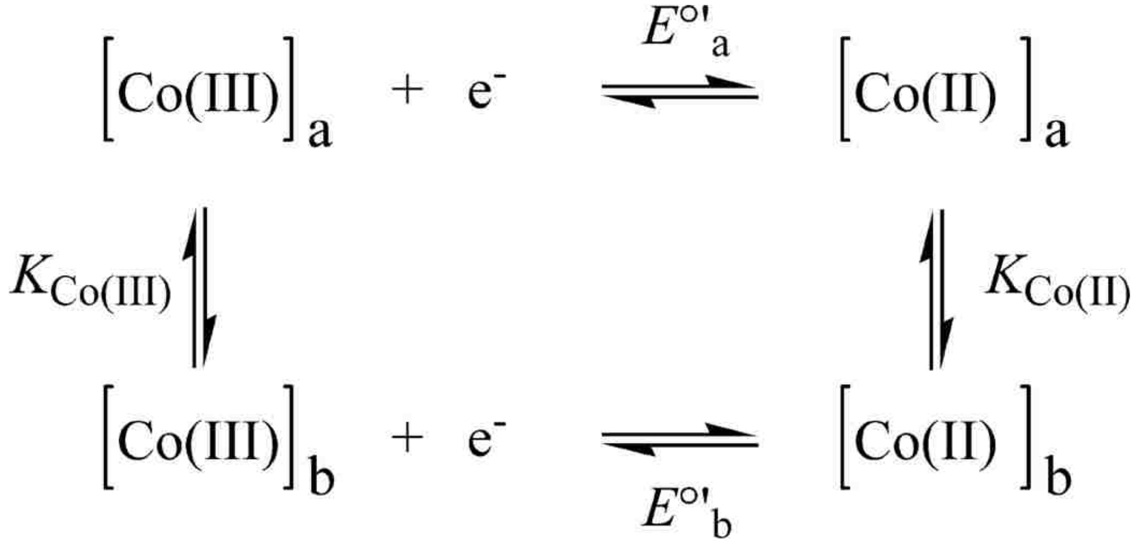

potentials (Figure 6.10B). As commonly observed for catalysis at redox polymer coated electrodes, [468] the electrocatalytic activity of cobaltabisdicarbollide-functionalized polythiophene films is strongly dependent on the film thickness. For the thinnest films, the increase in the film thickness produces the expected increase of the catalytic current as a result of an increase in the surface coverage of cobalt catalyst. The catalytic effect is maximum for a film electrogenerated with a ca. 50 mC cm^{-2} charge and decreases dramatically for thicker films. For the latter situation, the catalysis becomes kinetically controlled by the transport of charge and/or the diffusion of the substrate through the film, [468] which is entirely consistent with the thickness-dependent Co(III)/Co(II) electrochemical response (vide supra).

Analysis of the data reported on Figure 6.10B for the optimum polymer thickness (black curve, 50 mC cm^{-2} electropolymerization charge) shows that the overpotential for hydrogen evolution is significantly decreased by ca. 230 mV with respect to that obtained with the bare glassy carbon electrode (measured for a current density of 1.4 mA cm^{-2} in the presence of 20 mM HBF_4). Despite the improved performance of the optimized modified electrode for proton reduction, the absolute potential for catalysis remains fairly negative (ca. −0.85 V vs. SCE at 1.4 mA cm^{-2}, black curve Figure 6.10B). We note, however, that this potential compares well with the potential range where most of the synthetic metal complexes hydrogenase mimics that have been reported so far operate (in similar organic electrolytes). [469]

6.5 Concluding Remarks

The electrochemical oxidation of bis(bithienyl) and bis(terthienyl) cobalt(III)bisdicarbollide complexes yielded conducting metallopolymers with quaterthienyl and sexithienyl segments, respectively. The electrochemical response of such polymers showed two reversible well-separated redox processes attributed to the Co(III)/Co(II) couple and the *p*-doping of the organic polymer backbone. Although the metal-based process was totally reversible for thin films, a decrease in the rate of electron hopping between the metal centers was observed upon increasing the film thickness. This was consistent with an electron transfer controlled by the diffusion of electrolyte countercations through the film to ensure the electroneutrality. Moreover, the optical data indicated a weak electronic communication between the oligothienyl segments through the cobaltabisdicarbollide bridge. However, the presence of the metallic complex accounted for the lowly doped character of the polymer film and the measured conductivity values below 1×10^{-3} S cm^{-1}, which are much lower than those commonly found for doped polythiophene films. The electrocatalytic results suggest that conducting polymers containing in chain metallabisdicarbollide could find interesting applications as robust and efficient catalysts for the activation of small molecules, and especially for the important H^+/H_2 inter-conversion.[470] So far, little attention has been paid to the catalytic potential of metallabisdicarbollides, as most catalysis studies have involved the metal dicarbollide fragment as a substitute/alternative to a piano-stool metallocene framework. [471] We believe that the present work opens the way for refining this promising new type of electrocatalytic material in terms of the nature of the conducting polymer, length of monomer, nature of the metal, and thickness of polymer. Toward the challenging goal of preparing highly conducting carborane-based metallopolymers with versatile electrocatalytic properties, other electropolymerizable metallabisdicarbollides with metal cations, such as Fe, Ni, and Cu, will be investigated in order to obtain different overlaps of the electrochemical responses for the metal and the polymer backbone.

REFERENCES

(1) LeJeune, Z. M.; Kelley, A. T.; Ngunjiri, J.; Garno, J. C. In *Encyclopedia of Nanoscience and Nanotechnology*; Nalwa, H. S., Ed.; American Scientific Publishers: Stevenson Ranch, CA, in press, 2010.

(2) Ngunjiri, J. N.; Kelley, A. T.; LeJeune, Z. M.; Li, J.-R.; Lewandowski, B. R.; Serem, W. K.; Daniels, S. L.; Lusker, K. L.; Garno, J. C. Achieving precision and reproducibility for writing patterns of n-alkanethiol self-assembled monolayers with automated nanografting. *Scanning* **2008**, *30*, 123.

(3) Brown, T.; LeJeune, Z. M.; Liu, K.; Hardin, S.; Li, J.-R.; Rupnik, K.; Garno, J. C. Automated Scanning Probe Lithography With n-Alkanethiol Self-Assembled Monolayers on Au(111): Application for Teaching Undergraduate Laboratories. *J. Assoc. Lab. Autom.* **2010**, *in press,* available online.

4) Cruchon-Dupeyrat, S.; Porthun, S.; Liu, G.-Y. Nanofabrication using computer-assisted design and automated vector-scanning probe lithography. *Appl. Surf. Sci.* **2001**, *175-176*, 636.

(5) LeJeune, Z. M.; McKenzie, M.; Hao, E.; Chen, B.; Vicente, M. G. H.; Garno, J. C. In *SPIE Photonics West: Microfluidics, BioMEMS, and Medical Microsystems VIII*; Becker, H., Wang, W., Eds.; Society of Photo-Optical Instrumentation Engineers: San Francisco , CA, 2010; Vol. 7593, p 759311.

(6) Xu, S.; Laibinis, P. E.; Liu, G.-Y. Accelerating the kinetics of thiol self-assembly on gold - a spatial confinement effect. *J. Am. Chem. Soc.* **1998**, *120*, 9356.

(7) LeJeune, Z. M.; McKenzie, M.; Robert, S.; Vicente, M. G. H.; Chen, B.; Garno, J. C. Natural vs Spatially constrained assembly of 5,10,15,20-di-pyridin-4-yl-porphyrin on Au (111) from mixed solvents *ACS Nano* **2010**, to be *submitted*.

(8) Fabre, B.; Hao, E.; LeJeune, Z. M.; Amuhaya, E. K.; Barrière, F.; Garno, J. C.; Vicente, M. G. H.; Applied Materials and Interfaces, 2 (3), 691. Polythiophenes Containing In-Chain Cobaltabisdicarbollide Centers. *ACS Appl. Mater. Interfaces* **2010**, *2*, 691.

(9) Pron, A.; Rannou, P. Processible conjugated polymers: from organic semiconductors to organic metals and superconductors. *Prog. Polym. Sci.* **2002**, *27*, 135.

(10) Yang, X.; Loos, J. Toward high-performance polymer solar cells: The importance of morphology control. *Macromolecules* **2007**, *40*, 1353.

(11) Jung, G. Y.; Li, Z. Y.; Wu, W.; Chen, Y.; Olynick, D. L.; Wang, S. Y.; Tong, W. M.; Williams, R. S. Vapor-phase self-assembled monolayer for improved mold release in nanoimprint lithography. *Langmuir* **2005**, *21,* 1158.

(12) Shah, R. R.; Merreceyes, D.; Husemann, M.; Rees, I.; Abbott, N. L.; Hawker, C. J.; Hedrick, J. L. Using Atom Transfer Radical Polymerization To Amplify Monolayers of Initiators

Patterned by Microcontact Printing into Polymer Brushes for Pattern Transfer. *Macromolecules* **2000**, *33*, 597.

(13) Lercel, M. J.; Tiberio, R. C.; Chapman, P. F.; Craighead, H. G.; Sheen, C. W.; Parikh, A. N.; Allara, D. L. Self-Assembled Monolayer Electron-Beam Resists on GaAs and SiO2. *J. Vac. Sci. Technol. B* **1993**, *11*, 2823.

(14) Finnie, K. R.; Haasch, R.; Nuzzo, R. G. Formation and patterning of self-assembled monolayers derived from long-chain organosilicon amphiphiles and their use as templates in materials microfabrication. *Langmuir* **2000**, *16*, 6968.

(15) Xia, Y. N.; Whitesides, G. M. Soft lithography. *Annu. Rev. Mater. Sci.* **1998**, *28*, 153.

(16) Michel, B.; Bernard, A.; Bietsch, A.; Delamarche, E.; Geissler, M.; Juncker, D.; Kind, H.; Renault, J. P.; Rothuizen, H.; Schmid, H.; Schmidt-Winkel, P.; Stutz, R.; Wolf, H. Printing meets lithography: Soft approaches to high-resolution printing *IBM Journal of Research and Development* **2001**, *45*, 697.

(17) Wang, D. W.; Thomas, S. G.; Wang, K. L.; Xia, Y. N.; Whitesides, G. M. Nanometer scale patterning and pattern transfer on amorphous Si, crystalline Si, and SiO2 surfaces using self-assembled monolayers. *Appl. Phys. Lett.* **1997**, *70*, 1593.

(18) Hyun, J.; Sang, J. A.; Lee, W. K.; Chilkoti, A.; Zauscher, S. Molecular Recognition-Mediated Fabrication of Protein Nanostructures by Dip-Pen Lithography. *Nano Lett.* **2002**, *2*, 1203.

(19) Liu, J. F.; Cruchon-Dupeyrat, S.; Garno, J. C.; Frommer, J.; Liu, G.-Y. Three-dimensional nanostructure construction via nanografting: positive and negative pattern transfer. *Nano Lett.* **2002**, *2*, 937.

(20) Hofer, W. A.; Foster, A. S.; Shluger, A. L. Theories of scanning probe microscopes at the atomic scale. *Rev. Mod. Phys.* **2003**, *75*, 1287.

(21) Ralston, J.; Larson, I.; Rutland, M. W.; Feiler, A. A.; Kleijn, M. Atomic force microscopy and direct surface force measurements - (IUPAC technical report). *Pure Appl. Chem.* **2005**, *77*, 2149.

(22) Magonov, S. N. *Surface analysis with STM and AFM : experimental and theoretical aspects of image analysis*; VCH: Weinhem, 1996.

(23) Bonnell, D. A. *Scanning probe microscopy and spectroscopy : theory, techniques, and applications, 2nd ed.*; Wiley-VCH: New York, 2000.

(24) Sarid, D. *Scanning Force Microscopy: with applications to electric, magnetic, and atomic forces* Oxford: New York, 1991.

(25) Wiesendanger, R. *Scanning tunneling microscopy III: theory of STM and related scanning probe methods*; Springer-Verlag: Berlin; New York, 1993.

(26) Colton, R. J. Nanoscale measurements and manipulation. *J. Vac. Sci. Technol., B* **2004**, *22*, 1609.

(27) Hou, J. G.; Wang, K. D. Study of single molecules and their assemblies by scanning tunneling microscopy. *Pure Appl. Chem.* **2006**, *78*, 905.

(28) Vandeleemput, L. E. C.; Vankempen, H. Scanning tunneling microscopy. *Rep. Prog. Phys.* **1992**, *55*, 1165.

(29) Weisendanger, R. *Scanning Probe Microscopy Analytical Methods*; Springer-Verlag Berlin Heidelberg, 1998.

(30) Richards, D. Near-field microscopy: throwing light on the nanoworld. *Philos. Trans. R. Soc. London, Ser. A* **2003**, *361*, 2843.

(31) Buratto, S. K. Near-field scanning optical microscopy. *Current Opinion in Solid State & Materials Science* **1996**, *1*, 485.

(32) Hamers, R. J. Scanned probe microscopies in chemistry. *J. Phys. Chem.* **1996**, *100*, 13103.

(33) Xia, Y. N.; Rogers, J. A.; Paul, K. E.; Whitesides, G. M. Unconventional methods for fabricating and patterning nanostructures. *Chem. Rev.* **1999**, *99*, 1823.

(34) Liu, G.-Y.; Xu, S.; Qian, Y. Nanofabrication of self-assembled monolayers using scanning probe lithography. *Acc. Chem. Res.* **2000**, *33*, 457.

(35) Smith, R. K.; Lewis, P. A.; Weiss, P. S. Patterning self-assembled monolayers. *Prog. Surf. Sci.* **2004**, *75*, 1.

(36) Dubois, L. H.; Nuzzo, R. G. Synthesis, structure and properties of model organic-surfaces. *Annu. Rev. Mater. Sci.* **1992**, *43*, 437.

(37) Whitesides, G. M.; Laibinis, P. E. Wet chemical approaches to the characterization of organic surfaces: self-assembled monolayers, wetting, and the physical-organic chemistry of the solid-liquid interface *Langmuir* **1990**, *6*, 87.

(38) Laibinis, P. E.; Whitesides, G. M. Self-assembled monolayers of n-alkanethiolates on copper are barrier films that protect the metal against oxidation by air. *J. Am. Chem. Soc.* **1992**, *114*, 9022.

(39) Dimilla, P. A.; Folkers, J. P.; Biebuyck, H. A.; Harter, R.; Lopez, G. P.; Whitesides, G. M. Wetting and protein adsorption of self-assembled monolayers of alkanethiolates supported on transparent films of gold. *J. Am. Chem. Soc.* **1994**, *116*, 2225.

(40) Crooks, R. M.; Ricco, A. J. New organic materials suitable for use in chemical sensor arrays. *Acc. Chem. Res.* **1998**, 219.

(41) Flink, S.; Van Veggel, F.; Reinhoudt, D. N. Sensor functionalities in self-assembled monolayers. *Adv. Mater.* **2000**, *12*, 1315.

(42) Willner, I.; Katz, E. Integration of layered redox proteins and conductive supports for bioelectronic applications. *Angew. Chem. Int. Ed.* **2000**, *39*, 1180.

(43) Tour, J. M. Molecular electronics. Synthesis and testing of components. *Acc. Chem. Res.* **2000**, *33*, 791.

(44) Joachim, C.; Gimzewski, J. K.; Aviram, A. Electronics using hybrid-molecular and mono-molecular devices. *Nature* **2000**, *408*, 541.

(45) Sagiv, J. Organized monolayers by adsorption . 1. Formation and structure of oleophobic mixed monolayers on solid-surfaces. *J. Am. Chem. Soc.* **1980**, *102*, 92.

(46) Poirier, G. E. Characterization of organosulfur molecular monolayers on Au(111) using scanning tunneling microscopy. *Chem. Rev.* **1997**, *97*, 1117.

(47) Liu, Y.; Mu, L.; Liu, B. H.; Kong, J. L. Controlled switchable surface. *Chem. Eur. J.* **2005**, *11*, 2622.

(48) Laibinis, P. E.; Whitesides, G. M.; Allara, D. L.; Tao, Y. T.; Parikh, A. N.; Nuzzo, R. G. Comparison of the Structures and Wetting Properties of Self-Assembled Monolayers of Normal-Alkanethiols on the Coinage Metal-Surfaces, Cu, Ag, Au. *J. Am. Chem. Soc.* **1991**, *113*, 7152.

(49) Love, J. C.; Estroff, L. A.; Kriebel, J. K.; Nuzzo, R. G.; Whitesides, G. M. Self-assembled monolayers of thiolates on metals as a form of nanotechnology. *Chem. Rev.* **2005**, *105*, 1103.

(50) Shaporenko, A.; Ulman, A.; Terfort, A.; Zharnikov, A. Self-assembled monolayers of alkaneselenolates on (111) gold and silver. *J. Phys. Chem. B* **2005**, *109*, 3898.

(51) Ulman, A. *An introduction to ultrathin organic films from Langmuir-Blodgett to self-assembly*; Academic Press, New York, 1991.

(52) Schreiber, F. Structure and growth of self-assembling monolayers. *Prog. Surf. Sci.* **2000**, *65*, 151.

(53) Ulman, A. Formation and structure of self-assembled monolayers. *Chem. Rev.* **1996**, *96*, 1533.

(54) Fendler, J. H. Chemical self-assembly for electronic applications. *Chemistry of Materials* **2001**, *13*, 3196.

(55) Willey, T.; Vance, A.; Fadley, C. S. Rapid degradation of alkanethiol-based self-assembled monolayers on gold in ambient laboratory conditions. *Surface Science* **2005**, *567*, 188.

(56) Poirier, G. E.; Pylant, E. D. The Self-Assembly Mechanism of Alkanethiols on Au(111). *Science* **1996**, *272*, 1145.

(57) Poirier, G. E. Coverage-Dependent Phases and Phase Stability of Decanethiol on Au(111). *Langmuir* **1999**, *15*, 1167.

(58) Yang, G. H.; Liu, G.-Y. New insights for self-assembled monolayers of organothiols on Au(111) revealed by scanning tunneling microscopy. *J. Phys. Chem. B* **2003**, *107*, 8746.

(59) Willey, T. M.; Vance, A. L.; van Buuren, T.; Bostedt, C.; Terminello, L. J.; Fadley, C. S. Rapid degradation of alkanethiol-based self-assembled monolayers on gold in ambient laboratory conditions. *Surf. Sci.* **2005**, *576*, 188.

(60) Barrena, E.; Ocal, C.; Salmeron, M. Molecular packing changes of alkanethiols monolayers on Au(111) under applied pressure. *J. Chem. Phys.* **2000**, *113*, 2413.

(61) Barrena, E.; Ocal, C.; Salmeron, M. Structure and stability of tilted-chain phases of alkanethiols on Au(111). *J. Chem. Phys.* **2001**, *114*, 4210.

(62) Kessel, C. R.; Granick, S. Formation and Characterization of a Highly Ordered and Well-Anchored Alkylsilane Monolayer on Mica by Self-Assembly. *Langmuir* **1991**, *7*, 532.

(63) Maoz, R.; Cohen, S. R.; Sagiv, J. Nanoelectrochemical patterning of monolayer surfaces: Toward spatially defined self-assembly of nanostructures. *Adv. Mater.* **1999**, *11*, 55.

(64) Nuzzo, R. G.; Korenic, E. M.; Dubois, L. H. Studies of the temperature-dependent phase-behavior of long-chain normal-alkyl thiol monolayers on gold. *J. Chem. Phys.* **1990**, *93*, 767.

(65) Himmelhaus, M.; Gauss, I.; Buck, M.; Eisert, F.; Woll, C.; Grunze, M. Adsorption of docosanethiol from solution on polycrystalline silver surfaces: an XPS and NEXAFS study. *J. Electron. Spectrosc. Relat. Phenom.* **1998**, *92*, 139.

(66) Tillman, N.; Ulman, A.; Schildkraut, J. S.; Penner, T. L. Incorporation of phenoxy groups in self-assembled monolayers of trichlorosilane derivatives - effects on film thickness, wettability and molecular-orientation. *J. Am. Chem. Soc.* **1988**, *110*, 6136.

(67) Peanasky, J.; Schneider, H. M.; Granick, S.; Kessel, C. R. Self-assembled monolayers on mica for experiments utilizing the surface forces apparatus. *Langmuir* **1995**, *11*, 953.

(68) Schwartz, D. K.; Steinberg, S.; Israelachvili, J.; Zasadzinski, J. A. N. Growth of a self-assembled monolayer by fractal aggregation. *Phys. Rev. Lett.* **1992**, *69*, 3354.

(69) Lavrich, D.; Wetterer, S.; Bernasek, S.; Scoles, G. Physisorption and chemisorption of alkanethiols and alkylsulfides on Au (111). *J. Phys. Chem. B.* **1998**, *102*, 3456.

(70) Xu, S.; Cruchon-Dupeyrat, S.; Garno, J. C.; Liu, G.-Y. In situ studies of thiol self-assembly on gold from solution using atomic force microscopy. *J. Chem. Phys.* **1998**, *108,* 5002.

(71) Schreiber, F. Self-assembled monolayers: from ‘‘simple’’ model systems to biofunctionalized interfaces. *J. Phys.: Condens. Matter* **2004**, *16*, R881.

(72) Porter, M. D.; Bright, T. B.; Allara, D. L.; Chidsey, C. E. D. Spontaneously organized molecular assemblies .4. Structural characterization of normal-alkyl thiol monolayers on gold by optical ellipsometry, infrared-spectroscopy and electrochemistry. *J. Am. Chem. Soc.* **1987**, *109*, 3559.

(73) Fenter, P.; Eberhardt, A.; Liang, K. S.; Eisenberger, P. Epitaxy and chainlength dependent strain in self-assembled monolayers. *J. Chem. Phys.* **1997**, *106*, 1600.

(74) Poirier, G. E. Mechanism of Formation of Au Vacancy Islands in Alkanethiol Monolayers on Au(111). *Langmuir* **1997**, *13,* 2019.

(75) Qian, Y. L.; Yang, G. H.; Yu, J. J.; Jung, T. A.; Liu, G.-Y. Structures of annealed decanethiol self-assembled monolayers on Au(111): An ultrahigh vacuum scanning tunneling microscopy study. *Langmuir* **2003**, *19*, 6056.

(76) Camillone, N.; Eisenberger, P.; Leung, T. Y. B.; Schwartz, P.; Scoles, G.; Poirier, G. E.; Tarlov, M. J. New monolayer phases of n-alkane thiols self-assembled on Au(111) - preparation, surface characterization, and imaging. *J. Chem. Phys.* **1994**, *101*, 11031.

(77) Perez-Diez, I.; Luna, M.; F, T.; Ogletree, D.; Sanz, F.; Salmeron, M. Interaction of water with self-assembled monolayer of alkylsilane on mica. *Langmuir* **2004**, *20*, 1284.

(78) Sagiv, J.; Maoz, R. Hydrogen-bonded mutilayers of self-assembling silanes: structure elucidation by combined fourier transform infra-red spectroscopy and x-ray scattering techniques. *Supramolecular Science* **1995**, *2,* 9.

(79) Xiao, X. D.; Liu, G.-Y.; Charych, D. H.; Salmeron, M. Preparation, structure and mechanical stability of alkylsilane monolayers on mica. *Langmuir* **1995**, *11*, 1600.

(80) Xu, S.; Liu, G.-Y. Nanometer-scale fabrication by simultaneous nanoshaving and molecular self-assembly. *Langmuir* **1997**, *13,* 127.

(81) Brower, T. L.; Garno, J. C.; Ulman, A.; Liu, G. Y.; Yan, C.; Golzhauser, A.; Grunze, M. Self-assembled multilayers of 4,4 '-dimercaptobiphenyl formed by Cu(II)-catalyzed oxidation. *Langmuir* **2002**, *18*, 6207.

(82) Liu, G. Y.; Salmeron, M. Reversible Displacement of Chemisorbed n-Alkanethiol Molecules on Au (111) Surface:An Atomic Force Microscopy Study. *Langmuir* **1994**, *10,* 367.

(83) Xiao, X. D.; Liu, G. Y.; Charych, D. H.; Salmeron, M. Preparation, Structure, And Mechanical Stability Of Alkylsilane Monolayers On Mica. *Langmuir* **1995**, *11*, 1600.

(84) Milic, T.; Garno, J. C.; Batteas, J. D.; Smeureanu, G.; Drain, C. M. Self-organization of self-assembled tetrameric porphyrin arrays on surfaces. *Langmuir* **2004**, *20*, 3974.

(85) Headrick, J. E.; Armstrong, M.; Cratty, J.; Hammond, S.; Sheriff, B. A.; Berrie, C. L. Nanoscale patterning of alkyl monolayers on silicon using the atomic force microscope. *Langmuir* **2005**, *21*, 4117.

(86) Jourdan, J. S.; Cruchon-Dupeyrat, S. J.; Huan, Y.; Kuo, P. K.; Liu, G.-Y. Imaging nanoscopic elasticity of thin film materials by atomic force microscopy: Effects of force modulation frequency and amplitude. *Langmuir* **1999**, *15*, 6495.

(87) Chwang, A. B.; Granstrom, E. L.; Frisbie, C. D. Fabrication of a sexithiophene semiconducting wire: Nanoshaving with an atomic force microscope tip. *Advanced Materials* **2000**, *12*, 285.

(88) Brower, T. L.; Garno, J. C.; Ulman, A.; Liu, G.-Y.; Yan, C.; Golzhauser, A.; Grunze, M. Self-assembled multilayers of 4,4 '-dimercaptobiphenyl formed by Cu(II)-catalyzed oxidation. *Langmuir* **2002**, *18*, 6207.

(89) Zhou, D.; Bruckbauer, A.; Ying, L. M.; Abell, C.; Klenerman, D. Building three-dimensional surface biological assemblies on the nanometer scale. *Nano Letters* **2003**, *3*, 1517.

(90) Garno, J. C.; Yang, Y.; Amro, N. A.; Cruchon-Dupeyrat, S.; Chen, S.; Liu, G.-Y. Precise positioning of nanoparticles on surfaces using scanning probe lithography. *Nano Lett.* **2003**, *3*, 389.

(91) Hansma, H. G.; Vesenka, J.; Siegerist, C.; Kelderman, G.; Morrett, H.; Sinsheimer, R. L.; Elings, V.; Bustamante, C.; Hansma, P. K. Reproducible Imaging and Dissection of Plasmid DNA Under Liquid with the Atomic Force Microscope. *Science* **1992**, *256*, 1180.

(92) Weisenhorn, A. L.; Maivald, P.; Butt, H. J.; Hansma, P. K. Measuring adhesion, attraction, and repulsion between surfaces in liquids with an atomic-force microscope. *Phys. Rev. B.* **1992**, *45*, 11226.

(93) Xu, S.; Miller, S.; Laibinis, P. E.; Liu, G.-Y. Fabrication of nanometer scale patterns within self-assembled monolayers by nanografting. *Langmuir* **1999**, *15*, 7244.

(94) Yu, J.; Tan, Y. H.; Kuo, P. K.; Liu, G.-Y. A nanoengineering approach to regulate the lateral heterogeneity of self-assembled monolayers. *J. Am. Chem. Soc.* **2006**, *128*, 11574.

(95) Ryu, S.; Schatz, G. Nanografting: modeling and simulation. *J. Am. Chem. Soc* **2006**, *128*, 11563.

(96) Garno, J. C.; Zangmeister, C. D.; Batteas, J. D. Directed Electroless Growth of Metal Nanostructures on Patterned Self-Assembled Monolayers. *Langmuir* **2007**, *23*, 7874.

(97) Liu, M.; Amro, N. A.; Chow, C. S.; Liu, G.-Y. Production of nanostructures of DNA on surfaces. *Nano Lett.* **2002**, *2*, 863.

(98) Liu, M.; Liu, G.-Y. Hybridization with nanostructures of single-stranded DNA. *Langmuir* **2005**, *21*, 1972.

(99) O'Brien, J. C.; Jones, V. W.; Porter, M. D. Immunosensing Platforms Using Spontaneously Adsorbed Antibody Fragments on Gold. *Anal. Chem.* **2000**, *72*, 703.

(100) Delamarche, E.; Sundarababu, G.; Biebuyck, H.; Michel, B.; Gerber, C.; Sigrist, H.; Wolf, H.; Ringsdorf, H.; Xanthopoulos, N.; Mathieu, H. J. Immobilization of antibodies on a photoactive self-assembled monolayer on gold. *Langmuir* **1996**, *12*, 1997.

(101) Rowe, C. A.; Tender, L. M.; Feldstein, M. J.; Golden, J. P.; Scruggs, S. B.; MacCraith, B. D.; Cras, J. J.; Ligler, F. S. Array biosensor for simultaneous identification of bacterial, viral, and protein analytes. *Anal. Chem.* **1999**, *71*, 3846.

(102) Lynch, M.; Mosher, C.; Huff, J.; Nettikadan, S.; Johnson, J.; Henderson, E. Functional protein nanoarrays for biomarker profiling. *Proteomics* **2004**, *4*, 1695.

(103) Kane, R. S.; Takayama, S.; Ostuni, E.; Ingber, D. E.; Whitesides, G. M. Patterning proteins and cells using soft lithography. *Biomaterials* **1999**, *20*, 2363.

(104) James, C. D.; Davis, R. C.; Kam, L.; Craighead, H. G.; Isaacson, M.; Turner, J. N.; Shain, W. Patterned protein layers on solid substrates by thin stamp microcontact printing. *Langmuir* **1998**, *14*, 741.

(105) Lahiri, J.; Ostuni, E.; Whitesides, G. M. Patterning Ligands on Reactive SAMs by Microcontact Printing. *Langmuir* **1999**, *15*, 2055.

(106) Bernard, A.; Renault, J. P.; Michel, B.; Bosshard, H. R.; Delamarche, E. Microcontact printing of proteins. *Adv. Mater.* **2000**, *12*, 1067.

(107) Bernard, A.; Delamarche, E.; Schmid, H.; Michel, B.; Bosshard, H. R.; Biebuyck, H. Printing Patterns of Proteins. *Langmuir* **1998**, *14*, 2225.

(108) Whitesides, G. M.; Ostuni, E.; Takayama, S.; Jiang, X.; Ingber, D. E. Soft Lithography in Biology and Biochemistry. *Annu. Rev. Biomed. Eng.* **2001**, *3*, 335.

(109) Dontha, N.; Nowall, W. B.; Kuhr, W. G. Generation of biotin/avidin/enzyme nanostructures with maskless photolithography. *Anal. Chem.* **1997**, *69*, 2619.

(110) Blawas, A. S.; Oliver, T. F.; Pirrung, M. C.; Reichert, W. M. Step-and-Repeat Photopatterning of Protein Features Using Caged-Biotin-BSA: Characterization and Resolution. *Langmuir* **1998**, *14*, 4243.

(111) Nicolau, D. V.; Taguchi, T.; Taniguchi, H.; Yoshikawa, S. Micron-sized protein patterning on diazonaphthoquinone/novolak thin polymeric films. *Langmuir* **1998**, *14*, 1927.

(112) Delamarche, E.; Bernard, A.; Schmid, H.; Bietsch, A.; Michel, B.; Biebuyck, H. Microfluidic networks for chemical patterning of substrate: Design and application to bioassays. *J. Am. Chem. Soc.* **1998**, *120*, 500.

(113) Patel, N.; Sanders, G. H. W.; Shakesheff, K. M.; Cannizzaro, S. M.; Davies, M. C.; Langer, R.; Roberts, C. J.; Tendler, S. J. B.; Williams, P. M. Atomic force microscopic analysis of highly defined protein patterns formed by microfluidic networks. *Langmuir* **1999**, *15*, 7252.

(114) Wadu-Mesthrige, K.; Xu, S.; Amro, N. A.; Liu, G.-Y. Fabrication and imaging of nanometer-sized protein patterns. *Langmuir* **1999**, *15*, 8580.

(115) Wadu-Mesthrige, K.; Amro, N. A.; Liu, G.-Y. Immobilization of proteins on self-assembled monolayers. *Scanning* **2000**, *22*, 380.

(116) Wadu-Mesthrige, K.; Amro, N. A.; Garno, J. C.; Xu, S.; Liu, G.-Y. Fabrication of nanometer-sized protein patterns using atomic force microscopy and selective immobilization. *Biophys. J.* **2001**, *80*, 1891.

(117) Hu, Y.; Das, A.; Hecht, M. H.; Scoles, G. Nanografting de novo proteins onto gold surfaces. *Langmuir* **2005**, *21*, 9103.

(118) Case, M. A.; McLendon, G. L.; Hu, Y.; Vanderlick, T. K.; Scoles, G. Using nanografting to achieve directed assembly of de novo designed metalloproteins on gold. *Nano Lett.* **2003**, *3*, 425.

(119) Liu, G. Y.; Amro, N. A. Positioning protein molecules on surfaces: A nanoengineering approach to supramolecular chemistry. *Proc. Natl. Acad. Sci. U.S.A.* **2002**, *99*, 5165.

(120) Wong, S. S. *Chemistry of Protein Conjugation and Cross-linking*; CRC Press: Boca Raton, FL, 1991.

(121) MacBeath, G.; Koehler, A. N.; Schreiber, S. L. Printing small molecules as microarrays and detecting protein-ligand interactions en masse. *J. Am. Chem. Soc.* **1999**, *121*, 7967.

(122) Gu, J.; Yam, C. M.; Li, S.; Cai, C. Nanometric protein arrays on protein-resistant monolayers on silicon surfaces. *J. Am. Chem. Soc.* **2004**, *126*, 8098.

(123) Hyun, J.; Ahn, S. J.; Lee, W. K.; Chilkoti, A.; Zauscher, S. Molecular recognition-mediated fabrication of protein nanostructures by dip-pen lithography. *Nano Lett.* **2002**, *2*, 1203.

(124) Zhou, D.; Wang, X.; Birch, L.; Rayment, T.; Abell, C. AFM study on protein immobilization on charged surfaces at the nanoscale: Toward the fabricaiton of three-dimensional protein nanostructures. *Langmuir* **2003**, *19*, 10557.

(125) Kenseth, J. R.; Harnisch, J. A.; Jones, V. W.; Porter, M. D. Investigation of approaches for the fabrication of protein patterns by scanning probe lithography. *Langmuir* **2001**, *17*, 4105.

(126) Piner, R. D.; Zhu, J.; Xu, F.; Hong, S. H.; Mirkin, C. A. "Dip-pen" nanolithography. *Science* **1999**, *283*, 661.

(127) Barsotti, R. J.; O'Connel, M.; Stellacci, F. Morphology control in self-assembled monolayers written by Dip Pen Nanolithography. *Langmuir* **2004**, *20*, 4795.

(128) Weeks, B. L.; Noy, A.; Miller, A. E.; De Yoreo, J. J. Effect of dissolution kinetics on feature size in dip-pen nanolithography. *Phys. Rev. Lett.* **2002**, *88*, 255505/1.

(129) Hampton, J.; Dameron, A. A.; Weiss, P. S. Transport rates vary with deposition time in dip pen nanolithography. *J. Phys. Chem. B* **2005**, *109*, 23118.

(130) Hampton, J.; Dameron, A. A.; Weiss, P. S. Double-ink dip-pen nanolithography studies elucidate molecular transport. *J. Am. Chem. Soc.* **2006**, *128*, 1648.

(131) Peterson, P., J.; Weeks, B. L.; De Yoreo, J. J.; Schwartz, P. V. Effect of environmental conditions on dip pen nanolithography of mercaptohexadecanoic acid. *J. Phys. Chem. B* **2004**, *108*, 15206.

(132) Nafday, O.; Vaughn, M. W.; Weeks, B. L. Evidence of meniscus interface transport in dip pen nanolithography: An annular diffusion model. *J. Chem. Phys.* **2006**, *125*, 144703.

(133) Antoncik, E. Dip-Pen Nanolithography: A simple diffusion model. *Surf. Sci.* **2005**, *599*, L369.

(134) Manandhar, P.; Jang, J.; Schatz, G. C.; Ratner, M. A.; Hong, S. Anomalous surface diffusion in nanoscale direct deposition processes. *Phys. Rev. Lett.* **2003**, *90*.

(135) Jang, J.; Schatz, G. C.; Ratner, M. A. How narrow can a meniscus be? *Phys. Rev. Lett.* **2004**, *92*, 085504/1.

(136) Rozhok, S.; Piner, R.; Mirkin, C. A. Dip-pen nanolithography: What controls ink transport? *J. Phys. Chem. B* **2003**, *107*, 751.

(137) Ivanenisevic, A.; Mirkin, C. A. Dip pen nanolithgraphy on semiconductor surfaces. *J. Am. Chem. Soc.*

2001, *123*, 7887.

(138) Ginger, D.; Zhang, H.; Mirkin, C. A. The evolution of dip-pen nanolithography. *Angew. Chem. Int. Ed.* **2004**, *43*, 30.

(139) Rosi, N. L.; Mirkin, C. A. Nanostructures in Biodiagnostics. *Chem. Rev.* **2005**, *105*, 1547.

(140) Salaita, K.; Wang, Y. H.; Mirkin, C. A. Applications of dip-pen nanolithography. *Nat. Nanotechnol.* **2007**, *2*, 145.

(141) Zhang, H.; Amro, N. A.; Disawal, S.; Elghanian, R.; Shile, R.; Fragala, J. High-Throughput Dip-Pen Nanolithography Based Fabrication of Si Nanostructures. *Small* **2007**, *3*, 81.

(142) Zhang, H.; Mirkin, C. A. DPN-generated nanostructures made of gold, silver and palladium. *Chem. Mater.* **2004**, *16*, 1480.

(143) Ivanenisevic, A.; Mirkin, C. A. Site-directed exchange studies with combinatorial libraries of nanostructures. *J. Am. Chem. Soc.* **2002**, *124*, 11997.

(144) Hong, S.; Zhu, J.; Mirkin, C. A. A new tool for studying the in situ growth processes for self-assembled monolayers under ambient conditions *Langmuir* **1999**, *15*, 7897.

(145) Sheehan, P. E.; Whitman, L. J. Thiol diffusion and the role of humidity in "dip pen nanolithography". *Phys. Rev. Lett.* **2002**, *88*, 156104/1.

(146) Schwartz, P. V. Molecular transport from an atomic force microscope tip: A comparative study of dip-pen nanolithography. *Langmuir* **2002**, *18*, 4041.

(147) Hong, S.; Zhu, J.; Mirkin, C. A. Multiple ink nanolithography:toward a multiple-pen nano-plotter. *Science* **1999**, *286*, 523.

(148) Huang, L.; Chang, Y. S.; Kakkassery, J. J.; Mirkin, C. A. Dip pen nanolithography of high melting temperature molecules. *J. Phys. Chem. Lett. B* **2006**.

(149) Pena, D. J.; Raphael, M. P.; Byers, J. M. "Dip-Pen" nanolithography in registry with photolithography for biosensor development. *Langmuir* **2003**, *19*, 9028.

(150) Jung, H.; Kulkarni, R.; Collier, C. P. Dip-pen nanolithography of reactive alkoxysilanes on glass. *J. Am. Chem. Soc.* **2003**, *125*, 12096.

(151) Cho, Y.; Ivanisevic, A. Peptides on GaAs surfaces: Comparison between features generated by microcontact printing and dip-pen nanolithography. *Langmuir* **2006**, *22*, 8670.

(152) Degenhart, G. H.; Schonherr, B. D. H.; Vansco, G. J. Micro- and Nanofabrication of Robust Reactive Arrays Based on the Covalent Coupling of Dendrimers to Activated Monolayers. *Langmuir* **2004**, *20*, 6216.

(153) Su, M.; Dravid, V. P. Colored ink dip-pen nanolithography. *Appl. Phys. Lett.* **2002**, *80*, 4434.

(154) Zhou, H.; Li, Z.; Wu, A.; Wei, G.; Liu, Z. Direct patterning of rhodamine 6G molecules on mica by dip-pen nanolithography. *Appl. Surf. Sci.* **2004**, *236*, 18.

(155) Mulder, A.; Onclin, S.; Peter, M.; Hoogenboom, J. P.; Beijleveld, H.; terMaat, J.; Garcia-Parajo, M. F.; Ravoo, B. J.; Huskens, J.; vanHulst, N. F.; Reinhoudt, D. N. Molecular printboards on silicon oxide: Lithographic patterning of cyclodextrin monolayers with multivalent fluorescent guest molecules. *Small* **2005**, *1*, 242.

(156) Lee, K.-B.; Lim, J.-H.; Mirkin, C. A. Protein Nanostructures Formed via Direct-Write Dip-Pen Nanolithography. *J. Am. Chem. Soc.* **2003**, *125*, 5588.

(157) Li, B.; Zhang, Y.; Hu, J.; Li, M. Fabricating protein nanopatterns on a single DNA molecule with dip-pen nanolithography. *Ultramicroscopy* **2005**, *105*, 312.

(158) Demers, L.; Ginger, D.; Park, S.-J.; Li, Z.; Chung, S.-W.; Mirkin, C. A. Direct Pattening of Modified Oligonucleotides on Metals and Insulators by Dip-Pen Nanolithography. *Science* **2002**, *296*, 1836.

(159) Demers, L.; Park, S. J.; Taton, T. A.; Mirkin, C. A. Orthogonal assembly of nanoparticle building blocks on dip-pen nanolithographically generated templates of DNA. *Angew. Chem. Int. Ed.* **2001**, *40*, 3071.

(160) Li, Y.; Maynor, B. W.; Liu, J. Electrochemical AFM “Dip-Pen” Nanolithography. *J. Am. Chem. Soc.* **2001**, *123*, 2105.

(161) Porter, L. A.; Choi, H. C.; Schmeltzer, J. M.; Ribbe, A. E.; Elliott, L. C. C.; Buriak, J. M. Electroless Nanoparticle Film Deposition Compatible with Photolithography, Microcontact Printing, and Dip-Pen Nanolithography Patterning Technologies. *Nano Lett.* **2002**, *2*, 1369.

(162) Li, J.; Lu, C.; Maynor, B.; Huang, S.; Liu, J. Controlled Growth of Long GaN Nanowires from Catalys PatternsFabricated by "Dip-Pen" Nanolithographic Techniques. *Chem. Mater.* **2004**, *16*, 1633.

(163) Maynor, B. W.; Li, Y.; Liu, J. Au "Ink" for AFM "Dip-Pen" Nanolithography. *Langmuir* **2001**, *17*, 2575.

(164) Su, M.; Liu, X.; Li, S.-Y.; Dravid, V. P.; Mirkin, C. A. Moving beyond Molecules: Patterning Solid-State Features via Dip-Pen Nanolithography with Sol-Based Inks. *J. Am. Chem. Soc.* **2002**, *124*, 1560.

(165) Gundiah, G.; John, N. S.; Thomas, P. J.; Kulkarni, G. U.; Rao, C. N. R. Dip-Pen nanolithography with magnetic Fe2O3 nanocrystals. *Appl. Phys. Lett.* **2004**, *84*, 5341.

(166) Maynor, B. W.; Filocamo, S. F.; Grinstaff, M. W.; Liu, J. Direct-writing of polymer nanostructures: Poly(thiophene) nanowires on semiconducting and insulating surfaces. *J. Am. Chem. Soc.* **2002**, *124*, 522.

(167) Noy, A.; Miller, A. E.; Klare, J. E.; Weeks, B. L.; Woods, B. W.; DeYoreo, J. J. Fabrication of Luminescent Nanostructures and Polymer Nanowires Using Dip-Pen Nanolithography. *Nano Lett.* **2002**, *2*, 109.

(168) Liu, X.; Guo, S.; Mirkin, C. A. Surface and site-specific ring-opening metathesis polymerization initiated by dip-pen nanolithography. *Angew. Chem. Int. Ed.* **2003**, *42*, 4785

(169) Lim, J. H.; Mirkin, C. A. Electrostatically driven dip pen nanolithography of conducting polymers. *Adv. Mater.* **2002**, *14*, 1474.

(170) Lee, K. B.; Park, S. J.; Mirkin, C. A.; Smith, J. C.; Mrksich, M. Protein nanoarrays generated by dip-pen nanolithography. *Science* **2002**, *295*, 1702.

(171) Zhang, H.; Lee, K. B.; Li, Z.; Mirkin, C. A. Biofunctionalized nanoarrays of inorganic structures prepared by dip-pen nanolithography. *Nanotechnology* **2003**, *14*, 1113.

(172) Kwak, S. K.; Lee, G. S.; Ahn, D. J.; Choi, J. W. Pattern formation of cytochrome c by microcontact printing and dip-pen nanolithography. *Mater. Sci. Eng., C* **2004**, *24*, 151.

(173) Valiokas, R.; Vaitekonis, A.; Klenkar, G.; Trinkunas, G.; Liedberg, B. Selective recruitment of membrane protein complexes onto gold substrates patterned by dip-pen nanolithography. *Langmuir* **2006**, *22*, 3456.

(174) Wilson, D. L.; Martin, R.; Hong, S.; Cronin-Golomb, M.; Mirkin, C. A.; Kaplan, D. L. Surface organization and nanopatterning of collagen by dip-pen nanolithography. *Proc. Natl. Acad. Sci. U.S.A.* **2001**, *98*, 13660.

(175) Lee, S. W.; Oh, B. K.; Sanedrin, R. G.; Salaita, K.; Fujigaya, T.; Mirkin, C. A. Biologically active protein nanoarrays generated using parallel dip-pen nanolithography. *Adv.Mater.* **2006**, *18*, 1133.

(176) Smith, J. C.; Lee, K. B.; Wang, Q.; Finn, M. G.; Johnson, J. E.; Mrksich, M.; Mirkin, C. A. Nanopatterning the chemospecific immobilization of cowpea mosaic virus capsid. *Nano Lett.* **2003**, *3*, 883.

(177) Lee, K.-B.; Kim, E.-Y.; Mirkin, C. A.; Wolinsky, S. M. The use of nanoarrays for highly sensitive and selective detection of human immunodeficiency virus type 1 in plasma. *Nano Lett.* **2004**, *4*, 1869.

(178) Zhang, H.; Elghanian, R.; Amro, N. A.; Disawal, S.; Eby, R. Dip pen nanolithography stamp tip. *Nano Lett.* **2004**, *4*, 1649.

(179) Sheehan, P. E.; Whitman, L. J.; King, W. P.; Nelson, B. A. Nanoscale deposition of solid inks via thermal dip pen nanolithography. *Appl. Phys. Lett.* **2004**, *85*, 1589.

(180) Nelson, B. A.; King, W. P.; Laracuente, A. R.; Sheehan, P. E.; Whitman, L. J. Direct deposition of continuous metal nanostructures by thermal dip-pen nanolithography. *Appl. Phys. Lett.* **2006**, *88*, 0331041.

(181) Yang, M.; Sheehan, P. E.; King, W. P.; Whitman, L. J. Direct Writing of a Conducting Polymer with Molecular-Level Control of Physical Dimensions and Orientation. *J. Am. Chem. Soc.* **2006**, *128*, 6774.

(182) Bakbak, S.; Leech, P. J.; Carson, B. E.; Saxena, S.; King, W. P.; Bunz, U. H. F. 1,3-Dipolar Cycloaddition for the Generation of Nanostructured Semiconductors by Heated Probe Tips. *Macromolecules* **2006**, *39*, 6793.

(183) Nabil A Amro; Song Xu; Liu, G.-y. Patterning Surfaces Using Tip-Directed Displacement and Self-Assembly. *Langmuir* **2000**, *16*, 3006.

(184) Amro, N. A.; Xu, S.; Liu, G.-Y. Patterning surfaces using tip-directed displacement and self-assembly. *Langmuir* **2000**, *16*, 3006.

(185) Piner, R. D.; Hong, S.; Mirkin, C. A. Improved imaging of soft materials with modified AFM tips. *Langmuir* **1999**, *15*, 5457.

(186) Knapp, H. F.; Stemmer, A. Preparation, comparison and performance of hydrophobic AFM tips. *Surf. Interface Anal.* **1999**, *27*, 324.

(187) Wei, Z. Q.; Wang, C.; Bai, C. L. Surface imaging of fragile materials with hydrophobic atomic force microscope tips. *Surf. Sci.* **2000**, *467*, 185.

(188) Garno, J. C.; Yang, Y. Y.; Amro, N. A.; Cruchon-Dupeyrat, S.; Chen, S. W.; Liu, G. Y. Precise positioning of nanoparticles on surfaces using scanning probe lithography. *Nano Letters* **2003**, *3*, 389.

(189) Hacker, C. A.; Batteas, J. D.; Garno, J. C.; Marquez, M.; Richter, C. A.; Richter, L. J.; van Zee, R. D.; Zangmeister, C. D. Structural and chemical characterization of monofluoro-substituted oligo(phenylene-ethynylene) thiolate self-assembled monolayers on gold. *Langmuir* **2004**, *20*, 6195.

(190) Muller, W. T.; Klein, D. L.; Lee, T.; Clarke, J.; McEuen, P. L.; Schultz, P. G. A strategy for the chemical synthesis of nanostructures. *Science* **1995**, *268*, 272.

(191) Davis, J. J.; Bagshaw, C. B.; Busutti, K. L.; Hanyu, Y.; Coleman, K. S. Spatially controlled Suzuki and Heck catalytic molecular coupling. *J. Am. Chem. Soc.* **2006**, *128*, 14135.

(192) Blackledge, C.; Engebretson, D. A.; McDonald, J. D. Nanoscale site-selective catalysis of surface assemblies by palladium-coated atomic force microscopy tips: Chemical lithography without electrical current. *Langmuir* **2000**, *16*, 8317.

(193) Peter, M.; Li, X. M.; Huskens, J.; Reinhoudt, D. N. Catalytic probe lithography: Catalyst-functionalized scanning probes as nanopens for nanofabrication on self-assembled monolayers. *J. Am. Chem. Soc.* **2004**, *126*, 11684.

(194) Blasdel, L. K.; Banerjee, S.; Wong, S. S. Selective borohydride reduction using functionalized atomic force microscopy tips. *Langmuir* **2002**, *18*, 5055.

(195) Davis, J. J.; Coleman, K. S.; Busuttil, K. L.; Bagshaw, C. B. Spatially resolved Suzuki coupling reaction initiated and controlled using a catalytic AFM probe. *J. Am. Chem. Soc.* **2005**, *127*, 13082.

(196) Dagata, J. A.; Schneir, J.; Harray, H. H.; Evans, C. J.; Postek, M. T.; Bennett, J. Modification of hydrogen-passivated silicon by a scanning tunneling microscope operating in air. *Appl. Phys. Lett.* **1990**, *56*, 2001.

(197) Garcia, R.; Martinez, R. V.; Martinez, J. Nano-chemistry and scanning probe nanolithographies. *Chem. Soc. Rev.* **2006**, *35*, 29.

(198) Day, H. C.; Allee, D. R. Selective Area Oxidation of Silicon with a Scanning Force Microscope. *Appl. Phys. Lett.* **1993**, *62*, 2691.

(199) Tseng, A. A.; Notargiacomo, A.; Chen, T. P. Nanofabrication by scanning probe microscope lithography: A review. *Journal of Vacuum Science & Technology B* **2005**, *23*, 877.

(200) Lewis, M. S.; Gorman, C. B. Scanning tunneling microscope-based replacement lithography on self-assembled monolayers. Investigation of the relationship between monolayer structure and replacement bias. *J. Phys. Chem. B* **2004**, *108*, 8581.

(201) Liu, G. Y.; Xu, S.; Qian, Y. L. Nanofabrication of self-assembled monolayers using scanning probe lithography. *Accounts of Chemical Research* **2000**, *33*, 457.

(202) Sugimura, H.; Nakagiri, N. Degradation of a Trimethylsilyl Monolayer on Silicon Substrates Induced by Scanning Probe Anodization. *Langmuir* **1995**, *11*, 3623.

(203) Tseng, A. A.; Notargiacomo, A.; Chen, T. P. Nanofabrication by scanning probe microscope lithography: A review. *J. Vac. Sci. Technol., B* **2005**, *23*, 877.

(204) Martinez, R. V.; Garcia, R. Nanolithography Based on the Formation and Manipulation of Nanometer-Size Organic Liquid Menisci. *Nano Lett.* **2005**, *5*, 1161.

(205) Dubois, E.; Bubendorff, J. L. Kinetics of scanned probe oxidation: Space-charge limited growth. *J. Appl. Phys.* **2000**, *87*, 8148.

(206) Melinte, S.; Nysten, B.; Bayot, V. Nanolithographic patterning of thin metal films with a scanning probe microscope. *Superlattices Microstruct.* **1998**, *24*, 79.

(207) Gwo, S.; Yeh, C. L.; Chen, P. F.; Chou, Y. C.; Chen, T. T.; Chao, T. S.; Hu, S. F.; Huang, T. Y. Local electric-field-induced oxidation of titanium nitride films. *Applied Physics Letters* **1999**, *74*, 1090.

(208) Okada, Y.; Amano, S.; Kawabe, M.; Harris, J. S. Basic mechanisms of an atomic force microscope tip-induced nano-oxidation process of GaAs. *J. Appl. Phys.* **1998**, *83*, 7998.

(209) Chien, F. S. S.; Chou, Y. C.; Chen, T. T.; Hsieh, W. F.; Chao, T. S.; Gwo, S. Nano-oxidation of silicon nitride films with an atomic force microscope: Chemical mapping, kinetics, and applications. *Journal of Applied Physics* **2001**, *89*, 2465.

(210) Bloess, H.; Staikov, G.; Schultze, J. W. AFM induced formation of SiO2 structures in the electrochemical nanocell. *Electrochimica Acta* **2001**, *47*, 335.

(211) Dagata, J. A.; Inoue, T.; Itoh, J.; Yokoyama, H. Understanding scanned probe oxidation of silicon. *Appl. Phys. Lett.* **1998**, *73*, 271.

(212) Yang, M.; Zheng, Z.; Liu, Y.; Zhang, B. Scanned probe oxidation on an octadecyl-terminated silicon(111) surface with an atomic force microscope: kinetic investigations in line patterning. *Nanotechnology* **2006**, *17*, 330.

(213) Lee, H.; Kim, S. A.; Ahn, S. J.; Lee, H. Positive and negative patterning on a palmitic acid Languir-Blodgett monolayer on Si surface using bias-dependent atomic force microscopy lithography. *Appl. Phys. Lett.* **2002**, *81*, 138.

(214) Gordon, A. E.; Fayfield, R. T.; Litfin, D. D.; Higman, T. K. Mechanisms of surface anodization produced by scanning probe microscopes. *J. Vac. Sci. Technol. B* **1995**, *13*, 2805.

(215) Fontaine, P. A.; Dubois, E.; Stievenard, D. Characterization of scanning tunneling microscopy and atomic force microscopy-based techniques for nanolithography on hydrogen-passivated silicon. *J. Appl. Phys.* **1998**, *84*, 1776.

(216) Hattori, T.; Ejiri, Y.; Saito, K.; Yasutake, M. Fabrication of Nanometer-Scale Structures Using Atomic-Force Microscope with Conducting Probe. *Journal of Vacuum Science & Technology a-Vacuum Surfaces and Films* **1994**, *12*, 2586.

(217) Calleja, M.; Anguita, J.; Garcia, R.; Birkelund, K.; Perez-Murano, F.; Dagata, J. A. Nanometre-scale oxidation of silicon surfaces by dynamic force microscopy: reproducibility, kinetics and nanofabrication. *Nanotechnology* **1999**, *10*, 34.

(218) Chien, F. S. S.; Hsieh, W. F.; Gwo, S.; Vladar, A. E.; Dagata, J. A. Silicon nanostructures fabricated by scanning probe oxidation and tetra-methyl ammonium hydroxide etching. *Journal of Applied Physics* **2002**, *91*, 10044.

(219) Teuschler, T.; Mahr, K.; Miyazaki, S.; Hundhausen, M.; Ley, L. Nanometer-scale filed-induced oxidation of Si(111):H by a conducting-probe scanning force microscope: Doping dependence and kinetics. *Appl. Phys. Lett.* **1995**, *67*, 3144.

(220) Liu, S. T.; Maoz, R.; Sagiv, J. Planned nanostructures of colloidal gold via self-assembly on hierarchically assembled organic bilayer template patterns with in-situ generated terminal amino functionality. *Nano Lett.* **2004**, *4*, 845.

(221) Liu, S. T.; Maoz, R.; Schmid, G.; Sagiv, J. Template guided self-assembly of (Au55) clusters on nanolithographically defined monolayer patterns. *Nano Lett.* **2002**, *2*, 1055.

(222) Hoeppener, S.; Maoz, R.; Cohen, S. R.; Chi, L. F.; Fuchs, H.; Sagiv, J. Metal nanoparticles, nanowires, and contact electrodes self-assembled on patterned monolayer templates - A bottom-up chemical approach. *Adv. Mater.* **2002**, *14*, 1036.

(223) Maoz, R.; Frydman, E.; Cohen, S. R.; Sagiv, J. "Constructive nanolithography": Inert monolayers as patternable templates for in-situ nanofabrication of metal-semiconductor-organic surface structures - A generic approach. *Adv. Mater.* **2000**, *12*, 725.

(224) Yang, M.; Zheng, Z.; Liu, Y.; Zhang, B. Kinetics of atomic force microscope-based scanned probe oxidation on an octadecylated silicon(111) surface. *J. Phys. Chem. B* **2006**, *110*, 10365.

(225) Sugimura, H.; Nakagiri, N. Scanning probe anodization: Nanolithography using thin films of anodically oxidizable materials as resists. *J. Vac. Sci. Technol. A-Vacuum Surfaces and Films* **1996**, *14*, 1223.

(226) Maoz, R.; Cohen, S. R.; Sagiv, J. Nanoelectrochemical Patterning of Monolayer Surfaces: Toward Spatially Defined Self-Assembly of Nanostructures. *Adv. Mater.* **1999**, *11*, 55.

(227) Wouters, D.; Schubert, U. S. Constructive nanolithography and nanochemistry: Local probe oxidation and chemical modification. *Langmuir* **2003**, *19*, 9033.

(228) Nie, H.-Y.; McIntyre, N. S.; Lau, W. M. Nanolithography of a full-coverage octadecylphosphonic acid monolayer spin coated on a Si substrate. *Appl. Phys. Lett* **2007**, *90*, 203114.

(229) Zhao, J. W.; Uosaki, K. Formation of nanopatterns of a self-assembled monolayer (SAM) within a SAM of different molecules using a current sensing atomic force microscope. *Nano Lett.* **2002**, *2*, 137.

(230) Fuierer, R. R.; Carroll, R. L.; Feldheim, D. L.; Gorman, C. B. Patterning mesoscale gradient structures with self-assembled monolayers and scanning tunneling microscopy based replacement lithography. *Adv. Mater.* **2002**, *14*, 154.

(231) Gorman, C. B.; Carroll, R. L.; He, Y. F.; Tian, F.; Fuierer, R. Chemically well-defined lithography using self-assembled monolayers and scanning tunneling microscopy in nonpolar organothiol solutions. *Langmuir* **2000**, *16*, 6312.

(232) Schoer, J. K.; Zamborini, F. P.; Crooks, R. M. Scanning Probe Lithography. 3. Nanometer-Scale Electrochemical Patterning of Au and Organic Resists in the Absence of Intentionally Added Solvents or Electrolytes. *J. Phys. Chem.* **1996**, *100*, 11086.

(233) Schoer, J. K.; Crooks, R. M. Scanning Probe Lithography. 4. Characterization of Scanning Tunneling Microscope-Induced Patterns in *n*-Alkanethiol Self-Assembled Monolayers. *Langmuir* **1997**, *13*, 2323.

(234) Hurley, P. T.; Ribbe, A. E.; Buriak, J. M. Nanopatterning of alkynes on hydrogen-terminated silicon surfaces by scanning probe-induced cathodic electrografting. *J. Am. Chem. Soc.* **2003**, *125*, 11334.

(235) Li, C.; Wong, W. H. Model-based analysis of oligonucleotide arrays: Expression index computation and outlier detection. *Proc. Natl. Acad. Sci. U.S.A.* **2001**, *98*, 31.

(236) Anderson, J. R.; Chiu, D. T.; Jackman, R. J.; Cherniavskaya, O.; McDonald, J. C.; Wu, H. K.; Whitesides, S. H.; Whitesides, G. M. Fabrication of topologically complex three-dimensional microfluidic systems in PDMS by rapid prototyping. *Anal. Chem.* **2000**, *72*, 3158.

(237) Duffy, D. C.; McDonald, J. C.; Schueller, O. J. A.; Whitesides, G. M. Rapid prototyping of microfluidic systems in poly(dimethylsiloxane). *Anal. Chem.* **1998**, *70*, 4974.

(238) Fan, H. Y.; Lu, Y. F.; Stump, A.; Reed, S. T.; Baer, T.; Schunk, R.; Perez-Luna, V.; Lopez, G. P.; Brinker, C. J. Rapid prototyping of patterned functional nanostructures. *Nature* **2000**, *405*, 56.

(239) Gates, B. D.; Xu, Q. B.; Stewart, M.; Ryan, D.; Willson, C. G.; Whitesides, G. M. New approaches to nanofabrication: Molding, printing, and other techniques. *Chem. Rev.* **2005**, *105*, 1171.

(240) Critchley, K.; Jeyadevan, J. P.; Fukushima, H.; Ishida, M.; Shimoda, T.; Bushby, R. J.; Evans, S. D. A mild photoactivated hydrophilic/hydrophobic switch. *Langmuir* **2005**, *21*, 4554.

(241) Ryan, D.; Parviz, B. A.; Linder, V.; Semetey, V.; Sia, S. K.; Su, J.; Mrksich, M.; Whitesides, G. M. Patterning multiple aligned self-assembled monolayers using light. *Langmuir* **2004**, *20*, 9080.

(242) Critchley, K.; Zhang, L. X.; Fukushima, H.; Ishida, M.; Shimoda, T.; Bushby, R. J.; Evans, S. D. Soft-UV photolithography using self-assembled monolayers. *J. Phys. Chem. B* **2006**, *110*, 17167.

(243) Mooney, J. F.; Hunt, A. J.; McIntosh, J. R.; Liberko, C. A.; Walba, D. M.; Rogers, C. T. Patterning of functional antibodies and other proteins by photolithography of silane monolayers. *Proc. Natl. Acad. Sci. U.S.A.* **1996**, *93*, 12287.

(244) Sugimura, H.; Ushiyama, K.; Hozumi, A.; Takai, O. Micropatterning of alkyl- and fluoroalkylsilane self-assembled monolayers using vacuum ultraviolet light. *Langmuir* **2000**, *16*, 885.

(245) Dulcey, C. S.; Georger, J. H.; Krauthamer, V.; Stenger, D. A.; Fare, T. L.; Calvert, J. M. Deep UV Photochemistry of Chemisorbed Monolayers - Patterned Coplanar Molecular Assemblies. *Science* **1991**, *252*, 551.

(246) Brewer, N. J.; Janusz, S.; Critchley, K.; Evans, S. D.; Leggett, G. J. Photooxidation of self-assembled monolayers by exposure to light of wavelength 254 nm: A static SIMS study. *J. Phys. Chem. B* **2005**, *109*, 11247.

(247) McCoy, M. In *C&E News* 2007; Vol. 85, p 10.

(248) Leggett, G. J. Scanning near-field photolithography-surface photochemistry with nanoscale spatial resolution. *Chem. Soc. Rev.* **2006**, *35*, 1150.

(249) Sun, S.; Leggett, G. J. Matching the resolution of electron beam lithography by scanning near-field photolithography. *Nano Lett.* **2004**, *4*, 1381.

(250) Landraud, N.; Peretti, J.; Chaput, F.; Lampel, G.; Boilot, J. P.; Lahlil, K.; Safarov, V. I. Near-field optical patterning on azo-hybrid sol-gel films. *Appl. Phys. Lett* **2001**, *79*, 4562.

(251) Herndon, M. K.; Collins, R. T.; Hollingsworth, R. E.; Larson, P. R.; Johnson, M. B. Near-field scanning optical nanolithography using amorphous silicon photoresists. *Appl. Phys. Lett* **1999**, *74*, 141.

(252) Madsen, S.; Holme, N. C. R.; Ramanujam, P. S.; Hvilsted, S.; Hvam, J. M.; Smith, S. J. Optimizing the fabrication of aluminum-coated fiber probes and their application to optical near-field lithography. *Ultramicroscopy* **1998**, *71*, 65.

(253) Madsen, S.; Bozhevolnyi, S. I.; Birkelund, K.; Mullenborn, M.; Hvam, J. M.; Grey, F. Oxidation of hydrogen-passivated silicon surfaces by scanning near-field optical lithography using uncoated and aluminum-coated fiber probes. *J. Appl. Phys.* **1997**, *82*, 49.

(254) Kwon, S. J.; Jeong, Y. M.; Jeong, S. H. Fabrication of high-aspect-ratio silicon nanostructures using near-field scanning optical lithography and silicon anisotropic wet-etching process. *Appl. Phys. A* **2007**, *86*, 11.

(255) Massanell, J.; Garcia, N.; Zlatkin, A. Nanowriting on ferroelectric surfaces with a scanning near-field optical microscope. *Opt. Lett.* **1996**, *21*, 12.

(256) Richards, D.; Cacialli, F. Near-field microscopy and lithography of light-emitting polymers. *Philos. Trans. R. Soc. London, Ser. A* **2004**, *362*, 771.

(257) Sun, S. Q.; Montague, M.; Critchley, K.; Chen, M. S.; Dressick, W. J.; Evans, S. D.; Leggett, G. J. Fabrication of biological nanostructures by scanning near-field photolithography of chloromethylphenyisiloxane monolayers. *Nano Lett.* **2006**, *6*, 29.

(258) Montague, M.; Ducker, R. E.; Chong, K. S. L.; Manning, R. J.; Rutten, F. J. M.; Davies, M. C.; Leggett, G. J. Fabrication of biomolecular nanostructures by scanning near-field

photolithography of oligo(ethylene glycol)-terminated self-assembled monolayers. *Langmuir* **2007**, *23*, 7328.

(259) Sun, S. Q.; Leggett, G. J. Generation of nanostructures by scanning near-field photolithography of self-assembled monolayers and wet chemical etching. *Nano Lett.* **2002**, *2*, 1223.

(260) Sun, S.; Chong, K. S. L.; Leggett, G. J. Nanoscale molecular patterns fabricated by using scanning near-field optical lithography *J. Am. Chem. Soc. (communication)* **2002**, *124*, 2414.

(261) Sun, S. Q.; Chong, K. S. L.; Leggett, G. J. Photopatterning of self-assembled. monolayers at 244 nm and applications to the fabrication of functional microstructures and nanostructures. *Nanotechnology* **2005**, *16*, 1798.

(262) Minne, S. C.; Yaralioglu, G.; Manalis, S. R.; Adams, S. R.; Zesch, J.; Atalar, A.; Quate, C. F. Automated parallel high-speed atomic force microscopy. *App. Phys. Letts.* **1998**, *72*, 2340.

(263) Hong, S.; Mirkin, C. A. A nanoplotter with both parallel and serial writing capabilities. *Science* **2000**, *288*, 1808.

(264) Zhang, M.; Bullen, D.; Chung, S.; Hong, S.; Ryu, K. S.; Fan, Z.; Mirkin, C. A.; Liu, C. A MEMS nanoplotter with high-density parallel dip-pen nanolithography probe arrays. *Nanotechnology* **2002**, *13*, 212.

(265) Zou, J.; Bullen, D.; Wang, X.; Liu, C. Conductivity-based contact sensing for probe arrays in dip pen nanolithography. *Appl. Phys. Lett.* **2003**, *83*, 581.

(266) Bullen, D.; Chung, S.-W.; Wang, X.; Zou, J.; Mirkin, C. A.; Liu, C. Parallel dip-pen nanolithography with arrays of individually addressable cantilevers. *Appl. Phys. Lett.* **2004**, *84*, 789.

(267) Bullen, D.; Wang, X.; Zou, J.; Chung, S.; Mirkin, C. A.; Liu, C. Design, fabrication, and characterization of thermally actuated probe arrays for dip pen nanolithography. *J. Microelectromech. S.* **2004**, *13*, 594.

(268) Bullen, D.; Liu, C. Electrostatically actuated dip pen nanolithography probe arrays. *Sens. Actuators, A* **2006**, *125*, 504.

(269) Salaita, K.; Wang, Y.; Fragala, J.; Vega, R. A.; Liu, C.; Mirkin, C. A. Massively Parallel Dip-Pen Nanolithography with 55000-Pen Two-Dimensional Arrays. *Angew. Chem. Int. Ed.* **2007**, *45*, 7220.

(270) Aeschimann, L.; Meister, A.; Akiyaa, T.; Chui, B. W.; Niedermann, P.; Heinzelmann, H.; DeRooij, N. F.; Staufer, U.; Vettiger, P. Scanning probe arrays for lifesciences and nanobiology applications. *Microelectron. Eng.* **2006**, *83*, 1698.

(271) Minne, S. C.; Manalis, S. R.; Atalar, A.; Quate, C. F. Independent parallel lithography using the atomic force microscope. *J. Vac. Sci. Technol. B* **1996**, *14*, 2456.

(272) Rangelow, I. W.; Ivanov, T.; Ivanova, K.; Volland, B. E.; Grabiec, P.; Sarov, Y.; Persaud, A.; Gotszalk, T.; Zawierucha, P.; Zielony, M.; Dontzov, D.; Schmidt, B.; Zier, M.; Nikolov, N.; Kostic, I.; Engl, W.; Sulzbach, T.; Mielczarski, J.; Kolb, S.; Latimier, D. P.; Pedreau, R.; Djakov, V.; Huq, S. E.; Edinger, K.; Fortagne, O.; Almansa, A.; Blom, H. O. Piezoresistive and self-actuated 128-cantilever arrays for nanotechnology applications. *Microelectron. Eng.* **2007**, *84*, 1260.

(273) Vettiger, P.; Despont, M.; Drechsler, U.; Durig, U.; Haberle, W.; Lutwyche, M. I.; Rothuizen, H. E.; Stutz, R.; Widmer, R.; Binnig, G. K. The "Millipede" - More than one thousand tips for future AFM data storage. *IBM J. Res. Dev.* **2000**, *44*, 323.

(274) Binnig, G. In *US Patent*; Patent, U., Ed.; US Patent: US, 1986, p 318.

(275) Binnig, G.; Quate, C. F.; Gerber, C. Atomic Force Microscope. *Phys. Rev. Lett.* **1986**, *56*, 930.

(276) Glaunsinger, W. S.; Ramakrishna, B. L.; Garcia, A. A.; Pizziconi, V. NSF Highlights - Multidisciplinary Scanning Probe Microscopy Laboratory. *J. Chem. Educ.* **1997**, *74*, 310.

(277) Maye, M. M.; Luo, J.; Han, L.; Zhong, C. J. Chemical analysis using Scanning Force Microscopy - an undergraduate laboratory experiment. *J. Chem. Educ.* **2002**, *79*, 207.

(278) Furlan, P. Y. Engaging students in early exploration of nanoscience topics using hands-on activities and Scanning Tunneling Microscopy. *J. Chem. Educ.* **2009**, *86*, 705.

(279) vanderVegte, E. W.; Hadziioannou, G. Scanning Force Microscopy with chemical specificity: an extensive study of chemically specific tip-surface interactions and the chemical imaging of surface functional groups. . *Langmuir* **1997**, *13*, 4357.

(280) Yuan, C. B.; Chen, A.; Kolb, P.; Moy, V. T. Energy landscape of streptavidin-biotin complexes measured by atomic force microscopy. *Biochemistry* **2000**, *39*, 10219.

(281) Coury, L. A.; Johnson, M.; Murphy, T. J. Surface analysis by Scanning Tunneling Microscopy. *J. Chem. Educ.* **1995**, *72*, 1088.

(282) Pullman, D.; Peterson, K. I. Investigating intermolecular interactions via scanning tunneling microscopy - an experiment for the physical chemistry laboratory. *J. Chem. Educ.* **2004**, *81*, 549.

(283) Rapp, C. S. Getting close with the instructional Scanning Tunneling Microscope. *J. Chem. Educ.* **1997**, *74*, 1087.

(284) Aumann, K.; Muyskens, K. J. C.; Sinniah, K. Visualizing atoms, molecules, and surfaces by scanning probe microscopy. *J. Chem. Educ.* **2003**, *80*, 187.

(285) Giancarlo, L. C.; Fang, H.; Avila, L.; Fine, L. W.; Flynn, G. W. Molecular photography in the undergraduate laboratory: identification of functional groups using scanning tunneling microscopy. *J. Chem. Educ.* **2000**, *77*, 66.

(286) Braun, R. D. Braun RD. The modern student laboratory: scanning tunneling microscopy of silicon and carbon. *J. Chem. Educ.* **1992**, *69*, A90.

(287) Zhong, C. J.; Han, L.; Maye, M. M.; Luo, J.; Kariuki, N. N.; Jones, W. E., Jr Atomic scale imaging: a hands-on scanning probe microscopy laboratory for undergraduates. *J. Chem. Educ.* **2003**, *80*, 194.

(288) Lehmpuhl, D. W. Incorporating scanning probe microscopy into the undergraduate chemistry curriculum. *J. Chem. Educ.* **2003**, *80*, 478.

(289) Hepel, M. Electrochromic WO3 films: Nanotechnology experiments in instrumental analysis and physical chemistry laboratories. *J. Chem. Educ.* **2008**, *85*, 125.

(290) Bullen, H. A. Teaching surface characterization to undergraduates. *Anal. Bioanal. Chem.* **2007**, *387*, 1579.

(291) Poler, J. C. Surface oxidation kinetics: A scanning tunneling microscopy experiment. *J. Chem. Educ.* **2000**, *77*, 1198.

(292) Meenakshi, V.; Babayan, Y.; Odom, T. W. Benchtop nanoscale patterning using soft lithography. *J. Chem. Educ.* **2007**, *84*, 1795.

(293) Ito, T. Observation of DNA molecules using fluorescence microscopy and atomic force microscopy. *J. Chem. Educ.* **2008**, *85*, 680.

(294) Sullivan, T. S.; Geiger, M. S.; Keller, J. S.; Klopcic, J. T.; Peiris, F. C.; Schumacher, B. W.; Spater, J. S.; Turner, P. C. Innovations in nanoscience education at Kenyon College. *IEEE T. Educ.* **2008**, *51*, 234.

(295) NanoProfessor [http://www.nanoprofessor.net/]5/25/2010

(296) Educational resources. Agilent Tech Brief; USA: 2009. Agilent, 5400 SPM/AFM Microscope 5989–5842EN Rev Bhttp://cp.literature.agilent.com/litweb/pdf/5989-5842EN.pdf5/2010

(297) Agilent Technologies, Atomic Force Microscopy Resource Library. 2010.www.AFMuniversity.org5/25/2010

(298) Cappella, B.; Dietler, G. Force-distance curves by atomic force microscopy. *Surf. Sci. Reports* **1999**, *34*, 1.

(299) Wiesendanger, R. *Scanning probe microscopy and spectroscopy methods and applications*; Cambridge University Press, 1994.

(300) Kramer, S.; Fuierer, R. R.; Gorman, C. B. Scanning probe lithography using self-assembled monolayers. *Chem. Rev.* **2003**, *103*, 4367.

(301) Ngunjiri, J.; Garno, J. C. AFM-based lithography for nanoscale protein assays. *Anal. Chem.* **2008**, *80*, 1361.

(302) Liu, M.; Amro, N. A.; Liu, G. Y. Nanografting for surface physical chemistry. *Ann. Rev. Phys. Chem.* **2008**, *59*, 367.

(303) Porter, L. A.; Ribbe, A. E.; Buriak, J. M. Metallic nanostructures via static plowing lithography. *Nano Lett.* **2003**, *3*, 1043.

(304) Qin, G. T.; Cai, C. Z. Sub-10-nm patterning of oligo(ethylene glycol) monolayers on silicon surfaces via local oxidation using a conductive atomic force microscope. *Nanotechnology* **2009**, *20*.

(305) Garno, J. C.; Batteas, J. D. In *Applied Scanning Probe Methods, Industrial Applications*; Bhushan, B., Ed.; Springer-Verlag: Berlin Heidelberg New York, 2006; Vol. IV.

(306) Wouters, D.; Schubert, U. S. Nanolithography and nanochemistry: Probe-related patterning techniques and chemical modification for nanometer-sized devices. *Angew. Chem. Int. Ed.* **2004**, *43*, 2480.

(307) Rosa, L. G.; Liang, J. Atomic force microscope nanolithography: dip-pen, nanoshaving, nanografting, tapping mode, electrochemical and thermal nanolithography. *J. Phys.-Condens. Matter* **2009**, *21*.

(308) Klapetek, P.; Necas, D. Gwyddion. *Czech Metrology Institute* **2007**.

(309) Kadalbajoo, M.; Park, J.; Opdahl, A.; Suda, H.; Kitchens, C. A.; Garno, J. C.; Batteas, J. D.; Tarlov, M. J.; DeShong, P. Synthesis and structural characterization of glucopyranosylamide films on gold. *Langmuir* **2007**, *23*, 700.

(310) Kelley, A. T.; Ngunjiri, J. N.; Serem, W. K.; Lawrence, S. O.; Yu, J. J.; Crowe, W. E.; Garno, J. C. Applying AFM-based nanofabrication for measuring the thickness of nanopatterns: The role of head groups in the vertical self-assembly of omega-functionalized n-alkanethiols. *Langmuir* **2010**, *26*, 3040.

(311) Liang, J.; Rosa, L. G.; Scoles, G. Nanostructuring, Imaging and molecular manipulation of dithiol monolayers on Au(111) surfaces by atomic force Microscopy. *J.Phys. Chem. C* **2007**, *111*, 17275.

(312) Tan, Y. H.; Liu, M.; Nolting, B.; Go, J. G.; Gervay-Hague, J.; Liu, G. Y. A nanoengineering approach for iInvestigation and regulation of protein immobilization. *ACS Nano* **2008**, *2*, 2374.

(313) Ngunjiri, J.; Garno, J. C. In *Nanodevices for the Life Sciences* Kumar, C. S. S. R., Ed.; Wiley-VCH: 2006.

(314) Blattler, T.; Huwiler, C.; Ochsner, M.; Stadler, B.; Solak, H.; Voros, J.; Grandin, H. M. Nanopatterns with biological functions. *J. Nanosci. Technol.* **2006**, *6*, 2237.

(315) Bruckbauer, A.; Zhou, D. J.; Kang, D. J.; Korchev, Y. E.; Abell, C.; Klenerman, D. An addressable antibody nanoarray produced on a nanostructured surface. *J. Am. Chem. Soc.* **2004**, *126*, 6508.

(316) Castronovo, M.; Radovic, S.; Grunwald, C.; Casalis, L.; Morgante, M.; Scoles, G. Control of steric hindrance on restriction enzyme reactions with surface-bound DNA nanostructures. *Nano Lett.* **2008**, *8*, 4140.

(317) Mirmomtaz, E.; Castronovo, M.; Grunwald, C.; Bano, F.; Scaini, D.; Ensafi, A. A.; Scoles, G.; Casalis, L. Quantitative study of the effect of coverage on the hybridization efficiency of surface-bound DNA nanostructures. *Nano Lett.* **2008**, *8*, 4134.

(318) Schwartz, P. V. Meniscus force nanografting: Nanoscopic patterning of DNA. *Langmuir* **2001**, *17*, 5971.

(319) Tulpar, A.; Wang, Z. Y.; Jang, C. H.; Jain, V.; Heflin, J. R.; Ducker, W. A. Nanoscale patterning of ionic self-assembled multilayers. *Nanotechnology* **2009**, *20*.

(320) Greenberg, A. Integrating nanoscience into the classroom: Perspectives on nanoscience education projects. *Acs Nano* **2009**, *3*, 762.

(321) *Converging technologies for improving human performance: Nanotechnology, biotechnology, information technology and cognitive science.* ; Roco, M. C.; Bainbridge, W. S., Eds.; Kluwer Academic Publishers(Springer) Boston, 2003.

(322) Drain, C. M.; Varotto, A.; Radivojevic, I. Self-Organized Porphyrinic Materials. *Chem. Rev.* **2009**, *109*, 1630.

(323) Jiao, J.; Anariba, F.; Tiznado, H.; Schmidt, I.; Lindsey, J. S.; Zaera, F.; Bocian, D. F. Stepwise formation and characterization of covalently linked multiporphyrin-imide architectures on Si(100). *J. Am. Chem. Soc.* **2006**, *128*, 6965.

(324) Liu, C. Y.; Pan, H. L.; Fox, M. A.; Bard, A. J. Reversible charge trapping/detrapping in a photoconductive insulator of liquid crystal zinc porphyrin. *Chem. Mater.* **1997**, *9*, 1422.

(325) Murata, K.; Ito, S.; Takahashi, K.; Hoffman, B. M. Photocurrent from photocorrosion of aluminum electrode in porphyrin/Al Schottky-barrier cells. *Appl.Phys. Lett.* **1997**, *71*, 674.

(326) Maree, C. H. M.; Roosendaal, S. J.; Savenije, T. J.; Schropp, R. E. I.; Schaafsma, T. J.; Habraken, F. Photovoltaic effects in porphyrin polymer films and heterojunctions. *Journal of Applied Physics* **1996**, *80*, 3381.

(327) Harima, Y.; Okazaki, H.; Kunugi, Y.; Yamashita, K.; Ishii, H.; Seki, K. Formation of Schottky barriers at interfaces between metals and molecular semiconductors of p- and n-type conductances. *Appl. Phys.Letts.* **1996**, *69*, 1059.

(328) Baldo, M. A.; O'Brien, D. F.; You, Y.; Shoustikov, A.; Sibley, S.; Thompson, M. E.; Forrest, S. R. Highly efficient phosphorescent emission from organic electroluminescent devices. *Nature* **1998**, *395*, 151.

(329) Sendt, K.; Johnston, L. A.; Hough, W. A.; Crossley, M. J.; Hush, N. S.; Reimers, J. R. Switchable electronic coupling in model oligoporphyrin molecular wires examined through the measurement and assignment of electronic absorption spectra. *J. Am. Chem. Soc.* **2002**, *124*, 9299.

(330) McCreery, R. L.; Viswanathan, U.; Kalakodimi, R. P.; Nowak, A. M. Carbon/molecule/metal molecular electronic junctions: the importance of "contacts". *Faraday Discussions* **2006**, *131*, 33.

(331) Gardner, T. J.; Frisbie, C. D.; Wrighton, M. S. Systems for Orthogonal Self-Assembly of Electroactive Monolayers on Au and Ito - an Approach to Molecular Electronics. *J. Am. Chem. Soc.* **1995**, *117*, 6927.

(332) Auwarter, W.; Weber-Bargioni, A.; Riemann, A.; Schiffrin, A.; Groning, O.; Fasel, R.; Barth, J. V. Self-assembly and conformation of tetrapyridyl-porphyrin molecules on Ag(111). *J. Chem.Phys.* **2006**, *124*.

(333) Ogaki, K.; Batina, N.; Kunitake, M.; Itaya, K. In situ scanning tunneling microscopy of ordering processes of adsorbed porphyrin on iodine-modified Ag(111). *J. Phys. Chem.* **1996**, *100*, 7185.

(334) Jung, T. A.; Schlittler, R. R.; Gimzewski, J. K.; Tang, H.; Joachim, C. Controlled room-temperature positioning of individual molecules: Molecular flexure and motion. *Science* **1996**, *271*, 181.

(335) Guo, X. L.; Dong, Z. C.; Trifonov, A. S.; Miki, K.; Kimura, K.; Mashiko, S. STM-induced light emission from the surface of H2TBP porphyrin/PFP porphyrin/Cu(100). *Appl. Surf.Sci.* **2005**, *241*, 28.

(336) Scudiero, L.; Barlow, D. E.; Hipps, K. W. Physical properties and metal ion specific scanning tunneling microscopy images of metal(II) tetraphenylporphyrins deposited from vapor onto gold (111). *J. Phys. Chem.B* **2000**, *104*, 11899.

(337) Yoshimoto, S.; Yokoo, N.; Fukuda, T.; Kobayashi, N.; Itaya, K. Formation of highly ordered porphyrin adlayers induced by electrochemical potential modulation. *Chem. Commun.* **2006**, 500.

(338) Wan, L. J.; Shundo, S.; Inukai, J.; Itaya, K. Ordered adlayers of organic molecules on sulfur-modified Au(111): In situ scanning tunneling microscopy study. *Langmuir* **2000**, *16*, 2164.

(339) Xu, S.; Laibinis, P. E.; Liu, G. Y. Accelerating the kinetics of thiol self-assembly on gold - A spatial confinement effect. *J. Am. Chem. Soc.* **1998**, *120*, 9356.

(340) Bai, Y.; Buchner, F.; Kellner, I.; Schmid, M.; Vollnhals, F.; Steinruck, H. P.; Marbach, H.; Gottfried, J. M. Adsorption of cobalt (II) octaethylporphyrin and 2H-octaethylporphyrin on Ag(111): new insight into the surface coordinative bond. *New J. Phys.* **2009**, *11*, 15.

(341) Yang, Z. Y.; Durkan, C. Edge and terrace structure of CoTPP on Au(111) investigated by ultra-high vacuum scanning tunnelling microscopy at room temperature. *Surf. Sci.*, *604*, 660.

(342) Tanaka, H.; Ikeda, T.; Yamashita, K.; Takeuchi, M.; Shinkai, S.; Kawai, T. Network of Tris(porphyrinato)cerium(III) Arranged on the Herringbone Structure of an Au(111) Surface. *Langmuir*, *26*, 210.

(343) Yoshimoto, S.; Higa, N.; Itaya, K. Two-dimensional supramolecular organization of copper octaethylporphyrin and cobalt phthalocyanine on Au(III): Molecular assembly control at an electrochemical interface. *J. Am. Chem. Soc.* **2004**, *126*, 8540.

(344) Aratani, N.; Takagi, A.; Yanagawa, Y.; Matsumoto, T.; Kawai, T.; Yoon, Z. S.; Kim, D.; Osuka, A. Giant meso-meso-linked porphyrin arrays of micrometer molecular length and their fabrication. *Chem. -Eur. J.* **2005**, *11*, 3389.

(345) Otsuki, J.; Namiki, K.; Arai, Y.; Amano, M.; Sawai, H.; Tsukamoto, A.; Hagiwara, T. Face-on and Columnar Porphyrin Assemblies at Solid/Liquid Interface on HOPG. *Chem. Lett.* **2009**, *38*, 570.

(346) Smith, A. R. G.; Ruggles, J. L.; Yu, A. M.; Gentle, I. R. Multilayer Nanostructured Porphyrin Arrays Constructed by Layer-by-Layer Self-Assembly. *Langmuir* **2009**, *25*, 9873.

(347) Zanoni, R.; Aurora, A.; Cattaruzza, F.; Decker, F.; Fastiggi, P.; Menichetti, V.; Tagliatesta, P.; Capodilupo, A. L.; Lembo, A. Metalloporphyrins as molecular precursors of electroactive hybrids: A characterization of their actual electronic states on Si(100) and (111) by AFM and XPS. *MAT SCI ENG C-BIO S* **2007**, *27*, 1351.

(348) Maree, C. H. M.; Roosendaal, S. J.; Savenije, T. J.; Schropp, R. E. I.; Schaafsma, T. J.; Habraken, F. Photovoltaic effects in porphyrin polymer films and heterojunctions. *J. Appl. Phys.* **1996**, *80*, 3381.

(349) Qiu, X. H.; Wang, C.; Zeng, Q. D.; Xu, B.; Yin, S. X.; Wang, H. N.; Xu, S. D.; Bai, C. L. Alkane-assisted adsorption and assembly of phthalocyanines and porphyrins. *J. Am. Chem. Soc.* **2000**, *122*, 5550.

(350) Kang, B. K.; Aratani, N.; Lim, J. K.; Kim, D.; Osuka, A.; Yoo, K.-H. Electrical transport properties and their reproducibility for linear porphyrin arrays. *Mater. Sci. Eng., C* **2006**, *26*, 1023.

(351) Mizuseki, H.; Belosludov, R. V.; Farajian, A. A.; Igarashi, N.; Kawazoe, Y. Theoretical study on junctions in porphyrin oligomers for nanoscale devices. *Mater. Sci. Eng., C* **2005**, *25*, 718.

(352) Zanoni, R.; Aurora, A.; Cattaruzza, F.; Decker, F.; Fastiggi, P.; Menichetti, V.; Tagliatesta, P.; Capodilupo, A.-L.; Lembo, A. Metalloporphyrins as molecular precursors of electroactive hybrids: A characterization of their actual electronic states on Si(100) and (111) by AFM and XPS. *Mater. Sci. Eng., C* **2006**, *27*, 1351.

(353) Jiao, J.; Anariba, F.; Tiznado, H.; Schmidt, I.; Lindsey, J. S.; Zaera, F.; Bocian, D. F. Stepwise formation and characterization of covalently linked multiporphyrin-imide architectures on Si(100). *J. Am. Chem. Soc.* **2006**, *128*, 6965.

(354) Koo, J.-R.; Lee, H.-S.; Ha, Y.; Choi, Y.-H.; Kim, Y. K. Electrical properties of porphyrin-based switching devices. *Thin Solid Films* **2003**, *438-439*, 123.

(355) Umar, A. A. S., M.M.; Yahaya, M. Self-assembled monolayers of copper(II)meso-tetra(4-sulfanatophenyl) porphyrin as an optical gas sensor. *Sensors and Actuators B* **2004**, *101*, 231.

(356) Pierre Montméat, S. M., Eric Pasquinet, Lionel Hairault, Claude P. Gros, Jean-Michel Barbe, and; Guilard, R. Metalloporphyrins as sensing material for quartz–crystal microbalance nitroaromatics sensors. *IEEE SENSORS JOURNAL* **2005**, 1.

(357) Wiyaratn, W.; Hrapovic, S.; Liu, Y. L.; Surareungchai, W.; Luong, J. H. T. Light-assisted synthesis of Pt-Zn porphyrin nanocomposites and their use for electrochemical detection of organohalides. *Anal. Chem.* **2005**, *77*, 5742.

(358) Koepf, M.; Trabolsi, A.; Elhabiri, M.; Wytko, J. A.; Paul, D.; Albrecht-Gary, A. M.; Weiss, J. Building blocks for self-assembled porphyrinic photonic wires. *Org. Lett.* **2005**, *7*, 1279.

(359) Hasobe, T.; Kamat, P. V.; Troiani, V.; Solladie, N.; Ahn, T. K.; Kim, S. K.; Kim, D.; Kongkanand, A.; Kuwabata, S.; Fukuzumi, S. Enhancement of light-energy conversion efficiency by multi-porphyrin arrays of porphyrin-peptide oligomers with fullerene clusters. *J. Phys. Chem. B* **2005**, *109*, 19.

(360) Herrera, F. V.; Grez, P.; Schrebler, R.; Ballesteros, L. A.; Munoz, E.; Cordova, R.; Altamirano, H.; Dalchiele, E. A. Preparation and Photoelectrochemical Characterization of Porphyrin-Sensitized alpha-Fe2O3 Thin Films. *J. Electrochem.Soc.*, *157*, D302.

(361) Imahori, H.; Norieda, H.; Yamada, H.; Nishimura, Y.; Yamazaki, I.; Sakata, Y.; Fukuzumi, S. Light-harvesting and photocurrent generation by cold electrodes modified with

mixed self-assembled monolayers of boron-dipyrrin and ferrocene-porphyrin-fullerene triad. *J. Am. Chem. Soc.* **2001**, *123*, 100.

(362) Tour, J. M. Molecular electronics. Synthesis and testing of components. *Acc.Chem. Res.* **2000**, *33*, 791.

(363) Bain, C. D.; Troughton, E. B.; Tao, Y. T.; Evall, J.; Whitesides, G. M.; Nuzzo, R. G. Formation of monolayer films by the spontaneous assembly of organic thiols from solution onto gold. *J. Am. Chem. Soc.* **1989**, *111*, 321.

(364) Fenter, P.; Eberhardt, A.; Eisenberger, P. Self-assembly of n-alkyl thiols as disulfides on Au(111). *Science* **1994**, *266*, 1216.

(365) Barrena, E.; Palacios-Lidon, E.; Munuera, C.; Torrelles, X.; Ferrer, S.; Jonas, U.; Salmeron, M.; Ocal, C. The role of intermolecular and molecule-substrate interactions in the stability of alkanethiol nonsaturated phases on Au(111). *J. Am. Chem. Soc.* **2004**, *126*, 385.

(366) Xiao, X. D.; Liu, G.-Y.; Charych, D. H.; Salmeron, M. Preparation, structure and mechanical stability of alkylsilane monolayers on mica. *Langmuir*, *11*, 1600.

(367) Ulman, A. Formation and structure of self-assembled monolayers. *Chem. Rev.* **1996**, *96*, 1533.

(368) Garno, J. C.; Xu, C.; Bazzan, G.; Batteas, J. D.; Drain, C. M. In *Metal-Containing and Metallosupramolecular Polymers and Materials, ACS Symposium Series 928*; Schubert, U. S. N., G. R.; Manners, I. , Ed.; Oxford University Press: Oxford, 2006.

(369) Drain, C. M.; Milic, T.; Garno, J.; Smeureanu, G.; Batteas, J. D. Organizing self-assembled porphyrin arrays on metal and glass surfaces. *Polymer Preprints* **2004**, *45*, 346.

(370) George, H.; Palmer, R. E.; Guo, Q.; Bampos, N.; Sanders, J. K. M. Needles and clusters of zinc porphyrin molecules on mica. *Surf. Sci.* **2006**, *600*, 3274.

(371) Di Natale, C.; Macagnano, A.; Repole, G.; Saggio, G.; D' Amico, A.; Paolesse, R.; Boschi, T. The exploitation of metalloporphyrins as chemically interactive material in chemical sensors. *Mater. Sci. Eng., C* **1998**, *5*, 209.

(372) Snitka, V.; Rackaitis, M.; Rodaite, R. Assemblies of TPPS4 porphyrin investigated by TEM, SPM and UV-vis spectroscopy. *Sensors and Actuators B-Chemical* **2005**, *109*, 159.

(373) Kiba, T.; Suzuki, H.; Hosokawa, K.; Kobayashi, H.; Baba, S.; Kakuchi, T.; Sato, S. Supramolecular J-Aggregate Assembly of a Covalently Linked Zinc Porphyrin-beta-cyclodextrin Conjugate in a Water/Ethanol Binary Mixture. *J. Phys. Chem. B* **2009**, *113*, 11560.

(374) Jourdan, J. S.; Cruchon-Dupeyrat, S. J.; Huan, Y.; Kuo, P. K.; Liu, G. Y. Imaging nanoscopic elasticity of thin film materials by atomic force microscopy: Effects of force modulation frequency and amplitude. *Langmuir* **1999**, *15*, 6495.

(375) Cappella, B.; Sturm, H.; Weidner, S. M. Breaking polymer chains by dynamic plowing lithography. *Polymer* **2002**, *43*, 4461.

(376) Cappella, B.; Sturm, H. Comparison between dynamic plowing lithography and nanoindentation methods. *J. Appl. Phys.* **2002**, *91*, 506.

(377) Zhou, D. J.; Sinniah, K.; Abell, C.; Rayment, T. Use of atomic force microscopy for making addresses in DNA coatings. *Langmuir* **2002**, *18*, 8278.

(378) Zhou, D.; Bruckbauer, A.; Ying, L. M.; Abell, C.; Klenerman, D. Building three-dimensional surface biological assemblies on the nanometer scale. *Nano Lett.* **2003**, *3*, 1517.

(379) Moore, L.; LeJeune, Z. M.; Luces, C. A.; Gates, A. T.; Li, M.; El-Zahab, B.; Garno, J. C.; Warner, I. M. Lysine-based zwitterionic molecular micelle for simultaneous separation of acidic and basic proteins using open tubular capillary electrochromatography. *Anal. Chem.* **2010**, *82*, 3997.

(380) Yu, J. H.; Ngunjiri, J. N.; Kelley, A. T.; Gano, J. C. Nanografting versus solution self-assembly of alpha,omega-alkanedithiols on Au(111) investigated by AFM. *Langmuir* **2008**, *24*, 11661.

(381) Staii, C.; Wood, D. W.; Scoles, G. Ligand-induced structural changes in maltose binding proteins measured by atomic force microscopy. *Nano Lett.* **2008**, *8*, 2503.

(382) Josephs, E. A.; Ye, T. Nanoscale positioning of individual DNA molecules by an atomic force microscope. *J. Am. Chem. Soc.* **2010**, *132*, 10236.

(383) Fleischer, E. B.; Shachter, A. M. Coordination Oligomers and a Coordination Polymer of Zinc Tetraarylporphyrins. *Inorg. Chem.* **1991**, *30*, 3763.

(384) Zimmerman, S. C.; Zharov, I.; Wendland, M. S.; Rakow, N. A.; Suslick, K. S. Molecular Imprinting Inside Dendrimers. *J. Am. Chem. Soc.* **2003**, *125*, 13504.

(385) Alessio, E.; Macchi, M.; Heath, S. L.; Marzilli, L. G. Ordered Supramolecular Porphyrin Arrays from a Building Block Approach Utilizing Pyridylporphyrins and Peripheral Ruthenium Complexes and Identification of a New Type of Mixed-Metal Building Block. *Inorg. Chem.* **1997**, *36*, 5614.

(386) Adler, A. D.; Longo, F. R.; Finarelli, J. D.; Goldmacher, J.; Assour, J.; Korsakoff, L. A Simplified Synthesis for meso-Tetraphenylporphin. *J. Org. Chem.* **1967**, *32*, 476.

(387) Klapetek, P. N.; Czech Metrology Institute: Czech Republic, 2007.

(388) Milic, T.; Chi, N.; Yablon, D. G.; Flynn, G. W.; Batteas, J. D.; Drain, C. M. Controlled Hierarchical Self-Assembly and Deposition of Nanoscale Photonic Materails. *Angew. Chem. Int. Ed.* **2002**, *41*, 3.

(389) Mills, G.; Gordon, M. S.; Metiu, H. Oxygen adsorption on Au clusters and a rough Au(111) surface: The role of surface flatness, electron confinement, excess electrons, and band gap. *J. Chem.Phys.* **2003**, *118*, 4198.

(390) Liu, Z. P.; Hu, P.; Alavi, A. Catalytic role of gold in gold-based catalysts: A density functional theory study on the CO oxidation on gold. *J. Am. Chem. Soc.* **2002**, *124*, 14770.

(391) Mohr, C.; Hofmeister, H.; Radnik, J.; Claus, P. Identification of active sites in gold-catalyzed hydrogenation of acrolein. *J. Am. Chem. Soc.* **2003**, *125*, 1905.

(392) Tanaka, S.; Suzuki, H.; Kamikado, T.; Mashiko, S. Conformational study of porphyrin-based molecules using non-contact atomic force microscopy. *Nanotechnology* **2004**, *15*, S87.

(393) Yang, G.; Amro, N. A.; Starkewolfe, Z. B.; Liu, G.-Y. Molecular-Level Approach To Inhibit Degradations of Alkanethiol Self-Assembled Monolayers in Aqueous Media. *Langmuir* **2004**, *20*, 3995.

(394) DuBose, D. L.; Robinson, R. E.; Holovics, T. C.; Moody, D. R.; Weintrob, E. C.; Berrie, C. L.; Barybin, M. V. Interaction of Mono- and Diisocyanoazulenes with Gold Surfaces: First Examples of Self-Assembled Monolayer Films Involving Azulenic Scaffolds. *Lang.* **2006**, *22*, 4599.

(395) Xu, S.; Laibinis, P. E.; Liu, G.-Y. Accelerating the kinetics of thiol self-assembly on gold - a spatial confinement effect. *J. Am. Chem. Soc.* **1998**, *120*, 9356.

(396) Ryu, S.; Schatz, G. Nanografting: modeling and simulation. *J. Am. Chem. Soc.* **2006**, *128*, 11563.

(397) Car, R.; Parrinello, M. Unified Approach For Molecular Dynamics and Density Functional Theory. *Phys. Rev. Lett.* **1985**, *55*, 2471.

(398) Vanderbilt, D. Soft Self-Consistent Pseudopotentials in a Generalized Eigenvalue Formalism. *Phys. Rev. B* **1990**, *41*, 7892.

(399) Reed, C. A. Carboranes: A New Class of Weakly Coordinating Anions for Strong Electrophiles, Oxidants, and Superacids. *Acc. Chem. Res.* **1998**, *31*, 133.

(400) Plesek, J. *Chem. Rev.* **1992**, *92*, 269.

(401) Hawthorne, M. F.; Young, D. C.; Andrews, T. D.; Howe, D. V.; Pilling, R. L.; Pitts, A. D.; Reintjes, M.; Warren, L. F.; Wegner, P. A. .pi.-Dicarbollyl derivatives of the transition metals. Metallocene analogs. *J. Am. Chem. Soc.* **1968**, *90*, 879.

(402) Hawthorne, M. F.; Young, D. C.; Wegner, P. A. *J. Am. Chem. Soc.* **1970**, *87*, 1818.

(403) Gruner, B.; Plesek, J.; Baca, J.; Cisarova, I.; Dozol, J. F.; Rouquette, H.; Vinas, C.; Selucky, P.; Rais, J. Cobalt bis(dicarbollide) ions with covalently bonded CMPO groups as

selective extraction agents for lanthanide and actinide cations from highly acidic nuclear waste solutions. *New J. Chem.* **2002**, *26*, 1519.

(404) Stoica, A.-I.; Vinas, C.; Teixidor, F. 2009, p 4988.

(405) Rojo, I.; Teixidor, F.; Vinas, C.; Kivekas, R.; Sillanpaa, R. Relevance of the electronegativity of boron in eta(5)-coordinating ligands: Regioselective monoalkylation and monoarylation in cobaltabisdicarbollide [3,3 '-Co(1,2-C2B9H11)(2)](-) clusters. *Chem.-Eur. J.* **2003**, *9*, 4311.

(406) Hao, E. H.; Jensen, T. J.; Courtney, B. H.; Vicente, M. G. H. Synthesis and cellular studies of porphyrin-cobaltacarborane conjugates. *Bioconjugate Chem.* **2005**, *16*, 1495.

(407) Hao, E.; Zhang, M.; E, W. B.; Kadish, K. M.; Fronczek, F. R.; Courtney, B. H.; Vicente, M. G. H. Synthesis and Spectroelectrochemistry of N-Cobaltacarborane Porphyrin Conjugates. *Bioconjugate Chem.* **2008**, *19*, 2171.

(408) Hawthorne, M. F.; Ramachandran, B. M.; Kennedy, R. D.; Knobler, C. B. Approaches to rotary molecular motors. *Pure Appl. Chem.* **2006**, *78*, 1299.

(409) Hawthorne, M. F.; Zink, J. I.; Skelton, J. M.; Bayer, M. J.; Liu, C.; Livshits, E.; Baer, R.; Neuhauser, D. Electrical or photocontrol of the rotary motion of a metallacarborane. *Science* **2004**, *303*, 1849.

(410) Barth, R. F.; Coderre, J. A.; Vicente, M. G. H.; Blue, T. E. Boron neutron capture therapy of cancer: Current status and future prospects. *Clin. Cancer Res.* **2005**, *11*, 3987.

(411) Hawthorne, M. F.; Maderna, A. Applications of Radiolabeled Boron Clusters to the Diagnosis and Treatment of Cancer. *Chem. Rev.* **1999**, *99*, 3421.

(412) Soloway, A. H.; Tjarks, W.; Barnum, B. A.; Rong, F.-G.; Barth, R. F.; Codogni, I. M.; Wilson, J. G. The Chemistry of Neutron Capture Therapy. *Chem. Rev.* **1998**, *98*, 1515.

(413) Kaszynski, P.; Douglass, A. G. Organic derivatives of closo-boranes: a new class of liquid crystal materials. *J. Organomet. Chem.* **1999**, *581*, 28.

(414) Kottas, G. S.; Clarke, L. I.; Horinek, D.; Michl, J. Artificial Molecular Rotors. *Chem. Rev.* **2005**, *105*, 1281.

(415) Bekasova, N. I. Latest Advances in the Field of Carbaborane-containing Polymers. *Russ. Chem. Rev.* **1984**, *53*, 61.

(416) Kimura, H.; Okita, K.; Ichitani, M.; Sugimoto, T.; Kuroki, S.; Ando, I. Structural Study of Silylâˆ’Carborane Hybrid Diethynylbenzeneâˆ’Silylene Polymers by High-Resolution Solid-State 11B, 13C, and 29Si NMR Spectroscopy. *Chem. Mater.* **2002**, *15*, 355.

(417) Fox, M. A.; Wade, K. Model compounds and monomers for phenylene ether carboranylene ketone (PECK) polymer synthesis: preparation and characterization of boron-arylated ortho-carboranes bearing carboxyphenyl, phenoxyphenyl or benzoylphenyl substituents. *J. Mater. Chem.* **2002**, *12*, 1301.

(418) Colquhoun, H. M.; Herbertson, P. L.; Wade, K.; Baxter, I.; Williams, D. J. A Carborane-Based Analogue of Poly(p-phenylene). *Macromolecules* **1998**, *31*, 1694.

(419) Schoberl, U.; Magnera, T. F.; Harrison, R. M.; Fleischer, F.; Pflug, J. L.; Schwab, P. F. H.; Meng, X.; Lipiak, D.; Noll, B. C.; Allured, V. S.; Rudalevige, T.; Lee, S.; Michl, J. Toward a Hexagonal Grid Polymer: Synthesis, Coupling, and Chemically Reversible Surface-Pinning of the Star Connectors, 1,3,5-C6H3(CB10H10CX)3. *J. Am. Chem. Soc.* **1997**, *119*, 3907.

(420) Kabachii, Y. A.; Valetskii, P. M. Structural-Chemical Conception of Stabilization of Aromatic Polymers as Exemplified by Arylene Carboranes. *Int. J. Polym. Mater.* **1990**, *14*, 263.

(421) Masalles, C.; Borros, S.; Vinas, C.; Teixidor, F. Are low-coordinating anions of interest as doping agents in organic conducting polymers? *Adv. Mater.* **2000**, *12*, 1199.

(422) David, V.; Vinas, C.; Teixidor, F. Poly(3,4-ethylenedioxythiophene) doped with a non-extrudable metallacarborane anion electroactive during synthesis. *Polymer* **2006**, *47*, 4694.

(423) Masalles, C.; Llop, J.; Vinas, C.; Teixidor, F. Extraordinary overoxidation resistance increase in self-doped polypyrroles by using non-conventional low charge-density anions. *Adv. Mater.* **2002**, *14*, 826.

(424) Masalles, C.; Teixidor, F.; Borros, S.; Vinas, C. Cobaltabisdicarbollide anion [CO(C2B9H11)(2)](-) as doping agent on intelligent membranes for ion capture. *J. Organomet. Chem.* **2002**, *657*, 239.

(425) Fabre, B.; Clark, J. C.; Vicente, M. G. H. Synthesis and electrochemistry of carboranylpyrroles. Toward the preparation of electrochemically and thermally resistant conjugated polymers. *Macromolecules* **2006**, *39*, 112.

(426) BarrieÌ€re, F. d. r.; Fabre, B.; Hao, E.; LeJeune, Z. M.; Hwang, E.; Garno, J. C.; Nesterov, E. E.; Vicente, M. G. a. H. Electropolymerizable 2,2â€²-Carboranyldithiophenes. Structureâˆ’Property Investigations of the Corresponding Conducting Polymer Films by Electrochemistry, UVâˆ’Visible Spectroscopy and Conducting Probe Atomic Force Microscopy. *Macromolecules* **2009**, *42*, 2981.

(427) Fabre, B.; Chayer, S.; Vicente, M. G. H. First conducting polymer functionalized with covalently linked carborane units. *Electrochem. Commun.* **2003**, *5*, 431.

(428) Hao, E.; Fabre, B.; Fronczek, F. R.; Vicente, M. G. H. Poly[di(2-thiophenyl) carborane]s: conducting polymers with high electrochemical and thermal resistance. *Chem. Commun.* **2007**, 4387.

(429) Hao, E.; Fabre, B.; Fronczek, F. R.; Vicente, M. G. a. H. Syntheses and Electropolymerization of Carboranyl-Functionalized Pyrroles and Thiophenes. *Chem. Mater.* **2007**, *19*, 6195.

(430) Kokado, K.; Tokoro, Y.; Chujo, Y. Luminescent m-Carborane-Based Ï€-Conjugated Polymer. *Macromolecules* **2009**, *42*, 2925.

(431) Peterson, J. J.; Simon, Y. C.; Coughlin, E. B.; Carter, K. R. Polyfluorene with p-carborane in the backbone. *Chem. Commun.* **2009**, 4950.

(432) Holliday, B. J.; Swager, T. M. Conducting metallopolymers: the roles of molecular architecture and redox matching. *Chem. Commun.* **2005**, 23.

(433) *Density-Functional Theory of Atoms and Molecules*; Parr, R. G.; Yang, W. T., Eds.; Oxford University Press: Oxford, UK., 1989.

(434) Hohenberg, P.; Kohn, W. Inhomogeneous Electron Gas. *Phys. Rev. B* **1964**, *136*, B864.

(435) Becke, A. D. Density-Functional Thermochemistry .3. the Role of Exact Exchange. *J. Chem. Phys.* **1993**, *98*, 5648.

(436) Becke, A. D. A New Mixing of Hartree-Fock and Local Density-Functional Theories. *J. Chem. Phys.* **1993**, *98*, 1372.

(437) Becke, A. D. Density-Functional Exchange-Energy Approximation with Correct Asymptotic-Behavior. *Phys. Rev. A* **1988**, *38*, 3098.

(438) Lee, C. T.; Yang, W. T.; Parr, R. G. Development of the Colle-Salvetti Correlation-Energy Formula into a Functional of the Electron-Density. *Phys. Rev. B.* **1988**, *37*, 785.

(439) Frisch, M. J.; Trucks, G. W.; Schlegel, H. B.; Scuseria, G. E.; Robb, M. A.; Cheeseman, J. R.; Montgomery, J.; J. A., V., T.; Kudin, K. N.; Burant, J. C.; Millam, J. M.; Iyengar, S. S.; Tomasi, J.; Barone, V.; Mennucci, B.; Cossi, M.; Scalmani, G.; Rega, N.; Petersson, G. A.; Nakatsuji, H.; Hada, M.; Ehara, M.; Toyota, K.; Fukuda, R.; Hasegawa, J.; Ishida, M.; Nakajima, T.; Honda, Y.; Kitao, O.; Nakai, H.; Klene, M.; Li, X.; Knox, J. E.; Hratchian, H. P.; Cross, J. B.; Adamo, C.; Jaramillo, J.; Gomperts, R.; Stratmann, R. E.; Yazyev, O.; Austin, A. J.; Cammi, R.; Pomelli, C.; Ochterski, J. W.; Ayala, P. Y.; Morokuma, K.; Voth, G. A.; Salvador, P.; Dannenberg, J. J.; Zakrzewski, V. G.; Dapprich, S.; Daniels, A. D.; Strain, M. C.; Farkas, O.; Malick, D. K.; Rabuck, A. D.; Raghavachari, K.; Foresman, J. B.; Ortiz, J. V.; Cui, Q.; Baboul, A. G.; Clifford, S.; Cioslowski, J.; Stefanov, B. B.; Liu, G.; Liashenko, A.; Piskorz, P.; Komaromi, I.; Martin, R. L.; Fox, D. J.; Keith, T.; Al-Laham, M. A.; Peng, C. Y.; Nanayakkara, A.; Challacombe, M.; Gill, P. M. W.; Johnson, B.; Chen, W.; Wong, M. W.; Gonzalez, C.; Pople, J. A.; Gaussian, Inc.: Pittsburgh, PA, 2003.

(440) Hay, P. J.; Wadt, W. R. Abinitio Effective Core Potentials for Molecular Calculations - Potentials for K to Au Including the Outermost Core Orbitals. *J. Chem. Phys.* **1985**, *82*, 299.

(441) Hay, P. J.; Wadt, W. R. Abinitio Effective Core Potentials for Molecular Calculations - Potentials for the Transition-Metal Atoms Sc to Hg. *J. Chem. Phys.* **1985**, *82*, 270.

(442) Wadt, W. R.; Hay, P. J. Abinitio Effective Core Potentials for Molecular Calculations - Potentials for Main Group Elements Na to Bi. *J. Chem. Phys.* **1985**, *82*, 284.

(443) Flkiger, P.; Lthi, H. P.; Portmann, S.; Weber, J.; Swiss Center for Scientific Computing: Manno, Switzerland, 2000.

(444) *UTHSCSA Image Tool fro windows version 3.00*; Wilcox, D.; Dove, B.; McDavid, D.; Greer, D., Eds.; The University of Texas Health ScienceCenter: San Antonio, Tx., 1995-2002.

(445) Jiang, W.; Knobler, C. B.; Hawthorne, M. F. Synthesis and structural characterization of bis- and tris(closo-1,2-C2B10H11-1-yl)-substitute biphenyl and benzene. *Inorg. Chem.* **1996**, *35*, 3056.

(446) Zhu, Y. B.; Millet, D. B.; Wolf, M. O.; Rettig, S. J. Models for conjugated metal acetylide polymers: Ruthenium oligothienylacetylide complexes. *Organomet.* **1999**, *18*, 1930.

(447) Fox, M. A.; Gill, W. R.; Herbertson, P. L.; MacBride, J. A. H.; Wade, K.; Colquhoun, H. M. Deboronation of C-substituted ortho- and meta-closo-carboranes using "wet" fluoride ion solutions. *Polyhedron* **1996**, *15*, 565.

(448) Endo, Y.; Songkram, C.; Yamasaki, R.; Tanatani, A.; Kagechika, H.; Takaishi, K.; Yamaguchi, K. Molecular construction based on icosahedral carboranes and aromatic N,N '-dimethylurea groups. Aromatic layered molecules and a transition metal complex. *J. Organomet. Chem.* **2002**, *657*, 48.

(449) Rudakov, D. A.; Shirokii, V. L.; Knizhnikov, V. A.; Bazhanov, A. V.; Vecher, E. I.; Maier, N. A.; Potkin, V. I.; Ryabtsev, A. N.; Petrovskii, P. V.; Sivaev, I. B.; Bregadze, V. I.; Eremenko, I. L. Electrochemical synthesis of halogen derivatives of bis(1,2-dicarbollyl)cobalt(III). *Russ. Chem. Bull.* **2004**, *53*, 2554.

(450) Kennedy, R. D.; Knobler, C. B.; Hawthorne, M. F. Toward Unidirectional Rotary Motion in Nickelacarboranes: Characterization of Diastereomeric Nickel Bis(Dicarbollide) Complexes Derived from the [Nido-7-CH3-7,8-C2B9H11]âˆ’ Anion. *Inorg. Chem.* **2009**, *48*, 9377.

(451) Nunez, R.; Tutusaus, O.; Teixidor, F.; Vinas, C.; Sillanpaa, R.; Kivekas, R. Highly stable neutral and positively charged dicarbollide sandwich complexes. *Chem.-Eur. J.* **2005**, *11*, 5637.

(452) Higgins, S. J.; Jones, C. L.; Francis, S. M. Synthesis and electropolymerisation of 1,1 '-bis(5-oligothienyl)ferrocenes: poly(oligothiophene-ferrocene)-modified electrodes. *Synth. Met.* **1999**, *98*, 211.

(453) Zhu, Y.; Wolf, M. O. Electropolymerization of Oligothienylferrocene Complexes: Spectroscopic and Electrochemical Characterization. *Chem. Mater.* **1999**, *11*, 2995.

(454) *Electrochemical Methods: Fundamentals and Applications*; Bard, A. J.; Faulkner, L. R., Eds.; Wiley and Sons: New York, 1980.

(455) Kingsborough, R. P.; Swager, T. M. Electroactivity enhancement by redox matching in cobalt salen-based conducting polymers. *Adv. Mater.* **1998**, *10*, 1100.

(456) Audebert, P.; Capdevielle, P.; Maumy, M. Redox and Conducting Polymers Based on Salen-Type Metal Units - Electrochemical Study and Some Characteristics. *New J. Chem.* **1992**, *16*, 697.

(457) Matel, L.; Macasek, F.; Rajec, P.; Hermanek, S.; Plesek, J. B-Halogen Derivatives of the Bis(1,2-Dicarbollyl)Cobalt(Iii) Anion. *Polyhedron* **1982**, *1*, 511.

(458) Zotti, G.; Schiavon, G. Evolution of Insitu Conductivity of Polythiophene Deposits by Potential Cycling. *Synth. Met.* **1990**, *39*, 183.

(459) Fichou, D.; Horowitz, G.; Garnier, F. Polaron and Bipolaron Formation on Isolated-Model Thiophene Oligomers in Solution. *Synth. Met.* **1990**, *39*, 125.

(460) Havinga, E. E.; Rotte, I.; Meijer, E. W.; Tenhoeve, W.; Wynberg, H. Spectra and Electrical-Properties of Soluble Partially Alkyl-Substituted Oligomers of Thiophene up to 11 Rings. *Synth. Met.* **1991**, *41*, 473.

(461) Chosrovian, H.; Rentsch, S.; Grebner, D.; Dahm, D. U.; Birckner, E.; Naarmann, H. Time-Resolved Fluorescence Studies on Thiophene Oligomers in Solution. *Synth. Met.* **1993**, *60*, 23.

(462) Wallace, G. G.; Spinks, G. M.; Kane-Maguire, L. A. P.; Teasdale, P. R. In *Conductive Electroactive Polymers*; 2nd ed.; CRC Press: Boca Baton, Fl, 2003.

(463) Wu, C.-G.; Chang, S.-S. Nanoscale Measurements of Conducting Domains and Currentâˆ'Voltage Characteristics of Chemically Deposited Polyaniline Films. *J. Phys. Chem. B.* **2004**, *109*, 825.

(464) Lee, H. J.; Park, S.-M. Electrochemistry of Conductive Polymers. 30. Nanoscale Measurements of Doping Distributions and Currentâˆ'Voltage Characteristics of Electrochemically Deposited Polypyrrole Films. *J. Phys. Chem. B.* **2004**, *108*, 1590.

(465) Vidal, P. L.; Divisia-Blohorn, B.; Bidan, G.; Hazemann, J. L.; Kern, J. M.; Sauvage, J. P. pi-conjugated ligand polymers entwined around copper centres. *Chem.-Eur. J.* **2000**, *6*, 1663.

(466) Nishihara, H.; Kurashina, M.; Murata, M. Organometallic conducting polymers synthesized by metallacycling polymerization. *Macromol. Symp.* **2003**, *196*, 27.

(467) Hjelm, J.; Handel, R. W.; Hagfeldt, A.; Constable, E. C.; Housecroft, C. E.; Forster, R. J. Conducting Polymers Containing In-Chain Metal Centers: Homogeneous Charge Transport through a Quaterthienyl-Bridged {Os(tpy)2} Polymer. *J. Phys. Chem. B.* **2003**, *107*, 10431.

(468) Andrieux, C. P.; Saveant, J.-M. In *Molecular Design of Electrode Surfaces*; Murray, R. W., Ed.; Wiley and Sons: New York, 1992; Vol. XXII, p 207.

(469) Tard, C.; Pickett, C. J. Structural and Functional Analogues of the Active Sites of the [Fe]-, [NiFe]-, and [FeFe]-Hydrogenases. *Chem. Rev.* **2009**, *109*, 2245.

(470) Le Goff, A.; Artero, V.; Jousselme, B.; Tran, P. D.; Guillet, N.; Metaye, R.; Fihri, A.; Palacin, S.; Fontecave, M. From Hydrogenases to Noble Metal-Free Catalytic Nanomaterials for H-2 Production and Uptake. *Science* **2009**, *326*, 1384.

(471) Tutusaus, O.; Vinas, C.; Nunez, R.; Teixidor, F.; Demonceau, A.; Delfosse, S.; Noels, A. F.; Mata, I.; Molins, E. The Modulating Possibilities of Dicarbollide Clusters: Optimizing the Kharasch Catalysts. *J. Am. Chem. Soc.* **2003**, *125*, 11830.

APPENDIX A. LABORATORY PROTOCOL FOR PREPARING ORGANOSILANE NANOPORES ON POLISHED SILICA USING PARTICLE LITHOGRAPHY COMBINED WITH TEMPLATE IMMERSION

Cleaning of silica mesoparticle template

1. Standard dry form Angstromsphere silica powder (Fiber Optic Center, New Bedford, MA) need to be redispersed in solution prior to use as templates for particle lithography.
    a. Measure 10 ml of absolute ethanol using a graduated cylinder.
    b. Transfer into a glass bottle with cover.
    c. Add the previously weighed 0.1 g Silica particles. Cover.
    d. Sonicate for 30 min or longer until all the powder is completely redispersed in solution.
2. The first step is not needed if Silica particles are already suspended in solution, e.g. silica spheres from Thermo scientific.
3. Measure 400 uL of silica particles using a micropipette.
4. Transfer into a plastic centrifuge tube.
5. Add deionized water to about 1 mL.
6. Vortex mix for 2 min or until particles are completely suspended in solution.
7. Centrifuge for 10 min at 20000 rpm. Longer time may be needed for smaller particles.
8. Carefully remove the liquid portion with a Pasteur pipette and discard the liquid.
9. Repeat steps 5-8 twice for complete cleaning of the particles.
10. After the third rinse, measure about 200 uL of ethanol using a micropipette.
11. Add the measured ethanol to the solids left in centrifuge tube. This will be the particle template.
12. Vortex mix. Make sure all particles are uniformly dispersed in the solution.

Cleaning Si wafer

It is important that silica substrates must be properly cleaned prior to use. Cleaning with acidic piranha removes any organic residues and facilitates the formation of oxide layer on the surface. Proceed with caution when preparing piranha solution. A solution of piranha is highly energetic and may cause explosion. Use glass, pyrex containers for preparing the solution as piranha will melt plastics. All work must be performed inside the hood and proper protective measures such as gloves and eye goggles must be used. Glasswares must be properly cleaned and dried before use.

1. Cut pieces of silica into 1 x 1 cm^2.
2. Clean silica pieces with copious amount of ethanol. Let dry at ambient.
3. Measure 9 mL of sulfuric acid using graduated cylinder and transfer acid into a clean beaker.
4. Using a pipet, measure 3 mL of 30% hydrogen peroxide.
5. Add the measured amount of hydrogen peroxide to the beaker containing sulfuric acid. REMEMBER: Add slowly to avoid violent reaction.
6. Swirl mixture to mix completely.
7. Heat the solution in a hot water bath, keep the water bath temp at around 70^oC, do not boil the piranha solution.
8. Slowly and individually immerse silica pieces for 30 min. A longer immersion time promotes surface roughening. Make sure silica pieces are separated from each other in the beaker to prevent scratching and for uniform cleaning of substrates.
9. Using a tweezers, remove silica pieces and immediately rinse with copious amount of water.

10. Dry silica using a stream of Argon or Nitrogen gas. Use the substrates immediately. Do not let cleaned silica be exposed to ambient air for a long time since adventitious carbon can immediately deposit on the surface.

Deposition of template particles

1. Measure 20 uL of diluted particle template using a micropipette.
2. Deposit slowly to the center of cleaned silica wafer.
3. Let sample dry in ambient conditions for approximately 2 min.
4. Heat sample in oven for 20 min at 100 ºC.
5. Expose to ambient environment for 20 min. Record the humidity using a humidity meter.

Preparation of alkylsilane solution for immersion

Glasswares used for preparing silane solution need to be completely dried. Even minute amount of water present in the glasswares can make silane polymerized. The polymerized solution appears to have a milky color. The most common solvent used for silane is anhydrous toluene; however, bicyclohexyl also works well.

1. To preserve the integrity of the anhydrous toluene, use a syringe for drawing the solvent out of sure seal bottle by following the outlined steps.
   a. Fill syringe with Nitrogen gas. The volume of the Nitrogen gas should be approximately the same as the needed amount of solvent.
   b. Insert needle into the septum inlet making sure that the needle is above the surface of the liquid.
   c. Push the plunger of syringe to release gas inside the bottle.
2. Using the same syringe, slowly pull back plunger to draw about 5 mL of solvent back into the syringe.

3. Prepare 1 % silane solution in anhydrous toluene (5µl silane/5ml solvent).
4. Swirl the solution slowly to ensure complete mixing.
5. Immerse the template into the silane solution for 8h. Cover.

Rinsing of sample

1. Using tweezers, carefully remove sample from the solution of silane.
2. Individually rinse each sample with copious amount of deionized water, followed by ethanol.
3. Place the sample in a glass bottle with about 10 mL toluene. Do not crowd the bottle with samples to avoid scratches of samples. Cover the bottle.
4. Sonicate for 30 minutes. Do not let the water in the sonicator get hot. Place ice in the sonicator if water gets warm.
5. Rinse with ethanol, followed by toluene.
6. Sonicate again in fresh toluene for another 30 min or until the template is no longer visible.
7. Rinse with ethanol followed with water.
8. Sample should look like very clean silica. If not, continue sonicating in fresh toluene, and followed by sonication in clean ethanol.

APPENDIX B. LABORATORY PROTOCOL FOR PREPARING NANOGLOBULES OF OCTADECYLTRICHLOROSILANE ON POLISHED SILICA USING PARTICLE LITHOGRAPHY COMBINED WITH TEMPLATE IMMERSION

Cleaning of polystyrene latex mesospheres template

1. Measure 400 uL of polystyrene latex spheres using a micropipette.
2. Transfer into a plastic centrifuge tube.
3. Add deionized water to about 1 mL.
4. Mix sample using a vortex mixer for 2 min or until particles are completely suspended in solution.
5. Centrifuge for 15 min at 20000 rpm. Longer centrifugation time may be needed for smaller particles.
6. Carefully remove the liquid portion with a Pasteur pipette and discard the liquid.
7. Repeat steps 3-6 twice for complete cleaning of the particles.
8. After the third rinse, measure about 100 uL of absolute ethanol water using a micropipette.
9. Add the measured absolute ethanol to the solids left in centrifuge tube. This will be the particle template.
10. Vortex mix. Make sure all particles are uniformly dispersed in the solution.

Cleaning Si wafer

Refer to appendix A for preparation of silica substrates

Deposition of template particles

1. Measure 20 uL of diluted particle template using a micropipette.
2. Deposit slowly to the center of cleaned silica wafer.
3. Expose sample in ambient conditions until dry, approximately 2 min.
4. Heat sample in oven for 30 min at 75 ºC.

5. Expose to ambient environment for 30 min. Record the humidity using a humidity meter.

Preparation of alkylsilane solution for immersion

Glasswares used for preparing silane solution need to be completely dried. Even minute amount of water present in the glasswares can make silane polymerized. The polymerized solution appears to have a milky color.

1. Prepare 1 % octadecyltrichlorosilane(OTS) solution in bicyclohexyl (5µl OTS/5ml solvent).
2. Swirl the solution slowly to ensure complete mixing.
3. Immerse the template into the silane solution for 8h. Cover.

Rinsing of sample

Refer to appendix A for rinsing of samples.

APPENDIX C. PROTOCOLS FOR BACKFILLING NANOPORES OF OCTADECYLTRICHLOROSILANE (OTS) FILM WITH CHLOROMETHYLPHENYLTRICHLOROSILANE (CMPS)

1. Clean all glasswares thoroughly.
2. Dry glasswares using a vacuum oven at 120ºC to remove all traces of water.
3. Add 5 μL of Chloromethylphenyltrichlorosilane (CMPS) to 5 mL of anhydrous toluene. Refer to Appendix A. PREPARATION OF ALKYLSILANE SOLUTION FOR IMMERSION for details.
4. Immerse the sample into the CPS solution for desired time (30 min-24 h).
5. After the immersion step, individually rinse the sample with acetone.
6. Sonicate the sample in chloroform for 2 min four times.
7. Dry in Nitrogen or Argon gas.
8. Store in a close container.

APPENDIX D. VACUUM LINE OPERATION

Make sure the oil on the vacuum pump is on appropriate level before usage.

Preparation of sample for vacuum line deposition

1. Place about 20 uL of the sample for deposition on a quartz glass.
2. Let sample dry at ambient conditions.

Vacuum line operation

1. Open all the valves.
2. Purge the whole vacuum line through the gas inlet with nitrogen gas for about 3 min.
3. The valves are numbered and at the start of the operation should be:

    1 open

    2 close

    3 open

    4 close

    5 close
4. Fill Nitrogen dewar with liquid nitrogen slowly until it is three quarters full.
5. Turn on the vacuum pump.
6. Let the pump run for 15 min.
7. Place the substrate for deposition on the metal plate attached to the sample holder.
8. Cover with quartz glass, side with sample film facing the substrate.
9. Move up the substrate holder by turning the knob slowly so that the substrate is very close but not touching the quartz glass.
10. Open vacuum line to the sample by slowly opening valve 4. The whole system should be in vacuum now.

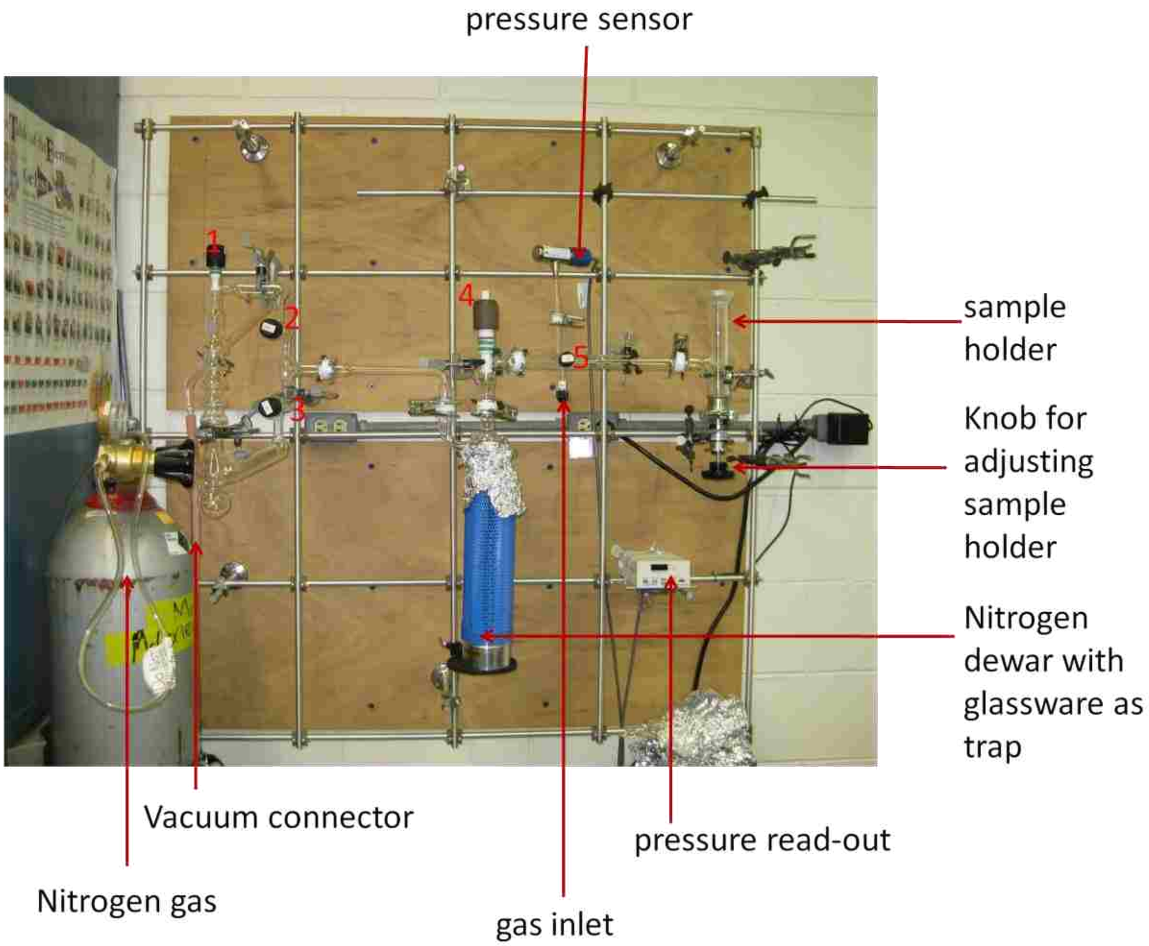

Figure D.1 Vacuum line setup for organic thin film deposition.

11. Turn on the digital pressure read out. Drop in pressure should be observed.
12. Place the UV lamp directly on top of quartz glass. Secure the UV lamp with clamps.
13. Cover the areas of the UV lamp that are not in contact with aluminum foil.
14. Monitor the pressure.
15. Refill liquid nitrogen in the dewar when the liquid level drops.
16. Time required for deposition is dependent on the type of sample.

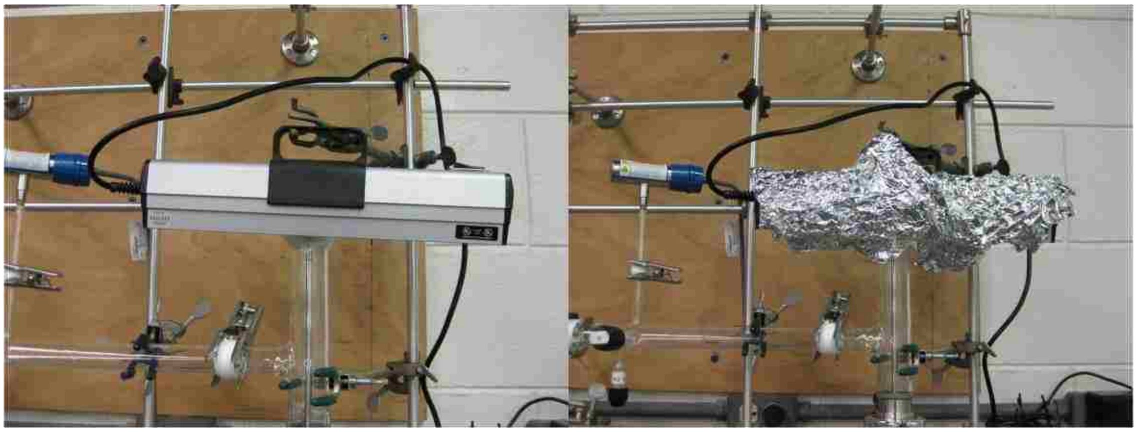

Figure D. 2 UV lamp is placed directly on top of the sample, secured tightly and covered with aluminum foil.

After sample deposition

1. Turn off UV lamp.
2. Remove UV lamp.
3. Open the valve for Nitrogen gas inlet, valve 4.
4. Slowly fill the vacuum line with Nitrogen while supporting the quartz glass. It will pop out if not handled correctly.
5. Turn off vacuum pump.

APPENDIX E: STANADARD OPERATING PROCEDURE FOR CURRENT SENSING AFM

Current sensing AFM(CS-AFM) or Conductive Probe AFM(CP-AFM) is an advance imaging mode which is use to characterize conductive materials on the surface. The probes used for CSAFM must be coated with a thin film of conducting metal; typical coatings are Platinum, Iridium, Gold. The conductivity of the sample as wel as topography and lateral force images are mapped with CSAFM. Consequently, current volatage(IV) plots at a specific location on the sample can be generated with CSAFM. A bias voltage is applied to the sample while the cantilever is kept grounded. A current flow, which is use to map the conductivity of the sample is generated when an applied voltage is applied between thesample and the conductive probe. The CSAFM is operated in contact mode while keeping the force applied to the AFM tip constant.

Figure E.1 Scanner and nose cone assembly for current sensing AFM. The nose cone for current sensing has four pins.

When imaging using CSAFM, surface contamination should be avoided at all times. The presence of water layer on the surface of sample can greatly affect the resolution. It is recommended that CSAFM be performed in a low humidity environment. The environmental chamber should be kept dry at all times and be closed tightly prior to imaging. A petri dish of drierite is recommended to be placed inside the environmental chamber to help remove moisture.

The nose cone for CSAFM must be properly inserted to the Agilent Multipurpose scanner. The nose cone assembly has a pre-amp that is color coded for sensitivity. Verify the color of the wire on the pre-amp prior to imaging. The existing pre-amp for CSAFM nosecone in the laboratory is green which has a sensitivity of 1 nA/V , bandwidth of 6.3 kHz and resistor of 1 GΩ.

1. Insert a conducting AFM tip and focus the laser.
2. Prepare the sample for mounting on the sample plate. A microscope glass must be placed in between the sample plate and the sample. It is important that the sample must be electrically isolated from the sample plate.
3. Attach a copper wire as an electrode connecting the sample and the sample. Insert the copper wire under the spring loaded electrode clip.

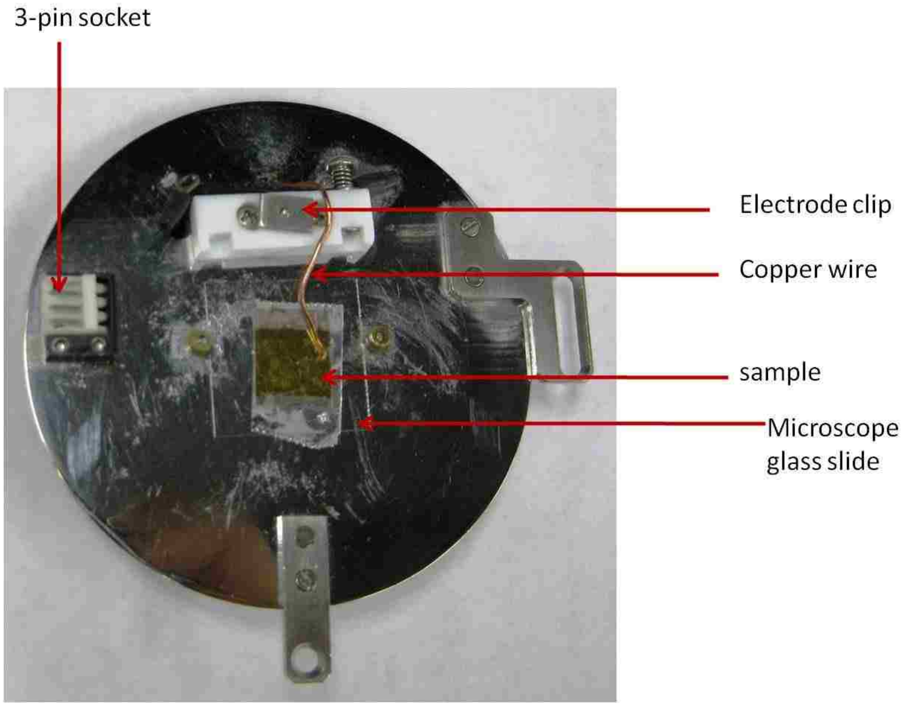

Figure E.2 Sample plate set-up of current sensing AFM.

4. Check that the copper wire touches the sample.
5. Check the continuity of the electrical connection by using a conductivity meter.
6. Plug the 3-pin socket of the sample plate to the 3-pin EC connector of the AC/MAC cable.
7. Mount the sample on the AFM microscope.
8. In the PicoScan, choose mode: CSAFM.
9. In the Buffer assignment window, activate topography, friction, deflection and AUX in BNC. The current channel is displayed in AUX in BNC.

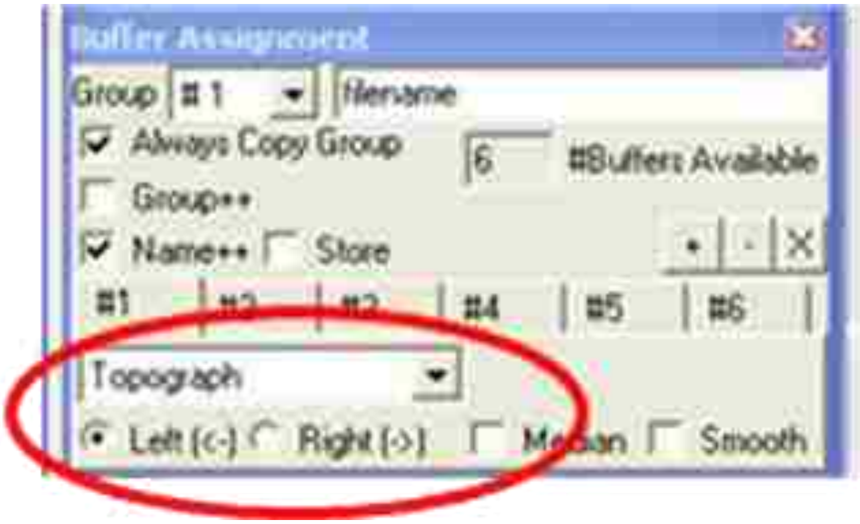

Group #1 filename

☑ Always Copy Group

6 #Buffers Available

☐ Group++

☑ Name++ ☐ Store

Topograph

● Left (<-) ○ Right (->) ☐ Median ☐ Smooth

10. The operation of CSAFM is the same as the contact mode such as setting set point, I/P gains, scan speed in the servo control window.
11. Approach the sample.
12. After approaching, in the servo control AFM window, enter the bias voltage. The The applied bias depends on the conductivity of the sample. (Start with a small voltage first, then increase if no signal is achieved.)
13. The current signal shown in the image channel is a positive which is viewed as high features when a negative bias is applied to the sample.

To acquire current-voltage (I-V) profiles:

1. Pick a certain location in the sample.
2. In the AC Mode Control Window, click sweep.

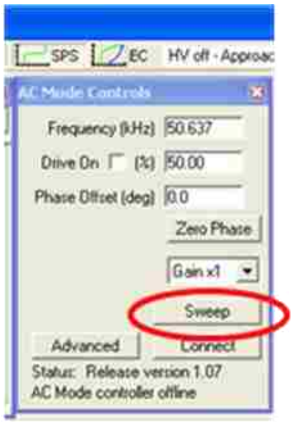

Frequency (kHz) 50.637
Drive On ☐ (%) 50.00
Phase Offset (deg) 0.0
Status: Release version 1.07
AC Mode controller offline

3. The AFM IV Spectroscopy should appear. If not, go to mode, choose AFM IV Spectroscopy.

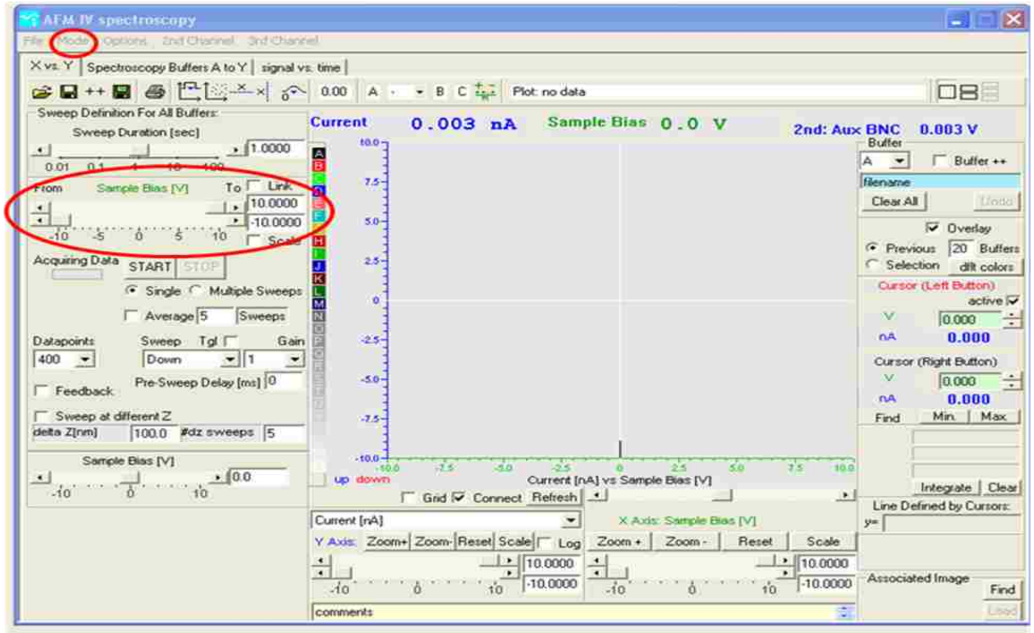

Plot: no data

Sweep Definition For All Buffers
Sweep Duration [sec] 1.0000
From Sample Bias [V] To ☐ Link 10.0000 -10.0000
☐ Scale
Acquiring Data
● Single ○ Multiple Sweeps
☐ Average 5 Sweeps
Datapoints 400
Sweep Down
Tgl ☐
Gain 1
☐ Feedback
Pre-Sweep Delay [ms] 0
☐ Sweep at different Z
delta Z[nm] 100.0 #dz sweeps 5
Sample Bias [V] 0.0

Current 0.003 nA Sample Bias 0.0 V 2nd: Aux BNC 0.003 V

Buffer A ☐ Buffer ++
filename
☑ Overlay
● Previous 20 Buffers
○ Selection dlt colors
Cursor (Left Button) active ☑
V 0.000
nA 0.000
Cursor (Right Button)
V 0.000
nA 0.000
y=

Current [nA]
Y Axis: 10.0000 -10.0000
X Axis: Sample Bias [V] 10.0000 -10.0000
comments

4. Select voltage to use by using the slider.
5. Click START.
6. Save the spectra.

7. Multiple spectra can be acquired at several locations on the sample by following the same steps in acquiring the spectra.

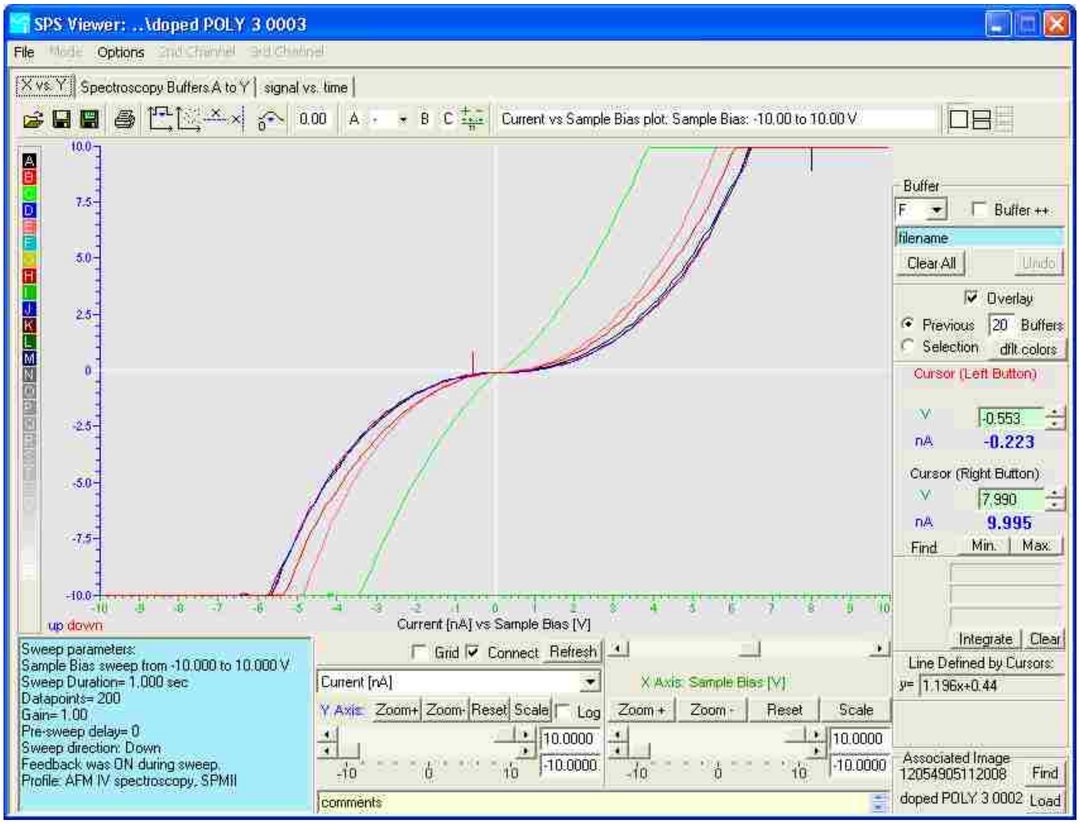
SPS Viewer: ..\doped POLY 3 0003

Current vs Sample Bias plot: Sample Bias: -10.00 to 10.00 V

Sweep parameters:
Sample Bias sweep from -10.000 to 10.000 V
Sweep Duration= 1.000 sec
Datapoints= 200
Gain= 1.00
Pre-sweep delay= 0
Sweep direction: Down
Feedback was ON during sweep.
Profile: AFM IV spectroscopy, SPMII

Buffer: F
☐ Buffer ++
☑ Overlay
● Previous 20 Buffers
○ Selection

Cursor (Left Button)
V -0.553
nA -0.223

Cursor (Right Button)
V 7.990
nA 9.995

Line Defined by Cursors:
y= 1.196x+0.44

Associated Image
12054905112008
doped POLY 3 0002

☐ Grid ☑ Connect
Current [nA]
Y Axis: 10.0000 / -10.0000 ☐ Log
X Axis: Sample Bias [V] 10.0000 / -10.0000

APPENDIX F. PICO PLUS TAPPING MODE OPERATING PROCEDURE

A. Mounting the sample and AFM tip.

1. Mount the sample on the Pico Plus sample holder.
2. Inspect that the right nose cone for tapping mode is inserted in the scanner.

   The oscillation of the cantilever is driven by the piezo-electric transducer in the nosecone.

   The nosecone assembly has two contact pins for the signal to be routed to the transducer.

Figure F.1 Nose cone assembly for tapping mode AFM.

3. Insert nosecone assembly to the scanner using a nose cone removal tool. Do not use a tweezer to prevent damage to the nose cone.
4. Insert a tapping mode tip on the tip holder.
5. Load the scanner in the system.
6. Load the sample plate.
7. Adjust its distance by pressing open and close in the black head electronics box. Close brings the sample closer to the scanner.

Figure F. 2 Head electronics box.

6. Make sure that the laser is on by turning the **On** button on the laser box controller.

7. On the desktop, open **UltraTV** so you can view the AFM tip.

8. Focus the laser on the tip of the AFM probe.

9. Adjust the Deflection and LFM so that both values are ‘0’.

B. AC Mode Software Controls

1. Open the Picoplus software in the desktop by clicking the PicoScan icon.

2. Under the **Mode** on the main menu, select AC AFM.

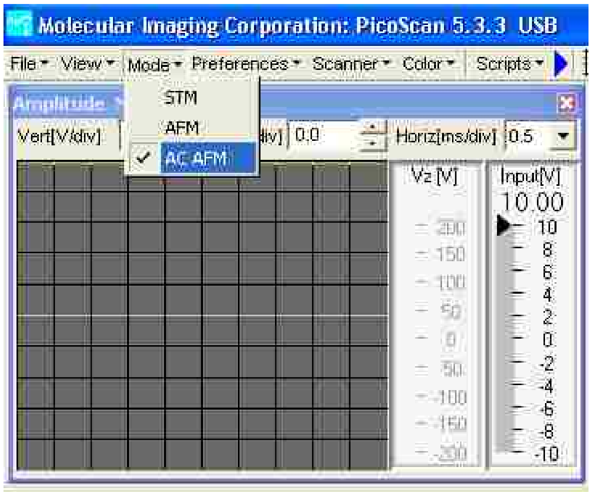

3. Under the **View** on the main menu, select **AC Mode Controls**, then

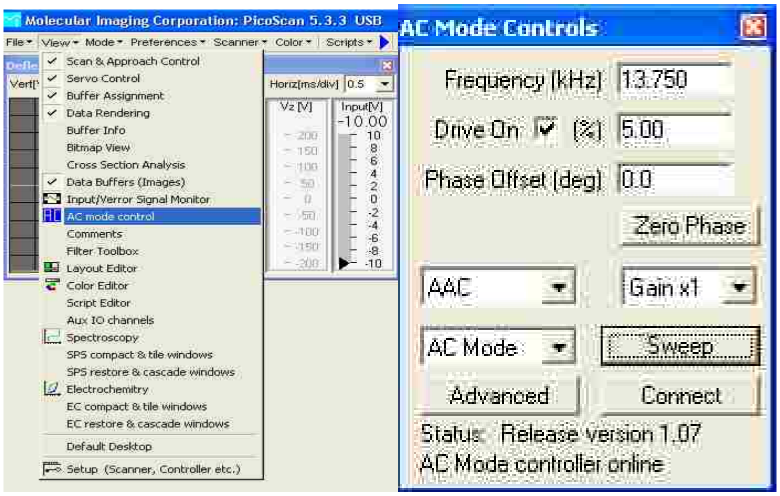

Frequency (kHz) 13.750

Drive On ☑ (%) 5.00

Phase Offset (deg) 0.0

AAC

Gain x1

AC Mode

Status: Release version 1.07

AC Mode controller online

4. Check **drive on.**

5. Enter **5** for the **drive %**

6. Set the **Gain** to **1x.**

7. Click the **Sweep** button. The AFM AC mode frequency plot will appear.

Scanning range high value

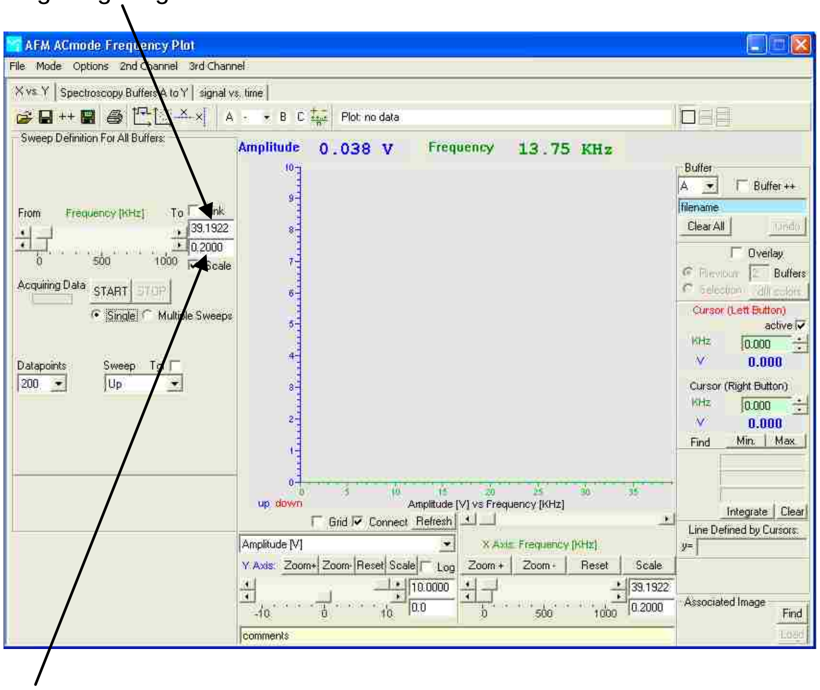

Amplitude 0.038 V Frequency 13.75 KHz

To: 39.1922, 0.2000 ☑ Scale

Datapoints: 200 Sweep: Up

Buffer: A

Cursor (Left Button): KHz 0.000, V 0.000

Cursor (Right Button): KHz 0.000, V 0.000

Y Axis: Amplitude [V] 10.0000 0.0

X Axis: 39.1922 0.2000

Scanning range low value

8. A full scale scan of the cantilever frequency should be performed.
    a. Drag the top frequency slider completely to the right and the bottom frequency slider to the left.
    b. Click the **start** button.

    The peak obtained corresponds to the resonant frequency of the cantilever.

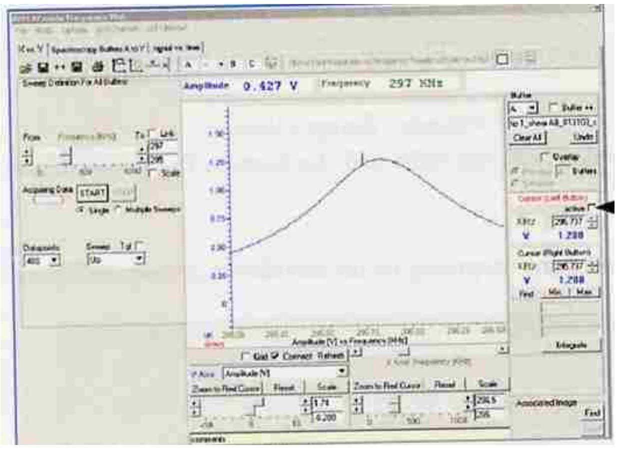

.

c. Narrow the resonance peak frequency by adjusting the frequency slider until the resonance peak is centered on the plot.

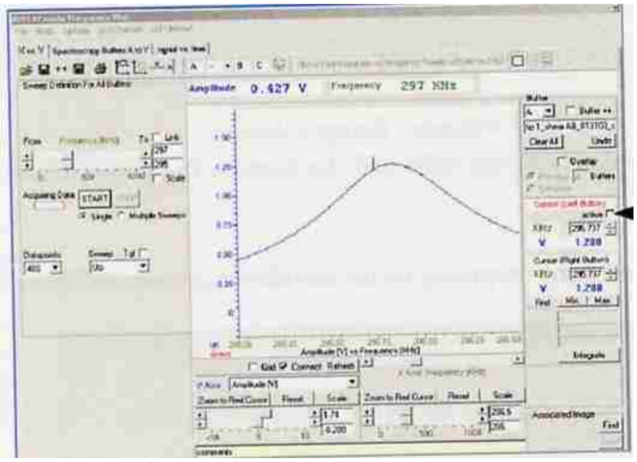

Amplitude 0.427 V Frequency 297 KHz

d. Click the **Start** button for another frequency sweep.

e. Repeat steps 8b-8d until the frequency range is less than 10 kHz and the amplitude is between 3-7.

f. Check the Active check box in the Frequency plot window.

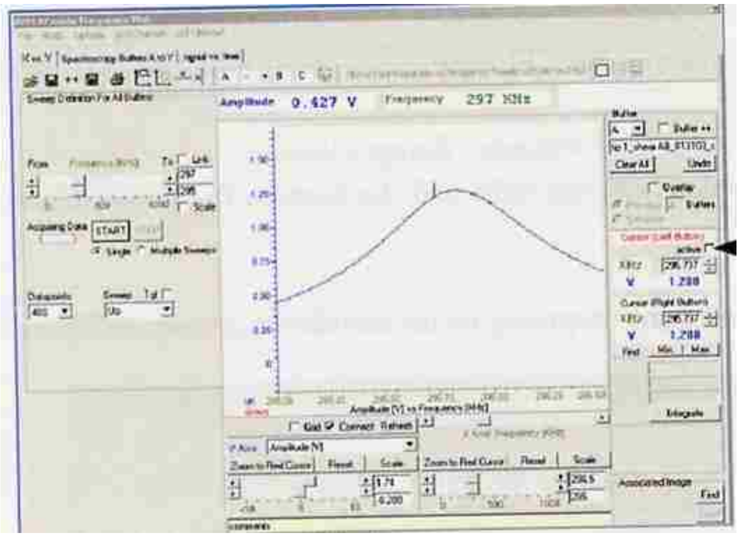

Amplitude 0.427 V Frequency 297 KHz

g. Left click on the left side of the peak maximum to get the exact resonance frequency.

h. Adjust the drive frequency to 5 ± 1 Volts.

i. Set the **Proportional (P)** gain to 0.5 and the **integral (I)** gain % to 1.000 in the Servo tab of the Servo Control window.

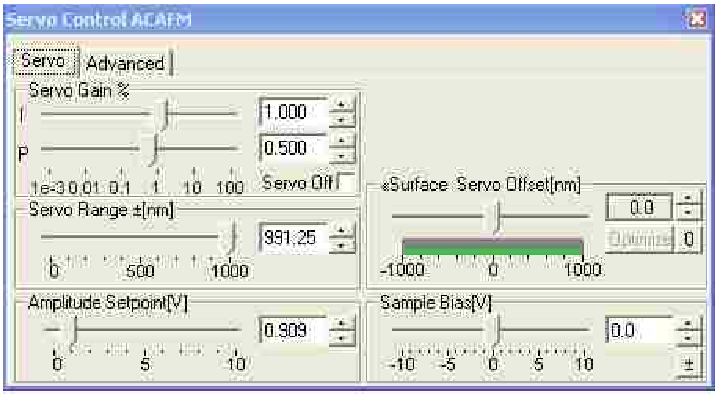

Servo Gain %
I 1.000
P 0.500
Servo Off ☐
Servo Range ±[nm] 991.25
Amplitude Setpoint[V] 0.909
Surface Servo Offset[nm] 0.0
Optimize 0
Sample Bias[V] 0.0

Make sure the Servo Range is set to its maximum value.

9. Ready to approach.

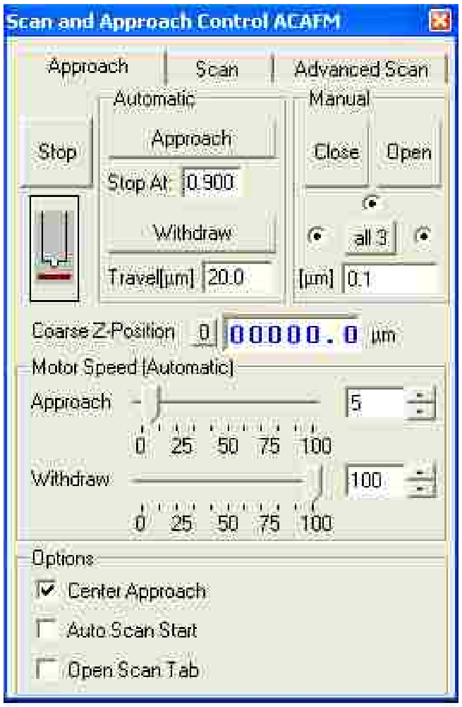

Stop At: 0.900
Travel[µm] 20.0
[µm] 0.1
Coarse Z-Position 0 00000.0 µm
Motor Speed (Automatic)
Approach 5
Withdraw 100
☑ Center Approach
☐ Auto Scan Start
☐ Open Scan Tab

The approach speed should be around 10.

The scan speed should be around 1.0-3.0.

10. Click Approach button. When it has engaged, this message will appear.

FORCE SETPOINT REACHED - SERVO ACTIVE

11. Adjust the amplitude setpoint below the initial amplitude.

12. Optimize imaging resolution by changing speed, I/P gains and set point.

APPENDIX G. LETTERS OF PERMISSION

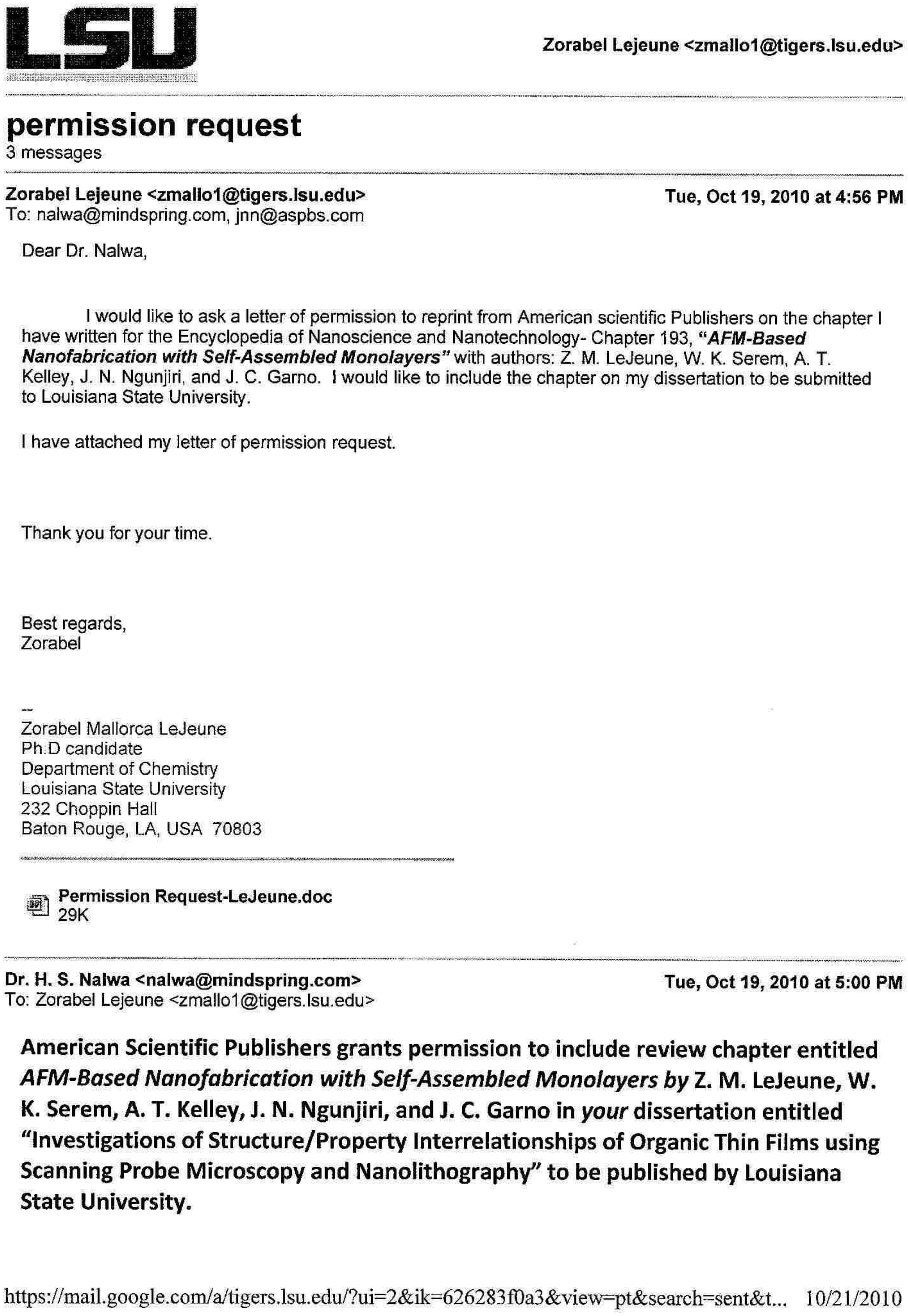

LSU

Zorabel Lejeune <zmallo1@tigers.lsu.edu>

permission request

3 messages

Zorabel Lejeune <zmallo1@tigers.lsu.edu> **Tue, Oct 19, 2010 at 4:56 PM**
To: nalwa@mindspring.com, jnn@aspbs.com

Dear Dr. Nalwa,

I would like to ask a letter of permission to reprint from American scientific Publishers on the chapter I have written for the Encyclopedia of Nanoscience and Nanotechnology- Chapter 193, ***"AFM-Based Nanofabrication with Self-Assembled Monolayers"*** with authors: Z. M. LeJeune, W. K. Serem, A. T. Kelley, J. N. Ngunjiri, and J. C. Garno. I would like to include the chapter on my dissertation to be submitted to Louisiana State University.

I have attached my letter of permission request.

Thank you for your time.

Best regards,
Zorabel

--
Zorabel Mallorca LeJeune
Ph.D candidate
Department of Chemistry
Louisiana State University
232 Choppin Hall
Baton Rouge, LA, USA 70803

Permission Request-LeJeune.doc
29K

Dr. H. S. Nalwa <nalwa@mindspring.com> **Tue, Oct 19, 2010 at 5:00 PM**
To: Zorabel Lejeune <zmallo1@tigers.lsu.edu>

American Scientific Publishers grants permission to include review chapter entitled *AFM-Based Nanofabrication with Self-Assembled Monolayers by* Z. M. LeJeune, W. K. Serem, A. T. Kelley, J. N. Ngunjiri, and J. C. Garno in *your* dissertation entitled "Investigations of Structure/Property Interrelationships of Organic Thin Films using Scanning Probe Microscopy and Nanolithography" to be published by Louisiana State University.

https://mail.google.com/a/tigers.lsu.edu/?ui=2&ik=626283f0a3&view=pt&search=sent&t... 10/21/2010

ELSEVIER LICENSE
TERMS AND CONDITIONS

Oct 21, 2010

This is a License Agreement between Zorabel M LeJeune ("You") and Elsevier ("Elsevier") provided by Copyright Clearance Center ("CCC"). The license consists of your order details, the terms and conditions provided by Elsevier, and the payment terms and conditions.

All payments must be made in full to CCC. For payment instructions, please see information listed at the bottom of this form.

Supplier	Elsevier Limited The Boulevard,Langford Lane Kidlington,Oxford,OX5 1GB,UK
Registered Company Number	1982084
Customer name	Zorabel M LeJeune
Customer address	790 Emory Valley Rd. Apt. 812 Oak Ridge, TN 37830
License number	2525970523104
License date	Oct 11, 2010
Licensed content publisher	Elsevier
Licensed content publication	Journal of the Association for Laboratory Automation
Licensed content title	Automated Scanning Probe Lithography With *n*-Alkanethiol Self-Assembled Monolayers on Au(111): Application for Teaching Undergraduate Laboratories
Licensed content author	Treva T. Brown, Zorabel M. LeJeune, Kai Liu, Sean Hardin, Jie-Ren Li, Kresimir Rupnik, Jayne C. Garno
Licensed content date	6 October 2010
Licensed content volume number	n/a
Licensed content issue number	n/a
Number of pages	1
Type of Use	reuse in a thesis/dissertation
Portion	full article
Format	both print and electronic
Are you the author of this Elsevier article?	Yes
Will you be translating?	No
Order reference number	
Title of your thesis/dissertation	INVESTIGATIONS OF STRUCTURE / PROPERTY INTERRELATIONSHIPS OF ORGANIC THIN FILMS USING SCANNING PROBE MICROSCOPY AND NANOLITHOGRAPHY

Expected completion date	Nov 2010
Estimated size (number of pages)	170
Elsevier VAT number	GB 494 6272 12

Terms and Conditions

INTRODUCTION

1. The publisher for this copyrighted material is Elsevier. By clicking "accept" in connection with completing this licensing transaction, you agree that the following terms and conditions apply to this transaction (along with the Billing and Payment terms and conditions established by Copyright Clearance Center, Inc. ("CCC"), at the time that you opened your Rightslink account and that are available at any time at http://myaccount.copyright.com).

GENERAL TERMS

2. Elsevier hereby grants you permission to reproduce the aforementioned material subject to the terms and conditions indicated.

3. Acknowledgement: If any part of the material to be used (for example, figures) has appeared in our publication with credit or acknowledgement to another source, permission must also be sought from that source. If such permission is not obtained then that material may not be included in your publication/copies. Suitable acknowledgement to the source must be made, either as a footnote or in a reference list at the end of your publication, as follows:

"Reprinted from Publication title, Vol /edition number, Author(s), Title of article / title of chapter, Pages No., Copyright (Year), with permission from Elsevier [OR APPLICABLE SOCIETY COPYRIGHT OWNER]." Also Lancet special credit - "Reprinted from The Lancet, Vol. number, Author(s), Title of article, Pages No., Copyright (Year), with permission from Elsevier."

4. Reproduction of this material is confined to the purpose and/or media for which permission is hereby given.

5. Altering/Modifying Material: Not Permitted. However figures and illustrations may be altered/adapted minimally to serve your work. Any other abbreviations, additions, deletions and/or any other alterations shall be made only with prior written authorization of Elsevier Ltd. (Please contact Elsevier at permissions@elsevier.com)

6. If the permission fee for the requested use of our material is waived in this instance, please be advised that your future requests for Elsevier materials may attract a fee.

7. Reservation of Rights: Publisher reserves all rights not specifically granted in the combination of (i) the license details provided by you and accepted in the course of this licensing transaction, (ii) these terms and conditions and (iii) CCC's Billing and Payment terms and conditions.

8. License Contingent Upon Payment: While you may exercise the rights licensed

immediately upon issuance of the license at the end of the licensing process for the transaction, provided that you have disclosed complete and accurate details of your proposed use, no license is finally effective unless and until full payment is received from you (either by publisher or by CCC) as provided in CCC's Billing and Payment terms and conditions. If full payment is not received on a timely basis, then any license preliminarily granted shall be deemed automatically revoked and shall be void as if never granted. Further, in the event that you breach any of these terms and conditions or any of CCC's Billing and Payment terms and conditions, the license is automatically revoked and shall be void as if never granted. Use of materials as described in a revoked license, as well as any use of the materials beyond the scope of an unrevoked license, may constitute copyright infringement and publisher reserves the right to take any and all action to protect its copyright in the materials.

9. Warranties: Publisher makes no representations or warranties with respect to the licensed material.

10. Indemnity: You hereby indemnify and agree to hold harmless publisher and CCC, and their respective officers, directors, employees and agents, from and against any and all claims arising out of your use of the licensed material other than as specifically authorized pursuant to this license.

11. No Transfer of License: This license is personal to you and may not be sublicensed, assigned, or transferred by you to any other person without publisher's written permission.

12. No Amendment Except in Writing: This license may not be amended except in a writing signed by both parties (or, in the case of publisher, by CCC on publisher's behalf).

13. Objection to Contrary Terms: Publisher hereby objects to any terms contained in any purchase order, acknowledgment, check endorsement or other writing prepared by you, which terms are inconsistent with these terms and conditions or CCC's Billing and Payment terms and conditions. These terms and conditions, together with CCC's Billing and Payment terms and conditions (which are incorporated herein), comprise the entire agreement between you and publisher (and CCC) concerning this licensing transaction. In the event of any conflict between your obligations established by these terms and conditions and those established by CCC's Billing and Payment terms and conditions, these terms and conditions shall control.

14. Revocation: Elsevier or Copyright Clearance Center may deny the permissions described in this License at their sole discretion, for any reason or no reason, with a full refund payable to you. Notice of such denial will be made using the contact information provided by you. Failure to receive such notice will not alter or invalidate the denial. In no event will Elsevier or Copyright Clearance Center be responsible or liable for any costs, expenses or damage incurred by you as a result of a denial of your permission request, other than a refund of the amount(s) paid by you to Elsevier and/or Copyright Clearance Center for denied permissions.

LIMITED LICENSE

The following terms and conditions apply only to specific license types:

15. **Translation**: This permission is granted for non-exclusive world **English** rights only unless your license was granted for translation rights. If you licensed translation rights you may only translate this content into the languages you requested. A professional translator must perform all translations and reproduce the content word for word preserving the integrity of the article. If this license is to re-use 1 or 2 figures then permission is granted for non-exclusive world rights in all languages.

16. **Website**: The following terms and conditions apply to electronic reserve and author websites:
Electronic reserve: If licensed material is to be posted to website, the web site is to be password-protected and made available only to bona fide students registered on a relevant course if:
This license was made in connection with a course,
This permission is granted for 1 year only. You may obtain a license for future website posting,
All content posted to the web site must maintain the copyright information line on the bottom of each image,
A hyper-text must be included to the Homepage of the journal from which you are licensing at http://www.sciencedirect.com/science/journal/xxxxx or the Elsevier homepage for books at http://www.elsevier.com , and
Central Storage: This license does not include permission for a scanned version of the material to be stored in a central repository such as that provided by Heron/XanEdu.

17. **Author website** for journals with the following additional clauses:

All content posted to the web site must maintain the copyright information line on the bottom of each image, and
he permission granted is limited to the personal version of your paper. You are not allowed to download and post the published electronic version of your article (whether PDF or HTML, proof or final version), nor may you scan the printed edition to create an electronic version,
A hyper-text must be included to the Homepage of the journal from which you are licensing at http://www.sciencedirect.com/science/journal/xxxxx , As part of our normal production process, you will receive an e-mail notice when your article appears on Elsevier's online service ScienceDirect (www.sciencedirect.com). That e-mail will include the article's Digital Object Identifier (DOI). This number provides the electronic link to the published article and should be included in the posting of your personal version. We ask that you wait until you receive this e-mail and have the DOI to do any posting.
Central Storage: This license does not include permission for a scanned version of the material to be stored in a central repository such as that provided by Heron/XanEdu.

18. **Author website** for books with the following additional clauses:
Authors are permitted to place a brief summary of their work online only.
A hyper-text must be included to the Elsevier homepage at http://www.elsevier.com

All content posted to the web site must maintain the copyright information line on the bottom of each image
You are not allowed to download and post the published electronic version of your chapter, nor may you scan the printed edition to create an electronic version.
Central Storage: This license does not include permission for a scanned version of the

material to be stored in a central repository such as that provided by Heron/XanEdu.

19. **Website** (regular and for author): A hyper-text must be included to the Homepage of the journal from which you are licensing at http://www.sciencedirect.com/science/journal/xxxxx. or for books to the Elsevier homepage at http://www.elsevier.com

20. **Thesis/Dissertation**: If your license is for use in a thesis/dissertation your thesis may be submitted to your institution in either print or electronic form. Should your thesis be published commercially, please reapply for permission. These requirements include permission for the Library and Archives of Canada to supply single copies, on demand, of the complete thesis and include permission for UMI to supply single copies, on demand, of the complete thesis. Should your thesis be published commercially, please reapply for permission.

21. **Other Conditions**: Please note that as one of the Authors of this article, you retain the right to include the journal article, in full or in part, in a thesis or dissertation. You do not require permission to do so.

v1.6

Gratis licenses (referencing $0 in the Total field) are free. Please retain this printable license for your reference. No payment is required.

If you would like to pay for this license now, please remit this license along with your payment made payable to "COPYRIGHT CLEARANCE CENTER" otherwise you will be invoiced within 48 hours of the license date. Payment should be in the form of a check or money order referencing your account number and this invoice number RLNK10863802.
Once you receive your invoice for this order, you may pay your invoice by credit card. Please follow instructions provided at that time.

Make Payment To:
Copyright Clearance Center
Dept 001
P.O. Box 843006
Boston, MA 02284-3006

If you find copyrighted material related to this license will not be used and wish to cancel, please contact us referencing this license number 2525970523104 and noting the reason for cancellation.

Questions? customercare@copyright.com or +1-877-622-5543 (toll free in the US) or +1-978-646-2777.

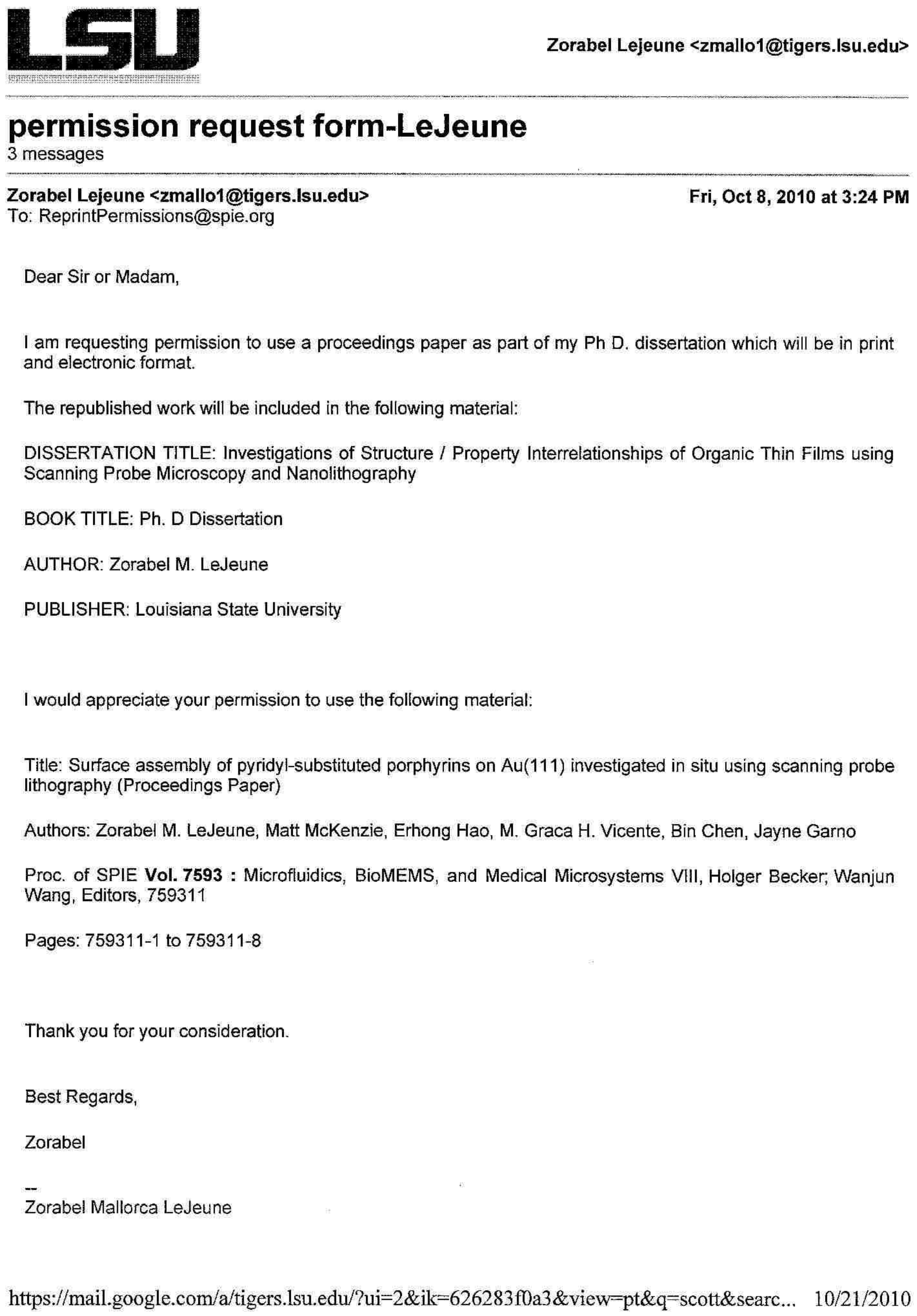

Zorabel Lejeune <zmallo1@tigers.lsu.edu>

permission request form-LeJeune

3 messages

Zorabel Lejeune <zmallo1@tigers.lsu.edu> **Fri, Oct 8, 2010 at 3:24 PM**
To: ReprintPermissions@spie.org

Dear Sir or Madam,

I am requesting permission to use a proceedings paper as part of my Ph D. dissertation which will be in print and electronic format.

The republished work will be included in the following material:

DISSERTATION TITLE: Investigations of Structure / Property Interrelationships of Organic Thin Films using Scanning Probe Microscopy and Nanolithography

BOOK TITLE: Ph. D Dissertation

AUTHOR: Zorabel M. LeJeune

PUBLISHER: Louisiana State University

I would appreciate your permission to use the following material:

Title: Surface assembly of pyridyl-substituted porphyrins on Au(111) investigated in situ using scanning probe lithography (Proceedings Paper)

Authors: Zorabel M. LeJeune, Matt McKenzie, Erhong Hao, M. Graca H. Vicente, Bin Chen, Jayne Garno

Proc. of SPIE **Vol. 7593 :** Microfluidics, BioMEMS, and Medical Microsystems VIII, Holger Becker; Wanjun Wang, Editors, 759311

Pages: 759311-1 to 759311-8

Thank you for your consideration.

Best Regards,

Zorabel

--
Zorabel Mallorca LeJeune

https://mail.google.com/a/tigers.lsu.edu/?ui=2&ik=626283f0a3&view=pt&q=scott&searc... 10/21/2010

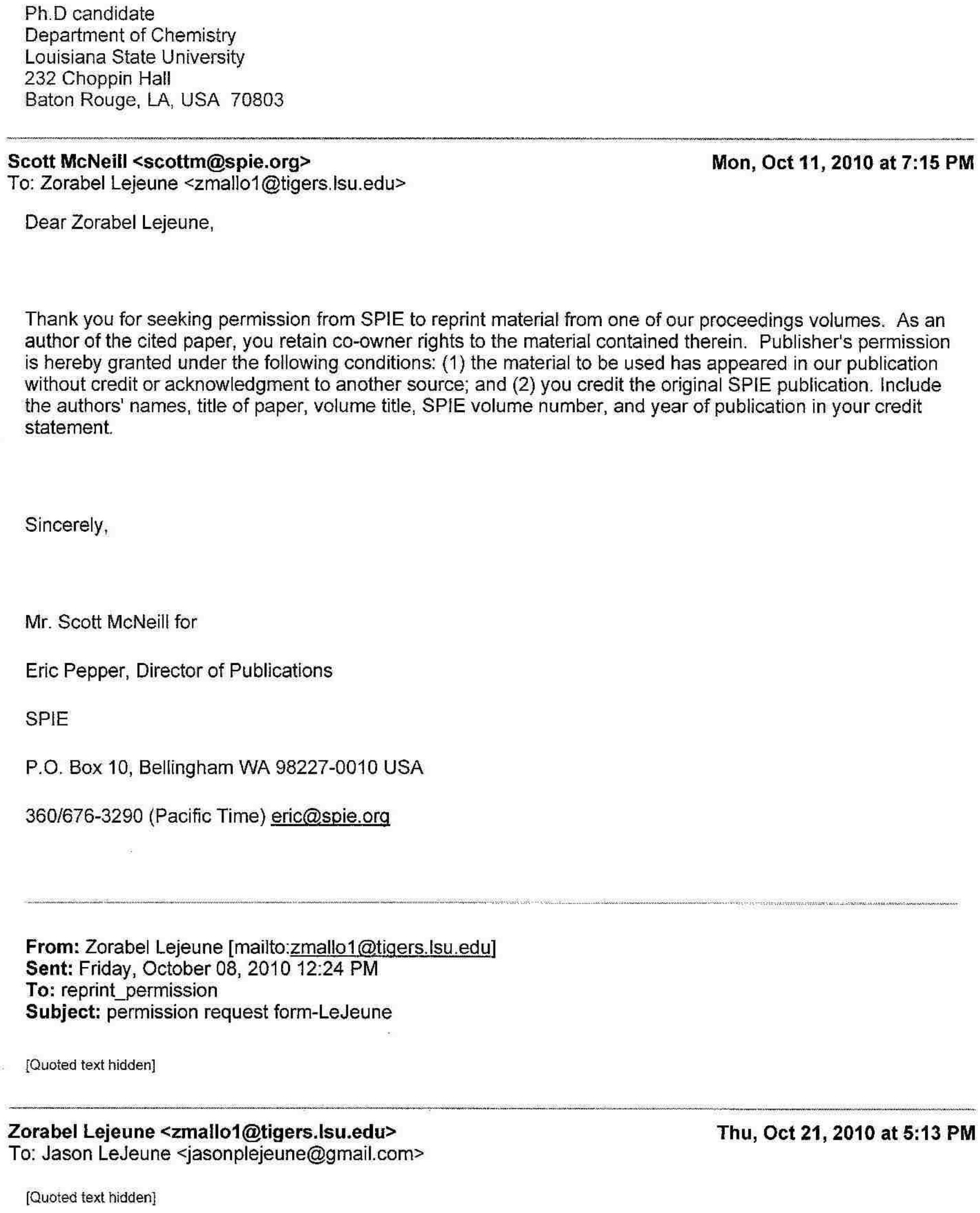

Ph.D candidate
Department of Chemistry
Louisiana State University
232 Choppin Hall
Baton Rouge, LA, USA 70803

Scott McNeill <scottm@spie.org> **Mon, Oct 11, 2010 at 7:15 PM**
To: Zorabel Lejeune <zmallo1@tigers.lsu.edu>

Dear Zorabel Lejeune,

Thank you for seeking permission from SPIE to reprint material from one of our proceedings volumes. As an author of the cited paper, you retain co-owner rights to the material contained therein. Publisher's permission is hereby granted under the following conditions: (1) the material to be used has appeared in our publication without credit or acknowledgment to another source; and (2) you credit the original SPIE publication. Include the authors' names, title of paper, volume title, SPIE volume number, and year of publication in your credit statement.

Sincerely,

Mr. Scott McNeill for

Eric Pepper, Director of Publications

SPIE

P.O. Box 10, Bellingham WA 98227-0010 USA

360/676-3290 (Pacific Time) eric@spie.org

From: Zorabel Lejeune [mailto:zmallo1@tigers.lsu.edu]
Sent: Friday, October 08, 2010 12:24 PM
To: reprint_permission
Subject: permission request form-LeJeune

[Quoted text hidden]

Zorabel Lejeune <zmallo1@tigers.lsu.edu> **Thu, Oct 21, 2010 at 5:13 PM**
To: Jason LeJeune <jasonplejeune@gmail.com>

[Quoted text hidden]

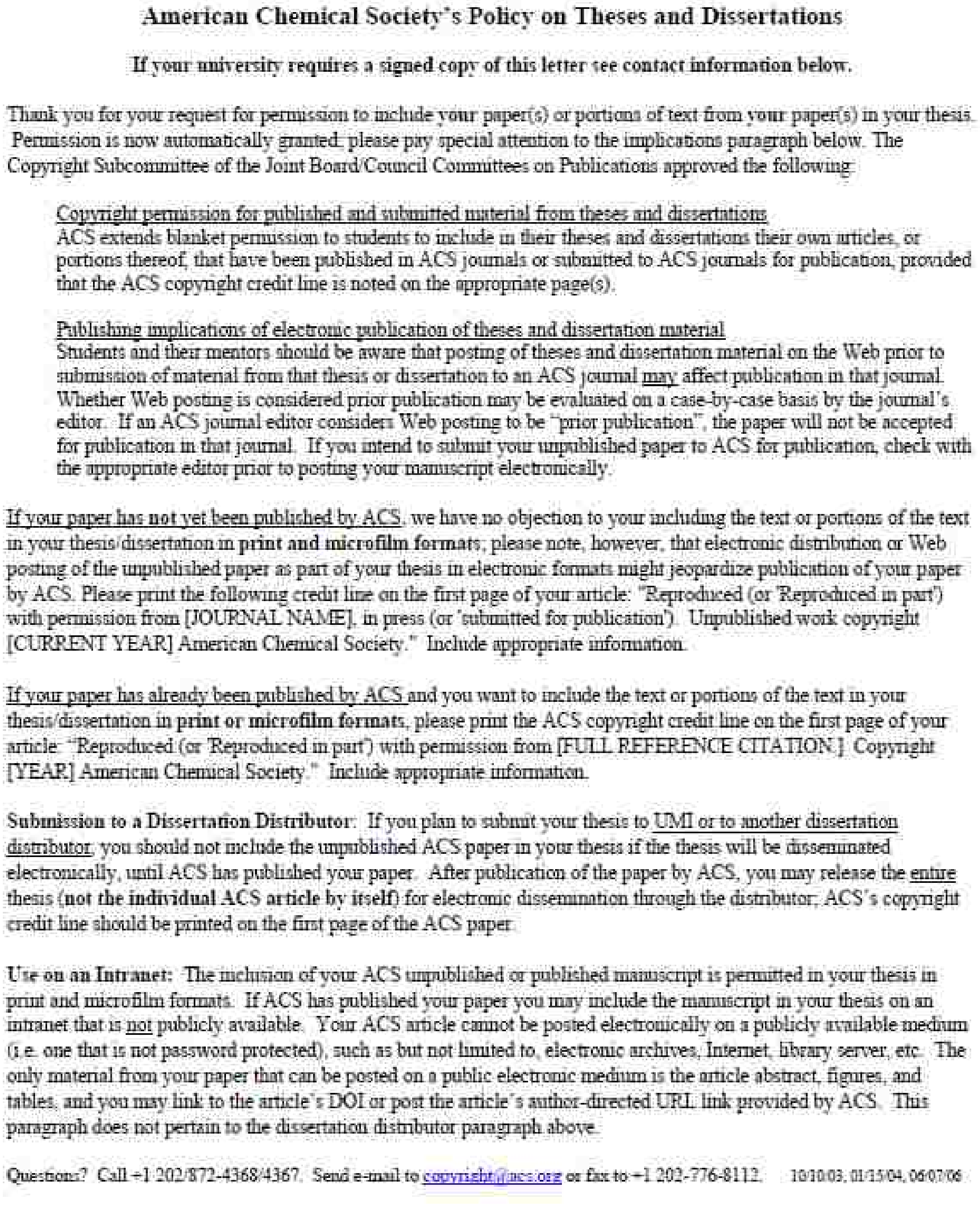

American Chemical Society's Policy on Theses and Dissertations

If your university requires a signed copy of this letter see contact information below.

Thank you for your request for permission to include your paper(s) or portions of text from your paper(s) in your thesis. Permission is now automatically granted; please pay special attention to the implications paragraph below. The Copyright Subcommittee of the Joint Board/Council Committees on Publications approved the following:

> Copyright permission for published and submitted material from theses and dissertations
> ACS extends blanket permission to students to include in their theses and dissertations their own articles, or portions thereof, that have been published in ACS journals or submitted to ACS journals for publication, provided that the ACS copyright credit line is noted on the appropriate page(s).
>
> Publishing implications of electronic publication of theses and dissertation material
> Students and their mentors should be aware that posting of theses and dissertation material on the Web prior to submission of material from that thesis or dissertation to an ACS journal may affect publication in that journal. Whether Web posting is considered prior publication may be evaluated on a case-by-case basis by the journal's editor. If an ACS journal editor considers Web posting to be "prior publication", the paper will not be accepted for publication in that journal. If you intend to submit your unpublished paper to ACS for publication, check with the appropriate editor prior to posting your manuscript electronically.

If your paper has **not** yet been published by ACS, we have no objection to your including the text or portions of the text in your thesis/dissertation in **print and microfilm formats**; please note, however, that electronic distribution or Web posting of the unpublished paper as part of your thesis in electronic formats might jeopardize publication of your paper by ACS. Please print the following credit line on the first page of your article: "Reproduced (or 'Reproduced in part') with permission from [JOURNAL NAME], in press (or 'submitted for publication'). Unpublished work copyright [CURRENT YEAR] American Chemical Society." Include appropriate information.

If your paper has already been published by ACS and you want to include the text or portions of the text in your thesis/dissertation in **print or microfilm formats**, please print the ACS copyright credit line on the first page of your article: "Reproduced (or 'Reproduced in part') with permission from [FULL REFERENCE CITATION.] Copyright [YEAR] American Chemical Society." Include appropriate information.

Submission to a Dissertation Distributor: If you plan to submit your thesis to UMI or to another dissertation distributor, you should not include the unpublished ACS paper in your thesis if the thesis will be disseminated electronically, until ACS has published your paper. After publication of the paper by ACS, you may release the entire thesis (**not the individual ACS article by itself**) for electronic dissemination through the distributor; ACS's copyright credit line should be printed on the first page of the ACS paper.

Use on an Intranet: The inclusion of your ACS unpublished or published manuscript is permitted in your thesis in print and microfilm formats. If ACS has published your paper you may include the manuscript in your thesis on an intranet that is not publicly available. Your ACS article cannot be posted electronically on a publicly available medium (i.e. one that is not password protected), such as but not limited to, electronic archives, Internet, library server, etc. The only material from your paper that can be posted on a public electronic medium is the article abstract, figures, and tables, and you may link to the article's DOI or post the article's author-directed URL link provided by ACS. This paragraph does not pertain to the dissertation distributor paragraph above.

Questions? Call +1 202/872-4368/4367. Send e-mail to copyright@acs.org or fax to +1 202-776-8112. 10/10/03, 01/15/04, 06/07/06

VITA

Zorabel Escondida Mallorca LeJeune was born in Pigcawayan, North Cotabato, Philippines, to Jessie and Remedios Mallorca. She graduated valedictorian from both Midsayap Pilot Elementary School and Notre Dame of Midsayap for Girls. Zorabel received her Bachelor of Science degree in agricultural chemistry from University of the Philippines Los Baños in 1999. Upon graduation, she joined the Quality Assurance and Chemistry Division of United Laboratories, Inc. In fall 2004, she enrolled in the doctoral program for analytical chemistry at Louisiana State University where she joined the research group of Dr. Jayne C. Garno.

During her graduate years, the LSU Department of Chemistry has given her several recognitions, including the Colgate-Palmolive and Departmental Teaching Scholar Award (2006) and the Outstanding Teaching Award in Analytical Chemistry (2007). For excellence in research, she was awarded the LSU Department of Chemistry Research Scholar in 2008 and Procter and Gamble Research Award in 2009. Her final year at LSU was culminated with James Traynham Distinguished Graduate Student Award.

Zorabel has participated in regional, national and international meetings presenting her research in contributed and invited talks, and poster presentations. To finance her attendance in conferences, she received multiple travel awards including Coates Graduate Award (2009), LSU graduate travel stipend (2006 and 2009), and National Science Foundation (DMR-0630575) Student Travel Award (2006). Her research projects along with her presentation skills garnered best poster awards at conferences both at Pittcon 2010 in Orlando Florida; and at the Society for Applied Spectroscopy (SAS) symposium during the 34th National Meeting, Federation of Analytical Chemistry & Spectroscopy Societies (FACSS 2007) in Memphis, Tennessee.

The degree of Doctor of Philosophy will be conferred to Zorabel at the Fall 2010 Commencement at Louisiana State University, Baton Rouge, Louisiana.